

NASA/CR—2005-213325



# Low Noise Exhaust Nozzle Technology Development

R.K. Majjigi, C. Balan, V. Mengle, J.F. Brausch, H. Shin, and J.W. Askew  
General Electric Aircraft Engines, Cincinnati, Ohio

---

February 2005

## The NASA STI Program Office . . . in Profile

Since its founding, NASA has been dedicated to the advancement of aeronautics and space science. The NASA Scientific and Technical Information (STI) Program Office plays a key part in helping NASA maintain this important role.

The NASA STI Program Office is operated by Langley Research Center, the Lead Center for NASA's scientific and technical information. The NASA STI Program Office provides access to the NASA STI Database, the largest collection of aeronautical and space science STI in the world. The Program Office is also NASA's institutional mechanism for disseminating the results of its research and development activities. These results are published by NASA in the NASA STI Report Series, which includes the following report types:

- **TECHNICAL PUBLICATION.** Reports of completed research or a major significant phase of research that present the results of NASA programs and include extensive data or theoretical analysis. Includes compilations of significant scientific and technical data and information deemed to be of continuing reference value. NASA's counterpart of peer-reviewed formal professional papers but has less stringent limitations on manuscript length and extent of graphic presentations.
- **TECHNICAL MEMORANDUM.** Scientific and technical findings that are preliminary or of specialized interest, e.g., quick release reports, working papers, and bibliographies that contain minimal annotation. Does not contain extensive analysis.
- **CONTRACTOR REPORT.** Scientific and technical findings by NASA-sponsored contractors and grantees.

- **CONFERENCE PUBLICATION.** Collected papers from scientific and technical conferences, symposia, seminars, or other meetings sponsored or cosponsored by NASA.
- **SPECIAL PUBLICATION.** Scientific, technical, or historical information from NASA programs, projects, and missions, often concerned with subjects having substantial public interest.
- **TECHNICAL TRANSLATION.** English-language translations of foreign scientific and technical material pertinent to NASA's mission.

Specialized services that complement the STI Program Office's diverse offerings include creating custom thesauri, building customized databases, organizing and publishing research results . . . even providing videos.

For more information about the NASA STI Program Office, see the following:

- Access the NASA STI Program Home Page at <http://www.sti.nasa.gov>
- E-mail your question via the Internet to [help@sti.nasa.gov](mailto:help@sti.nasa.gov)
- Fax your question to the NASA Access Help Desk at 301-621-0134
- Telephone the NASA Access Help Desk at 301-621-0390
- Write to:  
NASA Access Help Desk  
NASA Center for AeroSpace Information  
7121 Standard Drive  
Hanover, MD 21076

NASA/CR—2005-213325



# Low Noise Exhaust Nozzle Technology Development

R.K. Majjigi, C. Balan, V. Mengle, J.F. Brausch, H. Shin, and J.W. Askew  
General Electric Aircraft Engines, Cincinnati, Ohio

Prepared under Contract NAS3-25415

National Aeronautics and  
Space Administration

Glenn Research Center

---

February 2005

## Document History

This research was originally published internally as HSR044 in November 1996.

Note that at the time of research, the NASA Lewis Research Center was undergoing a name change to the NASA John H. Glenn Research Center at Lewis Field. Both names may appear in this report.

Available from

NASA Center for Aerospace Information  
7121 Standard Drive  
Hanover, MD 21076

National Technical Information Service  
5285 Port Royal Road  
Springfield, VA 22100

Available electronically at <http://gltrs.grc.nasa.gov>

# Table of Contents

	<u>Page</u>
<b>1.0 Summary</b> .....	1
<b>2.0 Introduction</b> .....	2
2.1 Approach .....	3
2.2 Technical Highlights .....	3
2.3 Report Structure .....	4
<b>3.0 Preliminary Exhaust System Definition</b> .....	5
3.1 Baseline Exhaust System Preliminary Design .....	5
3.2 Key Geometric Parameters .....	7
3.3 Key Performance Parameters .....	13
3.4 Key Acoustic Parameters .....	15
<b>4.0 Acoustic Test Program</b> .....	16
4.1 Acoustic Models and Test Matrix .....	16
4.1.1 Model Description .....	16
4.1.2 Model Instrumentation .....	17
4.1.3 Test Facility .....	18
4.1.4 Test Matrix .....	18
4.2 Acoustic Data Analyses .....	19
4.2.1 Influence of Suppressor Area Ratio .....	20
4.2.2 Influence of Mixing Area Ratio .....	25
4.2.3 Influence of Acoustic Treatment .....	28
4.2.4 Influence of Ejector Flap Length .....	30
4.2.5 Influence of Center Wedges .....	32
4.2.6 Influence of Flight Mach Number .....	33
4.2.7 Azimuthal Acoustic Characteristics .....	36
4.2.8 Influence of Jet Temperature on Ejector Flowfields .....	37

## Table of Contents (Concluded)

	<u>Page</u>
<b>5.0 Aeroperformance Test Program</b> .....	<b>95</b>
5.1 Aeroperformance Model and Test Matrix .....	95
5.1.1 Model Description .....	95
5.1.2 Model Design Parameters .....	96
5.1.3 Test Facility and Test Setup .....	97
5.1.4 Instrumentation .....	98
5.1.5 Test Configurations and Procedure .....	99
5.2 Aeroperformance Data Analyses .....	101
5.2.1 Basic Ejector Nozzle Characteristics .....	101
5.2.2 Effect of Free-Stream Mach Number .....	103
5.2.3 Effect of Chute Expansion Ratio (CER) .....	104
5.2.4 Effect of Mixing Area Ratio (MAR) .....	105
5.2.5 Effect of Suppressor Area Ratio (SAR) .....	106
5.2.6 Effect of Ejector Flap Length .....	106
5.2.7 Effect of Center Wedges .....	107
<b>6.0 Aerodynamic-Mixing Test Program</b> .....	<b>128</b>
6.1 Test Facility, Models, and Test Matrix .....	128
6.2 Experimental Results and Analysis .....	131
6.2.1 Baseline Model .....	131
6.2.2 Model with Central Primary Gap .....	135
6.2.3 Effect of Geometric Parameters .....	135
<b>7.0 Conclusions and Recommendations</b> .....	<b>153</b>
7.1 Conclusions .....	153
7.1.1 Acoustic Performance .....	153
7.1.2 Aeroperformance .....	154
7.1.3 Aeromixing .....	155
7.2 Recommendations .....	155
<b>8.0 Symbols and Nomenclature</b> .....	<b>156</b>
<b>9.0 References</b> .....	<b>160</b>

## 1.0 Summary

Since 1986, NASA and the U.S. aerospace industry have been assessing the economic viability and environmental acceptability of a second-generation supersonic civil transport, or *High Speed Civil Transport* (HSCT). Environmental acceptability in terms of airport community noise and economic viability are critical elements in this endeavor. Development of a propulsion system that satisfies strict airport noise regulations (FAR36 Stage III levels), at acceptable performance and weight, is critical to the success of any HSCT program. In support of HSCT development, GEAE (GE Aircraft Engines), under contract to the NASA Lewis Research Center (Contract NAS3-25415), has conducted this *Low Noise Exhaust Nozzle Technology Development* program. Three separate tests were conducted in GEAE's Cell 41 free-jet anechoic chamber, the NASA Langley 16-ft transonic wind tunnel, and GEAE's Aerodynamic Research Laboratory (ARL) to evaluate hot acoustic, ambient aerodynamic, and warm-mixing performance aspects of the two-dimensional (2D) mixer ejector exhaust system concept.

Of the many acoustic configurations tested, SAR 2.8 and SAR 3.3, treated-wall, long-flap (120-in full scale) configurations meet FAR36 Stage 3 sideline noise levels for ideal primary jet velocities ( $V_j \leq 2400$  ft/s. (SAR, suppressor area ratio, = mixed-flow area  $\div$  primary nozzle throat area.) For  $V_j < 2450$  ft/s, the SAR 2.8 nozzle is slightly quieter than the SAR 3.3 nozzle, but the trend reverses for  $V_j > 2500$  ft/s.

Ejector acoustic treatment yields about 3 EPNdB (effective perceived noise decibel) suppression at a nominal  $V_j = 2400$  ft/s, and the noise suppression due to treatment increases to approximately 4 EPNdB for  $V_j < 2000$  ft/s.

Increasing the flap length from 80 to 120 inches in full scale for treated configuration results in an average noise reduction of 2.6 EPNdB in the  $V_j$  range of 1600 to 2800 ft/s; the effect for hard-walled configurations is 1.7 EPNdB reduction in the same  $V_j$  range.

For  $V_j > 2200$  ft/s, mixing area ratio (MAR = overall exhaust system exit  $\div$  mixing-plane area) was identified as a very significant ejector nozzle parameter to influence both acoustic and aerodynamic performance characteristics. The MAR 0.95 nozzle is approximately 3 EPNdB quieter than the MAR 1.2 nozzle. Although MAR 1.2 entrains more secondary flow than MAR 0.95, noise levels for MAR 0.95 are significantly lower compared to MAR 1.2, due to various flowfield differences.

Two modes of ejector operation, subsonic and supersonic, were identified. Transition from subsonic to supersonic mode is affected by primary stream total temperature, and nozzle performance in the supersonic mode is higher. At low MAR (0.8), no transition to supersonic mode was observed.

Pumping and nozzle performance peaked at MAR = 1.0. A static coefficient of gross thrust of 0.95 was obtained under cold-flow conditions at MAR of 1.0. ( $C_{f_g}$  = measured  $\div$  ideal thrust at fully expanded isentropic flow.) Significant reduction in thrust minus drag coefficient was observed under wind-on conditions, about 5 points at nozzle pressure ratio of 4 (NPR = nozzle total pressure  $\div$  ambient pressure) and a free-stream Mach number of 0.32. Increasing SAR increased pumping and  $C_{f_g}$  at static conditions, but the benefits were not realized under wind-on conditions due to increased ram drag and external form and friction drag. A lower primary chute expansion ratio of 1.22 performed better than 1.38 at lower NPR due to reduced overexpansion losses. There was no significant difference between the 120 and 80-in full-scale flaps on performance. Based on laser velocimetry data, increased primary total temperature improved mixing.

## 2.0 Introduction

Since 1986, NASA and the U.S. aerospace industry have been assessing the economic viability and environmental acceptability of a second-generation supersonic civil transport, or *High Speed Civil Transport*. Environmental acceptability (in terms of airport community noise) and economic viability (in terms of a high-performance, lightweight propulsion system) are critical elements in this endeavor. Development of a propulsion system that satisfies strict airport noise regulations (FAR36 Stage III levels) and provides high levels of cruise and transonic performance with adequate takeoff performance, at an acceptable weight, is critical to the success of any HSCT program.

In support of HSCT development, GEAE, under contract to the NASA Lewis Research Center (NAS3-25415), conducted this *Low Noise Exhaust Nozzle Technology Development* program. The principal objectives were to:

1. Develop a preliminary design of an innovative 2D exhaust nozzle with the goal of meeting FAR36 Stage III noise levels and providing high levels of cruise performance with a high specific thrust cycle for a Mach 2.4 HSCT with a range of 5000 nmi and a payload of 51,900 lbm, for example: GEAE's GE21/F14 variable-cycle engine (VCE) study L1M.
2. Employ advanced acoustic and aerodynamic codes during preliminary design.
3. Develop a comprehensive acoustic and aerodynamic database through scale-model testing of low-noise, high-performance, 2D nozzle configurations, based on the preliminary design developed in Objective 1 above.
4. Verify acoustic and aerodynamic predictions by means of scale-model testing.

Objectives 1 and 2 were achieved during the *Base Program* of the contract, and the results are documented in Reference 1; significant conclusions are summarized below. Objectives 3 and 4 were achieved as part of the *Optional Program* of the contract and are documented in this report.

- Preliminary design of a two-dimensional, convergent/divergent (2DCD) suppressor ejector nozzle for a VCE powered (nominal airflow of 700 lbm/s at sea level), Mach 2.4 HSCT was evolved. It has the following key acoustic, aerodynamic, and mechanical design features:
  - Twenty-chute suppressor with an 80-in long, acoustically treated ejector flap
  - Convergent/divergent chutes
  - Aerodynamically efficient ejector/chute inlet
  - Nozzle weight of 5065 lbm with six actuators
- The following aero/acoustic performance was projected using existing codes and data bases:
  - Predicted noise suppression of 16.9 EPNdB at  $V_j = 2900$  ft/s
  - Predicted uninstalled supersonic  $C_{f_g} = 0.978$  (without leakage)
  - Goal uninstalled takeoff  $C_{f_g} = 0.95$ .
- FAR36 Stage III noise goals were predicted to be achievable for three takeoff scenarios:
  - a. Without *program lapse rate* (PLR) at 768,564 lbm takeoff gross weight (TOGW)
  - b. With PLR at 738,856 lbm TOGW
  - c. With PLR and 10% increase in takeoff lift/drag ratio at 708,146 lbm TOGW

- Impact of noise suppression, nozzle aerodynamic performance (cruise and takeoff), and nozzle weight on HSCT TOGW were assessed, and valuable sensitivities for future design trade studies were evolved, as summarized below:
  - Sideline noise higher by 1 EPNdB increases TOGW by 2.4%
  - Cruise performance reduced by 1% increases TOGW by 4.75%
  - Takeoff performance reduced by 1% increases TOGW by 0.8%
  - Nozzle weight increased by 2% increases TOGW by 0.35%

## 2.1 Approach

The conclusions of the *Base Program*, summarized above, indicated that a viable exhaust nozzle system in conjunction with a high-specific-thrust cycle was capable of meeting the noise suppression, nozzle performance, and weight goals for application to a Mach 2.4 HSCT, and this formed the key motivation to proceed with scale-model tests under the *Optional Program*. The approach for the *Optional Program* consisted of the following steps:

1. Develop comprehensive scale-model test programs with supportive diagnostic measurements to define the complex relationships among the mixing process of the engine primary air and ambient secondary air in the mixer/ejector nozzle, the resultant noise characteristics, and the impact on nozzle aerodynamic performance. The scope of the scale-model tests encompasses sufficient geometric and aerodynamic variations to provide a critical design database to help guide next-generation designs. Such a database would also be extremely valuable in the analytical/computational modeling of aero/acoustic phenomena of these complex mixer/ejector nozzles. (However, such activity was beyond the scope of the current program.)
2. Develop scale-model designs consistent with the preliminary design concept from the *Base Program*. Keep deviations from the preliminary design to a minimum.
3. Recognizing the significant challenge involved in achieving the projected noise suppression at high specific thrust, explore several acoustic risk-reduction concepts in the scale-model tests.
4. Compare the measured acoustic suppression and takeoff thrust performance levels to the projections made at the conclusion of the *Base Program*. Provide recommendations for the next-generation nozzle concepts.

## 2.2 Technical Highlights

The significant technical achievements of the *Optional Program* are described below.

Three scale-model test programs were successfully conducted in three separate facilities (acoustic tests in GEAE's Cell 41, nozzle aerodynamic thrust performance tests at NASA Langley's 16-ft transonic wind tunnel, and nozzle aerodynamics/mixing tests in GEAE's ARL). A high-quality, comprehensive database for acoustic, aeroperformance and aeromixing characteristics of 2DCD mixer ejector nozzles has been established; this database is very valuable in terms of developing understanding, as well as a guide for future design refinements. State-of-the-art laser diagnostic measurements were performed in the acoustic and aeromixing tests.

Noise suppression levels of 18.5 EPNdB relative to a reference conic nozzle were achieved at a mixed-flow velocity ( $V_{\text{mix}}$ ) of 2400 ft/s for the configuration with a SAR of 2.8 and treated ejector

flap length of 120 inches in full scale in GEAE's Cell 41 anechoic test facility, using approximately 1/7th scale models. The acoustic suppression data demonstrated in this test program have been instrumental in guiding the cycle downselect to a moderate-bypass-ratio mixed-flow turbofan (MFTF) with a mixer/ejector nozzle of 60 to 75% secondary flow entrainment ratio with takeoff jet velocities in the range of 2200 to 2400 ft/s. An HSCT powered by such a propulsion cycle/nozzle system is capable of achieving FAR36 Stage III sideline noise levels. The acoustic data also clearly indicated that achieving FAR36 Stage 3 noise levels at very high jet velocities (2800 ft/s and higher), with a mixer/ejector nozzle of a viable length, is a technical challenge for full-scale implementation.

Isolated nozzle thrust coefficients were measured over typical takeoff conditions in Langley's 16-ft transonic wind tunnel on approximately 1/11th scale models. Thrust data were acquired for wind tunnel Mach numbers up to about 0.7 to explore the impact of deploying the noise-suppression devices beyond the standard FAR36 Stage 3 monitoring points and address potential climb-to-cruise (CTC) noise concerns. Ejector mixing area ratio (ejector nozzle exit area  $\div$  mixing plane area) was identified as one of the key geometric parameters in terms of impact on takeoff thrust performance.

The mixer/ejector nozzle, at all test facilities, exhibited mode switching from subsonic to supersonic mode and hysteresis during NPR excursions. The critical nozzle pressure ratio ( $NPR_c$ ) at which the mode switch occurs is a function of MAR, SAR, chute expansion ratio (CER), and total temperature of the primary jet ( $T_{T8}$ ). The mode switch has a significant impact on takeoff thrust coefficient and dynamic stability but has minimal impact on acoustic suppression.

Cell 41 test results indicate total temperature of the primary stream has a significant impact on mixing of secondary and primary streams at the same primary nozzle NPR. Higher primary nozzle total temperature results in more rapid mixing of primary and secondary streams at a given primary nozzle pressure ratio. Hence, warm mixing tests carried out on 1/11th scale models in GEAE's ARL test facility indicate a pessimistic level of mixing effectiveness of mixer designs compared to mixing effectiveness at typical cycle temperatures.

## 2.3 Report Structure

Many figures are used to describe the tests and resulting data. To avoid unwieldy separation of the text pages, the illustrations in Sections 4, 5, and 6 in are presented collectively at the end of the sections.

**Section 3** briefly describes the preliminary design of the baseline exhaust system and the key geometric parameters that have significant influence on acoustic and aerodynamic performance issues addressed in this program.

**Section 4** describes the acoustic test program.

**Section 5** describes the aerodynamic performance test program.

**Section 6** describes the aerodynamic-mixing test program. Each of the above sections has a description of the model geometries and test matrices followed by analyses of key sets of data.

**Section 7** summarizes significant conclusions and offers recommendations for next-generation nozzle designs.

### 3.0 Preliminary Exhaust System Definition

The basic exhaust system considered in this program is of variable geometry, and the primary objective of the scale-model test program was to address acoustic and performance issues related to the takeoff mode configuration. A brief description of the cycle, full-scale preliminary design, and key overall geometric parameters that define the aerodynamic/acoustic performance at takeoff are discussed in this section.

#### 3.1 Baseline Exhaust System Preliminary Design

Figure 1 shows the preliminary design of the 2DCD mixer ejector nozzle evolved in the *Base Program* for the GE21/F14 Study LIM VCE to power a Mach 2.4 HSCT with a 5000-nmi range and a payload of 51,900 lbm. The nozzle is depicted in the takeoff position; the mixer chutes are deployed to break up the primary jet with alternating ambient flow entrained through the ejector inlet. Figure 2 shows the nozzle in supersonic and subsonic cruise modes; the mixer chutes are retracted from the primary stream and stowed.

Design point for the baseline exhaust system was selected to be the cycle condition that produced a net thrust of 50,000 lbf at an altitude of 689 ft and an airplane Mach number of 0.32 at a nominal airflow of 700 lbm/s, based on the airplane takeoff thrust requirements assumed in the preliminary design studies conducted in Reference 1. The cycle conditions corresponding to this thrust setting for the GE21/F14 Study LIM cycle are shown in Table 1.

Nozzle throat area is varied during takeoff as well as cruise conditions to accommodate engine flow variations. During takeoff, engine flow is held at the nominal value of 700 lbm/s as engine throttle is reduced from the sideline thrust setting to takeoff thrust (also commonly called community noise

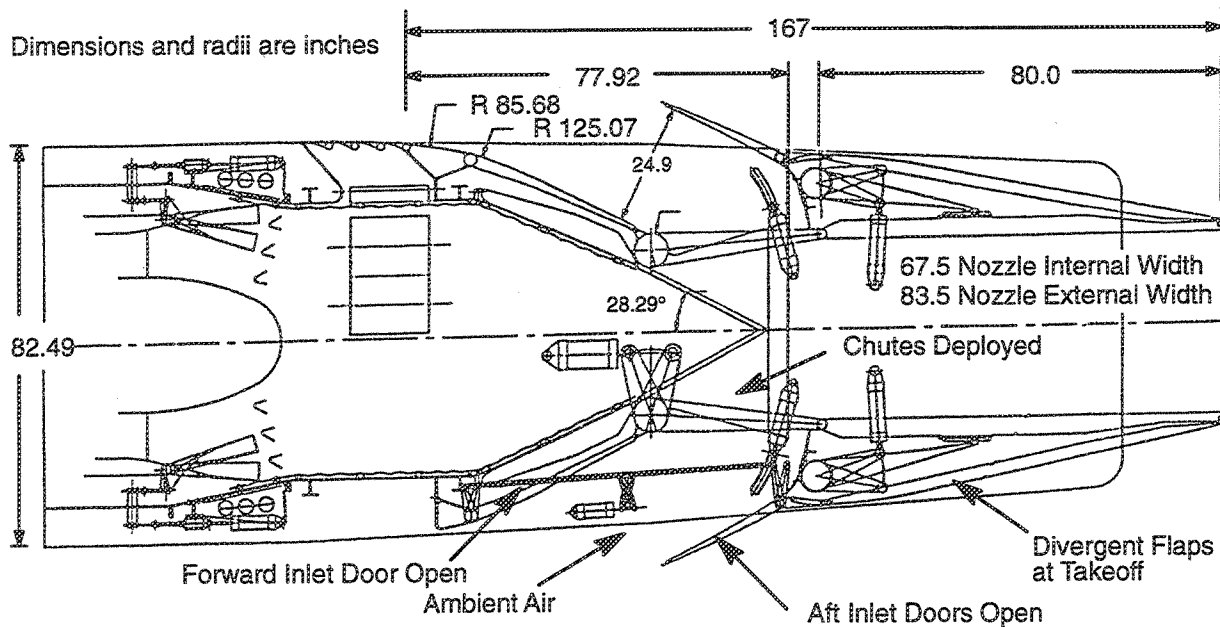


Figure 1. Preliminary design of the 2D mixer-ejector nozzle at takeoff

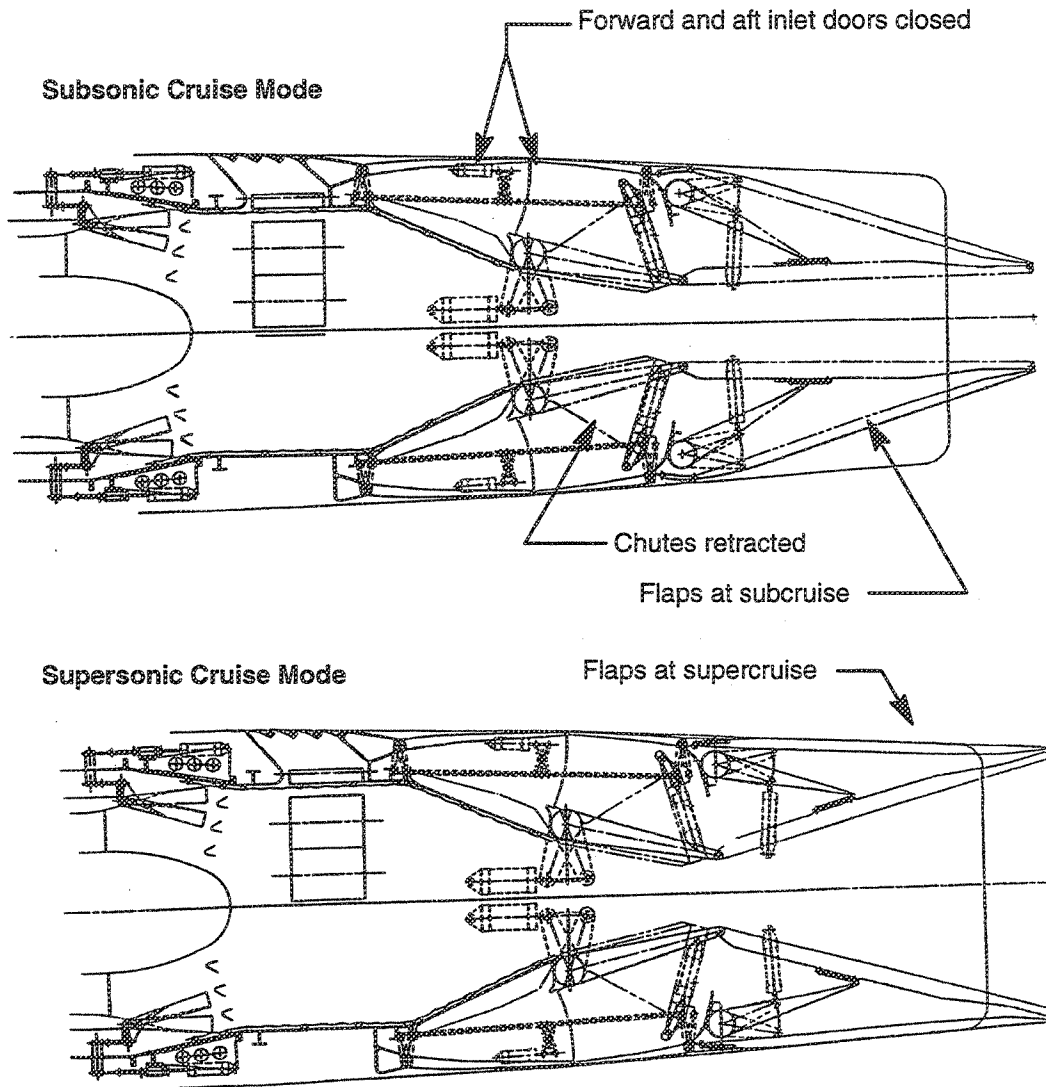


Figure 2. Two-Dimensional mixer-ejector nozzle in cruise mode configurations

Table 1. Preliminary design point cycle summary for 2D mixer-ejector exhaust system: GE21/F14 Study L1M; Mach 2.4 cruise, 700 lbm/s size

Altitude, ft	689	Power Code	68
Mach	0.322	$F_N$ , lbf	50,000
$T_{\text{ambient}}$ , °R	534.2	NPR	4.0
$P_{\text{ambient}}$ , psia	14.334	$T_7$ , °R	2040
Inlet Ram Recovery	0.97	$W_7$ , lbm/s	708.6
$T_2$ , °R	545.3	$A_{p8}$ , in <sup>2</sup>	1086
$P_2$ , psia	14.939	$A_{E8}$ , in <sup>2</sup>	1064

measurement). This thrust reduction is achieved by decreasing jet velocity, at an approximately constant engine air flow of 700 lbf/s, to help abate jet noise at the takeoff monitor. Such a thrust modulation requires an increase in nozzle throat area.

The required throat area variation for the engine operation is achieved in the full-scale preliminary design by two schemes as shown in Figure 3. In the scheme shown at the top, the primary nozzle throat area  $A_{p8}$  is controlled by holding the chutes fixed and rotating the convergent flap; this limits the nozzle SAR to 2.27 at the takeoff condition. In the scheme shown at the bottom,  $A_{p8}$  is controlled by holding the flap and rotating the chutes, which yields an SAR of 2.8 at the takeoff condition. However, this configuration yields a center streak of high-velocity flow in the primary stream, 2.72-in thick in full scale. From a noise-reduction consideration, a large SAR with no center streak of high-velocity jet is preferred. The decision to entrain larger amounts of ambient air at the risk of having a center streak of high-velocity primary jet was chosen as the preferred design feature for acoustic test programs.

Figure 4 is a photo of the exhaust system scale model with one sidewall removed, and Figure 5 is a schematic of the exhaust system model. It was recognized early in the program that efficient induction of ambient air into the ejector system is very essential. The mechanical implementation proposed in the preliminary design required the chutes to be rotated away from the main engine flow after takeoff, and such a scheme did not permit an aerodynamically “clean” ejector inlet — particularly at the confluence of the ejector inlet and chute geometries. The scale-model ejector inlet ramp has a very gentle radius and a shallow angle of approximately  $26^\circ$  to the horizontal. More recent mechanical designs and interactions with Boeing on installation considerations near the wing trailing edge for these types of mixer/ejector nozzles probably will dictate shorter and steeper inlet ramps that may reduce the inlet recovery and also secondary mass flow entrained relative to the inlet tested under this test series.

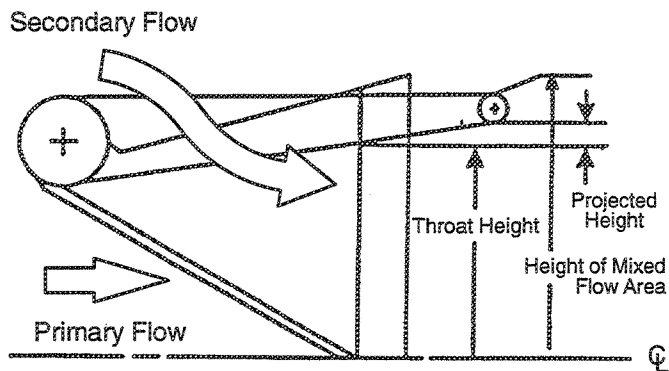
All of the scale models under this test program employ a fixed-position, flush-inlet-lip design with a large radius, designed to accommodate the large variations in mass flow ratios to be encountered in the test configurations due to changes in suppressor area ratio (SAR range of 2.8 to 3.9) as well as large variations in primary nozzle pressure ratio (NPR range of 1.5 to 4.0).

### 3.2 Key Geometric Parameters

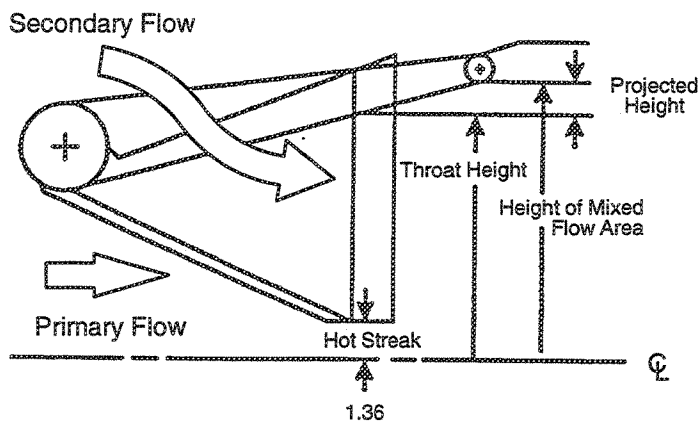
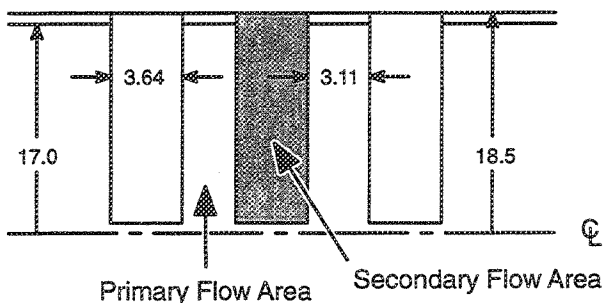
The overall exhaust system nomenclature are identified in Figure 6. The key dimension is flap/ejector length ( $L_{ej}$ ) measured from the suppressor exit to the exit of the nozzle (Figure 6). Identified in Figure 5, the primary dimensions at the exhaust-system exit (station 9) are width from sidewall to sidewall ( $w_9$ ) and the half height of the nozzle measured from the center line to the flap trailing edge ( $h_9$ ). The number of chutes in each half of the suppressor ( $n$ ) is an important overall parameter.

Figure 7 shows the key dimensions of the suppressor chutes. The three planes of importance are the primary throat (station 8), the suppressor exit (station 89), and the mixing plane (station “mix” or  $m$ ). Correspondingly, three heights of the suppressor as measured from the centerline of the nozzle are identified as  $h_8$ ,  $h_{89}$ , and  $h_{mix}$ . The gap between the centerline of the nozzle and the suppressor chute foot ( $h_{gap}$ ) is another important dimension. The key dimensions along the width of the suppressor are the primary and secondary flow passage widths at the throat plane,  $w_{p8}$  and  $w_{s8}$  respectively, and at the suppressor exit plane,  $w_{p89}$  and  $w_{s89}$  respectively. In all of these key geometric definitions, the wall thickness of the suppressor chutes is included as a part of the secondary flow passage.

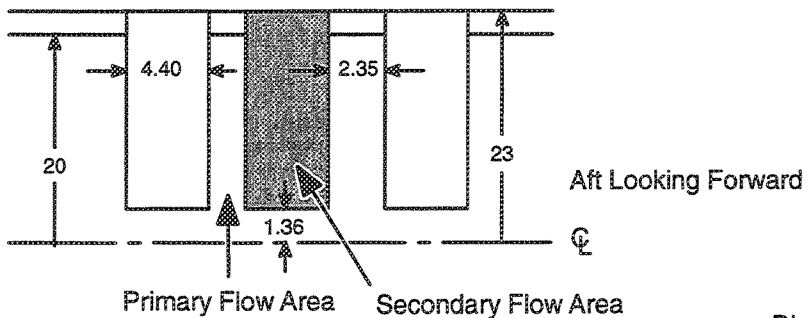
- $A_{Total} / A_8 = 2.27$
- No Center Streak
- $A_8 = 1060 \text{ in}^2$
- Vary Convergent Flap



Aft Looking Forward



- $A_{Total} / A_8 = 2.80$
- Center Streak = 2.72 in
- $A_8 = 1060 \text{ in}^2$
- Vary Ejector Chutes



Dimensions are full scale (inches)

Figure 3. Preliminary design concepts for variable throat area at cutback

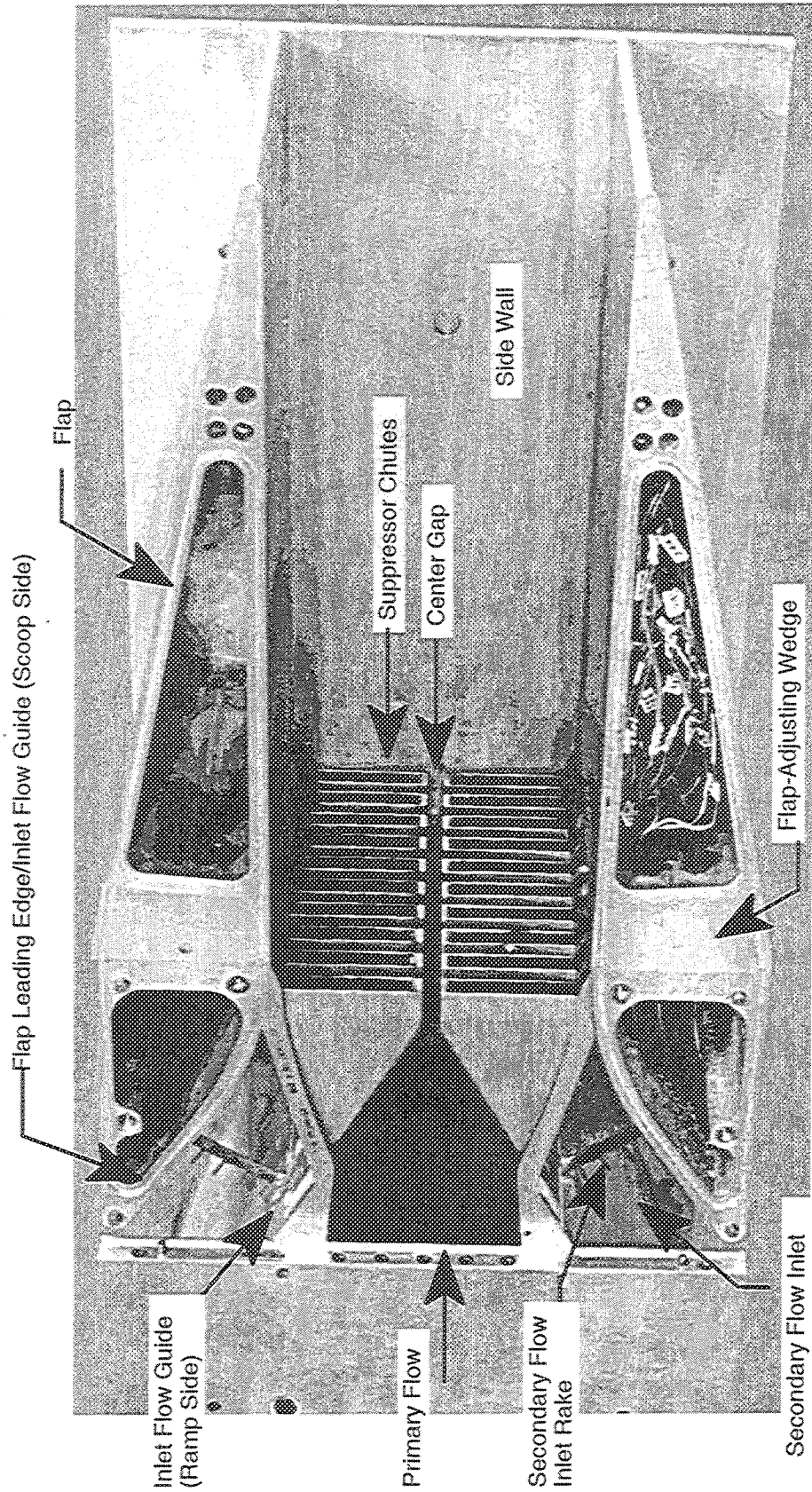


Figure 4. Mixer ejector nozzle scale model with one side wall removed

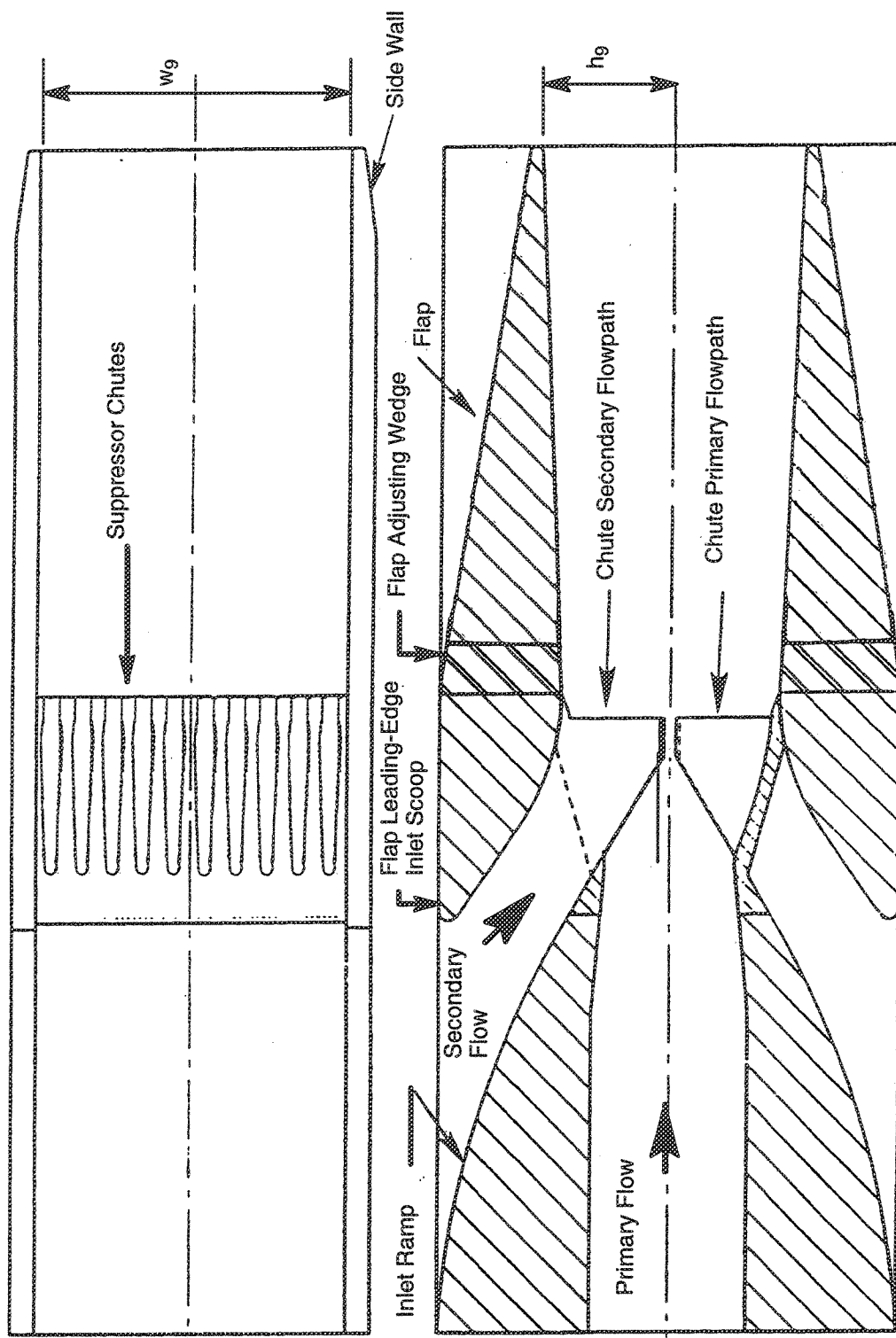


Figure 5. Schematic of exhaust system scale model

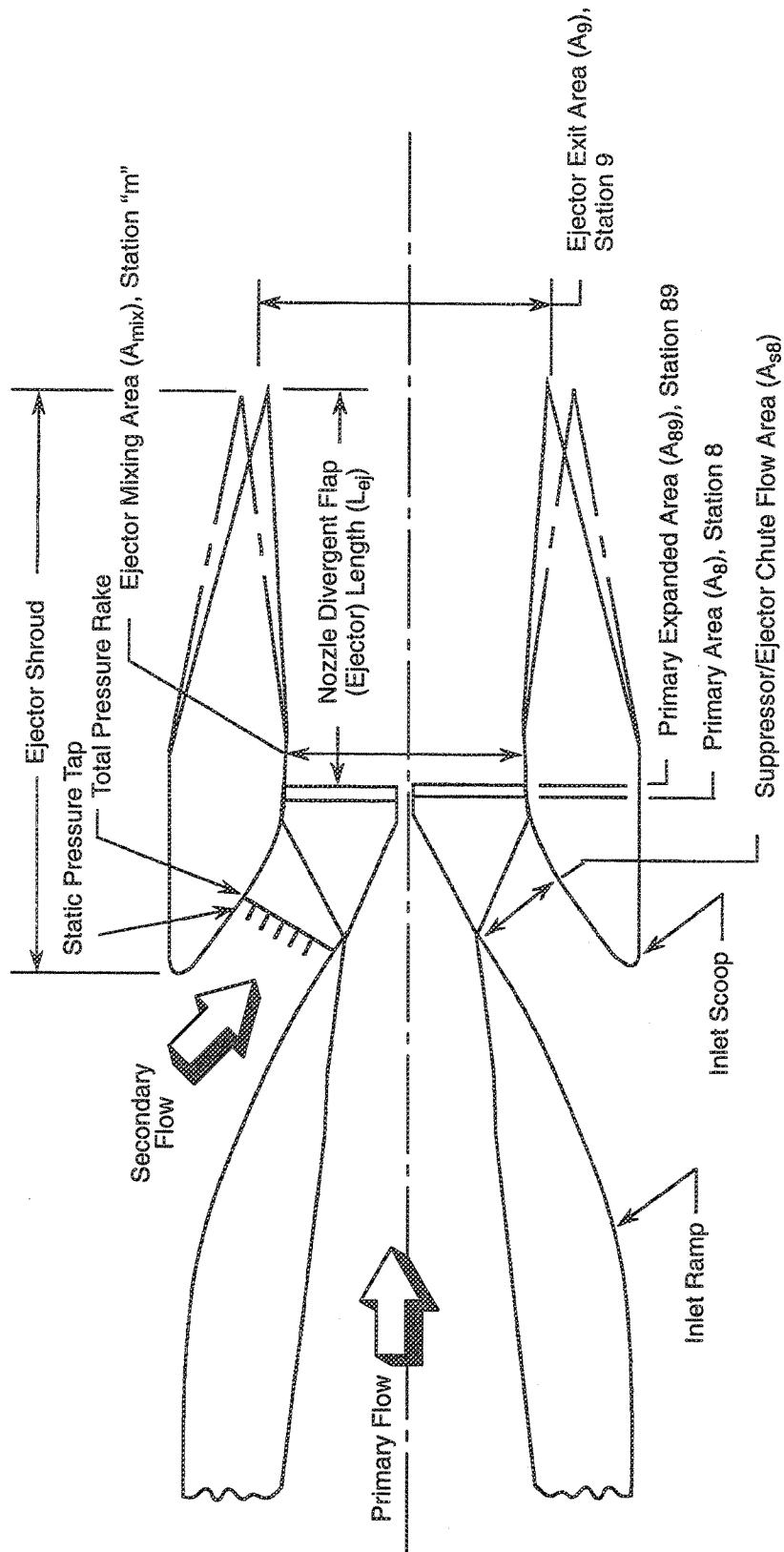


Figure 6. Exhaust system key dimensions

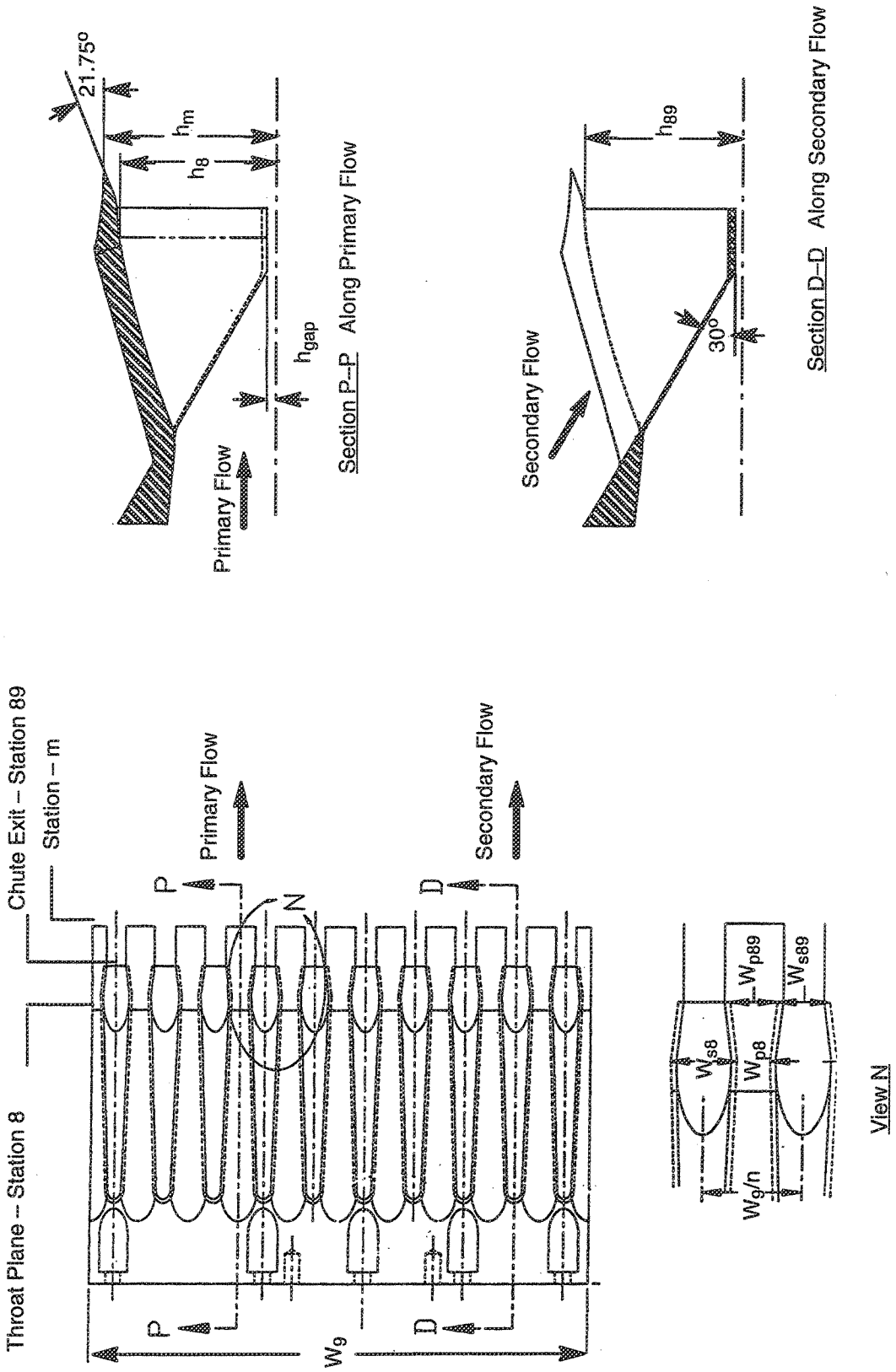


Figure 7. Basic key dimensions of the multichute suppressor

Based on these key dimensions, the following overall geometric parameters are defined.

Primary Nozzle Throat Area:  $A_{p8} = (h_8 - h_{gap}) \times w_{p8} \times 2n + 2 \times h_{gap} \times w_9$

Secondary Flow Area at Throat Plane:  $A_{s8} = (h_{mix} - h_{gap}) \times w_{s8} \times 2n$

By definition, the wall thicknesses of the chutes are included in the secondary flow chute width. Note that the height of the secondary flow passage used in the above definition is based on  $h_{mix}$ .

Total Mixed-Flow Area:  $A_m = A_{p8} + A_{s8} = 2 \times h_{mix} \times w_9 - 2n \times (h_{mix} - h_8) \times w_{p8}$

The total mixed-flow area is defined as the sum of the primary and secondary flow areas at the throat plane. This is also equivalent to the total flow area at the mixing-plane location minus the projected areas of the fingers or primary-chute extensions. A simpler definition could have been the total area downstream of the finger/primary chute extensions ( $2 \times h_m \times w_9$ ). For the purpose of this report, the differences between the definitions are insignificant and do not alter the conclusions.

Primary Flow Area at Suppressor Exit:  $A_{p89} = (h_{89} - h_{gap}) \times w_{p89} \times 2n + 2 \times h_{gap} \times w_9$

Exhaust Nozzle Exit Area:  $A_9 = 2 \times h_9 \times w_9$

Suppressor Area Ratio:  $SAR = A_{mix} / A_{p8}$

The suppressor area ratio is defined as the ratio of the mixed-flow area to the primary nozzle throat area. SAR plays an important role in the pumping characteristics. Larger SAR's lead to higher pumping and correspondingly reduced exhaust jet velocities. However, for a given primary mass flow/throat area, a larger SAR also implies a larger and heavier nozzle.

Chute Expansion Ratio:  $CER = A_{p89} / A_{p8}$

The chute expansion ratio is defined as the ratio of the primary flow area at the suppressor exit to the primary throat area. CER represents the degree of expansion achieved by the primary flow inside the suppressor chutes. An ideally expanded primary jet that matches the internal back pressure is expected to reduce internally generated shock noise and improve performance. A CER of 1.0 implies that the primary flow throat is located at the exit of the suppressor chutes. Please note, this definition is based on gross parameters defined at the throat and exit of the chute primary flowpath; any significant variation in local chute geometry should be considered in evaluating the effect of CER.

Mixing Area Ratio:  $MAR = A_9 / A_{mix}$

The mixing area ratio is defined as the ratio of the overall exhaust system exit area to the mixing plane area.

Ejector Length:  $L_{ej}$  is the length of the ejector (divergent flap) as measured from the suppressor exit plane to the exit of the overall nozzle. Longer ejectors increase acoustic-treatment area, which can effectively suppress the internally generated noise and aid in meeting the noise goals, at some increase in overall exhaust system weight and performance penalty.

### 3.3 Key Performance Parameters

Key performance parameters are listed in this section. Data-reduction procedures are not discussed in detail; however, the basic approach and assumptions are described to facilitate understanding of the significance and limitations of results.

**Free-Stream Conditions** – The free-stream conditions defined below include directly measured as well as calculated parameters. They are the same for both the acoustic and performance tests. In general, the primary difference between the wind tunnel and free-jet testing is that the wind tunnel tests were carried out at constant free-stream total pressure while the free-jet acoustic tests were carried out at constant ambient static pressure.

$M_0$	Free-stream Mach number, calculated
$P_{T0}$	Free-stream total pressure, measured (psia)
$P_0$	Free-stream or ambient static pressure, measured (psia)
$T_{T0}$	Free-stream total temperature, measured (°R)
$T_0$	Free-stream static temperature, calculated (°R)
$P_{Tp}$	Primary nozzle inlet total pressure, measured (psia)
$T_{Tp}$	Primary nozzle inlet total temperature, measured (°R)
$W_p$	Primary nozzle weight flow (lbm/s), calculated in acoustic test facility and measured in wind tunnel performance tests
$W_{pi}$	Primary nozzle ideal weight flow, calculated (lbm/s)
$NPR$	Primary nozzle pressure ratio, calculated as $P_{Tp} / P_0$
$V_j$	Primary nozzle ideal jet velocity, calculated based on $NPR$ and $T_{Tp}$
$F_i$	Primary nozzle ideal thrust based on measured weight flow rate, $W_p \times V_j$
$P_{Ts}$	Secondary inlet total pressure, measured (psia)
$W_s$	Secondary inlet weight flow, calculated (lbm/s)
$F-D$	Measured thrust minus drag corrected for balance tare
$F-D_{noz}$	Measured thrust minus nozzle drag (deduced from above)
$W_T$	Total nozzle flow rate: sum of primary + secondary, $W_p + W_s$ (lbm/s)

**Coefficients** – From the above parameters, the following coefficients are determined.

$C_{D8}$	Primary nozzle flow coefficient defined as the ratio of measured primary nozzle flow rate to the ideal primary nozzle flow rate: $W_p / W_i$
$C_{f-Dnoz}$	Thrust minus nozzle drag coefficient defined as the ratio of measured nozzle thrust minus drag to the primary nozzle ideal thrust: $(F-D_{noz}) / F_i$
$C_{fg}$	Nozzle thrust coefficient, estimated for the static case only. (Total external drag and ram drag due to secondary flow entrainment are zero at static conditions.) Same as $C_{f-Dnoz}$ for static case.
$\omega$	Pumping ratio, defined as the ratio of secondary to primary flow rates: $W_s / W_p$
$\omega\sqrt{\tau}$	Corrected pumping ratio: $(W_s / W_p) \sqrt{(T_{Ts} / T_{Tp})}$

### 3.4 Key Acoustic Parameters

Key acoustic parameters are illustrated in Figure 8 and listed below:

- EPNL Effective perceived noise level based on PNL, dB
- PNL Perceived noise level, dB
- PNLT Tone-corrected perceived noise level, dB
- SPL Sound pressure level, dB
- $\theta$  Polar directivity angle measured from the inlet axis, degrees
- $\phi$  Azimuthal angle measured from the nozzle major axis, degrees

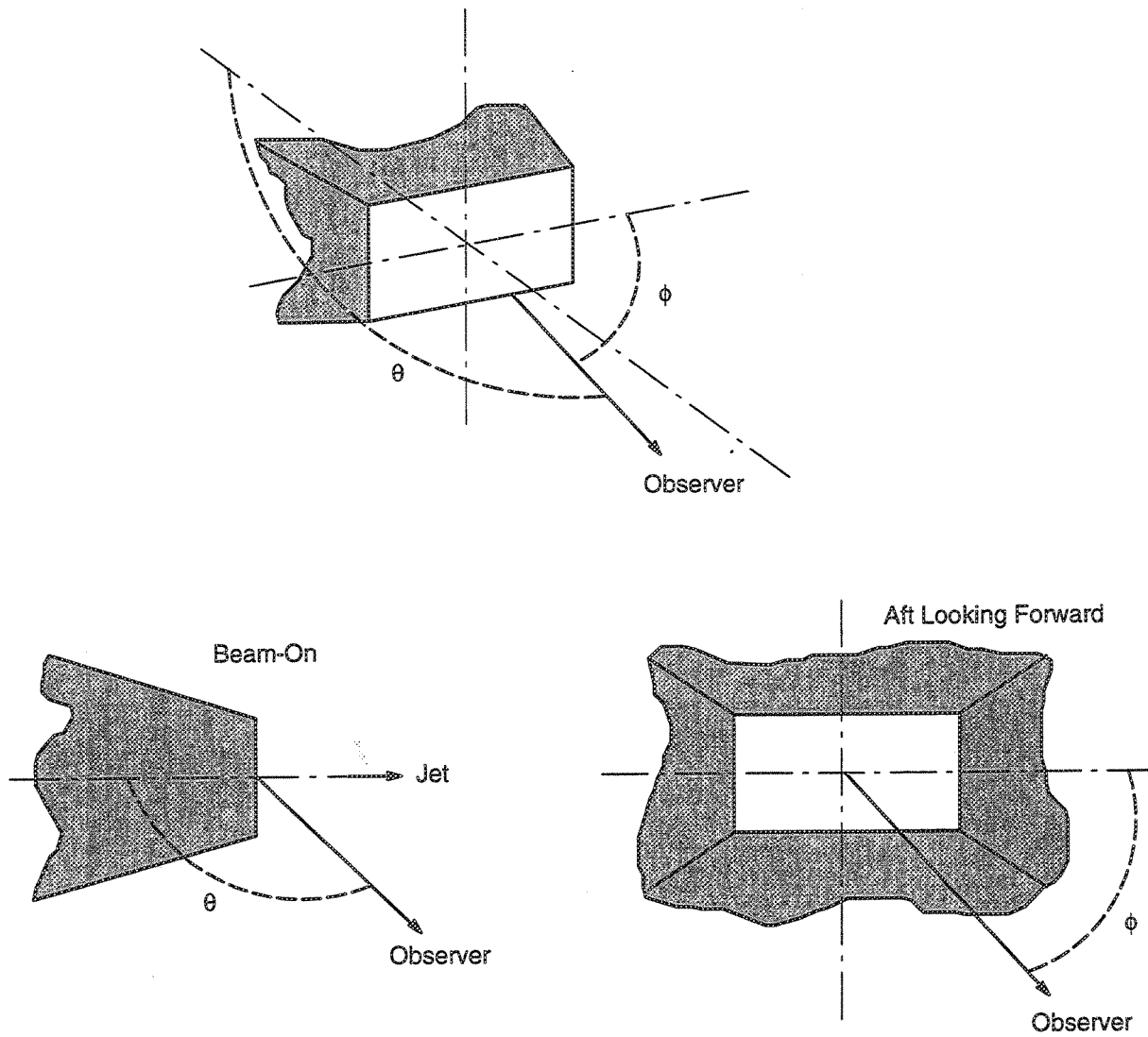


Figure 8. Key acoustic parameters

## 4.0 Acoustic Test Program

The acoustic performance of the 1/7th scale-model exhaust system in the takeoff mode configuration was evaluated in GEAE's Cell 41 anechoic test facility. This scale-model exhaust system was based on the full-scale preliminary design described in Section 3. In addition to the baseline design, several acoustic risk-reduction features were included in this test program to evaluate the overall noise-reduction potential of the baseline preliminary design concept.

The details of the acoustic scale model and acoustic performance are discussed in this section. Many figures are used to describe the models, tests, and resulting data. To avoid unwieldy separation of the text, the illustrations are presented collectively at the end of the section.

### 4.1 Acoustic Models and Test Matrix

#### 4.1.1 Model Description

A large-scale model is preferred for acoustic testing due to the following technical considerations:

1. To reduce the impact of scaling metal thickness and acoustic liners on full-scale projections of EPNL reductions.
2. To reduce the impact of uncertainty of atmospheric absorption models at very high frequencies (typically >32 kHz).
3. To ensure that model-scale Reynold's numbers are sufficiently large to adequately represent dominant full-scale flow phenomena such as boundary layer separation in the ejector inlet region and suppressor chutes.

Along with cost, test facility airflow capabilities at high temperature and burner operations limit the maximum size of the models that can be tested. A linear scale factor of 1/7 was chosen for the Cell 41 acoustic model as a compromise between these above considerations.

As pointed out in Section 3.1, the scale models employ a fixed-position, flush, inlet lip design with a large radius — designed to accommodate the large variations in mass flow ratios to be encountered in the test configurations due to changes in SAR (2.8 to 3.9) as well as large variations in primary NPR (1.5 to 4.0).

Mating of the nozzle design to flow delivery and free-jet closure required upstream transition from a large diameter. Figures 9 and 10 show the acoustic model system adapted to the Cell 41 test facility. Figure 11 shows the scale-model design that represents the "baseline" 2DCD mixer/ejector nozzle evolved in the *Base Program*. The baseline model has the following geometric attributes:

- Twenty convergent/divergent aligned chutes with CER = 1.43, and SAR = 2.8
- Ejector flap length = 80 inches in full scale (model flap length = 11 inches)
- Acoustic treatment applied to all of flap and sidewall areas
- Mixing area ratio variable (MAR = 1.4, 1.2, and 0.95)

Several acoustic risk-reduction and parametric variations from the above configuration were pursued in the scale model test program and are described below (see Figures 12 through 15):

- Revised baseline nozzle with 120-in ejector flap length full scale (model length = 17.1 in) to enhance mixing as well as to absorb mixing noise (see Figure 13)

- Twenty convergent/divergent aligned chutes with a CER of 1.43 at SAR = 3.3 to entrain more ambient air than the baseline and potentially reduce noise further.
- A mini wedge that essentially blocked off the center streak of high-velocity primary jet (see Figure 14).
- Acoustically treated center wedge with a porous surface at the wedge, starting at the leading edge, to further increase the acoustically treated surface area for noise reduction (see Figure 15).

The above acoustic risk-reduction features are expected to impact nozzle aerodynamic performance. The scale-model aerodynamic performance test program (see Section 3) included all of the above configurational variants to enable assessment of trades between enhanced noise suppression and  $C_{f_g}$ .

In order to assess noise reduction due to acoustic treatment on the ejector flaps and sidewalls, a treatment tray design based on past experience (Reference 2) was fabricated. The treatment trays are designed to fit within shell structures of the flaps, sidewalls, and center wedge. Typical tray design is shown in Figure 16, and details are described.

The above treatment is not representative of a full-scale design. The companion ejector liner treatment program is screening several designs for application to the full-scale engine in a duct environment for impedance and insertion-loss characteristics and will be recommending more realistic treatment designs for future demonstration in *Generation 2* nozzle designs. The current nozzle test program basically employed proven experience in treatment design.

#### 4.1.2 Model Instrumentation

The model instrumentation details are shown in Figures 17 through 22. Figure 17 is a schematic of the nozzle cross section with all of the instrumentation. Figures 18 through 22 illustrate the detailed model instrumentation and locations.

The secondary flow inlet instrumentation consisted of one row of static pressures along the inlet ramp (Figure 18) continuing into the suppressor chute (Figure 19) secondary flowpath. The static pressures inside the suppressor chute were located on the base of the secondary flow side and were staggered over many suppressor chutes to avoid significant interference with the flow field. Another row of static pressure taps along the inlet scoop side (Figure 20) continued along the flap (Figure 21) inside the ejector to the exit of the nozzle. This row of pressure taps was located at the secondary flow centerline of the chute. There is an additional row of static pressure taps along the inside of the flap from suppressor chute exit to the flap trailing edge, aligned with the centerline of a chute primary flowpath.

In addition to these static pressures, there were three total pressure rakes with eight elements each (Figure 22) in the ejector inlet. There were also two wall static pressures each at these rake locations (one on the scoop side and the other on the ramp side). The rake total pressures along with the wall statics were used to estimate the secondary mass flow rate.

The primary flow total pressure and total temperature at the charging station upstream of the test nozzle were measured by facility instrumentation, along with the free-jet and ambient conditions required to evaluate the data.

There were additional pressure and temperature diagnostic instrumentation that are not used in the data analysis.

### 4.1.3 Test Facility

The GEAE Cell 41 anechoic free-jet jet noise facility, Figure 23, is a cylindrical chamber 43-ft diameter and 72-ft tall. The inner surfaces of the chamber are lined with anechoic wedges made of fiberglass wool to render the facility anechoic above 220 Hz. The facility can accommodate dual-flow model configurations up to 22 in<sup>2</sup> and 24 in<sup>2</sup> equivalent throat areas in the inner (core) and outer (fan) flow streams respectively. The corresponding throat diameters for the two streams are 5.3 and 5.5 in. The streams of heated air for the dual-flow system, produced by two separate natural gas burners, flow through silencers and plenum chambers before entering the test nozzle. Each stream can be heated to a maximum of 1960°R with nozzle pressure ratios as high as 5.5, resulting in a maximum jet velocity of 3000 ft/s.

For this test program, a single-stream nozzle setup is used for all configurations (2D mixer/ejector nozzle and reference conic nozzle), and the flow is provided through the core burner/flow delivery plenum system.

The free-jet air stream system (flight simulation) consists of a 250,000-standard-ft<sup>3</sup>/min (at 50-in water column static pressure) fan and a 3,500-hp electric motor. The transition duct and silencer route the air from the fan discharge through the 48-in diameter, free-jet exhaust. The silencer reduces the fan noise by 30 to 50 dB. Free-jet airflow at maximum delivery rate permits simulation up to a Mach 0.4 free jet. Mach number is varied by adjusting the fan inlet vanes. The combined model, free-jet, and entrained airflow is exhausted through an exhaust stack silencer aligned directly over the model in the ceiling of the chamber. The exhaust stack is acoustically treated to reduce noise transfer from the facility to the surrounding community.

The facility is equipped with two microphone systems (see Figures 23 and 24) to measure the acoustic characteristics of the test models in the farfield: a fixed array and an array on a traversing tower. The fixed array has 16 microphones mounted from the false floor, the wall, and the ceiling of the test cell, at an azimuthal angle ( $\phi$ ) of 60° relative to the 2D nozzle major axis. These fixed microphones provide measurements at a minimum distance of 26.75 ft from the nozzle reference location and cover the polar angle range of  $\theta = 50^\circ$  to  $155^\circ$ . The traversing tower contains 13 microphones, mounted at polar angles ranging from 45° to 155°, and provides measurements at a minimum distance of 22 ft from the nozzle reference location. The traversing tower runs on tracks mounted on the floor of the test facility and can be remotely positioned at any azimuthal angle from 5° to 115° with respect to the fixed microphone array (see Figure 24). However, to ensure noninterference from proximity to wedges in the extreme positions, data acquisition is normally limited to  $\phi = 15^\circ$  to  $110^\circ$ .

### 4.1.4 Test Matrix

Scale-model acoustic and laser velocimetry measurements were conducted in GEAE's Cell 41. Figure 25 compares the exhaust nozzle total temperatures and nozzle pressure ratios of several candidate HSCT engine cycles along with the VCE-L1M cycle. Deviations are significant only after initiation of afterburning. Hence, the VCE-L1M was selected as a representative cycle for the acoustic test program.

Figure 26 shows how the VCE-L1M cycle was simulated in Cell 41, along with variations from the nominal cycle to investigate the effect of jet density on the jet noise characteristics of the mixer/ejector. This figure shows that Cell 41 has a facility temperature limit of 1960°R and can

simulate the LIM cycle with a proper combination of total temperature and nozzle pressure ratio up to an ideal jet velocity of about 2600 ft/s. Ideal jet velocities beyond 2600 ft/s are simulated in Cell 41, for the VCE-LIM cycle, by keeping the total temperature at 1960°R and increasing the nozzle pressure ratio. This is not considered to be a serious handicap in terms of cycle simulation because the technical interest in very high-specific-thrust cycles has diminished significantly since the inception of the program, and deviations from the cycles are only small up to 3000 ft/s, which is probably the highest jet velocity of interest.

Figure 27 is a flow chart describing acoustic data processing to project the model-scale data acquired in Cell 41 to full scale. Table 2 is a summary of the acoustic testing, and Table 3 summarizes the LDV testing.

## 4.2 Acoustic Data Analyses

This section summarizes the significant results of the acoustic and LDV testing and interpretation of the measured results and projections to full-scale noise levels. Full-scale EPNL projections for mixer/ejector nozzles are compared on an absolute level basis with the FAR36 Stage 3 noise rules to assess jet velocities at which Stage 3 levels are satisfied. Full-scale EPNL values are computed for a level flyover and a constant aircraft Mach number for a single-engine, free-field situation.

GEAE estimates the system noise corrections to the above EPNL values to be +4.0 EPNdB at the sideline monitor, to account for four engines, engine-to-engine shielding, extra ground attenuation (EGA), and soft-ground reflection.

Different airframe and engine manufacturers have their own proprietary system-noise correction procedures. Hence, GEAE decided to publish EPNL values on a single-engine, free-field basis to avoid ambiguity and also to permit other organizations to apply whatever system-noise correction procedures they normally employ to interpret these acoustic data.

Table 2. Acoustic test matrix summary

Configuration	SAR	Primary Throat Area, $A_{p8}$ (in <sup>2</sup> )	Model Flap Length (in)	Acoustic Treatment	Wedge	MAR
1	3.3	19.13	17.1	Yes	No	1.2
2	3.3	19.13	17.1	No	No	1.2
6	3.3	19.13	17.1	Yes	No	0.95
7	3.3	19.13	17.1	No	No	0.95
8	3.3	19.13	11.0	Yes	No	0.95
9	2.8	22.16	17.1	Yes	No	0.95
10	2.8	22.16	11.0	Yes	No	0.95
11	3.89	15.28	17.1	Yes	TCW	1.2
12	3.89	15.28	17.1	Yes	MCW	1.2
14	3.89	15.28	17.1	Yes	MCW	0.95
15	3.3	19.13	11.0	No	No	0.95
16	2.8	22.16	11.0	No	No	0.95
17	2.8	22.16	17.1	No	No	0.95

Table 3. Cell 41 laser velocimetry test matrix summary

Configuration	SAR	MAR	Flap Length, $L_{ej}$ (in)	$M_0$	NPR	$T_{18}$ (°R)	$V_j$ (ft/s)
2	3.3	1.2	17.1	0.32	3.40	1590	2384
7	3.3	0.95	17.1	0.32	3.00	1485	2200
					3.40	1590	2384
					4.00	1750	2637
					3.40	860	1750
15	3.3	0.95	11.0	0.32	3.00	1485	2200
					3.40	1590	2384
					4.00	1750	2637
					3.40	860	1750
16	2.8	0.95	11.0	0.0	3.40	1590	2384
				0.32	3.00	1485	2200
					3.40	1590	2384
					4.00	1750	2637
17	2.8	0.95	17.1	0.0	3.40	1590	2384
				0.32	3.00	1485	2200
					3.40	1590	2384
					4.00	1750	2637

Note: All laser velocimetry testing was conducted with hard wall and no centerbody/wedge.

Following is an outline of the subsections:

- 4.2.1 Influence of Suppressor Area Ratio
- 4.2.2 Influence of Mixing Area Ratio
- 4.2.3 Influence of Acoustic Treatment
- 4.2.4 Influence of Ejector Flap Length
- 4.2.5 Influence of Treated Center Wedge
- 4.2.6 Influence of Flight Mach Number
- 4.2.7 Azimuthal Acoustic Characteristics
- 4.2.8 Influence of Jet Temperature on Ejector Flowfields

#### 4.2.1 Influence of Suppressor Area Ratio

SAR is defined as the ratio of mixing plane area (the sum of primary and secondary flow areas at the chute exit plane) to the primary stream throat area ( $A_{p8}$ ). For a given inlet ramp definition and primary stream throat area, secondary flow entrainment ( $W_s$ ) is approximately proportional to the secondary inlet area and increases with SAR. The influence of SAR on acoustic suppression is explored in this subsection by comparing Configurations 6 and 9, with SAR's of 3.3 and 2.8 respectively. Both configurations have fully treated flaps and sidewalls 120-in long in full scale (17.1-in long in scale-model size) and have a MAR of 0.95. Figure 28 compares the two suppressor

configurations in scale-model dimensions; other pertinent dimensions and linear scale factors are shown for configurations with and without the center wedge. In order to keep hardware costs down and permit hardware adaptability to investigate several geometric features, two chute racks of slightly different primary stream throat areas (19.13 and 22.16 in<sup>2</sup>) were fabricated while keeping the rest of the hardware the same.

Figure 29 compares the measured EPNL of the SAR 3.3 and 2.8 configurations, with the reference conic (RC) nozzle. EPNL is shown as a function of ideally expanded jet velocity of the primary stream (based on isentropically expanding the primary stream to ambient pressure for a given stagnation temperature and nozzle pressure ratio) along the VCE-L1M cycle (see Figure 26), at a free-jet Mach number of 0.32 ( $V_0 = 360$  ft/s).

The acoustic data for the mixer/ejector nozzle are presented at an azimuthal angle ( $\phi$ ) of 25° relative to the major axis of the 2D nozzle, which corresponds to the typical location where the sideline noise peaks at an altitude of 689 ft and a sideline distance of 1476 ft. EPNL values are quoted on the basis of a single-engine, free-field noise for a level flyover. Boeing's airplane studies have indicated that a typical HSCT powered by a low-to-moderate bypass ratio MFTF or VCE have TOGW in the range of 720,000 to 750,000 lbm. FAR36 Stage 3 noise level for the 750,000-lbm TOGW airplane is 102.5 EPNdB, which translates to 98.5 EPNdB on a single-engine, free-field basis. For jet velocities below 2450 ft/s, the SAR 2.8 nozzle is slightly quieter than the SAR 3.3 nozzle, but the trend reverses for jet velocities higher than 2500 ft/s. At a jet velocity of 2400 ft/s, an EPNL noise suppression of about 18 to 18.5 EPNdB is achieved relative to an RC nozzle. Both configurations meet FAR36 Stage 3 sideline noise levels for jet velocities  $\leq 2400$  ft/s, under assumed system noise corrections of +4 EPNdB over single-engine, free-field EPNL.

The contribution of other noise components (such as turbomachinery, combustor, and airframe) ought to be accounted for in assessing total system EPNL for comparison with the FAR36 Stage 3 rule. Initial projections of the impact of noise components other than exhaust jet are estimated to contribute approximately 1.5 EPNdB above the exhaust jet noise levels at typical takeoff sideline conditions. Hence, exhaust jet noise EPNL on a single-engine, free-field basis should be about 97 EPNdB to meet a system EPNL of 102.5 EPNdB. This is achievable by the exhaust nozzle system tested, as indicated in Figure 29, for jet velocities less than or equal to 2400 ft/s. At lower jet velocities there is additional noise margin relative to Stage 3 rules, but this results in a larger engine, for a given thrust requirement, and a heavier airplane — which adversely affects the economics. The noise levels corresponding to the larger engine will increase by 10 times the logarithm of the ratio of the engine airflow sizes. This should be factored in while assessing noise margin for lower jet velocity designs.

The noise-generation mechanisms of 2D mixer/ejector nozzles are complex. Precise quantification of these mechanisms is beyond the scope of the current program. Internal noise is generated by 3D turbulent mixing of primary and secondary streams, imperfect expansion of the primary jet, eddy Mach wave radiation due to potentially highly supersonic flows just downstream of the mixing plane, noise leakage through the ejector inlet, and noise radiation of convecting turbulent eddies — as well as duct-termination effects. External noise generation (downstream of the nozzle exit plane) is influenced by exit plane mean and turbulence profiles along with the decay rate of the external plume and aspect ratio of the nozzle. The relative domination of internal and external noise contribution depends on levels of pumping, mixing rates, primary jet velocity, ejector length, treatment effectiveness, and flight effects.

Detailed comparisons of SAR 2.8 and 3.3 configurations in terms of PNLT directivities and spectral data as well as diagnostic flowfield data in terms of secondary flow entrainment, static pressure distributions, and jet plume velocity are shown next to interpret the noise suppression of these two configurations at three jet velocities.

Figure 30 compares the measured pumping ratio ( $W_s / W_p$ ) along the VCE-L1M cycle for SAR 2.8 and 3.3 nozzles. The secondary flow is computed based on the three 8-element total pressure rakes mounted in the secondary inlet area, and the primary flow is computed based on facility rake total temperature, total pressure, and nozzle throat area  $A_{p8}$ . These airflow measurements are not as accurate as they would be if the streams were metered, but that was beyond the scope of the test program and facility instrumentation capabilities. However, relative trends and principal physical mechanisms can be explained and interpreted by these pumping data. The pumping ratio drops as jet velocity is increased since the nozzle pressure ratio is increasing at the same time along the throttle line. The SAR 3.3 nozzle has a secondary area approximately 28% larger than the SAR 2.8 nozzle, and measured pumping ratios for the SAR 3.3 nozzle are about 25% larger at all the jet velocities, relative to the SAR 2.8 nozzle. This seems to indicate that primary chute blockage effects on secondary inlet entrainment are not significant. At a jet velocity of 2400 ft/s, the SAR 3.3 and 2.8 nozzles entrain about 73% and 58% of primary flow, respectively.

Figures 31 and 32 compare the internal static pressure distributions along the ejector flap for SAR 2.8 and 3.3 nozzles at a jet velocity of 2400 ft/s. Figure 31 shows the static pressure distributions along the center of a secondary flow passage, and Figure 32 shows the same along the center of a primary flow passage. Note that SAR variation has minimal effect on the static pressure distributions, and both configurations show rapid acceleration just downstream of the chute exit plane to half atmospheric pressure before recompressing to atmospheric pressure. However, it should be pointed out that the static pressures immediately downstream of the chute exit along the secondary flow centerlines are located in the region between the primary chute extensions. The flow features in this region are complex and 3D in nature, and these data should not be used to arrive at significant conclusions regarding the chute exit flow conditions. The static pressure distributions, downstream of the primary chute extensions, indicate that the ejector is operating in “subsonic mode” for both SAR values. This is discussed in detail in Section 5.

Nozzle exit velocity profiles and plume decay comparisons for the SAR 3.3 and 2.8 nozzles are discussed at a jet velocity of approximately 2400 ft/s. LV data were acquired only on hard-wall model configurations because the acoustic treatment trays in the treated configurations had to be repacked due to *astroquartz* degradation. A technical judgement was made during the test that LV data for the hard-walled configurations is representative of treated configurations having the same geometric parameters (such as SAR, MAR, and ejector flap length) and that many of the reasonings based on hard-wall LV data are applicable to the treated configurations also. This hypothesis needs to be checked in detail for its validity, but that activity is beyond the scope of the current program.

Figure 33 shows typical LV traverse locations at the mixer/ejector nozzle exit plane, and Figure 34 shows LV traverse summary for the external jet plume survey. Figure 35 compares the velocity profiles for SAR 2.8 and 3.3 nozzles at the center of a primary chute along the minor axis of the nozzle; Figure 36 compares the velocity profiles along the major axis of the nozzles. Note that the SAR 2.8 nozzle exhibits slightly higher peak jet velocity compared to the SAR 3.3 nozzle along the minor axis (about 1500 versus 1380 ft/s). The peak velocities tend to appear at the nozzle top and bottom edges — a result of the hot primary chute design with nominal primary flow exit angle of

about 15° relative to the nozzle axis, near the flap region. Such an angle tends to preserve the high velocities near the flaps rather than along the nozzle center line. This tendency was noted in the aerodynamic-mixing test data presented in Section 6.

The primary chute passages have an aspect ratio (height/width) of approximately 9.5 to 11.5, based on SAR (see Figure 28). Jet mixing for such high-aspect-ratio jets is dominated by shear-layer vorticity (due to large shear perimeter) instead of streamwise vorticity. In such instances, the hot primary jet impinges on the flap and is deflected away. However, because the primary jet is relatively narrow, it does not form a “mushroom” as observed in low-aspect-ratio chute designs such as P&W’s vortical mixer design (Reference 3). Figure 36 shows that velocity variations in the spanwise direction (chute to chute) is minimal for both SAR values — indicating excellent spanwise mixing has been achieved by these designs at the nozzle exit plane. Both SAR’s indicate jet velocities are approximately 1300 ft/s in the spanwise direction.

The above understanding of the flowfield will now be used to explain some of the measured noise differences between the SAR 2.8 and 3.3 nozzles. Figure 37 compares the PNL directivities of SAR 2.8 and 3.3 configurations at a jet velocity of 2400 ft/s, along with the RC nozzle data. Note the significant peak PNL suppression as well as substantial PNL suppression, both at forward and at aft quadrant angles, achieved by the mixer/ejectors relative to the conic nozzle. Note that the peak PNL for the conic nozzle occurs at a polar angle of 130°, whereas it occurs at 120° for the mixer/ejectors. This observation is consistent with observed data for other suppressor nozzles (Reference 4, Chapter 7) and is a consequence of the reduction in the eddy convection Mach number for the mixer/ejector relative to the conic nozzle — which is a result of the secondary flow entrainment and increased shear perimeter. The reduction in eddy convection Mach number results in lower convective amplification of the jet mixing noise in the aft quadrant.

The SAR 2.8 nozzle shows approximately 1.5 PNdB reduction relative to the SAR 3.3 nozzle at the peak angle and is in general quieter at most angles in the forward quadrant. The SAR 3.3 nozzle is only slightly quieter at very shallow aft quadrant angles. This set of PNL directivities results in an EPNL benefit of 0.4 dB for the SAR 2.8 nozzle relative to SAR 3.3 nozzle.

Figure 38 shows the spectral composition for the SAR 2.8, SAR 3.3, and conic nozzles at 60°, 90°, peak, and 140° polar angles. Both the mixer/ejector nozzles show about 20 dB spectral reductions at low frequencies (such as at 400 Hz); this is a direct result of the decay of the primary jet velocity by the mixer/ejectors (ejector exit velocity is about 1300 ft/s, whereas conic nozzle exit velocity is about 2400 ft/s). The increased mixing of the entrained ambient air by the 20-chute mixer results in generation of noise at smaller equivalent length scales (and hence higher frequencies), and the noise has been partially absorbed by the acoustic treatment. Note that, at the peak angle, SAR 2.8 nozzle has a slightly higher low-frequency content compared to the SAR 3.3 nozzle and lower noise levels for frequencies above 1 kHz, resulting in a net peak PNL benefit for the SAR 2.8 nozzle. Since SAR 2.8 nozzle entrained about 25% less secondary flow compared to the SAR 3.3 nozzle, nozzle exit peak velocity for SAR 2.8 was measured to be slightly higher compared to SAR 3.3 nozzle (1500 versus 1380 ft/s). This results in slightly higher noise levels at lower frequencies (typically less than 400 Hz) which are dominantly created downstream of the nozzle exit plane. However, lower level of entrainment probably implies lower levels of “bulk mixing” within the confines of the ejector flaps and sidewalls and hence lower levels of internal noise associated with smaller length scales (and associated higher frequencies, typically 1 kHz or higher).

Spectral measurements for SAR 2.8 and 3.3 nozzles at 90° show similar features at the peak angle, but the levels are higher at the peak angle due to the eddy convection amplification that occurs in the aft quadrant but is minimal at 90°. The RC nozzle spectrum at 90° clearly shows the presence of shock noise peak at 315 Hz.

Spectral data at 60° for SAR 2.8 and 3.3 do not show any clear trend. The conic nozzle spectrum shows the clear dominance of the shock noise in the forward quadrant with a peak frequency at 250 Hz. The reduction of peak frequency associated with shock-associated broadband noise as angle to inlet axis is reduced from 90° is due to convection factor  $1/(1 + M_c \cos \theta)$ , where  $M_c$  is eddy convection Mach number and  $\theta$  is angle to the inlet axis (Reference 4).

At 140°, the spectral contents of SAR 2.8 and 3.3 noise signatures are dominated by lower frequencies and spectral shapes resemble those of the conic nozzle, which is reflective of the mean flow shrouding of the high frequencies that occurs at shallow angles to the jet axis (which are typically in the so-called “shadow zone”). The lower frequencies do not suffer from such effects. (Reference 4 presents a detailed discussion.) Note that SAR 2.8 has slightly higher levels than SAR 3.3 between 100 Hz and 1 kHz, probably due to higher exit velocity of the SAR 2.8 nozzle compared to the SAR 3.3 nozzle. Lower levels for SAR 2.8 nozzle for frequencies above 1 kHz are again attributable to lower “bulk mixing” for SAR 2.8 compared to SAR 3.3.

Next, acoustic and flowfield features of SAR 2.8 and 3.3 nozzles are compared at a jet velocity of 2637 ft/s, for a free-stream Mach number of 0.32. See Figures 33 and 34 for definition and location of LV traverse.

The SAR 2.8 nozzle exhibits a peak jet velocity of about 1800 ft/s compared to approximately 1630 ft/s for the SAR 3.3 nozzle along the minor axis (see Figure 39). Also, the SAR 2.8 nozzle exhibits more variation in maximum to minimum velocity than the SAR 3.3 nozzle. Note the presence of the center high-velocity jet that was not so prominent at a jet velocity of 2400 ft/s (Figure 35). These flowfield features indicate that, as primary jet velocity is increased, the higher pumping helps bring peak velocities lower and provide a more uniformly mixed exit profile. Also, at higher primary jet velocity, the center streak of high-velocity primary jet does not mix as effectively and could contribute significantly to externally generated noise.

Figure 40 compares the velocity distributions along the nozzle major axis just downstream of the SAR 2.8 and 3.3 nozzles. The SAR 3.3 nozzle shows a more uniformly mixed-out profile compared to the SAR 2.8 nozzle in the spanwise direction (chute-to-chute direction), another indication that higher entrainment improves mixing as core velocity is increased.

Figures 41 and 42 compare the PNLT directivity and spectral content at selected angles, respectively, for the SAR 2.8 and 3.3 nozzles and the conic nozzle at a primary core jet velocity of 2637 ft/s. It is clearly evident that, in terms of PNLT directivity, the SAR 2.8 nozzle is higher in PNLT levels than SAR 3.3 at all angles, resulting in a 2.5 EPNdB increase (Figure 29), which is most likely due to the higher nozzle exit velocity for the lower SAR nozzle due to reduced entrainment. As core velocity is increased, the eddy convection Mach number increases and the mixing effectiveness is reduced, resulting in higher nozzle exit velocities and relatively more unmixed velocity profiles. As a result the dominant jet noise sources are located external to the nozzle; hence, the externally generated noise becomes more significant than the noise generated internal to the ejector due to the primary and secondary mixing process. Thus, as core jet velocity is increased beyond a certain value, the SAR 3.3 nozzle is lower in noise level than the SAR 2.8 nozzle.

Spectral data in Figure 42 show higher spectral levels for SAR 2.8 relative to the SAR 3.3 nozzle for frequencies less than or equal to 4 kHz and no noticeable differences at frequencies higher than 4 kHz. Based on these data, a hypothesis could be made that very high frequencies (associated with small length scales which typically occur close to the mixer exit plane) are contained within the confines of the ejector, and at high core jet velocities internally generated noise levels by a lower SAR nozzle are not necessarily higher compared to a higher SAR nozzle. In fact, lower entrainment (due to lower SAR) probably results in similar or slightly lower levels of internally generated noise. The validity of this hypothesis will be assessed when effect of SAR at a lower jet velocity (2200 ft/s) is examined next.

Figures 43 and 44 compare the PNLT directivity and spectral content at selected angles, respectively, for the SAR 2.8 and 3.3 nozzles and the conic nozzle at a primary core jet velocity of 2200 ft/s. The SAR 3.3 nozzle has higher PNLT values than the SAR 2.8 nozzle at most of the angles except at very shallow angles to jet axis which results in about a 1.5-EPNdB increase (Figure 29). The spectral comparisons at the peak angle and 90° (see Figure 44) show that the SAR 3.3 nozzle has higher noise levels for frequencies above 1 kHz relative to the SAR 2.8 nozzle, and a slight reversal at low frequencies. At lower jet velocities such as 2200 ft/s, externally generated noise is less dominant than internally generated noise due to reduced eddy convection Mach number. Hence, when internal noise is more dominant, higher SAR nozzles tend to create higher noise levels due to inherently the higher bulk mixing associated with larger levels of entrainment. Note that, even at a shallow aft angle of 140°, the SAR 2.8 nozzle has lower higher frequency content. One does notice at shallow angles to jet axis (such as greater than or equal to 140°) the SAR 3.3 nozzle is quieter than the SAR 2.8 nozzle due to predominance of low-frequency content, which tends to be lower for higher SAR nozzles due to reduced nozzle exit velocity (see Figure 44, 140° spectrum).

The above discussion clearly indicates that noise generation mechanisms of the mixer/ejector nozzles are complex, covering a wide range of turbulence length scales and frequencies, and the dominance of these different mechanisms are dependent on SAR and jet velocity. Broad generalizations that larger SAR will yield lower jet noise levels are not necessarily true.

#### 4.2.2 Influence of Mixing Area Ratio

MAR is defined as the ratio of nozzle exit area to the area at the chute exit where the primary and secondary streams start to mix. If  $MAR < 1$ , it implies a decrease in nozzle cross-sectional area from the mixer exit to the nozzle exit. Conversely, if  $MAR > 1$ , it implies an increase in nozzle cross-sectional area from the mixer exit to the nozzle exit. Nozzle aerodynamic performance tests at ambient temperature, conducted at NASA Langley's 16-ft wind tunnel (see Section 5), clearly indicated a significant effect of MAR on ejector operation (mode switch), flap static pressure distributions, and  $C_{f_g}$ . Correspondingly, influence of MAR on acoustics and hot flowfield was investigated in Cell 41 at two values of MAR: 0.95 and 1.2.

Figure 45 compares measured single-engine, free-field EPNL variation as a function of ideally expanded primary jet velocity along the VCE-L1M cycle line for Configuration 1 ( $MAR = 1.2$ ) and Configuration 6 ( $MAR = 0.95$ ) along with the RC nozzle. Both the mixer/ejector nozzles have a SAR value of 3.3, employ acoustic treatment, and have a flap length of 17.1 inches, scale model size (120 inches full scale). The acoustic data are scaled to the full-size nozzle ( $A_{p8} = 1086 \text{ in}^2$ ) at the sideline azimuthal location and a slant range of 1629 ft at a free-stream Mach number of 0.32. It is noted that for  $V_j > 2200 \text{ ft/s}$ , the MAR 0.95 nozzle is approximately 3 EPNdB quieter than the MAR 1.2 nozzle,

which is very significant in light of the data from NASA Langley 16-ft wind tunnel tests indicating an optimum MAR in the range of 1.0 from takeoff  $C_{f_g}$  considerations.

The aerodynamic data obtained in Cell 41 in terms of flap static pressure distributions, secondary flow entrainment based on inlet rake measurements, and laser velocimeter data are discussed next to investigate and explain the measured acoustic differences between these two configurations.

Figure 46 compares the PNLT directivity of MAR 1.2 and 0.95 configurations, along with the RC nozzle at  $V_j \approx 2400$  ft/s. Note that MAR 0.95 yields an almost uniform PNLT reduction of approximately 4 PNdB for the  $50^\circ$  to  $120^\circ$  range relative to MAR 1.2.

At angles aft of the peak noise angle of  $120^\circ$ , PNLT levels for MAR 0.95 are lower compared to MAR 1.2, but the PNLT difference between the two configurations is less. Figure 47 compares the spectral content of these configurations at four angles for  $V_j \approx 2400$  ft/s. Spectral data for the RC nozzle are included. Note that spectral data at  $60^\circ$  and  $90^\circ$  show spectral reductions of approximately 1 to 3 dB for frequencies less than 100 Hz for MAR 0.95 relative to MAR 1.2; for frequencies between 100 Hz to 4 kHz spectral reductions in the range of 3 to 7 dB are noted, and these differences are reduced at higher frequencies. Spectral data at the peak noise angle show approximately 5 to 7 dB reductions for MAR 0.95 compared to MAR 1.2 in the peak *Noy weighting* region of 1 to 4 kHz but less than 1 dB at frequencies below 100 Hz. Spectral comparisons at  $140^\circ$  indicate lower noise levels for MAR 0.95 compared to MAR 1.2 for frequencies greater than 1 kHz. However, there is a slight increase in SPL for frequencies less than 200 Hz for MAR 0.95 relative to MAR 1.2, which results in reduction in noted PNLT differences between the two MAR configurations at  $140^\circ$ .

Next, measured flowfield data are used to explain some of the measured acoustic data discussed above. (See Figures 33 and 34 for definition and location of LV traverses discussed below.)

Figure 48 compares velocity distributions along the minor (Y) axis ( $Z = 0$ , see Figure 33) of the two nozzle configurations with MAR's of 1.2 and 0.95, just downstream of the nozzle exit, for  $V_j \approx 2400$  ft/s. As noted and explained in Section 4.2.1, LV data were acquired on all of the hard-wall model configurations with corresponding nozzle geometric parameters of the treated configurations such as SAR, MAR, and ejector length. MAR 1.2 exhibits higher peak velocity and more "unmixedness" compared to MAR 0.95, which contributes to higher levels of noise in the middle to high frequency range for MAR 1.2 compared to MAR 0.95.

Figure 49 compares the velocity distributions along the major (Z) axis, or chute to chute ( $Y = 0$ ), at the same axial location as for Figure 48 (just downstream of the nozzle exit). Note that the velocity profile for MAR 0.95 is much more uniformly mixed in the chute-to-chute direction and lower in peak velocity compared to the MAR 1.2 case. Also, both the configurations have the same internal flow width of 9.643 inches in scale-model size. However, the jet plume for MAR 0.95 fills the entire nozzle width except possibly for sidewall boundary layers; whereas, for MAR 1.2 the plume is significantly narrower along the major axis.

Additional traverses taken parallel to the major axis but at several Y locations taken for MAR 1.2 are shown in Figure 50. These data show that, except for the traverse along  $Y = 0$  (that is, traverses with  $Y \neq 0$ ), there are possible regions of reverse flow (negative velocities) that are indicative of flow separation in the sidewall regions for the MAR 1.2 case. Also, there seems to be relatively large peak velocity variation (approximately 200 ft/s) from one traverse to the other, indicating rather poor mixing in the vertical direction (the Y direction) for MAR 1.2 case.

Corresponding chute-to-chute distributions for MAR 0.95 at similar Y locations are shown in Figure 51. In the case of MAR 0.95, note the relatively flat distributions at all Y locations except  $Y = 3.0$  traverse, which is located very close to the ejector flap and may be influenced by flap boundary layer. The maximum velocities vary in the range of 1300 to 1400 ft/s among all the traverses presented. There are no indications of separated flow in the sidewall regions.

All these flow features indicate a well-mixed flow at lower peak velocities is exiting the mixer/ejector for MAR 0.95 compared to the MAR 1.2 configuration, resulting in reduced noise levels for MAR 0.95 compared to MAR 1.2, particularly in the high-frequency region of the spectrum.

Next, plume decay along the nozzle centerline ( $Y = Z = 0$ ) for MAR 0.95 and 1.2 are compared in Figure 52. At  $X = 0$ , MAR 1.2 has a jet velocity of approximately 1400 ft/s, and MAR 0.95 has approximately 1320 ft/s. Although the plume development along the nozzle centerline for both MAR's is somewhat similar for  $X \leq 60$  inches (approximately six nozzle widths), MAR 0.95 shows a slightly faster decay for  $X > 60$  inches, which is probably the principal reason for reduced noise in the low-frequency region for MAR 0.95 compared to MAR 1.2. A more definitive statement could be made only after more exhaustive mapping of the flowfield and a reliable jet-noise predictive model for rectangular jets is developed. Based on the noted differences in the flowfield features for MAR 1.2 and 0.95, an empirical understanding has evolved that explains the measured noise differences between MAR 1.2 and 0.95 configurations.

Next, effect of MAR on ejector flap static pressure distribution and secondary flow entrainment ratio ( $W_s/W_p$ ), and the relationships to noise data are discussed. Figure 53 compares the ejector flap static pressure distributions for the two configurations at  $V_j \approx 2400$  ft/s, with a free-stream Mach number of 0.32. The axial flap static pressure distributions correspond to the center of a cold chute. Static pressure drops to approximately  $0.7 P_0$  for MAR 0.95 just downstream of the chute exit and then climbs rapidly to slightly above ambient pressure, before approaching  $P_0$  at the nozzle exit; this is indicative of a compound "subsonic" mode of ejector operation. Since the ratio of static pressure to ambient pressure in the secondary flow passage did not reach the critical pressure ratio (approximately 0.528, based on a specific heat ratio,  $\gamma$ , of 1.4), secondary flow in the vicinity of chute exit did not reach sonic conditions. The secondary flow will probably be accelerated by the primary stream, by virtue of the mixing, and may indeed be supersonic further downstream. For MAR 1.2, however, the static pressure in the secondary chute passage is below the critical value of 0.528; the secondary flow passage is "choked" near the chute exit, and the secondary flow continues to accelerate further downstream — keeping static pressure at about half the ambient pressure.

Static pressure increases quite rapidly after 40% of the ejector flap length, probably through a series of oblique shocks, to reach ambient pressure at the nozzle exit. A series of oblique shocks is believed to be the mechanism (rather than a single normal shock) based on the axial extent of the compression process, as well as internal LV measurements taken on geometrically similar chute configuration in the ARL facility (see Section 6). For MAR 0.95, nozzle exit plane area being less than the mixing plane area, the nozzle exit plane could indeed become the "minimum" area for a range of NPR, resulting in so-called "unchoking" of the secondary stream. This would result in the "subsonic" mode of ejector operation. This is probably the situation for  $V_j \approx 2400$  ft/s,  $NPR \approx 3.4$ , and  $T_8 = 1590^\circ\text{R}$ . For MAR 1.2, the nozzle exit area being larger, the mixing plane area cannot be the minimum area for any NPR, and ejector mode is principally controlled by the ejector inlet performance and not at all by the nozzle exit plane. For the condition under discussion, the ejector is operating in the "supersonic" mode for MAR 1.2. The differences in the internal flowfield due

to “subsonic” mode for MAR 0.95 and “supersonic” mode for MAR 1.2 and associated difference in the internal shock structures can be expected to contribute to the differences in the very high-frequency portions of the spectrum (see Figure 47). Axial extent of “supersonic” flow is longer (based on flap static pressure distribution), and possibly stronger shock structures exist closer to the nozzle exit plane for MAR 1.2 than for MAR 0.95. These factors, along with the measured differences in the LV flow features described above, contribute to higher high-frequency content for MAR 1.2 compared to MAR 0.95.

Figure 54 compares the secondary flow entrainment ratio ( $W_s / W_p$ ) for Configurations 1 (MAR 1.2) and 6 (MAR 0.95) along the VCE–L1M cycle, for a free-stream Mach number of 0.32. The data are based on secondary flow rate computed from ejector inlet total rakes and ideal primary flow rate based on given primary stream rake data and a reference model throat area. Note that MAR 0.95 entrains less secondary flow at all the conditions but is still lower in noise at all the conditions. At lower  $V_j$ , which also correspond to lower NPR, the differences in ( $W_s / W_p$ ) for the two MAR values increase. At lower  $V_j$  (and NPR), the secondary flow has less of a tendency to choke at the mixing plane; at the same time, the nozzle exit plane becomes the “minimum” area for MAR 0.95 and can effectively control secondary flow,  $W_s$ . For MAR 1.2, however, exit plane does not “control” secondary flow, and whatever the secondary inlet can pump gets entrained. At higher  $V_j$  (and NPR), the differences in entrained mass flow rates are reduced since, at high NPR, the ejector is operating in a “compound” supersonic mode, and the mixing plane indeed becomes the flow-controlling area for both the MAR values. Although MAR 1.2 entrains more secondary flow than MAR 0.95, as we have seen, noise levels for MAR 0.95 are significantly lower compared to MAR 1.2, due to various flowfield differences discussed in this section. Hence, it should be kept in mind that noise characteristics of these mixer/ejector nozzles are not at all single-valued functions of entrainment ratio; many factors impact measured noise characteristics.

### 4.2.3 Influence of Acoustic Treatment

Effect of acoustic treatment on the mixer-ejector noise characteristics is analyzed in this subsection. Figure 55 compares the EPNL variation with  $V_j$  for Configuration 7 (SAR 3.3, MAR 0.95, full-scale ejector flap length 120 inches, acoustically treated wall), scaled to full size ( $A_{p8} = 1086 \text{ in}^2$ ) at the sideline azimuthal location for a free-stream Mach number of 0.32. RC nozzle data are also included. Note that at nominal  $V_j = 2400 \text{ ft/s}$ , acoustic treatment yields approximately 3-EPNdB noise suppression, and the noise suppression due to treatment increases to approximately 4 EPNdB for velocities  $< 2000 \text{ ft/s}$ . However, as  $V_j$  increases to approximately 2600 ft/s, noise suppression by the acoustic treatment decreases to approximately 2.5 EPNdB. Increase in jet velocity beyond 2600 ft/s results in reduced noise suppression by the acoustic treatment.

Detailed analyses of the effects of acoustic treatment on PNLT directivity and spectral content at selected conditions discussed next. Figure 56 compares the PNLT directivity of Configurations 7 (hard wall) and 6 (acoustically treated wall) at  $V_j = 2400 \text{ ft/s}$  at the sideline azimuthal location. Again, RC nozzle data are shown. Note that approximately 2-PNdB noise reduction due to acoustic treatment is measured at the peak angle of  $120^\circ$ , and larger levels of PNLT reductions (approximately 3 to 5 PNdB) are noted in the forward quadrant. At shallow angles to the jet axis ( $\theta > 130^\circ$ ), noise suppression by the acoustic treatment is reduced.

Further insight into the effect of treatment may be gained by examining the spectral data next. Figure 57 shows the spectral effectiveness of acoustic treatment for  $V_j = 2400 \text{ ft/s}$  at four selected angles

(60°, 90°, peak PNL T angle, and 140°). Spectral data at 60° show that acoustic treatment suppresses frequencies above approximately 1 kHz, and noise suppression levels of approximately 5 to 6 dB are achieved for frequencies of 3.15 kHz and higher. For frequencies less than 1 kHz, no differences between hard-wall and treated configurations are noticeable. This is consistent with the empirical knowledge that lower frequencies are predominantly created at large downstream distances, probably downstream of the nozzle exit plane where acoustic treatment has no conceivable impact. Spectral suppression by acoustic treatment at 90° shows similar features as the spectra at 60°, except slightly reduced suppression by the treatment at frequencies greater than 4 kHz. Acoustic treatment does not absorb frequencies below approximately 630 Hz at 90°. Next, spectral data at the peak angle (120°) show that acoustic treatment provides a peak spectral suppression of approximately 2 to 3 dB in the frequency range of 0.8 to 3.15 kHz. No suppression by the treatment is noted for frequencies below 400 Hz. The spectral data at a shallow angle to the jet axis (140°) show increased dominance of the lower frequencies due to mean flow shrouding of the high frequencies. Although treatment absorbs the high-frequency components as effectively as at 120°, PNL T reduction by the treatment is only approximately 1 PNdB at 140° due to higher low-frequency amplitude.

It is reasonable to assume that acoustic treatment impacts only acoustic sources located and radiating within the confines of the ejector. Hence, the treatment data may be used as a diagnostic means to separate noise components generated within the confines of the ejector and external to the nozzle exit plane. However, one needs to employ caution in doing so for reasons described below.

As the above data show, lower frequencies (less than 400 Hz) are not suppressed by acoustic treatment at all angles. Hence, one may conclude that frequencies less than 400 Hz are generated by sources downstream of the nozzle exit plane. However, the lower frequency limit, at which the onset of treatment effectiveness begins, is a function of angular location. This relates to the extended source characteristics and multiple length scales of these jets. There is a range of mid-to-high frequencies (approximately 1 to 4 kHz) that are probably generated within the ejector as well as just downstream of the nozzle exit plane (due to the high levels of mixing occurring both within the ejector and just downstream of the nozzle exit plane), and effective radiation to far field is dependent on the directivity angle.

Aft-quadrant radiation of these sources is more efficient than in the forward quadrant due to convective amplification of such sources. This explains why the lower frequency limit at which the treatment effectiveness is noted is reduced in the aft quadrant and accounts for the slightly reduced spectral suppression in the aft quadrant. Hence, one cannot categorically state which frequencies are generated within the confines of the ejector.

Next, acoustic treatment effectiveness at jet velocities other than 2400 ft/s are discussed. Figure 58 shows the PNL T directivity comparisons of Configurations 6 (treated) and 7 (hard wall) at  $V_j \approx 2600$  ft/s. Acoustic treatment yielded approximately 1.5-EPNdB noise suppression relative to the hard wall at  $V_j \approx 2600$  ft/s (Figure 55). Acoustic treatment is less effective at the peak noise angle as well as other angles compared to the  $V_j \approx 2400$  ft/s case (Figures 56 and 58). Reasons for reduced effectiveness of the acoustic treatment as  $V_j$  is increased can be found in the spectral comparisons of hard-wall and treated configurations shown in Figure 59. Slightly reduced effectiveness of treatment in the frequency range of 1 to 4 kHz and increased dominance of low-frequency components over high-frequency components for  $V_j \approx 2600$  ft/s compared to  $V_j \approx 2400$  ft/s are the reasons for reduced treatment effectiveness. As  $V_j$  increases, the mixing effectiveness of the mixer/ejector nozzle is reduced; relatively stronger jet noise sources are located

external to the ejector nozzle, making the externally generated noise more dominant than the internally generated noise. Higher grazing flow Mach numbers over the acoustic treatment also reduce the effectiveness of treatment because acoustic waves are convected by the mean flow at higher speeds over the liners and thereby reduce “residence” time for the internal sources within the confines of the ejector. The above physical reasons are cited as possible mechanisms for reduced effectiveness of the acoustic treatment.

Next, the effect of acoustic treatment is examined at a lower  $V_j$  (1900 ft/s). Acoustic treatment yielded additional approximately 4-EPNdB reduction relative to the hard wall (see Figure 55), clearly indicating improved suppression by the treatment at lower  $V_j$ . Figure 60 compares the PNL directivities of Configurations 6 (treated) and 7 (hard wall) at  $V_j = 1900$  ft/s. One notices almost 4-EPNdB reduction at the peak noise angle of  $120^\circ$  and similar levels of reduction forward of the peak noise angle and at  $130^\circ$ .

At angles aft of  $130^\circ$ , treatment effectiveness is reduced. Figure 61 compares the spectral content of the hard-wall and treated configurations (7 and 6, respectively) at four select angles for  $V_j = 1900$  ft/s. Treatment effectiveness extends to much lower frequencies at  $V_j = 1900$  ft/s compared to  $V_j = 2400$  ft/s (Figures 57 and 61), indicating that significant noise generation is occurring within the confines of the ejector, at lower  $V_j$ , which the acoustic treatment is suppressing. Spectral suppression of approximately 6 dB is noted at 1 kHz due to the treatment at the peak noise angle of  $120^\circ$  at  $V_j = 1900$  ft/s, but about 3-dB suppression was noted at 1 kHz for  $V_j = 2400$  ft/s at  $120^\circ$ .

#### 4.2.4 Influence of Ejector Flap Length

Ejector flap length ( $L_{ej}$ ) is an important design parameter. It has significant impact on acoustic suppression, cruise performance, nozzle weight and envelope, and installation on the HSCT. These effects in turn influence aircraft TOGW (economic viability) and environmental acceptability. Understanding the influence of ejector flap length (hard walled as well as acoustically treated) on acoustic suppression will enable assessment of system trades for acceptable economics and environmental acceptability. Influence of ejector flap length for the hard-wall case is discussed first, followed by discussion of the acoustically treated wall case.

Figure 62 compares full-scale projected EPNL variation at the sideline azimuthal location for a free-stream Mach number of 0.32, with  $V_j$  for Configuration 7 (full-scale  $L_{ej} = 120$  in, hard wall, SAR = 3.3, and MAR = 0.95) and Configuration 15 (full-scale  $L_{ej} = 80$  in, hard wall, SAR = 3.3, and MAR = 0.95). In the range of  $V_j$  between approximately 1600 and 2600 ft/s, an average reduction of approximately 1.7 EPNdB is realized by the 120-in hard-walled flap relative to the 80-in hard-walled flap.

Figure 63 similarly compares the full-scale projected EPNL variation with  $V_j$  for Configuration 6 (full-scale  $L_{ej} = 120$  in, acoustically treated wall, SAR = 3.3, and MAR = 0.95) and configuration 8 (full-scale  $L_{ej} = 80$  in, acoustically treated wall, SAR = 3.3, and MAR = 0.95) at the sideline azimuthal location for a free-stream Mach number of 0.32. In the range of  $V_j$  between approximately 1600 and 2600 ft/s, an average reduction of approximately 2.6 EPNdB is realized by the 120-in acoustically treated flap relative to the 80-in acoustically treated flap. Detailed directivity and spectral comparisons at select conditions along with the diagnostic flowfield data are used next to explain the above noted influence of  $L_{ej}$  on EPNL values.

Figure 64 compares the PNL directivity of Configurations 7 and 15 at  $V_j = 2400$  ft/s, for a free-stream Mach number of 0.32, at the sideline azimuthal location. Configuration 15 ( $L_{ej} = 80$  in,

hard wall) has a peak PNL<sub>T</sub> of approximately 104 PNdB at 90°; configuration 7 ( $L_{ej} = 120$  in, hard wall) has a peak PNL<sub>T</sub> of 102.5 PNdB at 120°. Almost 4-PNdB reductions are noted due to increased flap length at 60°. Effect of flap length on PNL<sub>T</sub> values at shallow angles to the jet axis ( $\theta > 130^\circ$ ) is small.

Figure 65 compares the spectral content of Configurations 7 and 15 at four selected angles for the above condition. Note that the long hard-walled configuration has lower noise levels than the short hard-walled configuration at all frequencies, with larger differences in the approximately 1 to 4 kHz range at all angles. Since the lower frequency noise component dominates the 140° spectrum, and since low-frequency component is not significantly different for the two  $L_{ej}$  values, PNL<sub>T</sub> differences at 140° are approximately 1 PNdB. However, at 60° and 90°, the noted reduction in high-frequency content (typically in the 1 to 4 kHz range) due to flap length increase results in approximately 4-PNdB reduction.

Next, LV flowfield data are used to explain the measured noise reductions due to flap length increase. Figure 66 compares the axial velocity distribution along the minor axis ( $Z = 0$ , see Figures 33 and 34 for definition of the coordinate system for the LV data) just downstream of the ejector nozzle for Configurations 7 ( $L_{ej} = 120$  in, hard wall) and 15 ( $L_{ej} = 80$  in, hard wall) at  $V_j = 2400$  ft/s, with a free-stream Mach number of 0.32. It is clear that increased flap length results in a more uniformly mixed exit velocity profile, and the 80-in flap configuration has higher peak velocity than the 120-in flap configuration.

Figure 67 shows the effect of flap length on the axial velocity distribution along the major axis ( $Y = 0$ , see Figures 33 and 34 for definition of the coordinate system for LV data), just downstream of the ejector nozzle. Note the relatively smooth, well-mixed velocity profile in the chute-to-chute direction for the 120-in flap compared to the 80-in flap. Thus, ejector flap length increase helps mix the primary and secondary flows in the chute-to-chute direction as well, which results in a more uniform velocity profile at the exit of the ejector. The  $L_{ej} = 120$ -in flap extends the physical shrouding of the noise sources by 40 inches compared to the 80-in flap. The so-called physical shrouding is effective in the forward quadrant, and probably at 90°, since aft-quadrant radiation is driven by eddy convection, which probably is equally effective for both flap lengths. Both of these aspects are contributing to the reduction in the spectral reductions noted in the middle to high frequencies.

Figure 68 shows the effect of ejector flap length on plume decay along the nozzle centerline for the above condition. It is noted that the plume corresponding to the longer flap is more uniformly mixed, has reduced gradients in the velocity profiles. Since low frequencies are generated at large distances from the nozzle exit plane, and the nozzle with longer flap has features for reduced noise as described above, a slight reduction in low-frequency content is noticeable for the longer flap case.

Figure 69 shows the influence of  $L_{ej}$  on secondary flow entrainment ratio ( $W_s / W_p$ ), for SAR 3.3 and 2.8 configurations, along the VCE-L1M cycle points for a free-stream Mach number of 0.32. Note that  $L_{ej}$  has minimal effect on the pumping. Pumping of secondary flow is principally a function of SAR, MAR, and secondary inlet geometry (and hence secondary inlet recovery). Since all these parameters stayed the same when  $L_{ej}$  was changed, secondary flow entrainment was not affected by  $L_{ej}$  changes.

Next, influence of increasing  $L_{ej}$  for acoustically treated configurations is discussed. As noted in Figures 62 and 63, increasing the flap length from 80 to 120 inches in full scale for treated

configurations ( $SAR = 3.3$ ,  $MAR = 0.95$ ,  $M_0 = 0.32$ , and sideline location) results in an average noise reduction of 2.6 EPNdB in the  $V_j$  range of 1600 to 2600 ft/s; whereas, the effect of  $L_{ej}$  increase for hard-wall configurations is 1.7-EPNdB reduction in the same  $V_j$  range. This implies that the 0.9 EPNdB reduction is provided by the acoustic treatment in the additional 40-in length of the flap. Also, note that EPNL reduction due to treatment is fairly uniform over most of the  $V_j$  range.

Figure 70 shows the influence of treated flap length on PNLT directivity at  $V_j = 2400$  ft/s. Effect of  $L_{ej}$  for treated configurations is similar, compared to the hard-wall configurations (Figures 64 and 70), in the sense that longer flap yields more PNLT reductions in the forward quadrant and at  $90^\circ$  compared to the aft quadrant. The PNLT reductions due to increased  $L_{ej}$  for treated configurations are noted to be larger compared to hard-wall configurations.

Figure 71 shows the influence of treated flap length on spectra at four selected angles at  $V_j = 2400$  ft/s. Effect of  $L_{ej}$  for treated configurations is again similar compared to the hard-wall configurations (Figures 65 and 71). Note that increasing  $L_{ej}$  for treated configurations yields spectral reductions in the mid-frequency region (approximately 0.4 to 4 kHz). For frequencies greater than 4 kHz, effect of  $L_{ej}$  is minimal, implying such high-frequency sources are sufficiently closer to chute exit and were not impacted by increased flap length. Frequencies less than 400 Hz are generated so far downstream of the ejector exit that increased flap length has only a slight effect.

#### 4.2.5 Influence of Center Wedges

As described in Section 4.1, *Acoustic Models and Test Matrix*, the influence of two types of wedges on acoustics was investigated. Test data are described in this section. The two types of wedges were:

1. **Mini Center Wedge (MCW)** – A short wedge that blocks off the hot central streak of the nozzle
2. **Treated Center Wedge (TCW)** – A longer wedge that also blocks off the hot central streak but extends the full length of the nozzle flap (120 inches in full scale) and has acoustic treatment on the top and bottom sides of the wedge

A corresponding discussion on the effect of center wedges on nozzle aerodynamic performance is presented in Section 5.2.7.

Figure 72 compares the single-engine, free-field EPNL values of Configurations 1 (no wedge), 12 (with MCW) and 11 (with TCW). RC nozzle data are included also. All three configurations have acoustic treatment on the flaps and sidewalls, which are 120 inches full-scale. The flaps were positioned to yield a MAR of 1.2 for all three configurations. The scale-model acoustic data are scaled to a full-scale  $A_{p8}$  of  $1086 \text{ in}^2$  and correspond to sideline azimuthal location. Note that the full-length TCW yielded approximately 1.7 and 4 EPNdB additional noise reduction compared to the no-wedge case at  $V_j = 2400$  and 2200 ft/s, respectively. The MCW yielded less than 1-EPNdB suppression relative to the no-wedge case for  $V_j = 2200$  ft/s, but for  $V_j = 2000$  ft/s noise levels increased compared to the no-wedge case.

Figure 73 compares the PNLT directivities of Configurations 1, 11, and 12 along with the RC nozzle at  $V_j = 2400$  ft/s. Note that the TCW yields approximately 2-dB peak PNLT reduction relative to the no-wedge case and approximately 1.5-dB PNLT reduction at all other angles. The PNLT levels of the MCW are between the no-wedge and TCW cases.

Figure 74 compares the spectral measurements at four select angles for  $V_j = 2400$  ft/s for the above configurations. The TCW configuration yields lower spectral levels at all frequencies, at all angles,

relative to the no-wedge case — indicating possible high-frequency noise suppression due to the wedge treatment and low-frequency noise suppression possibly due to flowfield modification by the wedge (as discussed later). The MCW acoustic data hover between the no-wedge and TCW cases.

Figure 75 compares the flap static pressure distributions of Configurations 1, 11, and 12 at  $V_j = 2400$  ft/s. Note that the no-wedge and MCW flap static pressure distributions indicate the ejector is operating in a “supersonic” mode, with a fairly strong shock towards the flap trailing edge, to reach ambient static pressure; whereas, the TCW configuration is in a “subsonic” mode. The flap static pressure essentially reaches ambient value at approximately 20% of the flap length. It is reasonable to anticipate that the presence of the TCW would have a significant effect on the mixing of the secondary and primary streams and the ejector mode, particularly at  $NPR = 3.4$  ( $V_j = 2400$  ft/s), which is in the transitory NPR range for mode switch (see Section 4.2.2).

The above discussion clearly indicates that the center wedges (TCW and MCW) influence ejector internal flowfields significantly, which in turn affects low- as well as high-frequency content. However, Configuration 6 (MAR 0.95, without any center wedge) yielded approximately 3 EPNdB additional noise reduction compared to Configuration 1 (MAR 1.2, without a center wedge) for  $V_j = 2200$  ft/s (see Section 4.2.2, *Influence of Mixing Area Ratio*). The added weight, complexity, and performance loss of a long, treated wedge (in relation to the noise-suppression benefit provided by the TCW) was deemed not a favorable design trade to be pursued. MAR seemed to be a more effective controlling parameter to simultaneously achieve noise suppression and improve takeoff  $C_{f_g}$  (see Sections 4.2.2 and 5.2.4). Hence, subsequent acoustic tests focussed on wedgeless configurations. This investigation indicated that acoustic suppression cannot be simply increased by increasing the acoustic-treatment area by a scheme such as a treated center wedge.

#### 4.2.6 Influence of Flight Mach Number

Aircraft flight Mach number ( $M_0$ ) is simulated in Cell 41 facility, by a 4-ft diameter free jet over the jet noise models, to essentially capture the dynamic effect of flight on jet noise sources. The microphones are outside the free jet in a static environment. Noise radiated from the dynamically altered jet noise sources due to relative motion of the immediately surrounding ambient medium must propagate through the turbulent free-jet shear layer, resulting in refraction as well as scattering of the noise signal. GEAE developed a free-jet to flight transformation technique by comparing the flight-transformed, free-jet data of four nozzle types with the true-moving-frame experimental data of the same four nozzles. This technique was developed in the mid-1970’s and is documented in Reference 5.

Several methods that have been developed over the years for free-jet to flight transformation can be found in the literature, for point as well as distributed noise sources. However, the authors of this report don’t know of any published, systematic comparisons of the techniques or validation with true flight data for supersonic jet noise. Hence, the following investigation of the influence of  $M_0$  was conducted in Cell 41, using GEAE’s free-jet to flight transformation technique.

Figure 76 compares the effect of a simulated flight Mach number of 0.32 on EPNL for Configuration 9 (SAR 2.8, 120-in full-scale flap length, treated walls, MAR 0.95) and an RC nozzle along the VCE-L1M cycle operating line. Note the EPNL reductions at all jet velocities for both nozzles. The noise reductions due to simulated flight for the RC nozzle are approximately 1.5 EPNdB for  $V_j = 2600$  ft/s, approximately 4 EPNdB for  $V_j$  in the range of 2200 to 2400 ft/s, approximately 6.5 EPNdB for  $V_j = 1900$  ft/s, and increase as  $V_j$  is further reduced. For the mixer/ejector nozzle

Configuration 9, noise suppression trend due to simulated flight is different. One notices approximately 6 to 7 EPNdB reduction due to simulated flight for  $V_j$  in the range of 2400 to 2900 ft/s. The noise reduction due to flight, in fact, decreases as  $V_j$  is reduced below 2200 ft/s, and almost no noise reduction due to flight is noted at  $V_j \approx 1100$  ft/s.

Figure 77 compares the effect of simulated flight on PNL T directivities of the RC nozzle and Configuration 9 at  $V_j \approx 1900$  ft/s ( $NPR \approx 2.5$ ). Note the significant peak PNL T (approximately 7.5 dB) noise reduction of the RC nozzle at the polar angle of  $140^\circ$ , due to simulated flight. At a polar angle of  $90^\circ$  (the angle where dynamic effects on source strength dominate over Doppler effects due to relative motion), simulated flight reduces PNL T by approximately 3.5 dB. At a forward quadrant angle, such as  $60^\circ$ , where shock noise of nonisentropically expanded supersonic jets typically is higher in amplitude than jet-mixing noise, no significant amplification of shock noise due to flight is noted for the RC nozzle. (This will be explained further using spectral data.) The effect of simulated flight for Configuration 9 as a function of polar angle is somewhat similar to the RC nozzle. The peak PNL T levels are reduced by approximately 3.7 dB due to simulated flight. At the  $90^\circ$  polar angle PNL T is reduced by approximately 3.5 dB, and almost no noise reduction is noted at  $60^\circ$  for Configuration 9.

Figure 78 compares the influence of simulated flight on spectral content of the RC nozzle and Configuration 9, at four selected polar angles, for  $V_j \approx 1900$  ft/s. The  $90^\circ$  spectrum is predominantly influenced by jet source strength effects; the effects of convective amplification and relative motion between source and a static observer (Doppler effect) are minimal because the observer is at  $90^\circ$  relative the source. Simulated flight basically reduces the mean shear of the all jet sources due to reduced velocity gradient with the ambient, and this typically reduces noise levels at  $90^\circ$ . The effect of simulated flight on the shock-noise source at  $90^\circ$  is about the same as for mixing-noise source. For the RC nozzle spectrum at  $90^\circ$ , one notices fairly uniform noise reduction at all frequencies due to flight, which is reflective of the source strength reduction effect of the simulated flight. For Configuration 9, one notices significant spectral reduction at frequencies near 1 kHz and almost no spectral reduction at frequencies  $> 3.15$  kHz. The noise sources for the RC nozzle near the exit plane of the nozzle suffer a mean shear reduction proportional to a velocity gradient of  $(V_j - V_0)/V_j$ , where  $V_0$  is flight speed, compared to the static case, and noise reduction at  $90^\circ$  due to flight is proportional to the mean shear reduction described above. In the case of a mixer/ejector nozzle, although the primary nozzle is at an ideally expanded  $V_j$ , the velocity at the ejector exit is significantly lower compared to  $V_j$  due to deceleration by entrained secondary air. The sources downstream of the ejector exit are thus generating noise at a much lower jet velocity than  $V_j$ , say  $V_{exit}$ . Now, the effect of simulated flight on sources downstream of the ejector exit is a mean shear reduction proportional to a velocity gradient  $(V_{exit} - V_0)/V_{exit}$ , which is indeed greater than  $(V_j - V_0)/V_j$ . Hence, one notices much larger reduction of middle to low frequencies (frequencies  $< 1$  kHz) for the mixer/ejector compared to the RC nozzle for a given  $V_j$ . Reduction of high-frequency noise (frequencies  $> 3.15$  kHz) due to simulated flight for mixer/ejector is significantly less than for middle-to-low frequencies. This is probably because these sources, internal to the ejector, are more influenced by secondary flow entrainment and are "insulated" from free-stream flow by the ejector walls. The effect of simulated flight on the internally located sources is probably a second-order effect, in the sense that the effect of simulated flight on internal sources is felt through modification of the secondary flow entrainment.

The influence of simulated flight on spectral content at a polar angle of  $140^\circ$  is discussed next. At  $140^\circ$ , notice the larger spectral reduction due to flight for Configuration 9 at middle-to-low frequencies (frequencies  $< 1$  kHz) compared to  $90^\circ$ . The flight effect at angles away from  $90^\circ$  consists of source strength alteration due to mean shear reduction, source convection effects, relative motion between noise sources and observer, and motion of nozzle relative to the static observer (Doppler effect). Since the simulated flight reduces relative velocity, convective amplification of such sources in the aft quadrant is less compared to the static case. However, diminished mean shear reduction due to simulated flight implies that sources are convecting faster relative to a static observer for the simulated flight situation. In the aft quadrant, this implies that noise sources are approaching the observer at a higher speed, and this would tend to increase the noise levels. However, since the nozzle is moving away from the static observer in the “true flight” situation, for an observer located in the aft quadrant, noise levels in the aft quadrant should be lower. The sum total of noise source strength reduction at  $90^\circ$ , reduced convective amplification of the noise sources in the aft quadrant, and motion of nozzle relative to a static observer seem to overcome any associated amplification due to sources approaching the observer at a higher speed. The result is larger spectral reduction at  $140^\circ$  compared to  $90^\circ$ .

As at  $90^\circ$ , for the high-frequency sources (frequencies  $> 3.15$  kHz), which are probably located internal to the ejector, flight effect is minimal. Similarly, RC nozzle spectral reductions due to flight at  $140^\circ$  are larger compared to  $90^\circ$ . Since the peak PNLT angle for Configuration 9 is approximately  $120^\circ$ , the spectral reductions due to flight for frequencies  $< 1$  kHz are larger than those at  $90^\circ$  and smaller than those at  $140^\circ$ . The peak PNLT angle for the RC nozzle is  $140^\circ$ .

The  $60^\circ$  spectra of Configuration 9 shows reduced flight effect compared to  $90^\circ$  in the middle-to-low frequencies. In the forward quadrant, noise sources are moving away from a static observer at a speed faster than for the static case due to reduced velocity gradient. This should result in a lower noise level in the forward quadrant compared to the static case. However, since the nozzle is approaching the static observer in a true flight situation, noise levels will increase. Reduced convective amplification of noise sources would reduce “deamplification” in the forward quadrant. The sum total of all the four effects described above results in a reduced flight effect in the frequency range of 1 kHz. In the case of the RC nozzle, the presence of shock noise at this underexpanded condition ( $NPR = 2.5$ ) tends to dominate the spectral content and result in almost no noticeable flight effect.

Next, effect of simulated flight Mach number is discussed at  $V_j = 2400$  ft/s for Configuration 9 and the RC nozzle. Acoustic data were obtained for Configuration 9 at  $M_0 = 0.0, 0.12, 0.24,$  and  $0.32$ ; for the RC nozzle acoustic data were obtained at  $M_0 = 0$  and  $0.32$ . Figure 79 compares the PNLT directivity data for Configuration 9 (sideline azimuthal location) for  $M_0 = 0, 0.12, 0.24,$  and  $0.32$  and for the RC nozzle for  $M_0 = 0$  and  $0.32$ . Note the continuous reduction in PNLT at the polar angle of  $90^\circ$  and in the aft quadrant as  $M_0$  is increased. Note that PNLT reduction with  $M_0$  is not uniform — in the sense that PNLT reductions from  $M_0$  of 0 to 0.12 are large compared to going from  $M_0$  0.12 to 0.24. The PNLT trend with  $M_0$  is somewhat mixed in the forward quadrant, particularly forward of the polar angle of  $70^\circ$ . Further insight into effect of flight Mach number can be gained by examining the spectral distributions at several angles (see Figure 80).

As discussed above, the  $90^\circ$  spectra are principally influenced by dynamic effects on source strength. The  $90^\circ$  spectra of Configuration 9 at several free-stream Mach numbers indicate almost uniform spectral reductions in the middle-to-low frequency range (frequencies  $< 1$  kHz), as  $M_0$  is increased

from 0 to 0.32, which is reflective of the source strength reduction due to uniformly increasing the flight velocity of noise sources which are predominantly located downstream of the ejector exit. The trend with  $M_0$  for higher frequencies (frequencies > 3.15 kHz) is nonuniform reduction, due to second-order effects of flight velocity on noise sources located internal to the ejector walls. As the contribution of the middle-to-low frequencies decreases due to increasing  $M_0$  in relation to the high frequencies, PNL values at  $90^\circ$  are controlled by the higher frequencies, which do not seem to reduce much with  $M_0$ . Hence, PNL values at  $90^\circ$  show a nonuniform reduction with  $M_0$ .

Next, the spectral data for configuration 9 at  $140^\circ$  are examined. Notice the predominance of low frequencies and somewhat uniform reduction in low frequencies with  $M_0$  and small effect of  $M_0$  on high frequencies. Now, the flight effect comprises dynamic effect on source strengths, convective amplification modification, relative velocity effect of noise source motion, and Doppler effect of nozzle motion relative to the observer. Because of the interaction of all these effects and reduced dominance of lower frequencies at higher  $M_0$ , PNL reductions at  $140^\circ$  are not uniform with  $M_0$  increase. The spectral data at  $60^\circ$  show a nonuniform trend with  $M_0$  due to the combination of the four effects mentioned.

The above discussion indicates that the effect of flight  $M_0$  on the acoustics of mixer/ejector nozzles is significantly influenced by the split between internal and external noise source strengths.

It is also evident that several mechanisms are operative in determining the effect of  $M_0$  on the acoustic features of mixer/ejector nozzles. These mechanisms seem to dominate differently at various ranges of  $M_0$ . A clear understanding of these mechanisms is still to be achieved. In the absence of such understanding, it is not prudent to generalize the effect of  $M_0$  on mixer/ejector nozzle acoustics or to extrapolate beyond the database.

#### 4.2.7 Azimuthal Acoustic Characteristics

The nonaxisymmetric geometry of the mixer/ejector nozzle is expected to produce nonaxisymmetric acoustic characteristics. The traversing microphone tower along with the fixed microphone array in Cell 41 were used to obtain acoustic data at three azimuthal locations for the rectangular mixer/ejector nozzle (see Section 4.1).

Figure 81 compares the EPNL data of Configuration 6 (SAR 3.3, MAR 0.95, 120-in full-scale flap length, fully treated walls) at three azimuthal angles ( $25^\circ$ ,  $60^\circ$ , and  $90^\circ$  relative to the major axis), for a simulated flight Mach number of 0.32. An azimuthal angle of  $25^\circ$  relative to the major axis corresponds to an aircraft altitude of 689 ft and a sideline distance of 1476 ft and is a representative location at which the sideline noise peaks. An azimuthal angle of  $90^\circ$  corresponds to the fly-over situation at the cut-back noise monitor. The azimuthal location of the fixed microphone array in Cell 41 corresponds to  $60^\circ$  relative to the major axis. The acoustic data at  $25^\circ$  and  $90^\circ$  are from the traversing tower; the acoustic data at  $60^\circ$  are from the fixed microphone array. The scale-model acoustic data are projected to an  $A_{p8} = 1086 \text{ in}^2$  and a sideline distance of 1629 ft. The aspect ratio of the ejector exit at MAR 0.95 is approximately 1.5.

Note that at all jet velocities the EPNL levels at  $25^\circ$  azimuthal location are the lowest. As the azimuthal angle increases, the EPNL values increase. At  $V_j \approx 2400 \text{ ft/s}$ , EPNL level at the  $25^\circ$  azimuthal location is approximately 2.5 EPNdB lower compared to  $90^\circ$ . This EPNL difference increases to a maximum of approximately 4 EPNdB at  $V_j \approx 1900 \text{ ft/s}$  and reduces at  $V_j$  below 1900 ft/s. Also, note that as  $V_j$  increases beyond 2400 ft/s, the azimuthal variation in EPNL reduces. It

is anticipated that the azimuthal acoustic characteristics are generated due to the rectangular geometry. The jet plume in the vicinity of the nozzle exit still retains significant nonaxisymmetry (see Section 4.2.1) and gradually becomes axisymmetric far downstream from the exit plane. One normally associates low-frequency noise generation with the far downstream distances. As  $V_j$  increases, the externally generated noise component becomes dominant (Section 4.2.1), and the contribution of low-frequency sources to the EPNL increases. Now, since these sources are located in regions where the jet plume is developing into an axisymmetric jet, one would expect reduced azimuthal acoustic variations at high  $V_j$  (such as 2600 ft/s).

Figure 82 compares the azimuthal variation of PNL directivities of Configuration 6 at  $V_j \approx 2400$  ft/s. PNL directivity at the azimuthal angle of  $25^\circ$  is uniformly lower compared to  $90^\circ$  at all polar angles. PNL directivity at  $60^\circ$  is between the other two azimuthal locations. Note that the peak PNL occurs at  $120^\circ$  polar angle for all three azimuthal locations.

Next, Figure 83 compares the azimuthal spectral characteristics at four selected polar angles. The spectral data at all four polar angles (more so at the peak PNL angle and  $90^\circ$ ) show that low-frequency noise (frequencies  $< 200$  Hz) is fairly uniform at all three azimuthal locations, reaffirming the axisymmetric plume evolution at far-downstream distances, where low-frequency noise generation takes place. Azimuthal variation seems to be the greatest in the frequency range of 0.4 to approximately 4 kHz. Frequencies above 4 kHz do not exhibit significant azimuthal variation. This may be tied to the axial distribution of these sources. High frequencies (above 4 kHz) are probably generated close to the chute exit, and accompanying multiple reflections and scattering within the ejector walls may lead to an insensitivity to azimuthal angle. The middle frequencies (0.4 to approximately 4 kHz) are generated closer to the ejector exit and downstream of the ejector exit where plume development is significantly nonaxisymmetric, resulting in the noted azimuthal variations.

The azimuthal variation depends upon the split between the internal and external noise components, aspect ratio of the ejector exit, and probably the chute aspect ratio. Until further investigations are conducted where the above parameters are varied systematically, it may not be prudent to generalize azimuthal variations noted on this mixer/ejector nozzle.

#### 4.2.8 Influence of Jet Temperature on Ejector Flowfields

Simulation of jet total temperature and nozzle pressure ratio in exhaust nozzle jet noise investigations is very critical. Jet velocity is a function of both total temperature and nozzle pressure ratio, and jet velocity has a dominant effect on jet noise. Simulation of jet velocity in aerodynamic/acoustic investigations through a representative combination of total temperature and nozzle pressure ratio as would occur in an engine cycle results in appropriate aero/thermodynamic parameters such as jet density and total enthalpy as well as plume shock structure of nonideally expanded supersonic jets. These parameters have a significant influence on jet mixing noise as well as shock-associated broadband noise. Hence, scale-model jet noise investigations simulate appropriate jet aero/thermodynamic parameters, and the scale model data are then scaled to full scale using Strouhal parameter:

$$f \times d / V_j$$

where  $f$  is the frequency,  $d$  is a characteristic length scale (such as jet diameter) and  $V_j$  is the jet velocity.

Classical aerodynamic studies and investigations of ejectors have indicated through 1D ideal calculations, as well as experimental measurements, that the ratio of total-temperature-corrected secondary to primary airflow

$$(W_s \sqrt{T_{Ts}}) / (W_p \sqrt{T_{Tp}})$$

can be correlated with nozzle pressure ratio (Reference 6). Hence, ejector aerodynamic investigations have been performed with cold-flow models and projected to hot-flow conditions, using the above principle, as a cost-saving means. For the same reason, single- and two-flow nozzle aerodynamic performance investigations in the past have been performed with cold-flow models, and the measured cold-flow performance was projected to hot conditions after accounting for specific heat ratio ( $\gamma$ ) dependence on static temperature as well as thermodynamic mixing efficiency dependence on temperature.

Because of the above considerations, it was deemed necessary to investigate the effect of temperature on mixer/ejector flowfields. The aerodynamic-mixing investigations described in Section 5 were conducted at a primary total temperature of approximately 860°R as a means to investigate flowfields with less expensive models (compared to acoustic models) that withstand temperatures of up to approximately 2000°R. The applicability of the aerodynamic-mixing test data to interpret/project selected flowfield parameters to higher temperature should be assessed for the conduct of future tests at temperatures significantly lower than the cycle temperatures. Also, understanding the effect of primary stream total temperature on ejector flowfields and mixing effectiveness merits attention.

This section summarizes the effect of primary stream total temperature on following:

- a. Corrected entrainment flow ratio:  $(W_s \sqrt{T_{Ts}}) / (W_p \sqrt{T_{Tp}})$
- b. Flap static pressure distribution
- c. Exhaust plume velocity distributions, as measured by LV

The test data described in this section were acquired on the acoustic model system in Cell 41 at a range of total temperatures of approximately 700° to 1950°R. Figure 84 compares variation of corrected entrainment flow ratio for Configuration 2 (SAR 3.3, MAR 1.2,  $L_{ej} = 120$ -in full scale,  $M_0 = 0$ ) and Configuration 7 (SAR 3.3, MAR 0.95,  $L_{ej} = 120$ -in full scale,  $M_0 = 0$ ) as a function of NPR. The cold-flow tests were conducted holding the total temperature of the primary stream at approximately 700°R and varying NPR from approximately 3 to 4.5. The hot-flow tests were conducted along the VCE-L1M cycle. Secondary flow was computed based on the total pressures measured by three sets of rakes in the secondary inlet (see Section 4.2.1). Primary flow was computed based on total pressure and total temperature rakes at the facility charging station and using design  $A_{p8}$  for the primary stream. It is arguably an inaccurate measurement, compared to using a venturi to meter the flow. However, within the accuracy of this technique, on a corrected entrainment-flow ratio basis, the data seem to collapse reasonably well. At the NPR's at which the data were obtained, MAR does not seem to affect entrainment flow ratio, presumably because the ejector is operating in a compound supersonic-flow mode wherein the secondary flow chokes slightly downstream of the mixing plane and becomes the metering station for the secondary flow. From this set of comparisons, it is again "confirmed" that ejector secondary to primary flow ratio can be reasonably collapsed on a total-temperature-corrected basis.

Figure 85 compares the ejector flap static pressure axial distribution normalized by ambient static pressure for Configuration 2 (SAR 3.3, MAR 1.2,  $L_{ej} = 120$ -in full scale,  $M_0 = 0$ ) at NPR = 3.4 and

4.0. The static pressure data are from the row of probes in line with the middle of the secondary chute passage. Distributions along the middle of primary chute passage are not illustrated, but they are very similar. It is noted that, for both the NPR's, this configuration is operating in the "supersonic" mode. The effect of primary stream total temperature on the static pressure distributions is small and probably within the experimental variability.

Flap static pressure distributions for Configuration 7 (SAR 3.3, MAR 0.95,  $L_{ej} = 120$ -in full scale,  $M_0 = 0$ ) at NPR's of 3.4 and 4.0 are shown in Figure 86. The flap static pressure distribution at NPR = 4.0 are somewhat similar at approximately  $700^\circ$  and  $1757^\circ\text{R}$ ; at both the temperatures, the nozzle is operating in the "supersonic" mode. However, the flap static pressure distributions at NPR = 3.4 indicate the ejector is operating in a "supersonic" mode at a primary total temperature of approximately  $700^\circ\text{R}$  and in a "subsonic" mode at a primary total temperature of approximately  $1600^\circ\text{R}$ .

This set of data clearly indicates that primary stream total temperature has a significant effect on "mode transition" of the ejector. The phenomenon of "mode transition" is dependant on many factors, such as: MAR, total temperature, and SAR. The phenomenon involves acceleration of the secondary stream by the primary to locally supersonic conditions due to momentum transfer and/or "pinching" of the secondary stream passages by an overexpanding primary stream. Such physical phenomenon are influenced by thermodynamic quantities such as jet densities and specific heat ratios of primary and secondary streams. Thus, the phenomenon of "mode transition" should be investigated with proper simulation of primary stream total temperature. However, if the ejector is either in "subsonic" or "supersonic" mode over the range of primary stream total temperatures being investigated, the flap static pressure distributions measured with low values of primary stream total temperature are still applicable for high values of primary stream total temperature.

Influence of primary stream total temperature on jet plume downstream of the nozzle exit, as measured by LV is discussed next. Figure 87 compares the axial velocity profiles at the nozzle exit for Configuration 15 (SAR 3.3, MAR 0.95,  $L_{ej} = 80$ -in full scale,  $M_0 = 0.32$ ) at total temperatures of  $1590^\circ$  and  $860^\circ\text{R}$ . NPR is maintained at 3.4. The LV traverse is taken approximately 0.6 inch downstream of the nozzle exit, along the minor axis of the nozzle (see Figures 33 and 34). The measured jet velocities at the nozzle exit for the case of  $1590^\circ\text{R}$  are obviously higher compared to  $860^\circ\text{R}$ , since the primary jet velocity is higher compared to the  $860^\circ\text{R}$  case. However, note that the velocity profiles are "smoother" for lower temperature, and the peak-to-valley variation for lower temperature tends to be slightly higher. The velocity profile at  $1590^\circ\text{R}$  exhibits asymmetry about the nozzle centerline; such asymmetry is much smaller at  $860^\circ\text{R}$ .

Next, Figure 88 compares the influence of primary stream total temperature on axial velocity profiles at the nozzle exit, along the major axis of the nozzle (see Figures 33 and 34). As shown in Figure 7, there are 10 equal-width secondary chutes, 9 equal-width primary chutes, and 2 half-width primary chutes on the top and bottom sides of the nozzle. At  $860^\circ\text{R}$ , nine high-velocity peaks and eight low-velocity valleys are clearly noticeable, indicative of the centers of primary chutes and secondary chutes, respectively. (Flow in the half-width primary chutes along the sidewalls has mixed well with the secondary flow in the adjacent secondary chutes, and the boundary layer growth along the sidewalls is sufficient that one picks up only nine high-velocity peaks and eight low-velocity valleys.) At  $1590^\circ\text{R}$ , the velocity profile along the major axis (chute-to-chute direction) is nominally at a higher value compared to  $860^\circ\text{R}$  case, but no peaks and valleys are clearly discernable, and in general the profile is better mixed compared to the  $860^\circ\text{R}$  case.

Figure 89 compares the effect of primary stream total temperature on external plume decay along the nozzle axis. Jet velocity for the 1590°R case is approximately 1320 ft/s, and it is approximately 1180 ft/s for the 860°R case. At an axial distance of 120 in from the nozzle exit in scale model (approximately 12.5 nozzle widths), the jet velocity for both cases is approximately 600 ft/s, indicating the jet plume decays faster if primary stream total temperature is higher at same NPR. The above flowfield observations are all consistent with the following rationale.

Holding the same NPR during these studies implies the primary stream Mach numbers are approximately the same, except for differences in specific heat ratios and associated impacts on ejector “mode transition.” The impact of these two differences on the nozzle exit flowfields probably is not large. Higher primary stream total temperature creates a larger velocity gradient as well as a larger static temperature gradient between the primary and secondary streams. This promotes mixing due to “momentum mixing” as well as “thermal diffusion.” Hence, when the primary stream temperature is increased, the jet velocity profiles indicate a higher level of mixing, resulting in more uniform profiles. Thus, the assessment of mixing or “mixedness” from cold-flow tests will be on the lower side compared to what one would obtain in a hot-flow test.

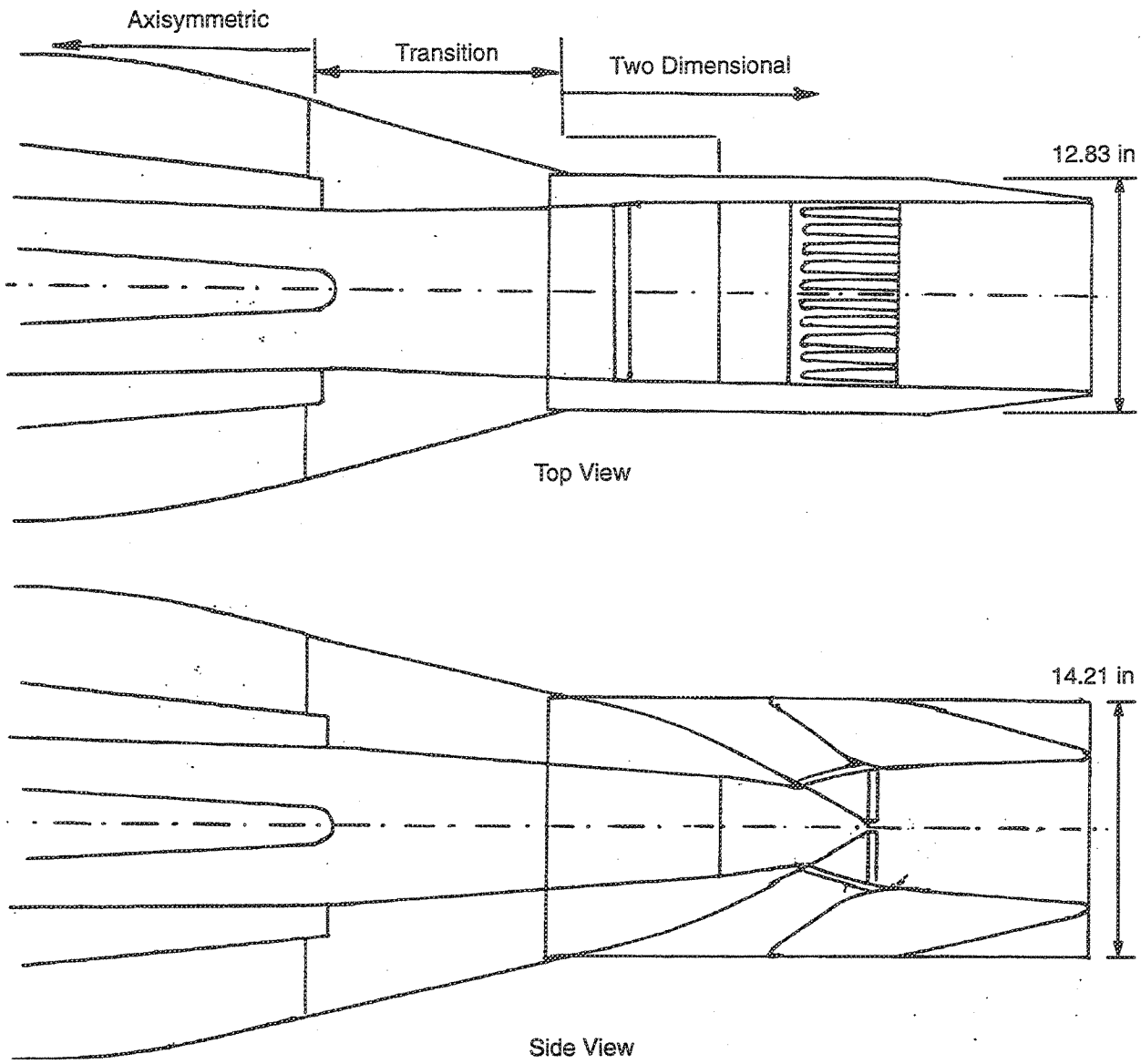


**Figure 9. Acoustic scale-model cross section adapted to Cell 41**

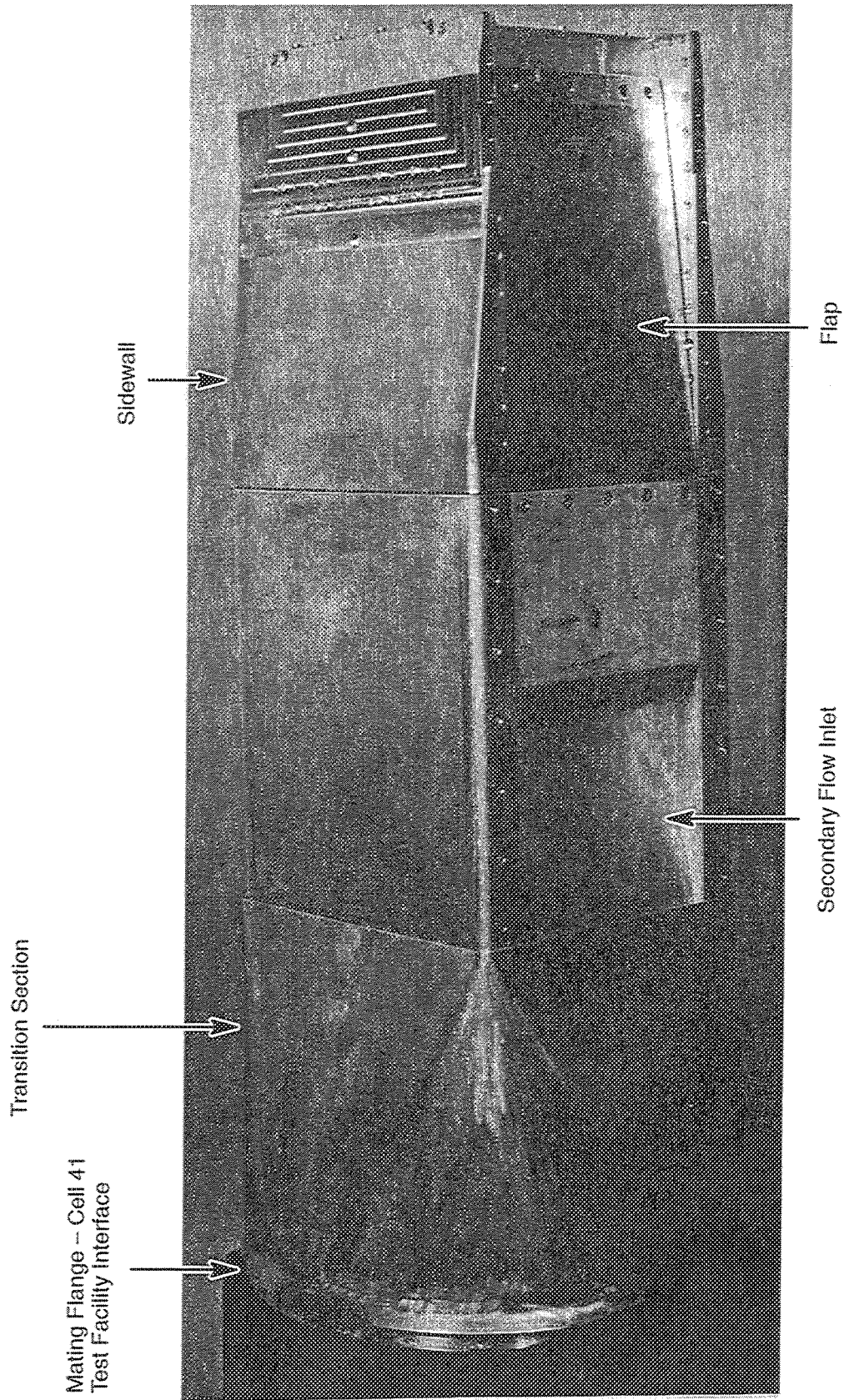


Figure 10. Photograph of the Cell 41 1/7th scale 2D mixer/ejector exhaust system acoustic model

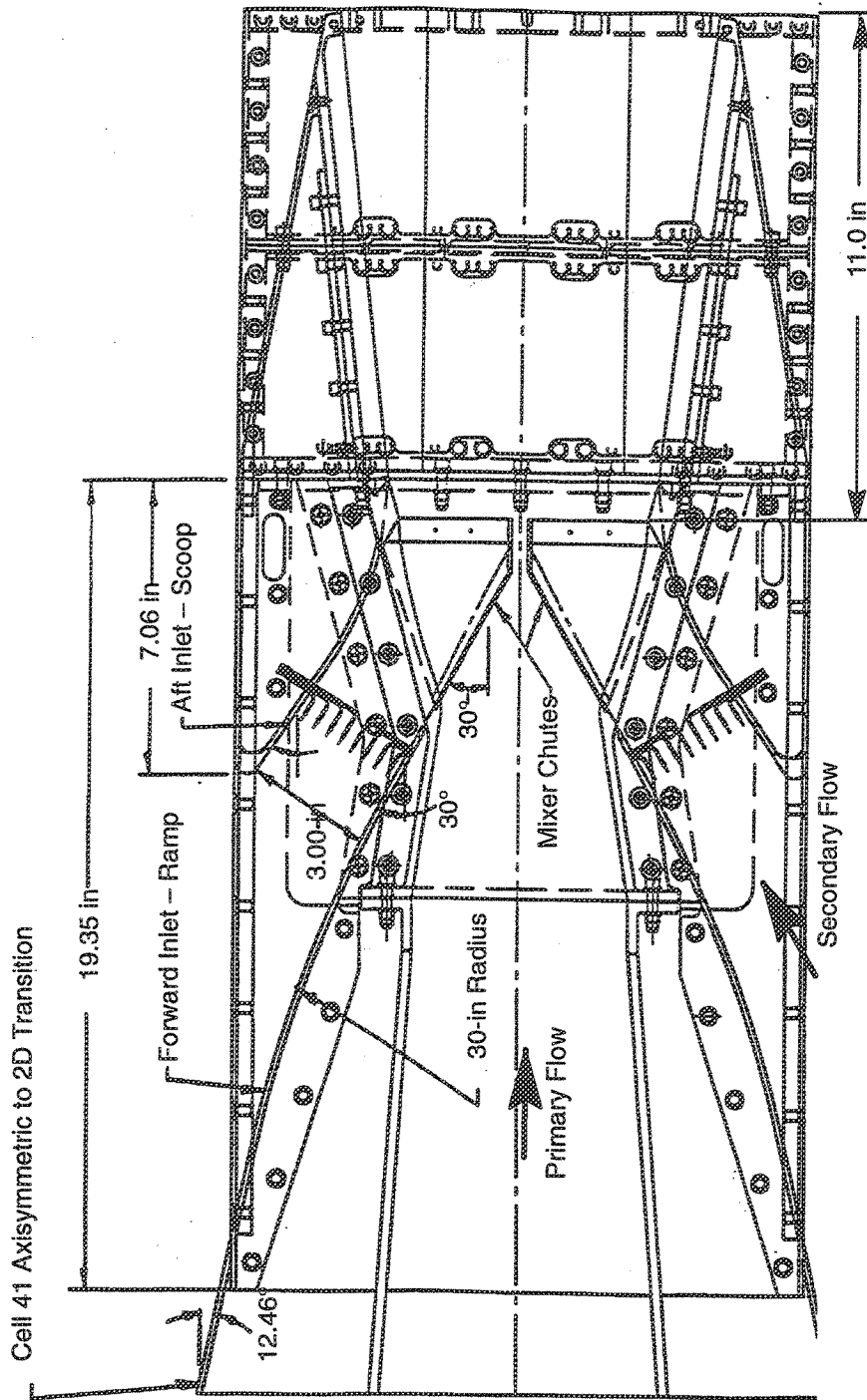


Figure 11. Cross section of the 1/7th scale Cell 41 acoustic model of the 2D mixer/rejector exhaust system

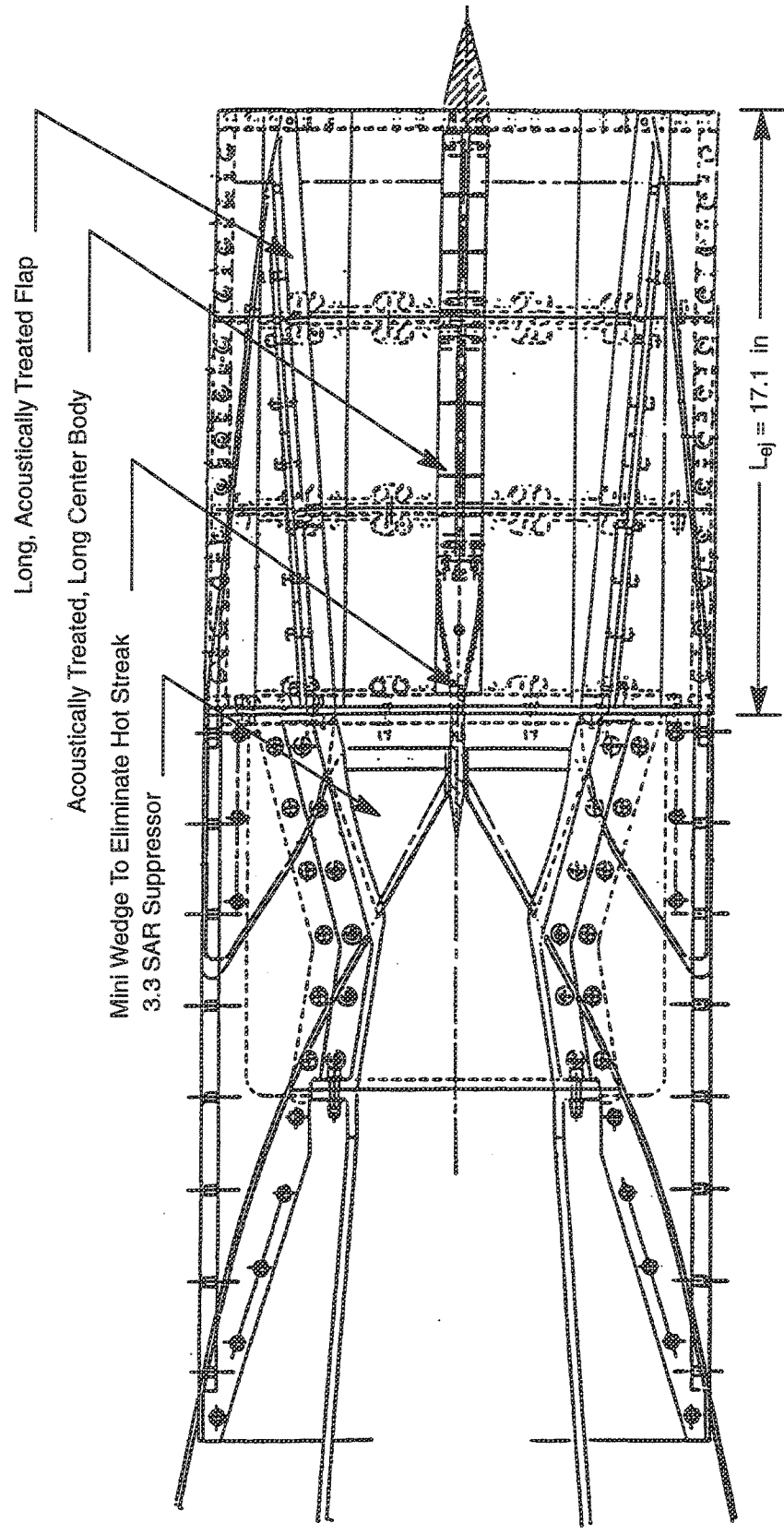


Figure 12. Schematic of the acoustic risk-reduction features of the 2D mixer/ejector nozzle scale model

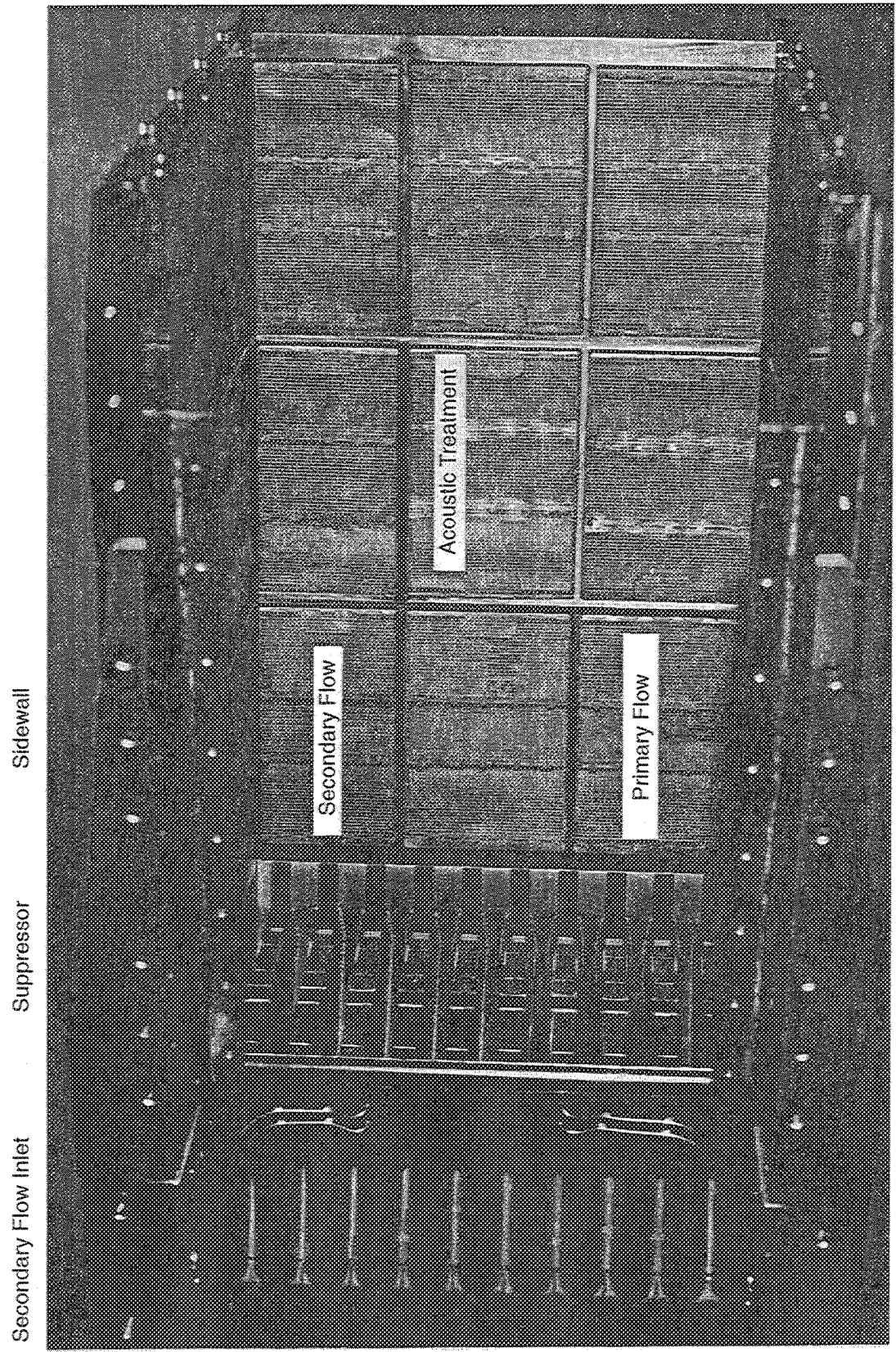


Figure 13. View of 2D mixer/ejector acoustic scale model with one flap removed — showing internal details of long-flap configuration

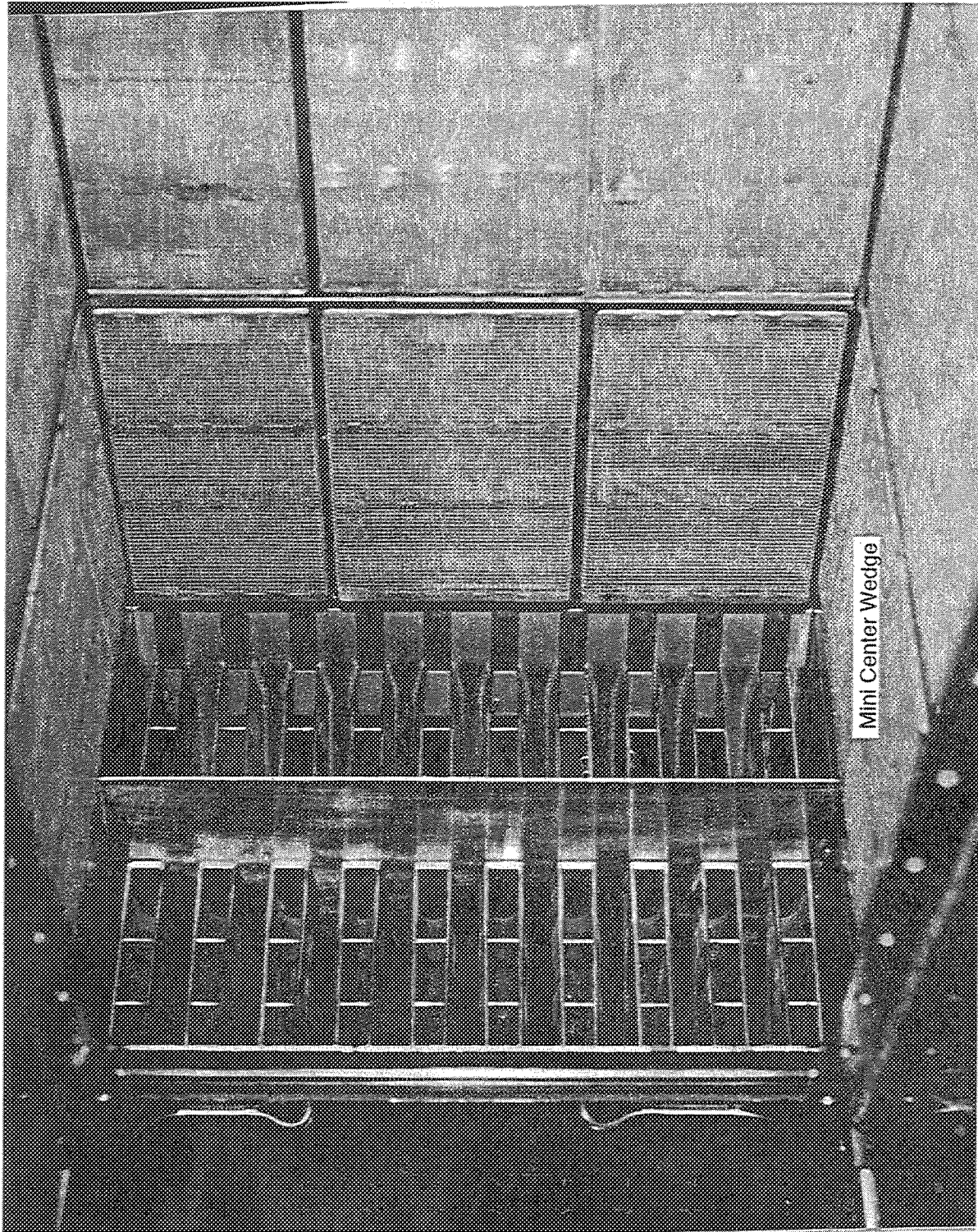


Figure 14. Photograph of the 2D mixer/ejector acoustic scale model with mini center wedge to eliminate center hot streak

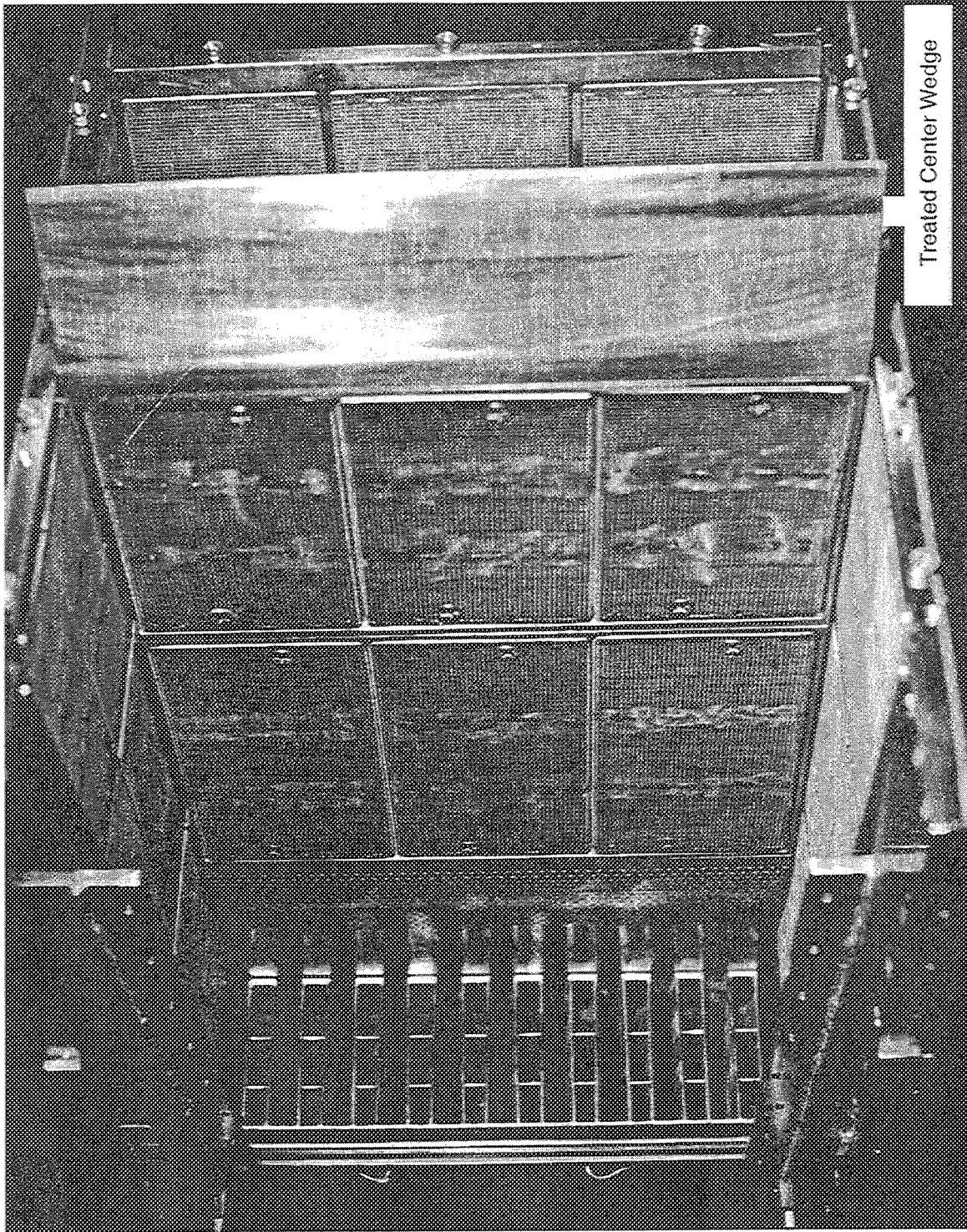


Figure 15. SAR = 2.8 long-flap configuration 2D mixer/ejector acoustic scale model with treated center wedge

- Faceplate:
- 37% porous perforated Hastalloy X, 24 gage (0.025 in)
  - 0.045-in holes with 0.067-in spacing on centers
  - 225 holes per in<sup>2</sup>
- Foam Metal Insert: Retimet metal foam, 0.08-in thick, 95% porous, 0.03-in pore size applied to prevent Astroquartz degradation due to turbulence
- Bulk Absorber: Astroquartz 550, 0.0002-in maximum fiber diameter, 0.2-in thick sheets compressed to a density of 1 lbm/ft<sup>3</sup>
- Compartments: Trays divided into hard-walled compartments to prevent compaction and/or degradation of the bulk absorber due to flow and to allow configuration variations — hard wall, treated wall, and treatment density combinations
- Hard-Wall Configurations: 0.03-in thick sheet metal trimmed to fit compartment dimensions, inserted between faceplate and foam metal

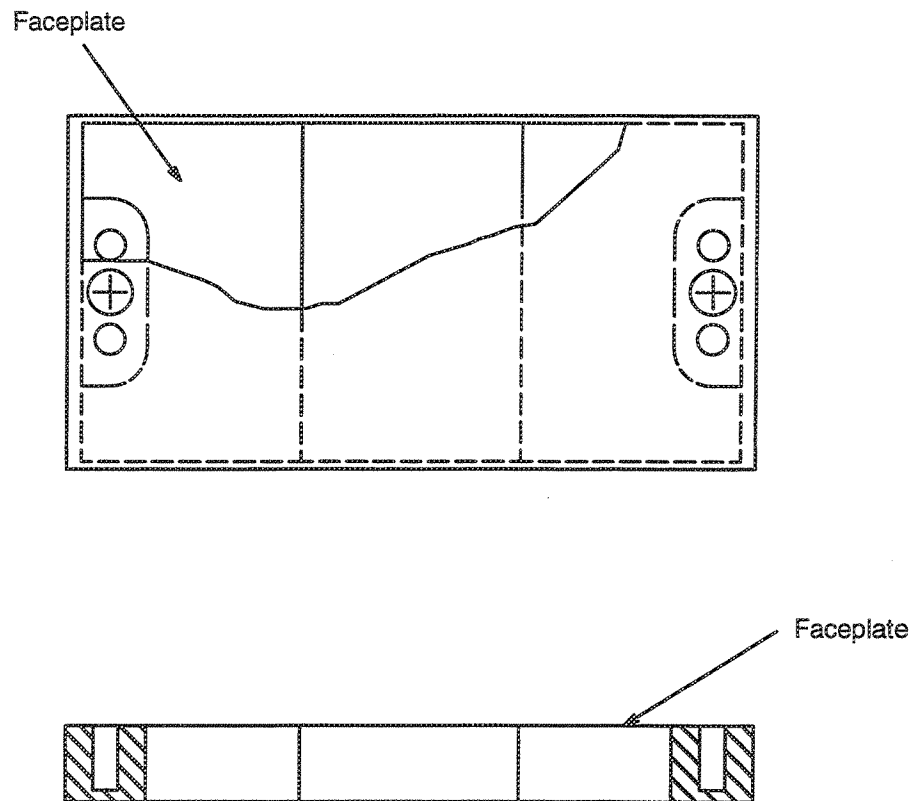


Figure 16. Typical scale-model acoustic treatment tray design

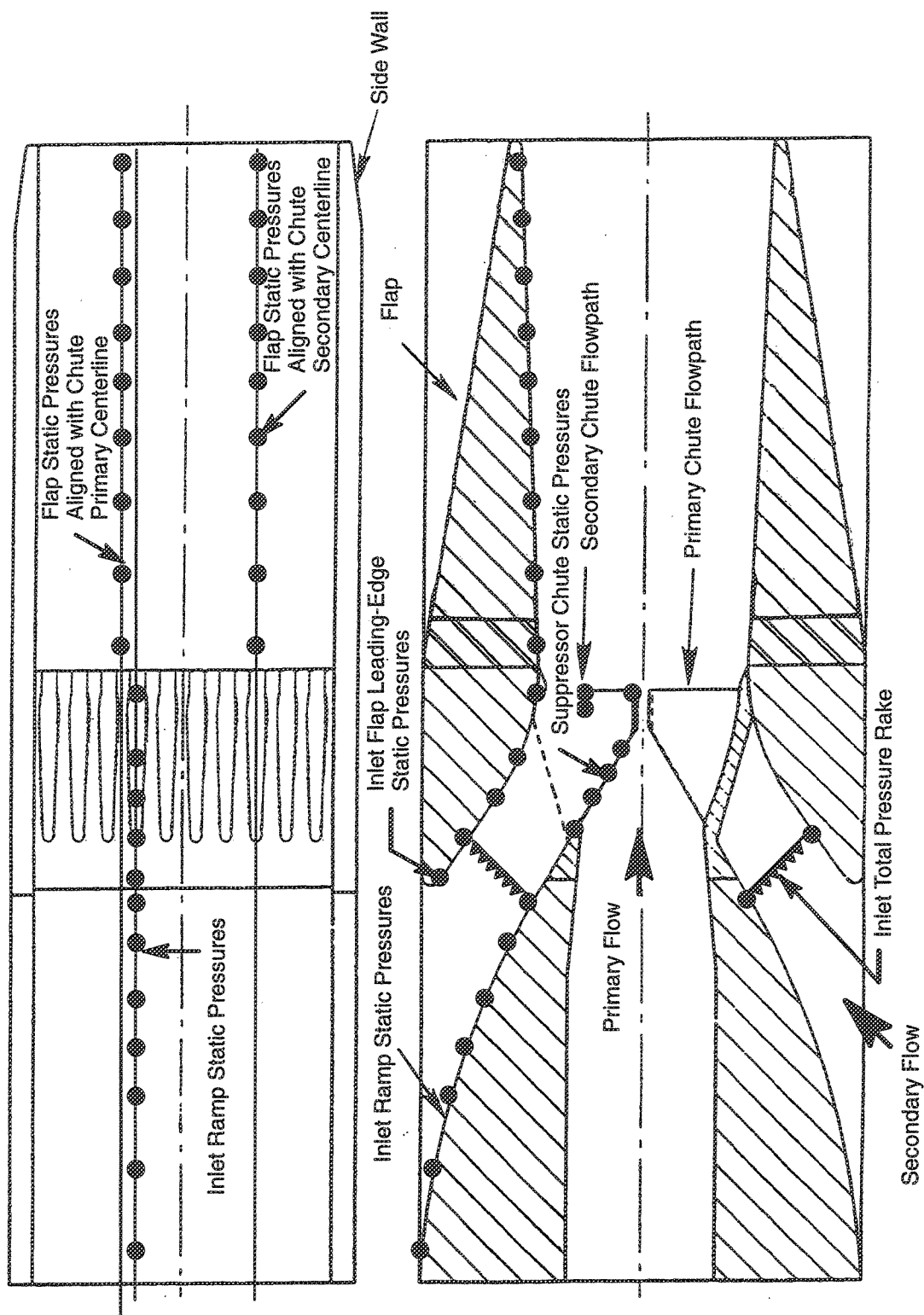


Figure 17. Schematic of the key acoustic model instrumentation

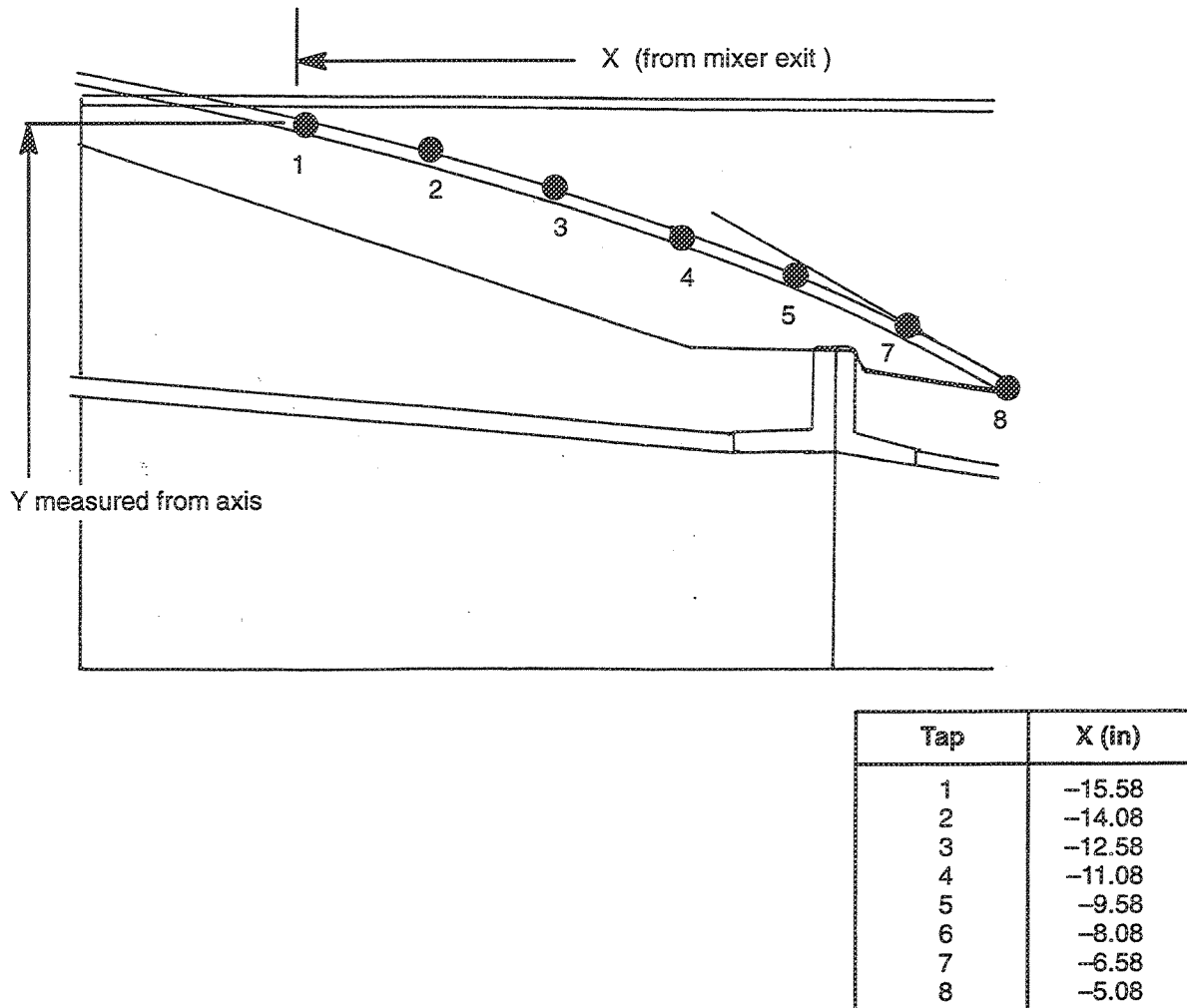
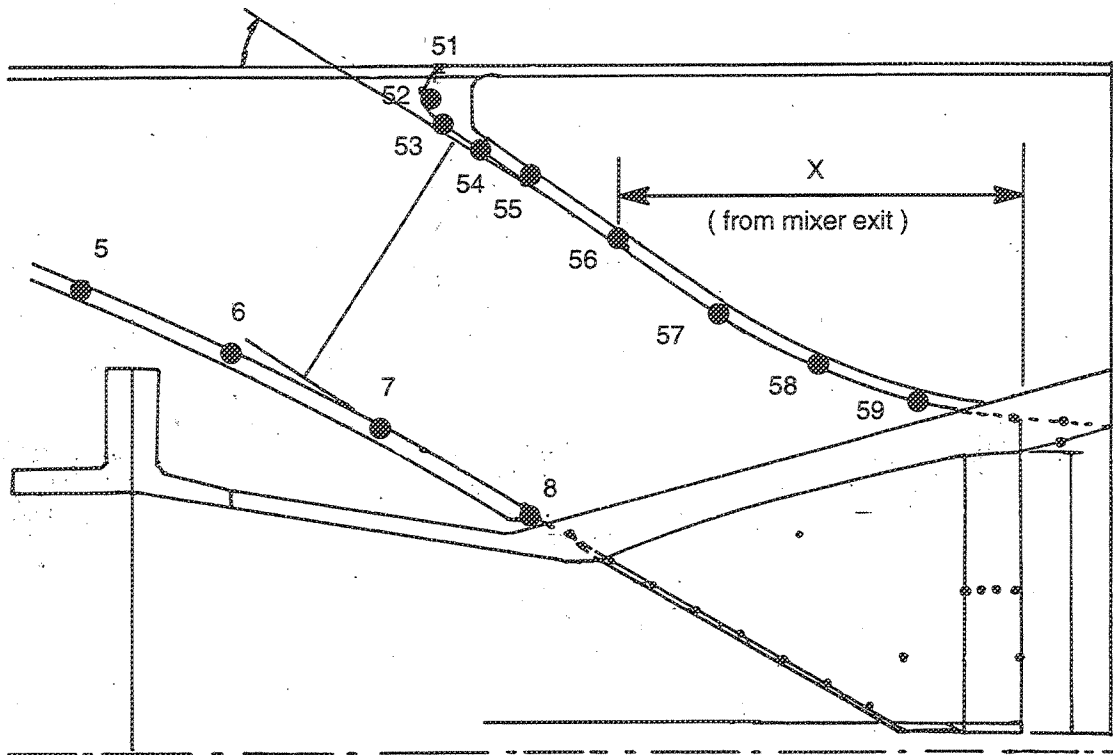
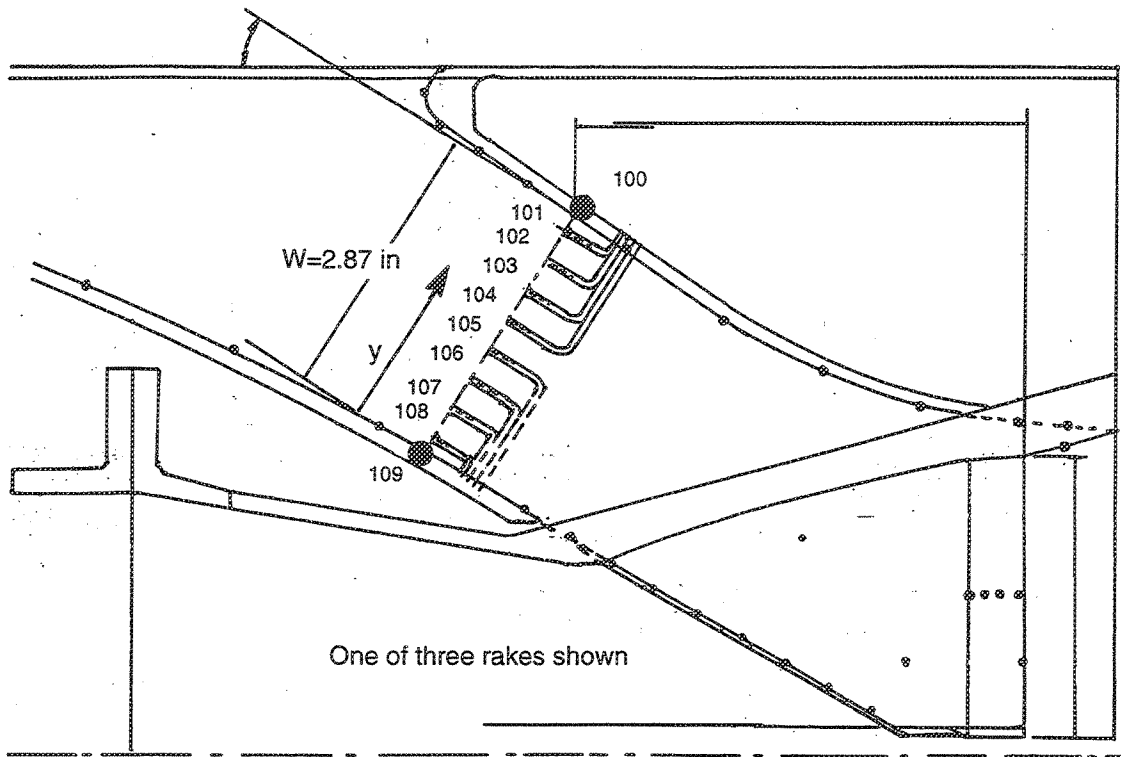


Figure 18. Cross section of inlet ramp of the 2D mixer-ejector nozzle showing static pressure taps



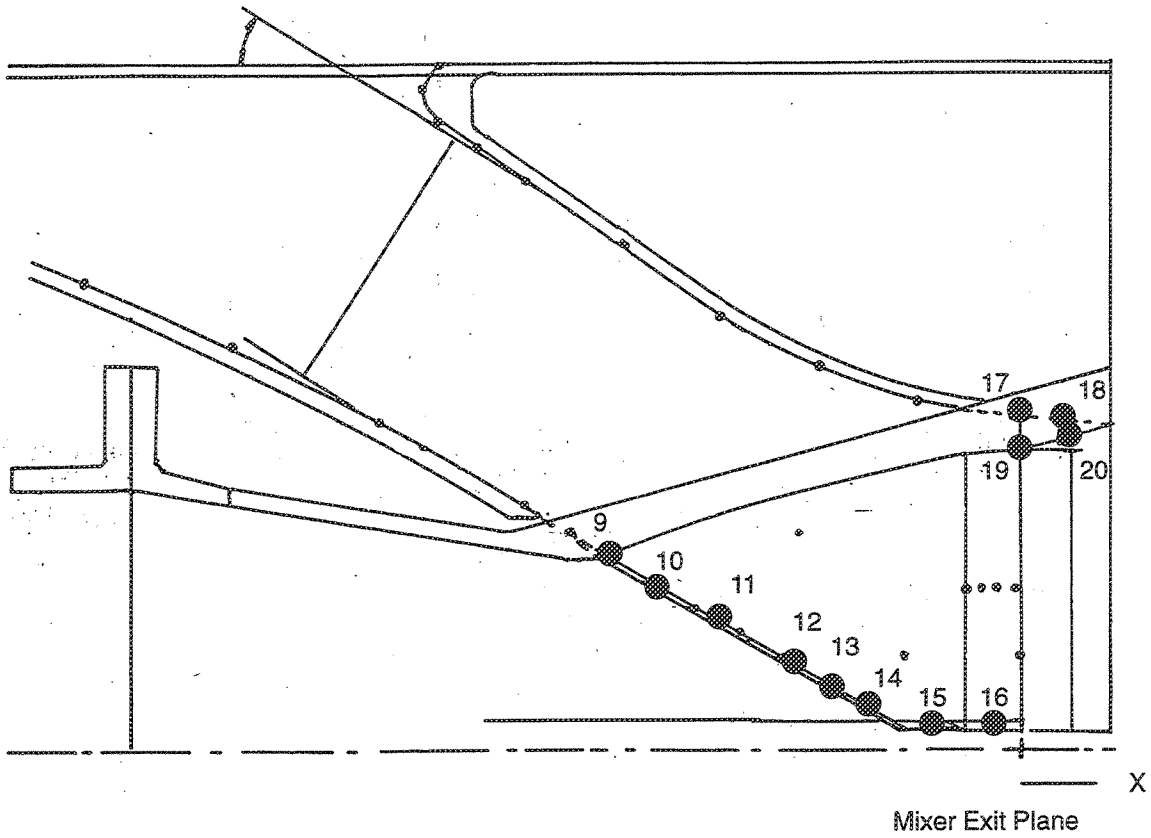
Tap	X (in)
51	-5.980
52	-6.135
53	-5.980
54	-5.580
55	-5.080
56	-4.080
57	-3.080
58	-2.080
59	-1.050

Figure 19. Static pressure taps along the inlet flow guide/flap leading edge



Y (in)	Rake 1, Tap	Rake 2, Tap	Rake 3 Tap
0.000	109	119	129
0.179	108	118	128
0.538	107	117	127
0.897	106	116	126
1.256	105	115	125
1.614	104	114	124
1.973	103	113	123
2.332	102	112	122
2.691	101	111	121
2.870	100	110	120

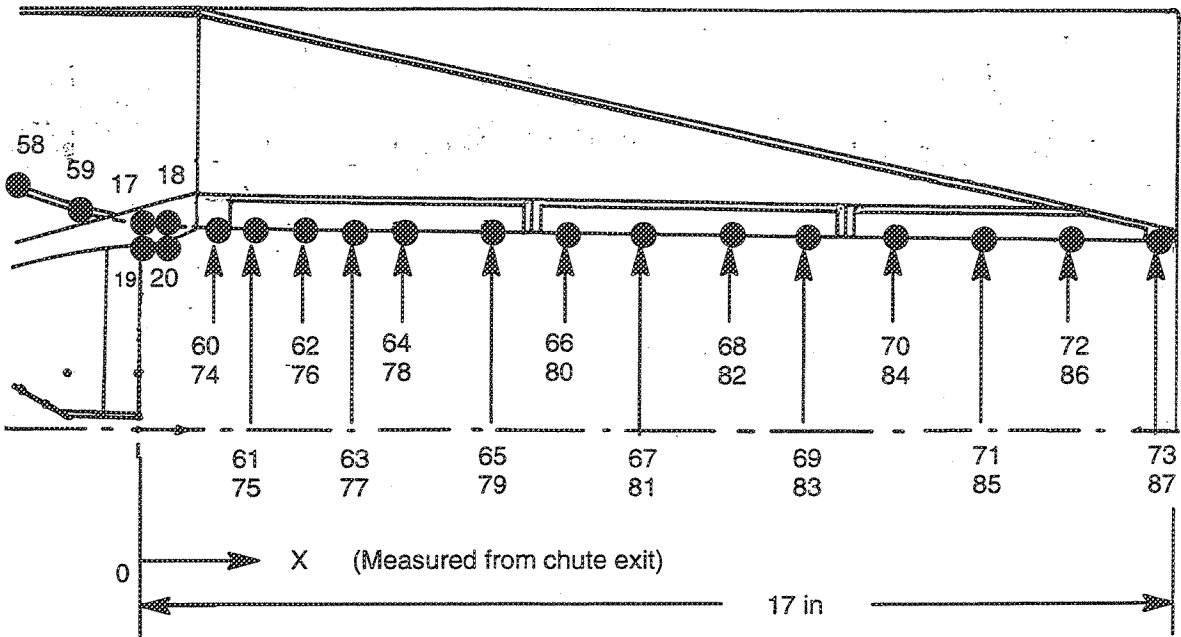
Figure 20. Inlet total pressure rake instrumentation for 2DME nozzle



Tap	X, in	Remarks/Location
9	-4.40	Chute base
10	-3.73	Chute base
11	-3.05	Chute base
12	-2.38	Chute base
13	-1.70	Chute base
14	-1.47	Chute base
15	-1.03	Chute base
16	-0.46	Chute base
17	-0.09	Secondary chute exit
18	+0.40	Secondary chute exit
19	-0.02	Primary extension
20	+0.40	Primary extension

Figure 21. Mixer chute static pressure tap locations

Note: only top flap is shown: Row 1 located 1.92 in from flap center line  
 Row 2 located 1.46 in from flap center line



X (in)	Row 1, Tap	Row 2, Tap
1.17	60	74
1.92	61	75
2.67	62	76
3.42	63	77
4.17	64	78
5.67	65	79
7.01	66	80
8.34	67	81
9.68	68	82
11.01	69	83
12.29	70	84
13.79	71	85
15.29	72	86
16.79	73	87

Figure 22. Cross section of the 2D mixer-ejector nozzle showing the flap static pressure taps

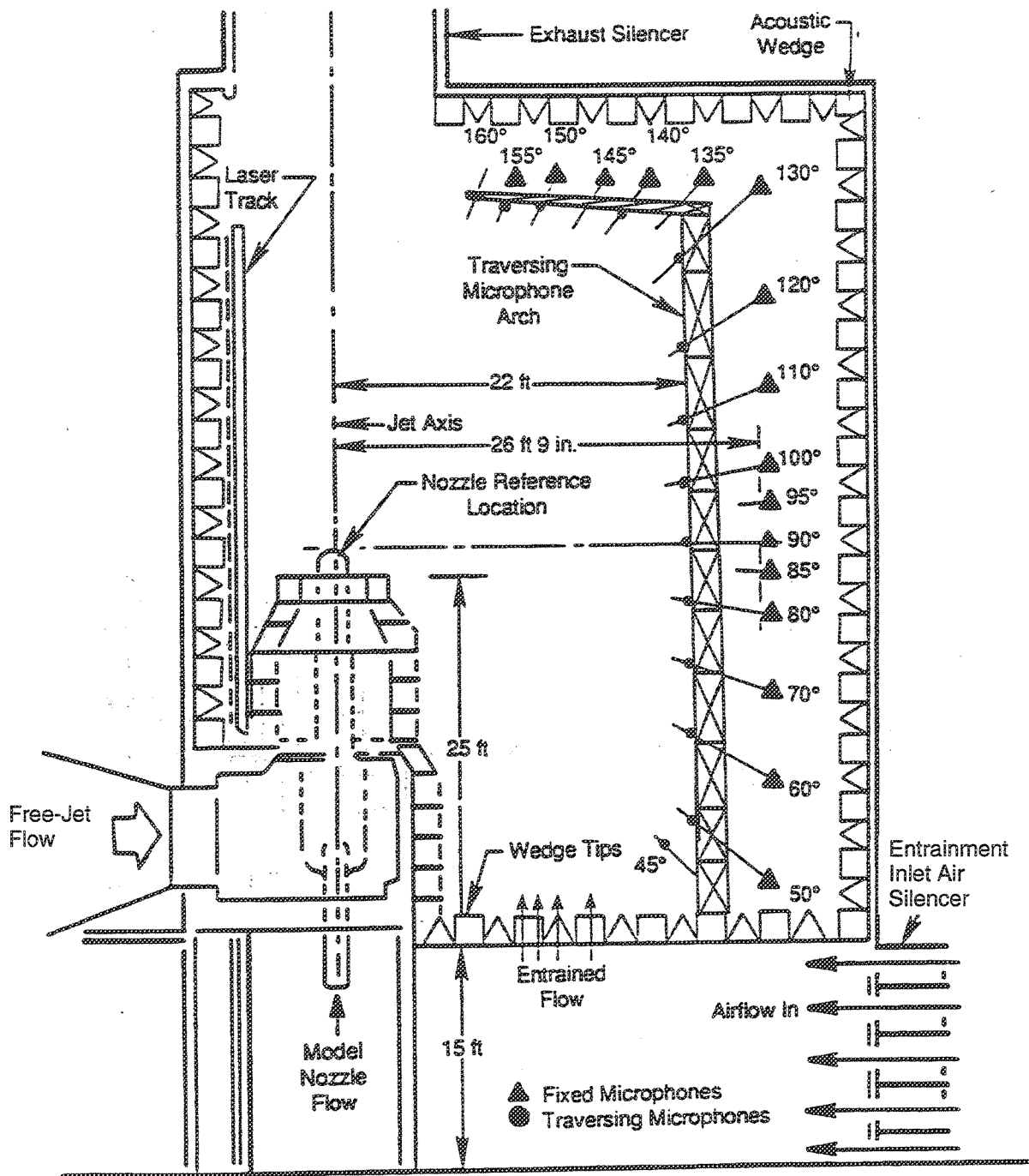


Figure 23. Cell 41 anechoic free-jet facility: microphone positions in the azimuth plane

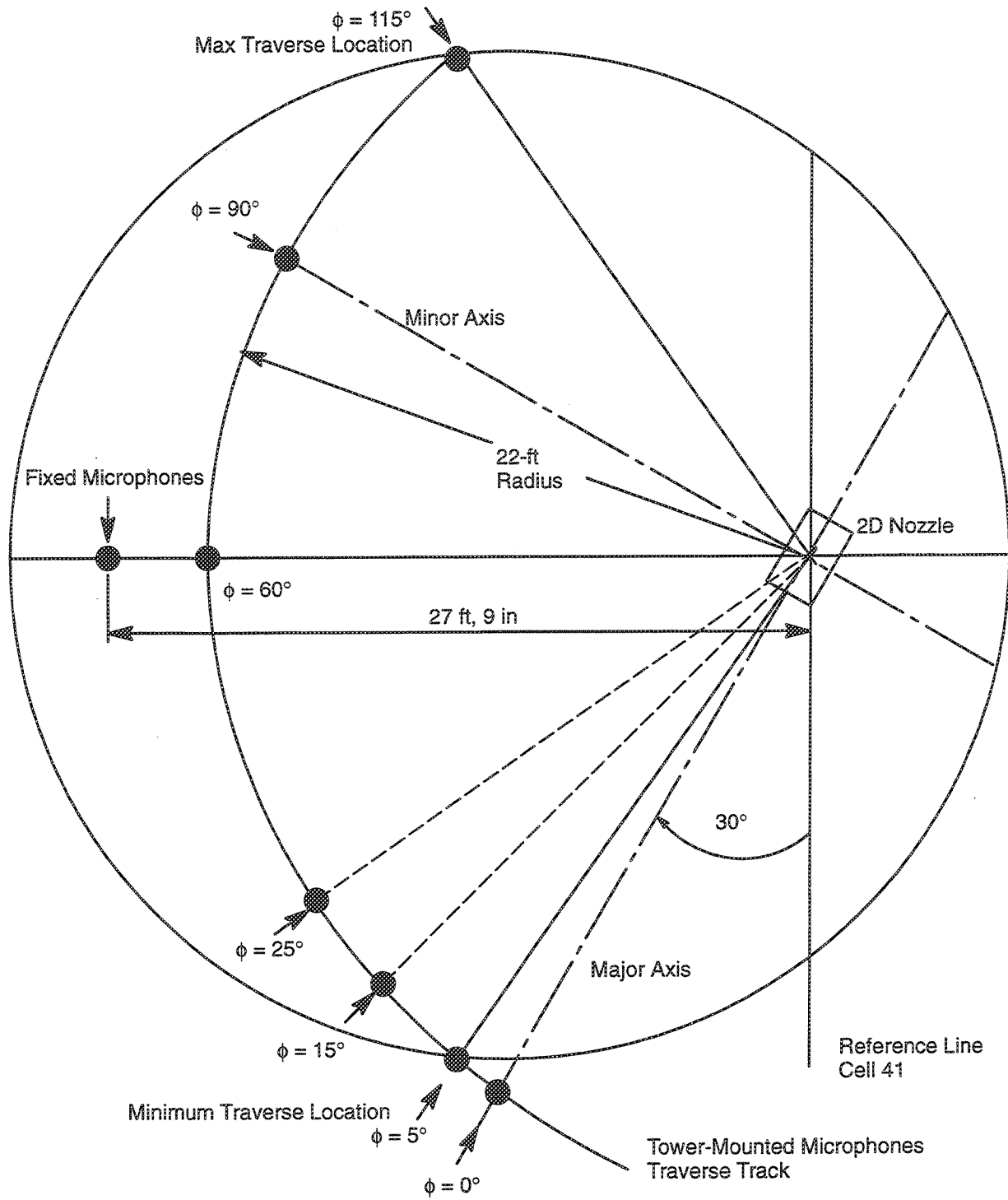


Figure 24. Plan View of test facility showing the tower mounted traverse microphone track relative to the 2D mixer/ejector exhaust nozzle scale model installation in Cell 41

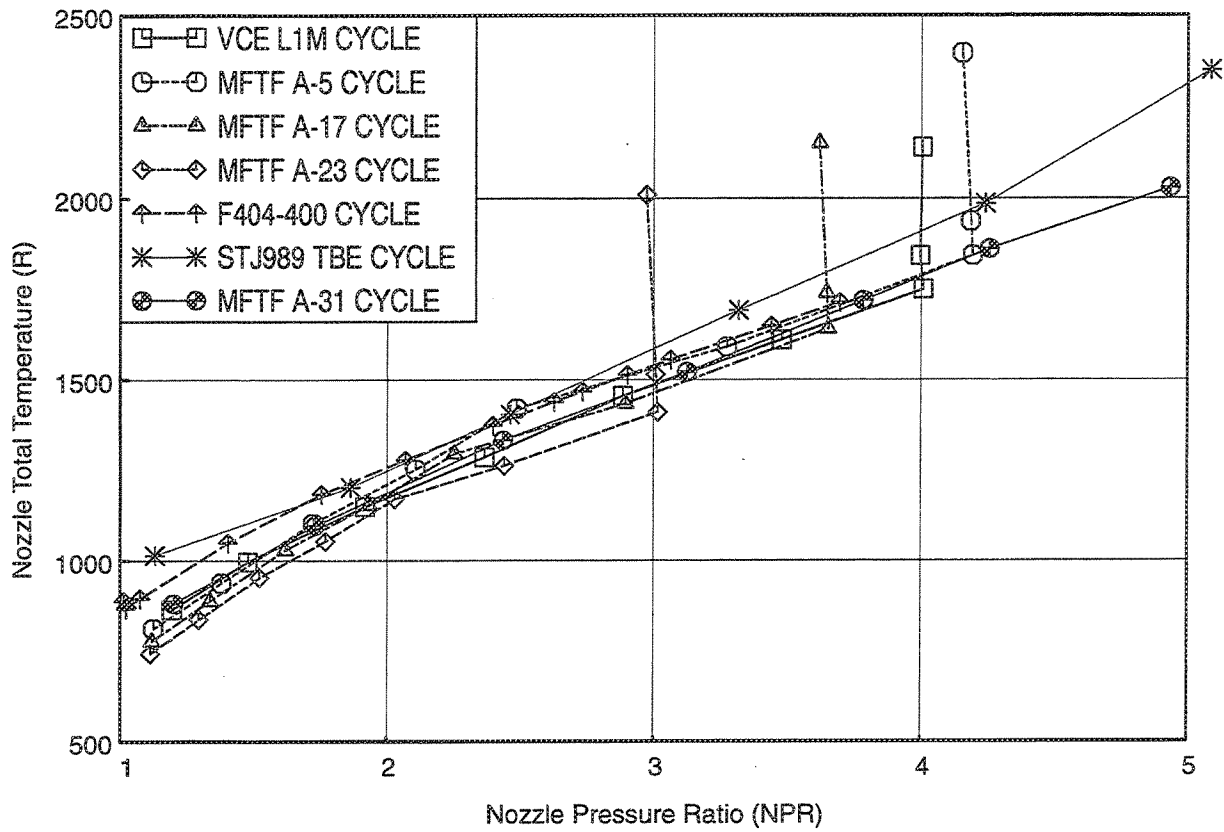


Figure 25. Test point selection for GEAE 2DCD acoustic test

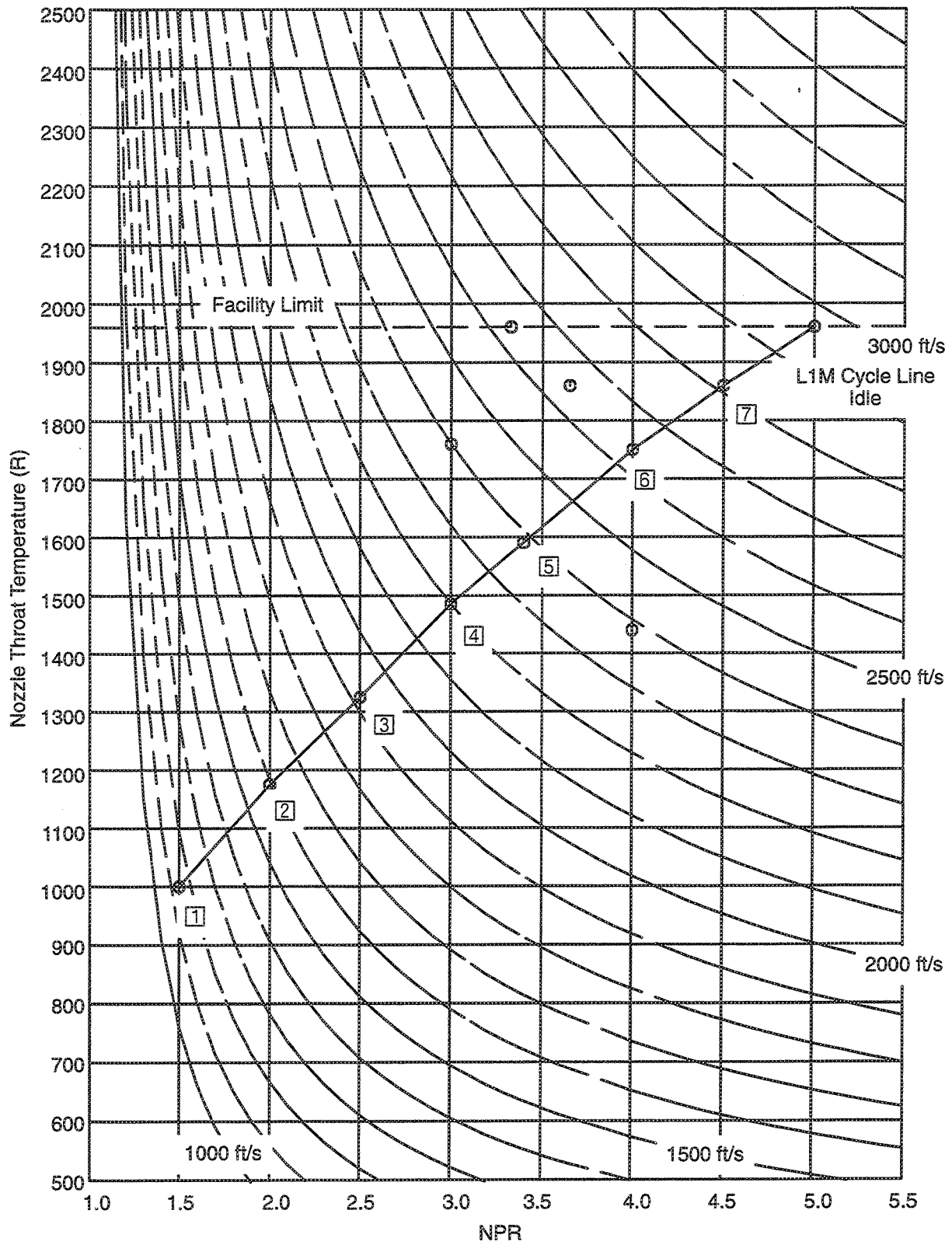


Figure 26. Test point selection for GEAE 2DCD acoustic test

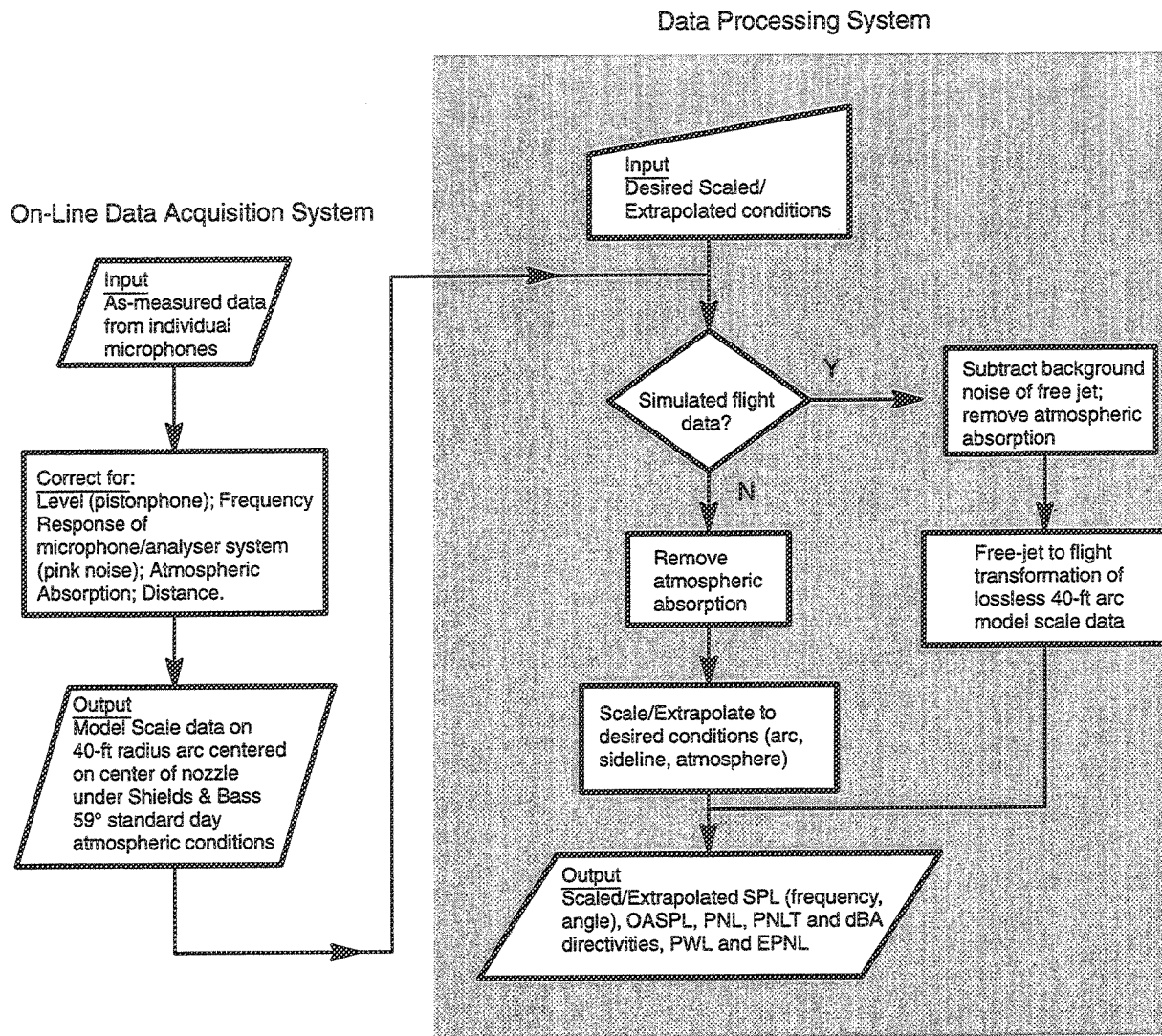
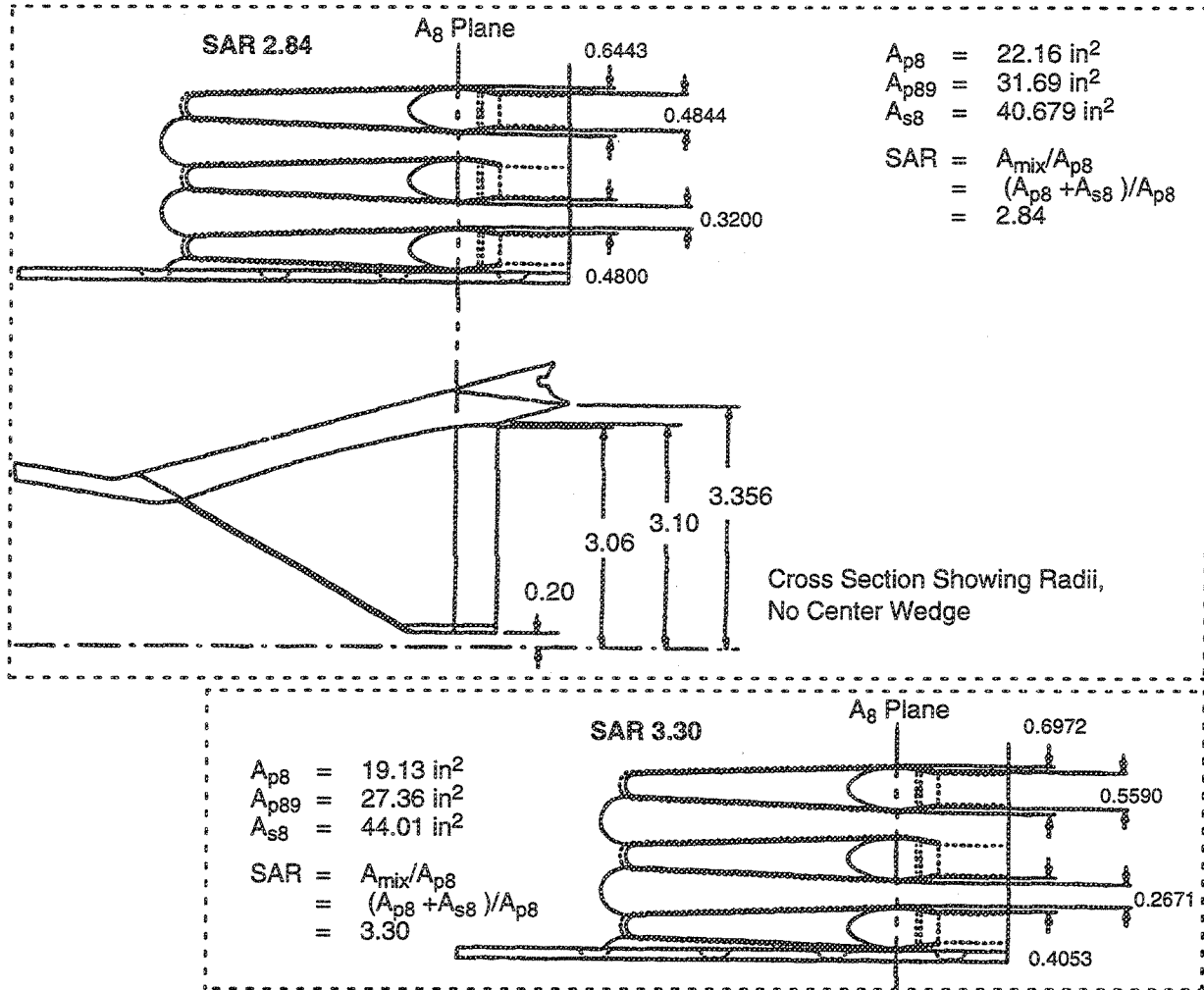


Figure 27. Cell 41 acoustic data acquisition and processing schematic

### Chute Convergent-Divergent Design Assumptions

- Chute exit plane local static pressure: 11.0 psia
- Takeoff design NPR = 4.00; therefore,  $P_{T8} = 58.8$  psia
- NPR based on  $58.8/11.0 = 5.34$
- With  $\gamma = 1.33$  (Specific heat at constant pressure + specific heat at constant volume) Facility Max.  $T_8 = 1960^\circ R$ ,  $A_{exit}/A_8 = 1.43$
- $A_{exit} + A_8 = 31.69$  for SAR = 2.8 and 27.37 for SAR = 3.3

Designed for shock-free operation at cycle NPR = 4.0 with anticipated local NPR = 5.34



	SAR	Linear Scale Factor*	$A_8$ , in <sup>2</sup>	Equivalent Diameter, in	$A_{s8}$ , in <sup>2</sup>	$A_{mix}$ , in <sup>2</sup>	Chute Tip-to-Tip Gap, in
Without Wedge	2.84	1/7	22.16	5.31	40.67	62.83	0.40
	3.3	1/7.53	19.13	4.94	44.01	63.15	0.40
With Wedge	3.22	1/7.702	18.31	4.83	40.67	58.98	0
	3.88	1/8.43	15.28	4.41	44.01	59.29	0

\* Based on 1086 in<sup>2</sup>  $A_8$  of GE21/F14 Study L1M cycle at 50,000-lbf hot-day takeoff thrust

Figure 28. Comparison of SAR 2.8 and 3.3 acoustic scale-model suppressor designs

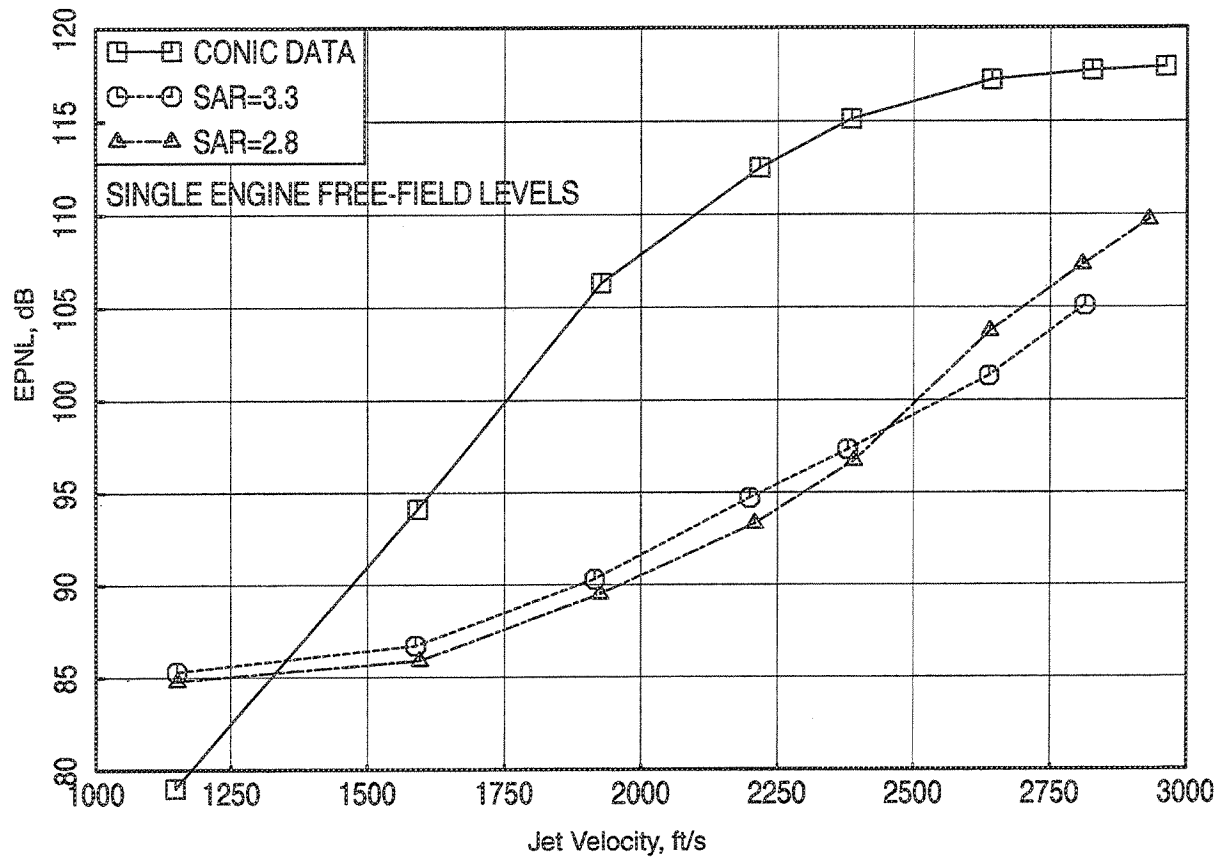


Figure 29. SAR effect on EPNL as a function of  $V_j$ ; 120-in treated flap,  $MAR = 0.95$ ,  $M_0 = 0.32$ , sideline microphones

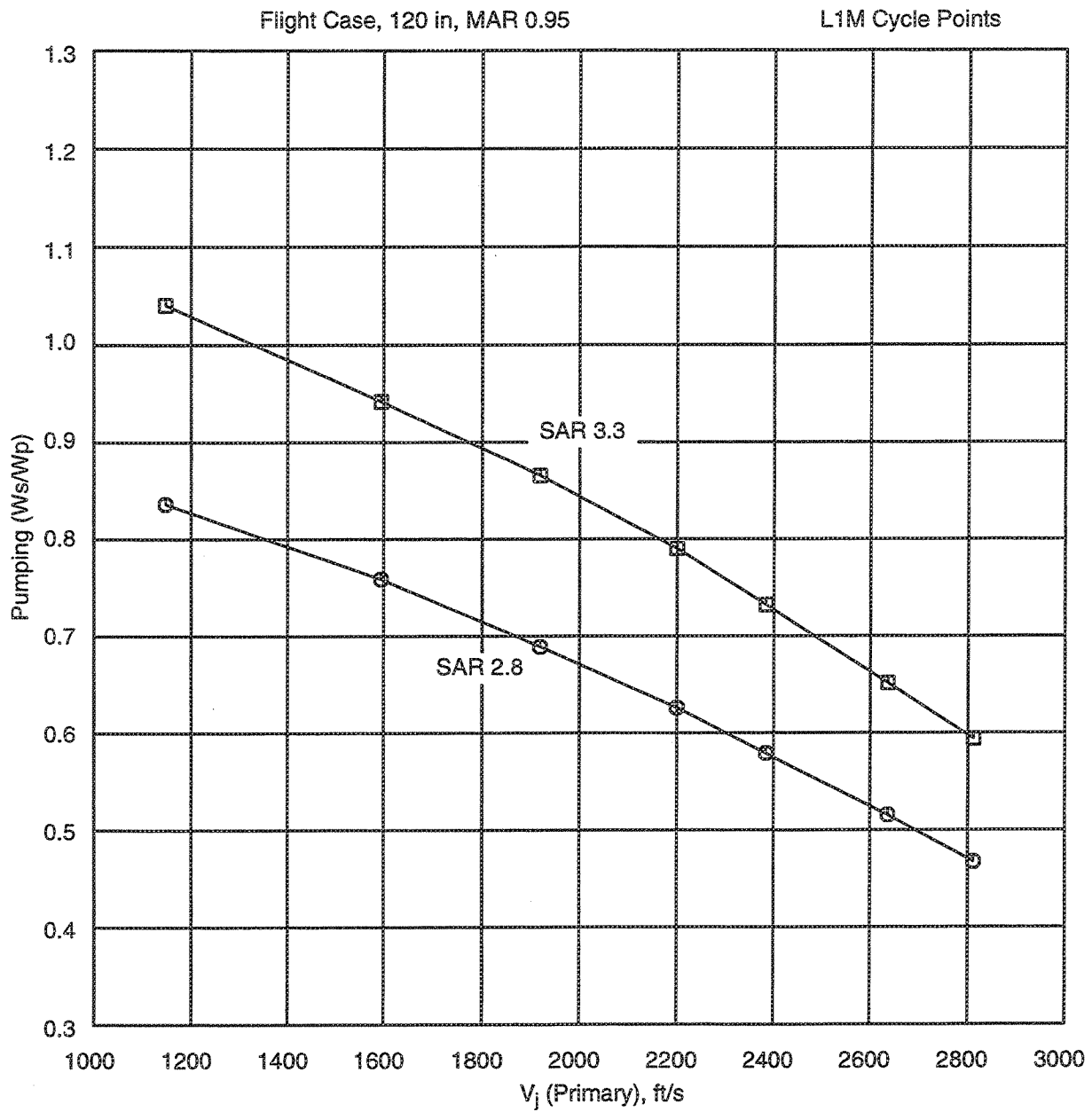


Figure 30. Comparison of pumping ratio for SAR 2.8 and 3.3 nozzles

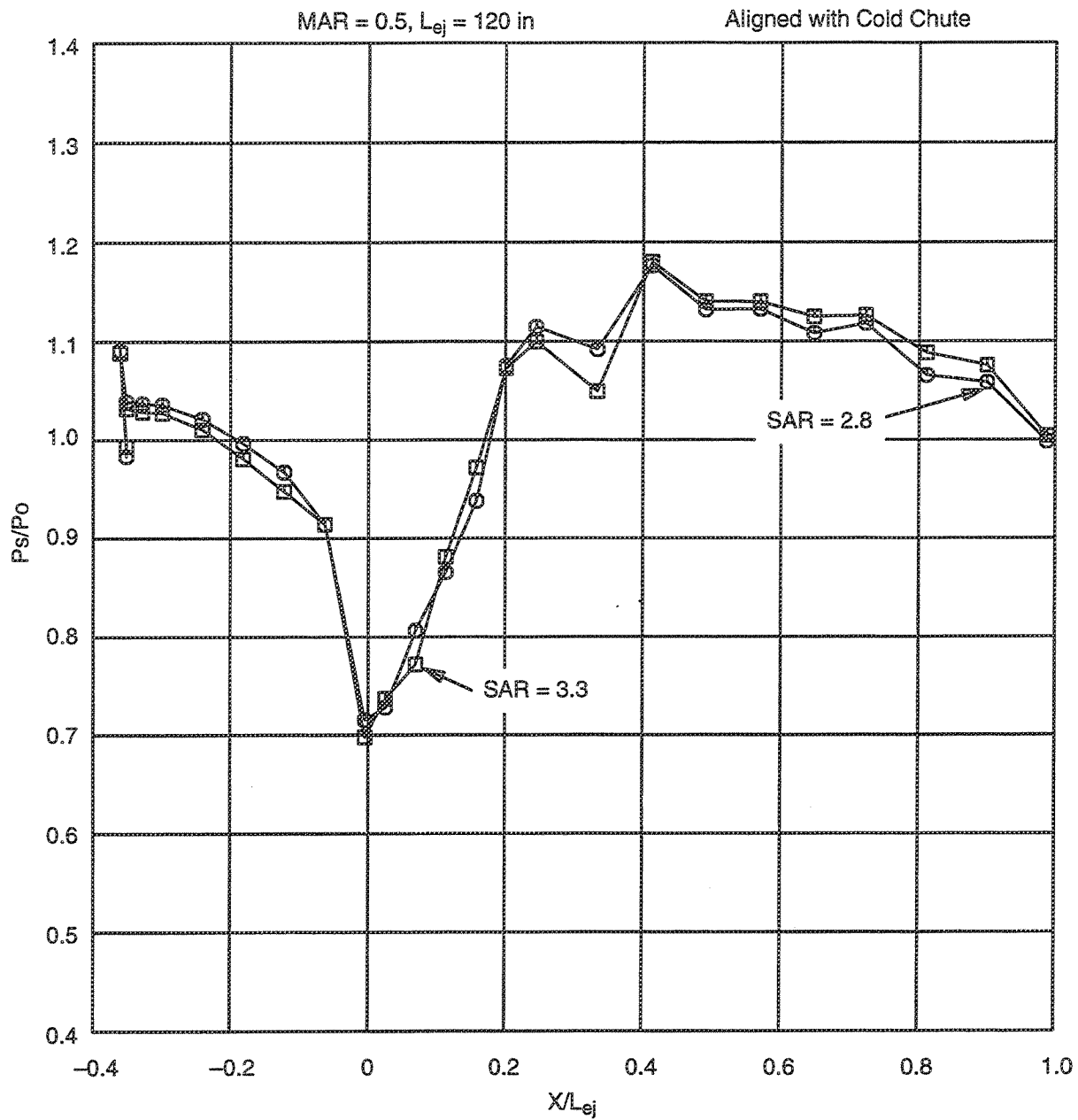


Figure 31. Flap static pressure distribution along the centerline of the secondary flow passage:  
 NPR = 4,  $V_j = 2400$  ft/s,  $M_0 = 0.32$

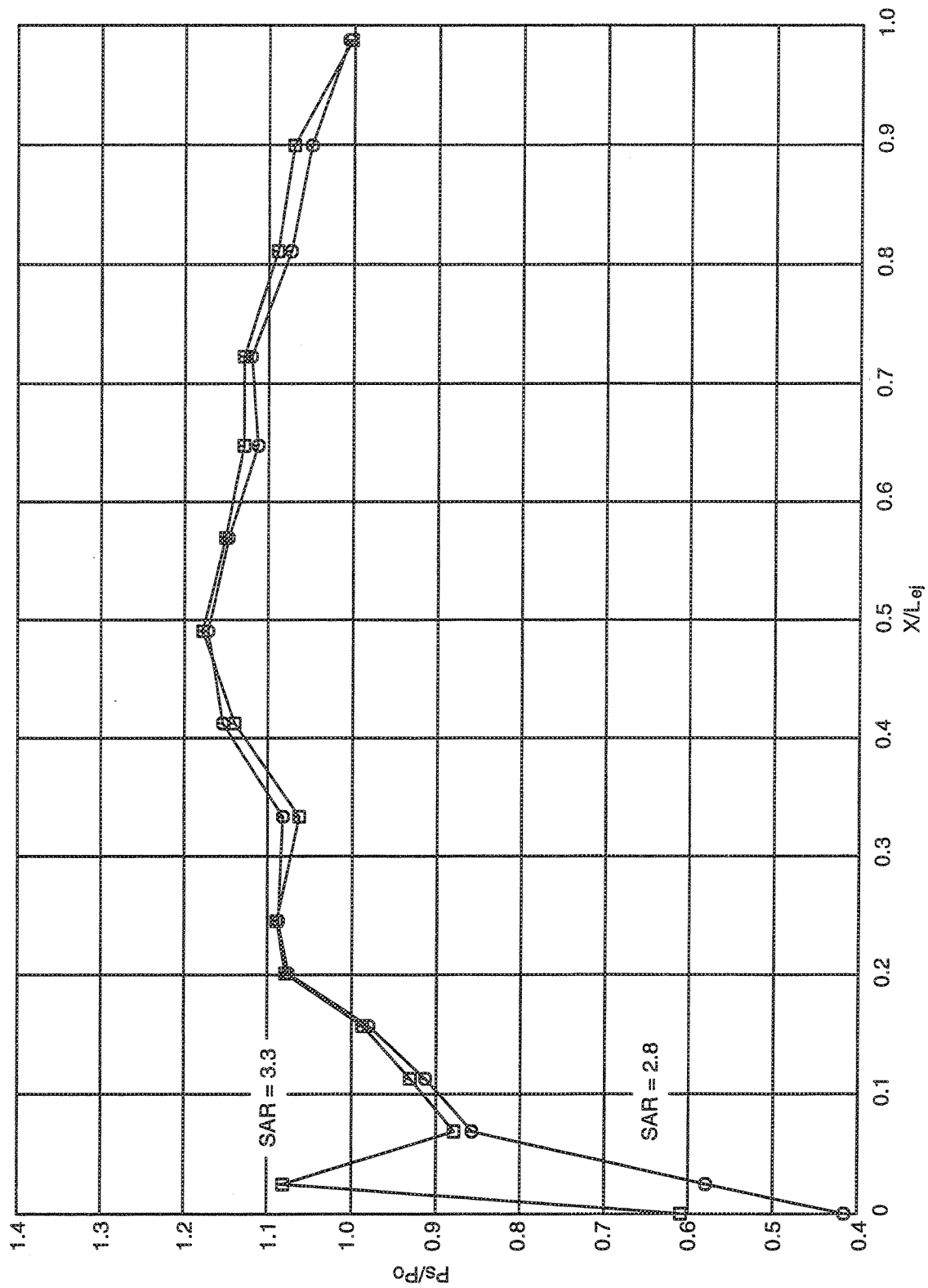


Figure 32. Flap static pressure distribution along the centerline of the primary flow passage: NPR = 4,  $V_j = 2400$  ft/s,  $M_0 = 0.32$

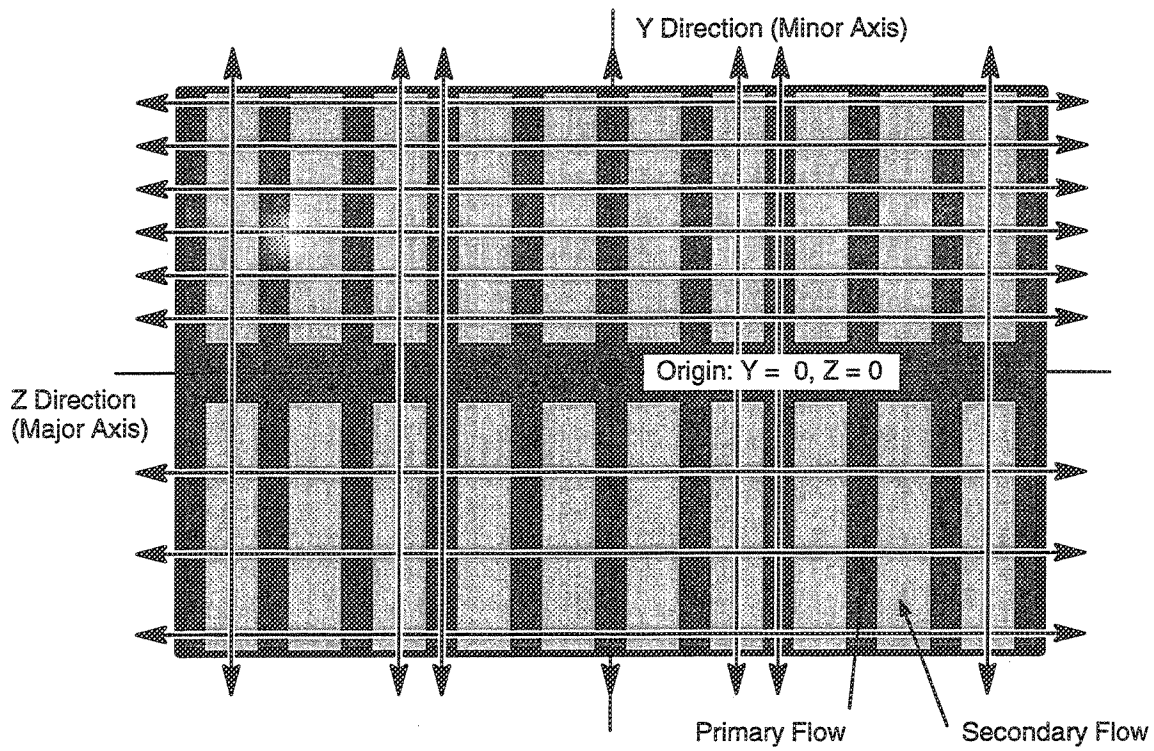


Figure 33. Typical LV survey (traverse) locations at nozzle exit

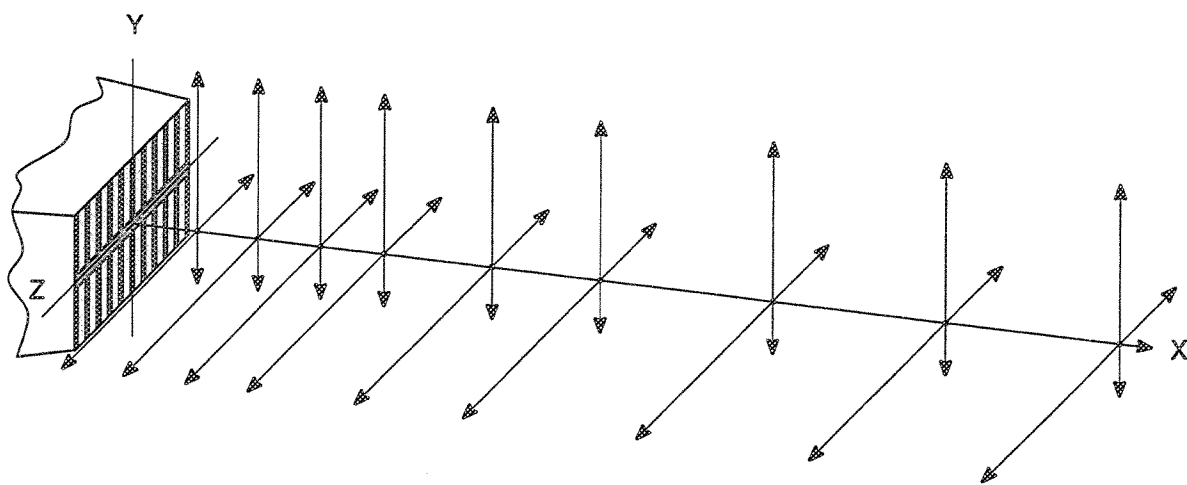


Figure 34. Typical LV traverse locations for exit-plume survey

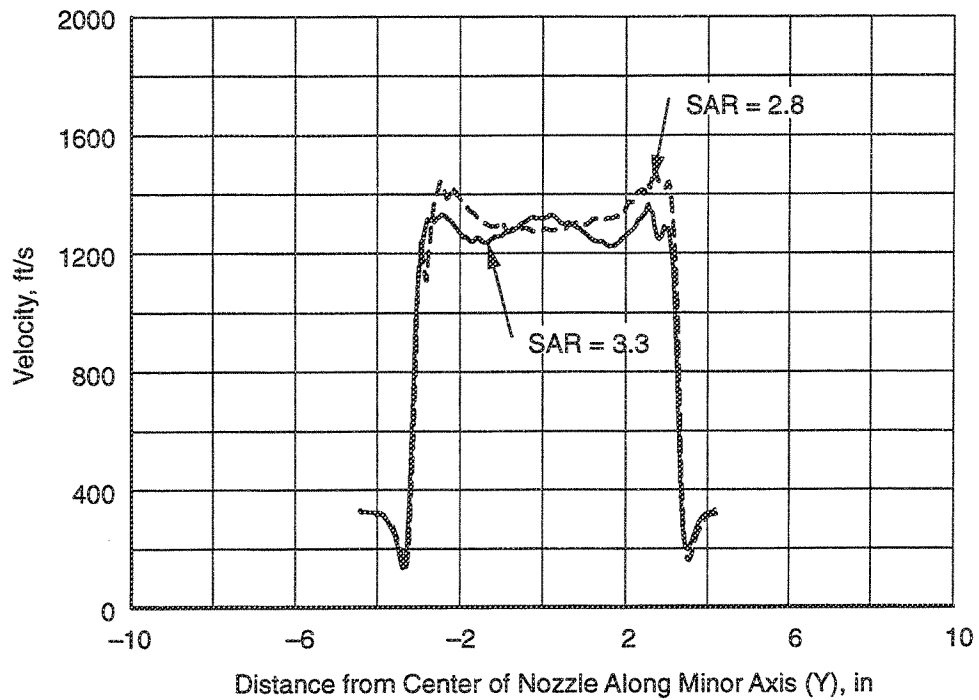


Figure 35. SAR effect on primary chute centerline exit velocity profiles along nozzle minor axis: NPR = 3.4,  $V_j = 2384$  ft/s,  $T_8 = 1590^\circ\text{R}$ ,  $M_0 = 0.32$

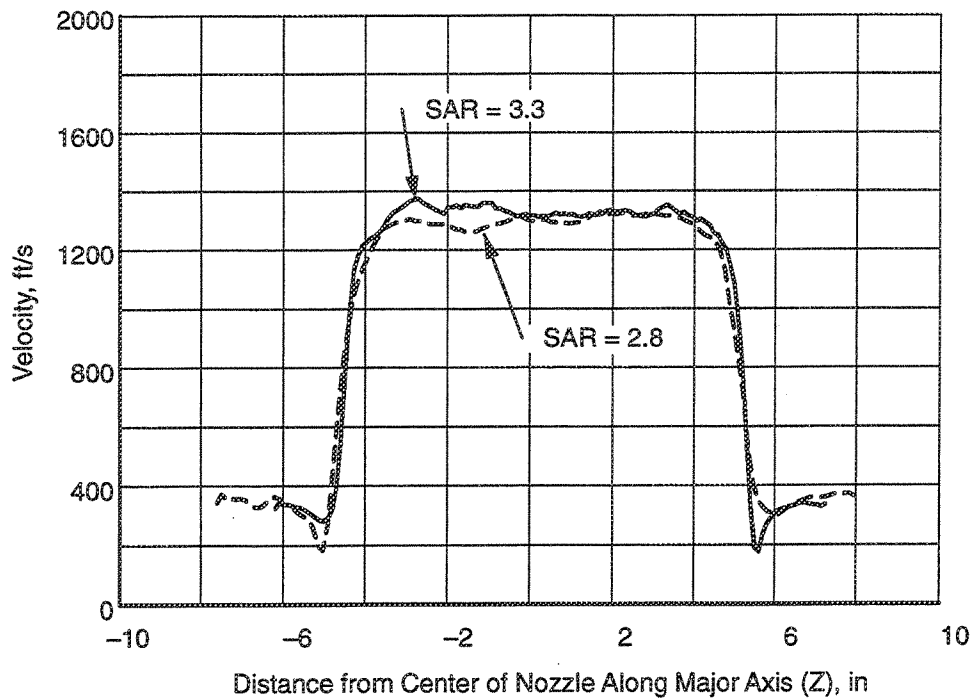


Figure 36. SAR effect on primary chute centerline exit velocity profiles along nozzle major axis: NPR = 3.4,  $V_j = 2384$  ft/s,  $T_8 = 1590^\circ\text{R}$ ,  $M_0 = 0.32$

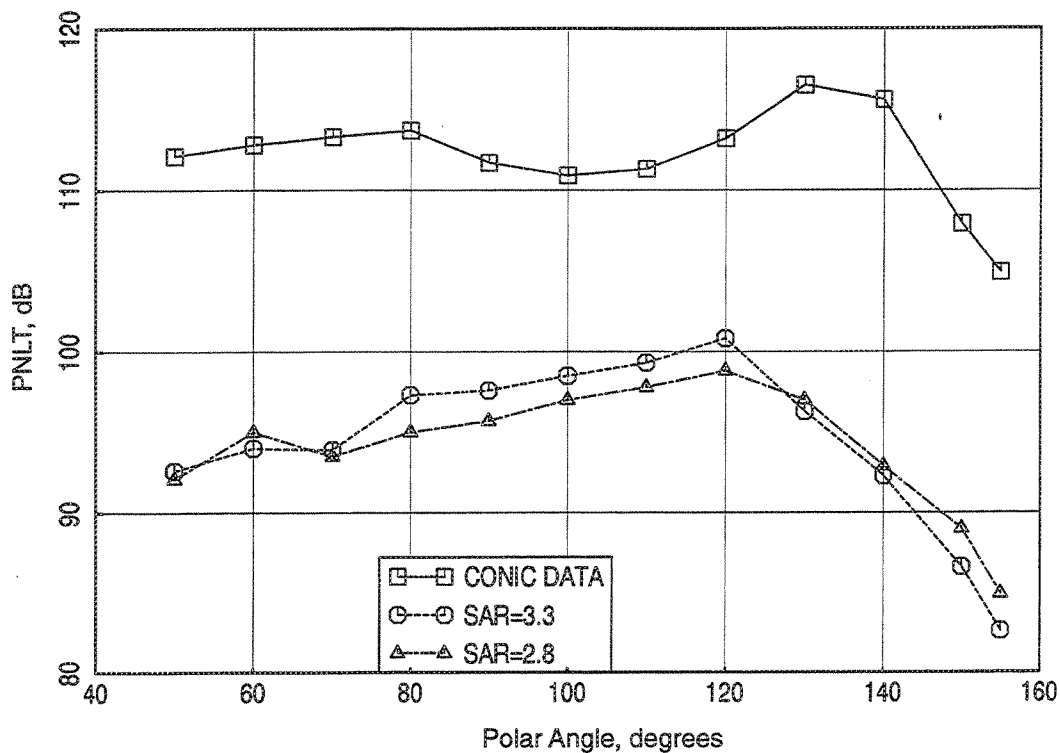


Figure 37. SAR effect on PNLT directivities: 120-in treated flap, MAR = 0.95,  $M_0 = 0.32$ ,  $V_j = 2384$  ft/s, NPR = 3.4,  $T_8 = 1590^\circ\text{R}$ , sideline microphones

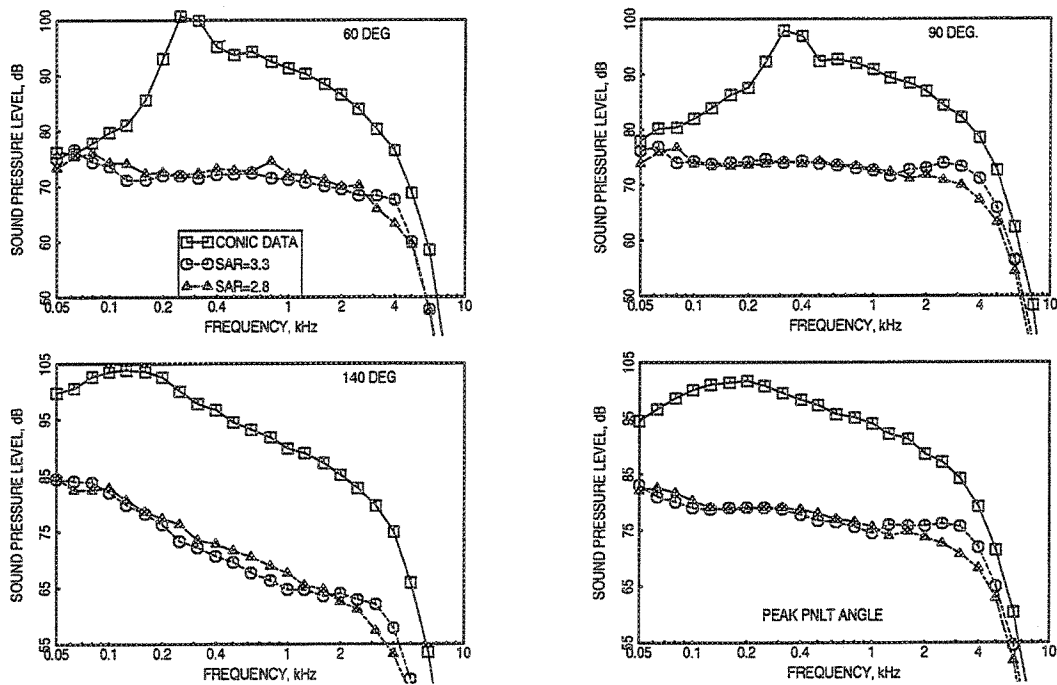


Figure 38. SAR effect on SPL spectra: 120-in treated flap, MAR = 0.95,  $M_0 = 0.32$ ,  $V_j = 2384$  ft/s, NPR = 3.4,  $T_8 = 1590^\circ\text{R}$ , sideline microphones

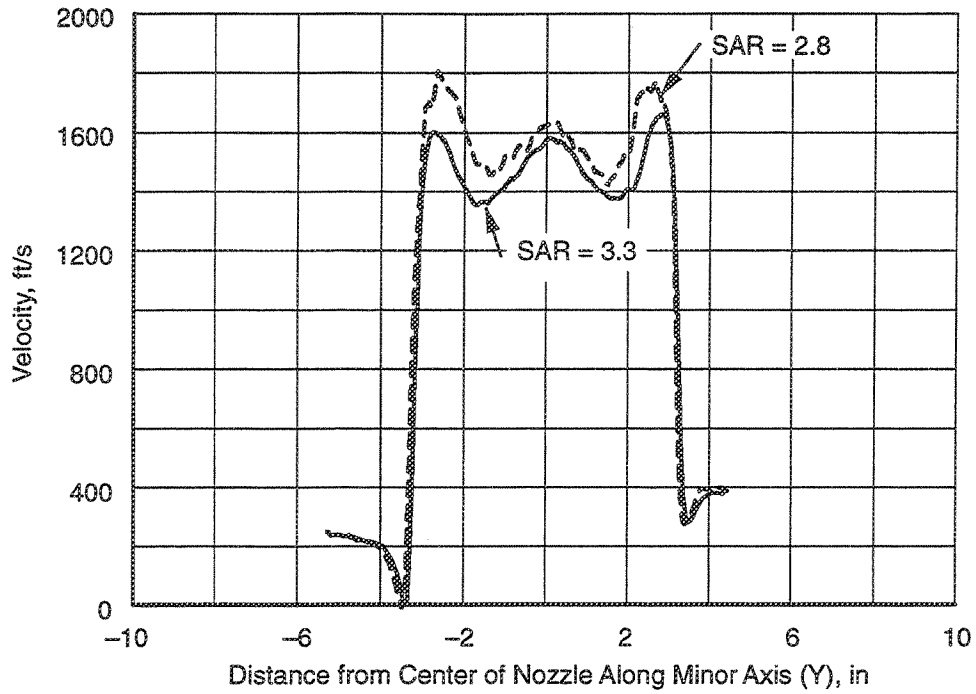


Figure 39. SAR effect on primary chute centerline exit velocity profiles along nozzle minor axis: NPR = 4,  $V_j = 2637$  ft/s,  $T_8 = 1750^\circ\text{R}$ ,  $M_0 = 0.32$

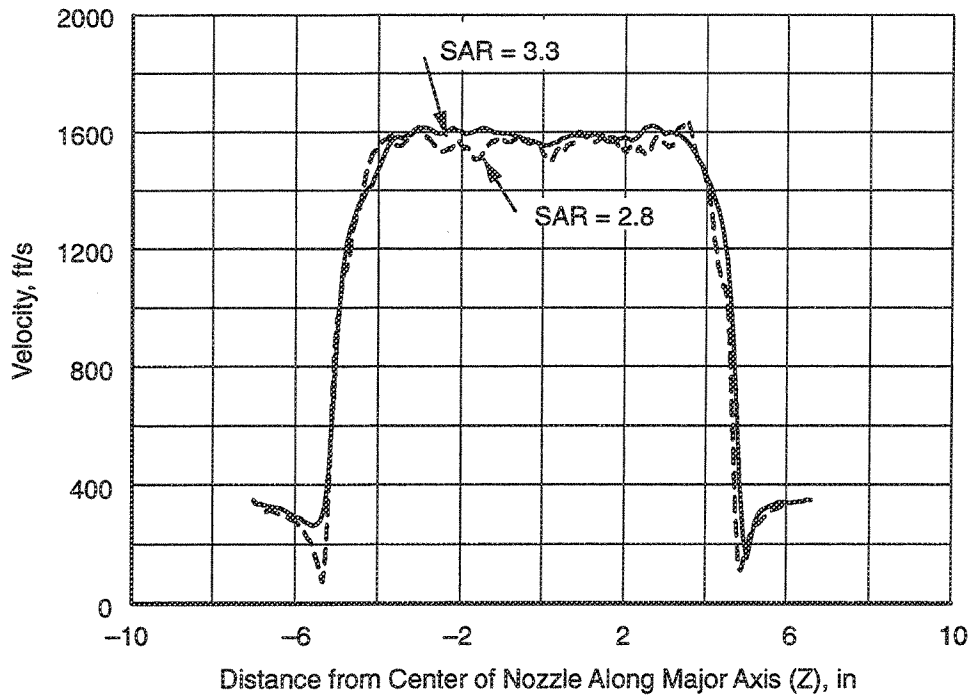


Figure 40. SAR effect on primary chute centerline exit velocity profiles along nozzle major axis: NPR = 4,  $V_j = 2637$  ft/s,  $T_8 = 1750^\circ\text{R}$ ,  $M_0 = 0.32$

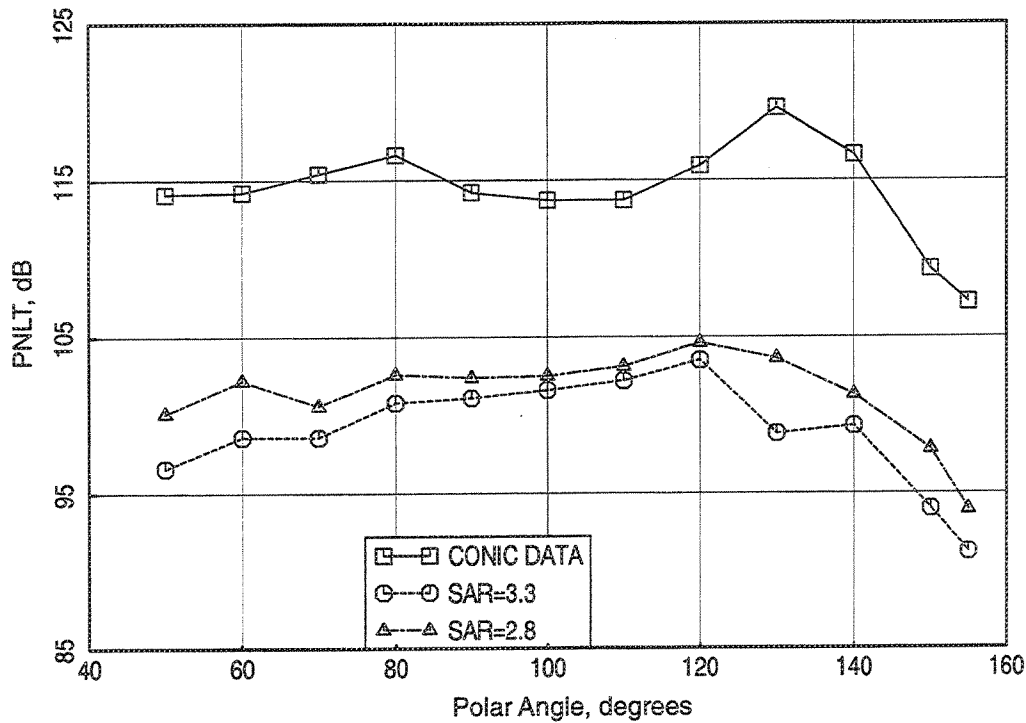


Figure 41. SAR effect on PNLT directivities: 120-in treated flap, MAR = 0.95,  $M_0 = 0.32$ ,  $V_j = 2637$  ft/s, NPR = 4,  $T_3 = 1750^\circ$  R, sideline microphones

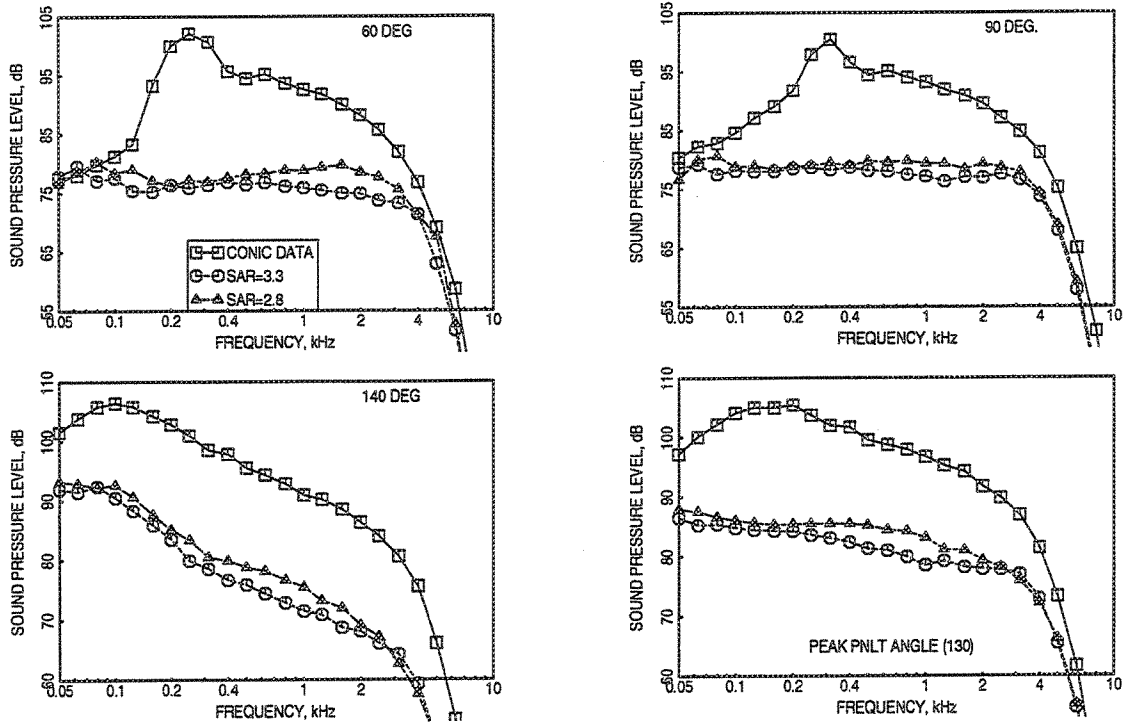


Figure 42. SAR effect on SPL spectra: 120-in treated flap, MAR = 0.95,  $M_0 = 0.32$ ,  $V_j = 2637$  ft/s, NPR = 4,  $T_3 = 1750^\circ$  R, sideline microphones

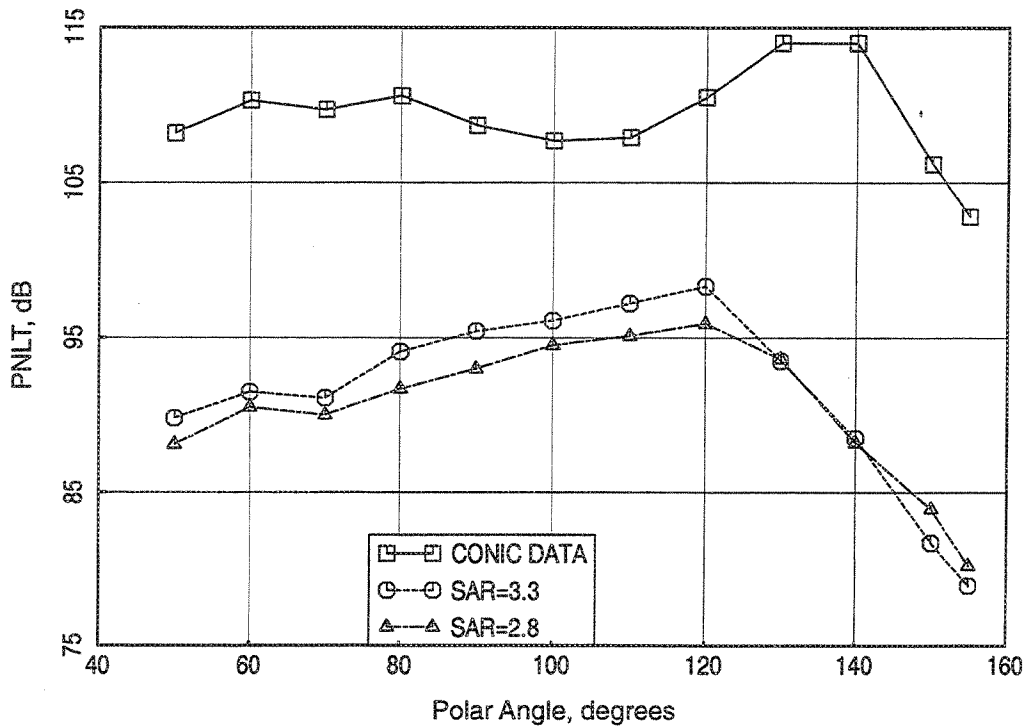


Figure 43. SAR effect on PNLT directivities: 120-in treated flap,  $MAR = 0.95$ ,  $M_0 = 0.32$ ,  $V_j = 2200$  ft/s,  $NPR = 3$ ,  $T_g = 1485^\circ R$ , sideline microphones

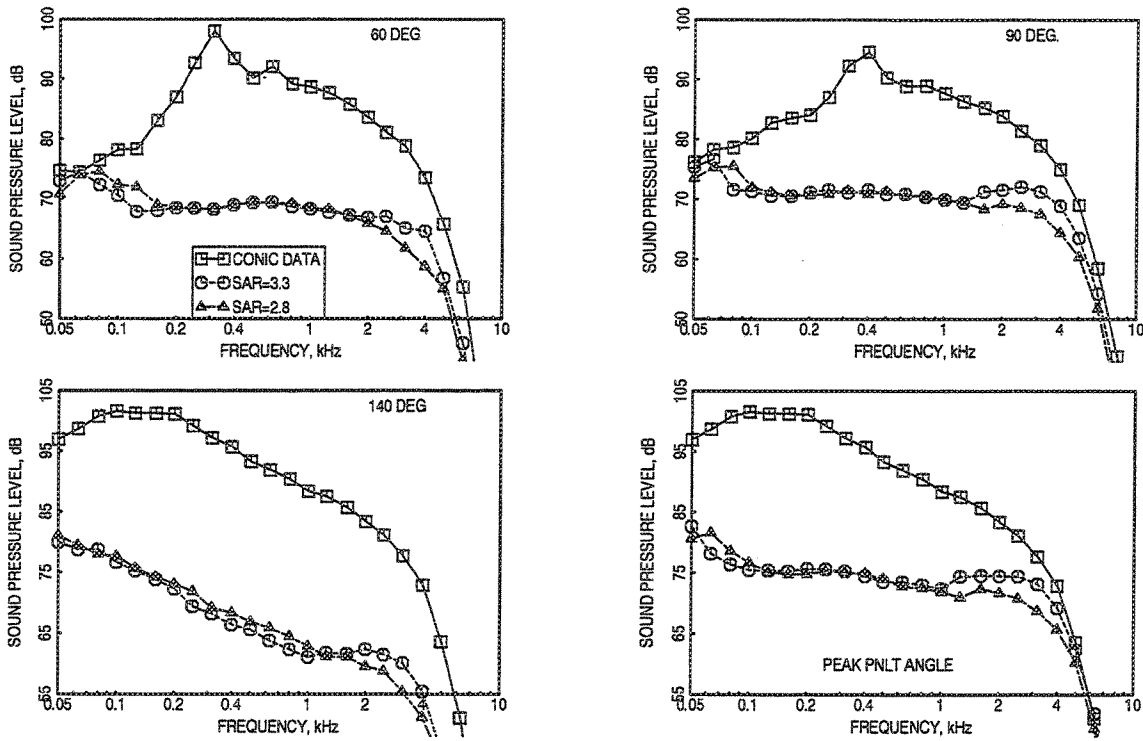


Figure 44. SAR effect on SPL spectra: 120-in treated flap,  $MAR = 0.95$ ,  $M_0 = 0.32$ ,  $V_j = 2200$  ft/s,  $NPR = 3$ ,  $T_g = 1485^\circ R$ , sideline microphones

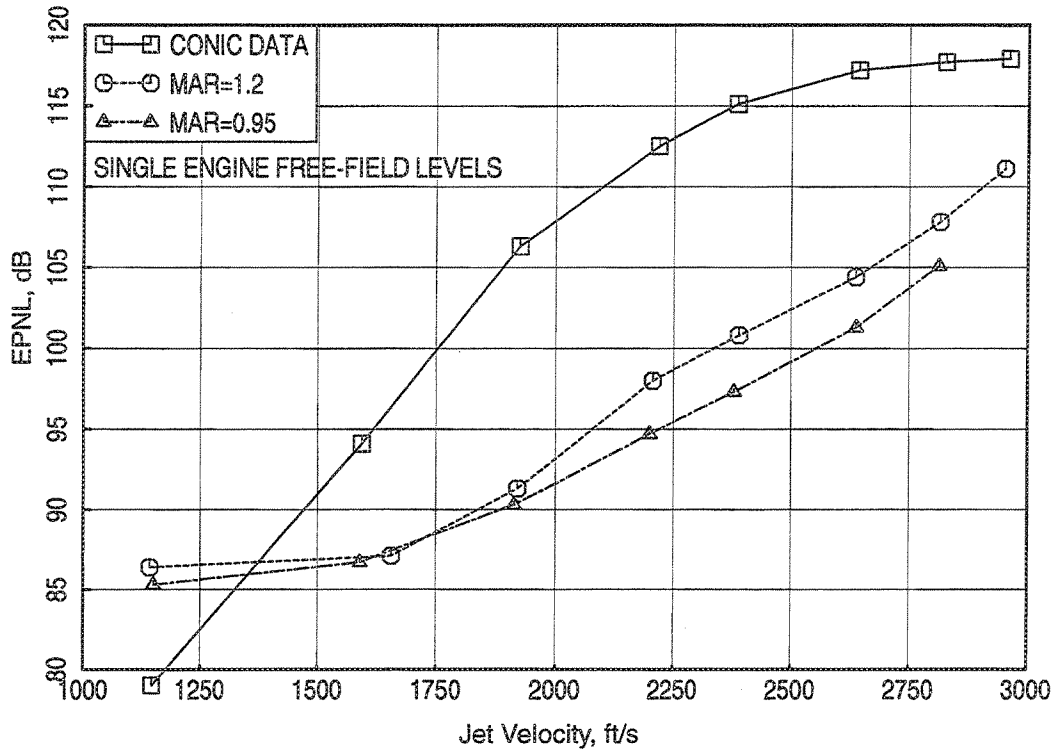


Figure 45. MAR effect on EPNL as a function of  $V_j$ ; 120-in treated flap, SAR = 3.3,  $M_0 = 0.32$ , sideline microphones

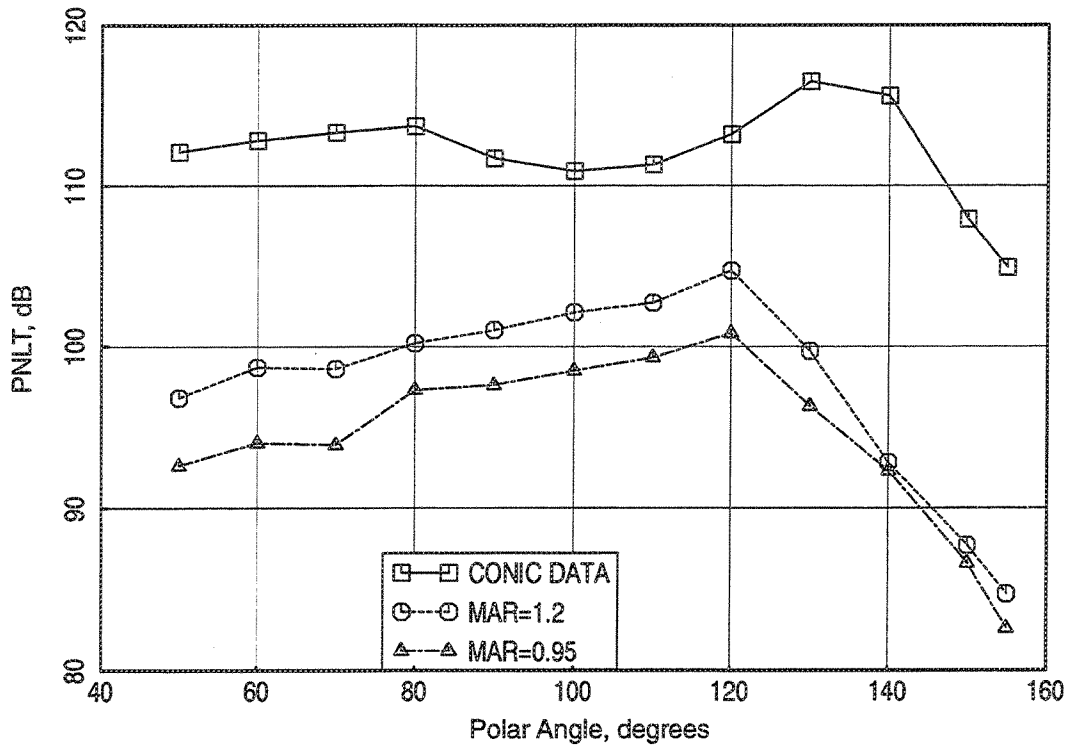


Figure 46. MAR effect on PNLT directivities: 120-in treated flap, SAR = 3.3,  $M_0 = 0.32$ ,  $V_j = 2384$  ft/s, NPR = 3.4,  $T_8 = 1580^\circ\text{R}$ , sideline microphones

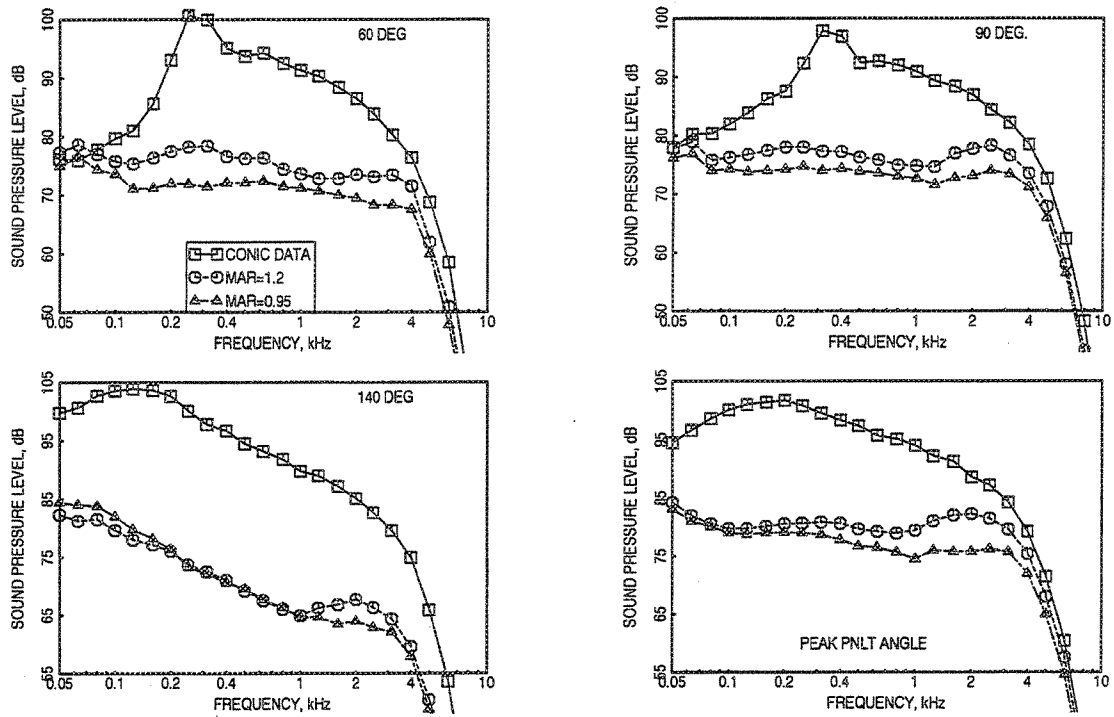


Figure 47. MAR effect on SPL spectra: 120-in treated flap, SAR = 3.3,  $M_0 = 0.32$ ,  $V_j = 2384$  ft/s, NPR = 3.4,  $T_8 = 1580^\circ\text{R}$ , sideline microphones

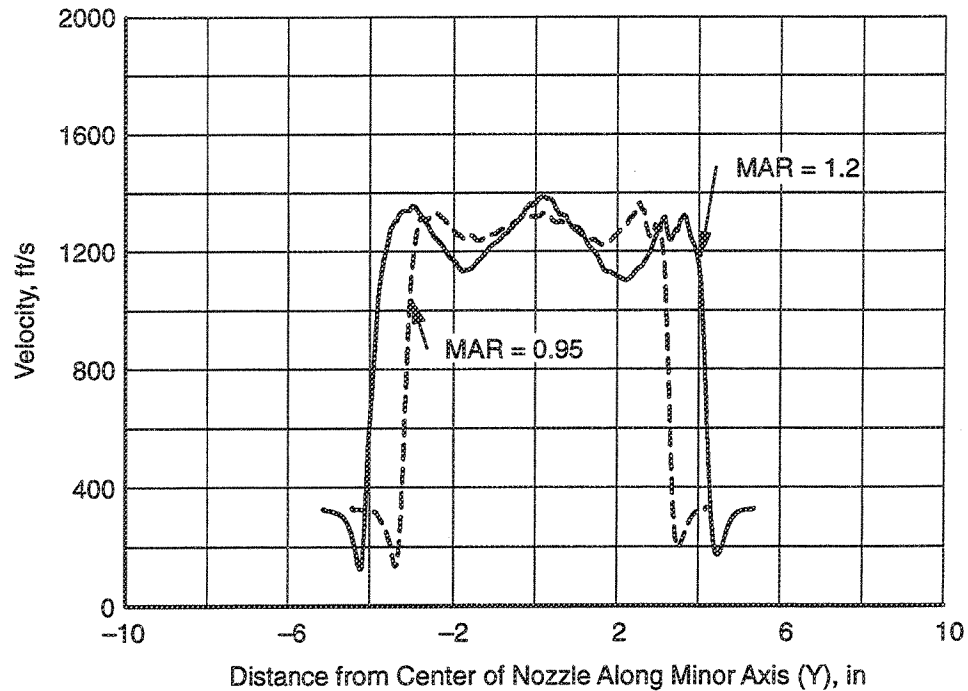


Figure 48. MAR effect on primary chute centerline exit velocity profiles along nozzle minor axis: NPR = 3.4,  $V_j = 2384$  ft/s,  $T_8 = 1580^\circ\text{R}$ ,  $M_0 = 0.32$

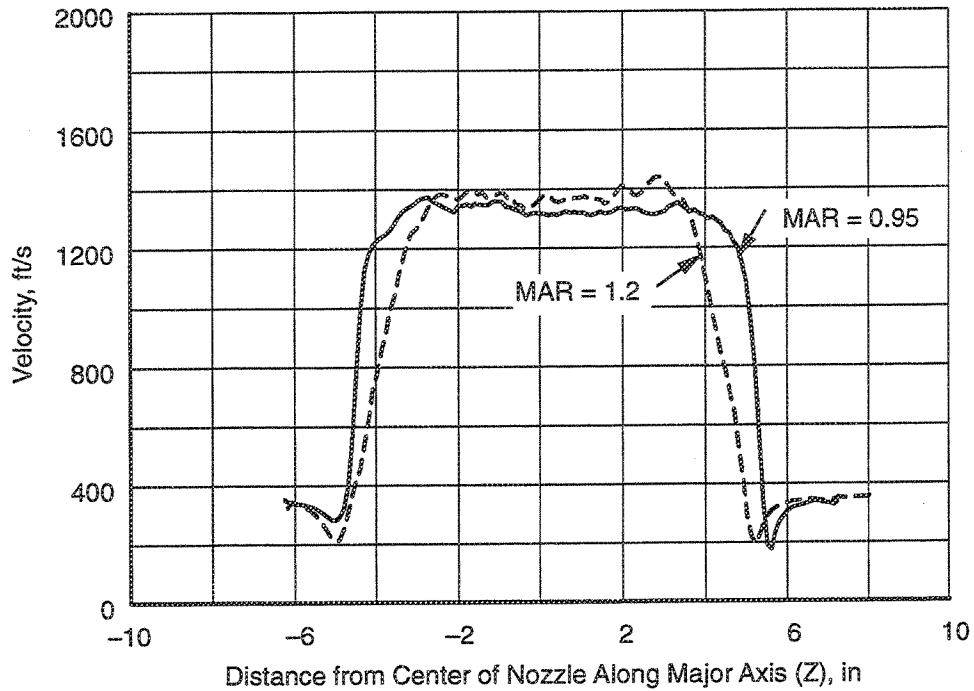


Figure 49. MAR effect on primary chute centerline exit velocity profiles along nozzle major axis: NPR = 3.4,  $V_j = 2384$  ft/s,  $M_0 = 0.32$

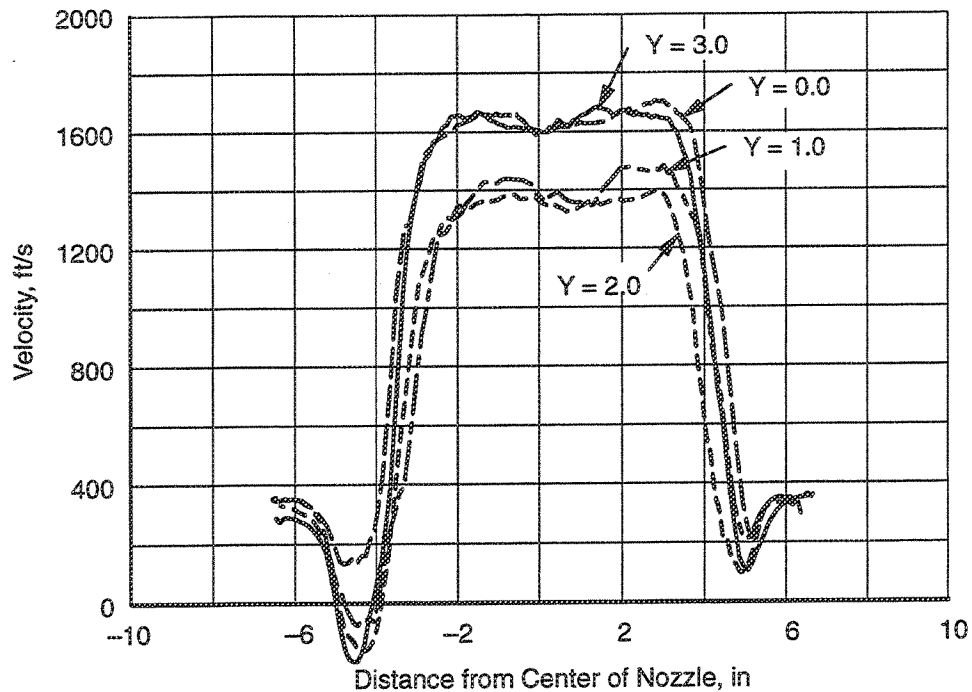


Figure 50. Exit plane velocity distribution across the width of the nozzle at various heights: MAR = 1.2, SAR = 3.3, NPR = 4,  $V_j = 2384$  ft/s,  $T_8 = 1580^\circ$  R,  $M_0 = 0.32$

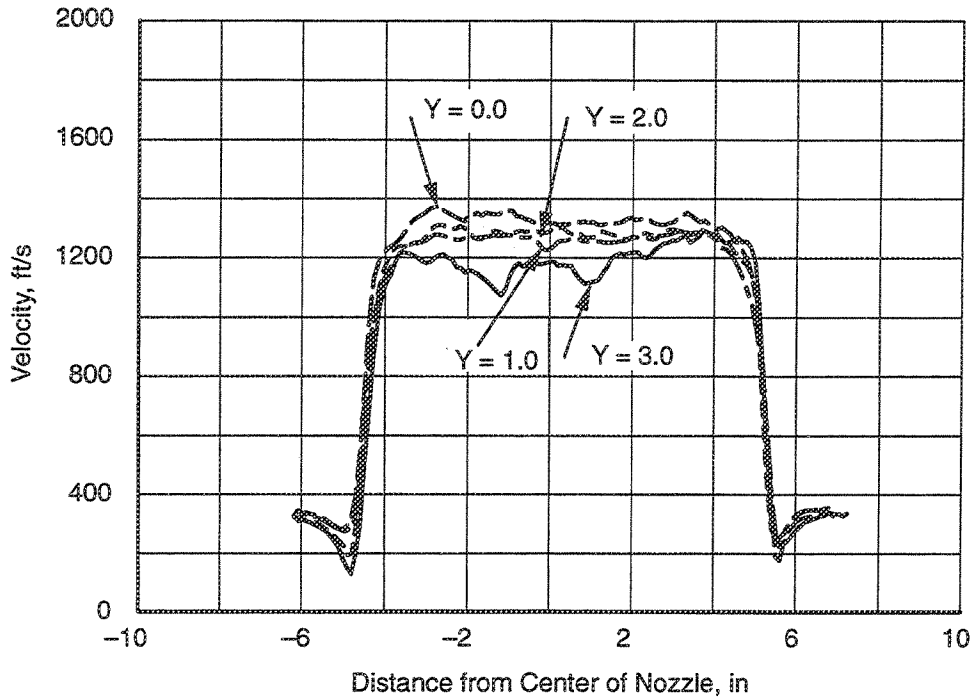


Figure 51. Exit plane velocity distribution across the width of the nozzle at various heights: MAR = 0.95, SAR = 3.3, NPR = 4,  $V_j = 2384$  ft/s,  $T_8 = 1580^\circ\text{R}$ ,  $M_0 = 0.32$

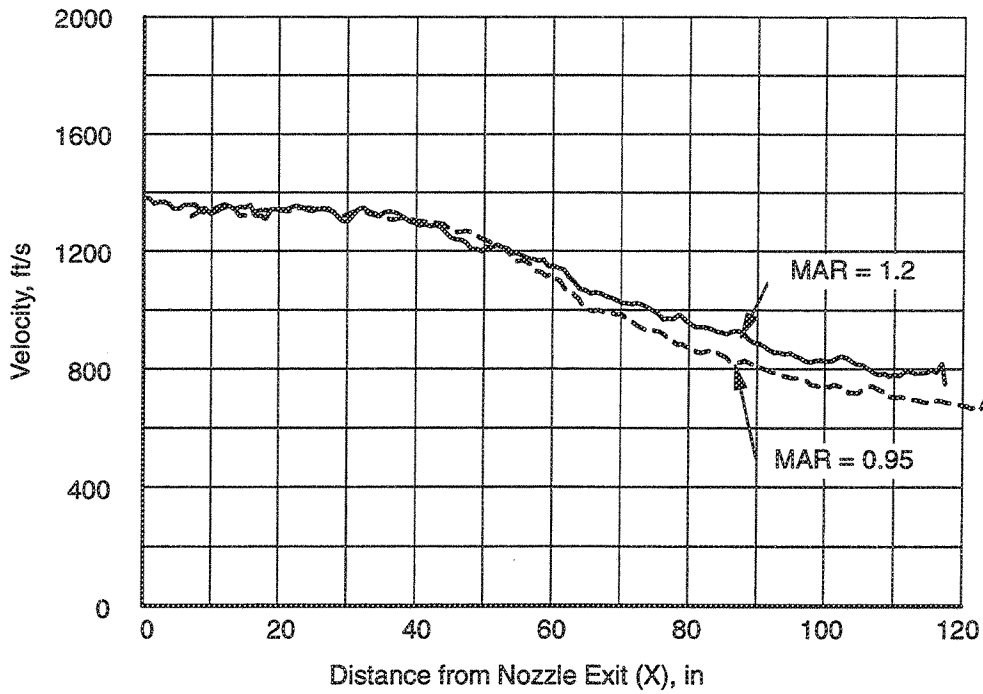


Figure 52. MAR effect on plume decay along the nozzle centerline: SAR = 3.3, long flap, NPR = 3.4,  $V_j = 2384$  ft/s,  $M_0 = 0.32$

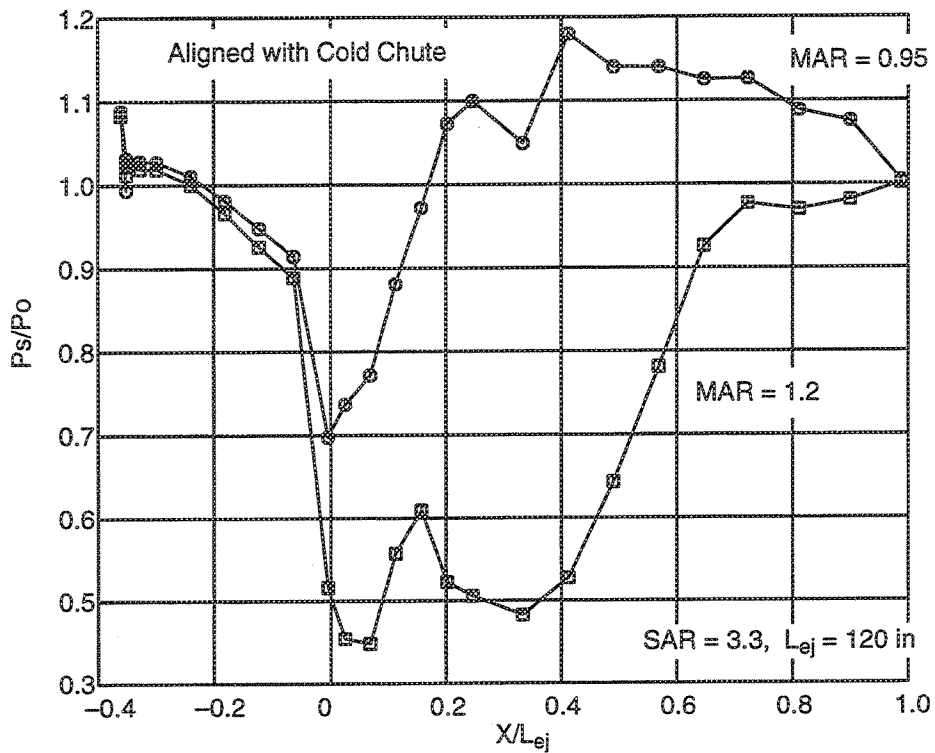


Figure 53. Static pressure distribution at 2400 ft/s,  $M_0 = 0.32$

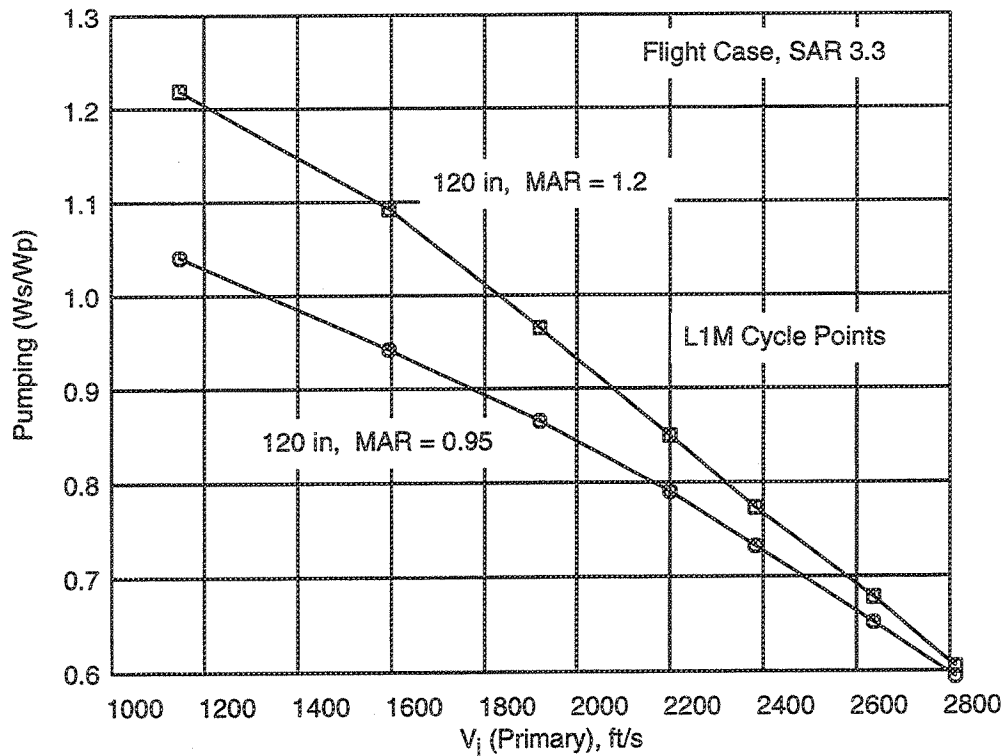


Figure 54. Effect of MAR on Pumping

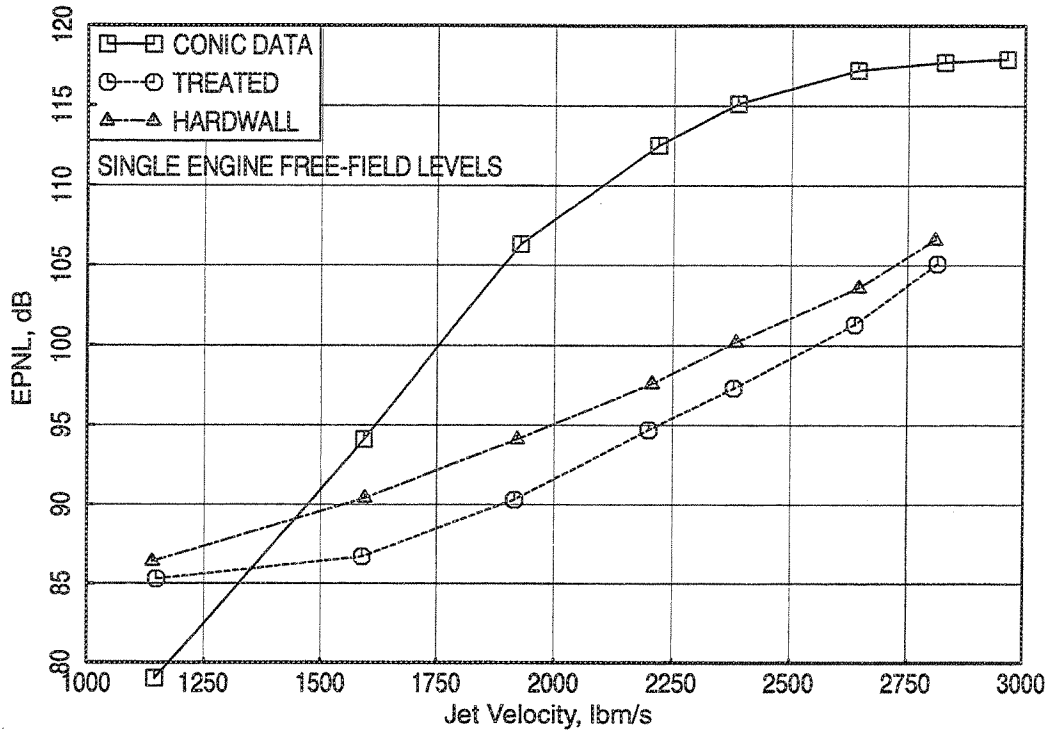


Figure 55. Treatment effect on EPNL as a function of  $V_j$ : 120-in flap, SAR = 3.3, MAR = 0.95,  $T_g = 1580^\circ\text{R}$ ,  $M_0 = 0.32$ , sideline microphones

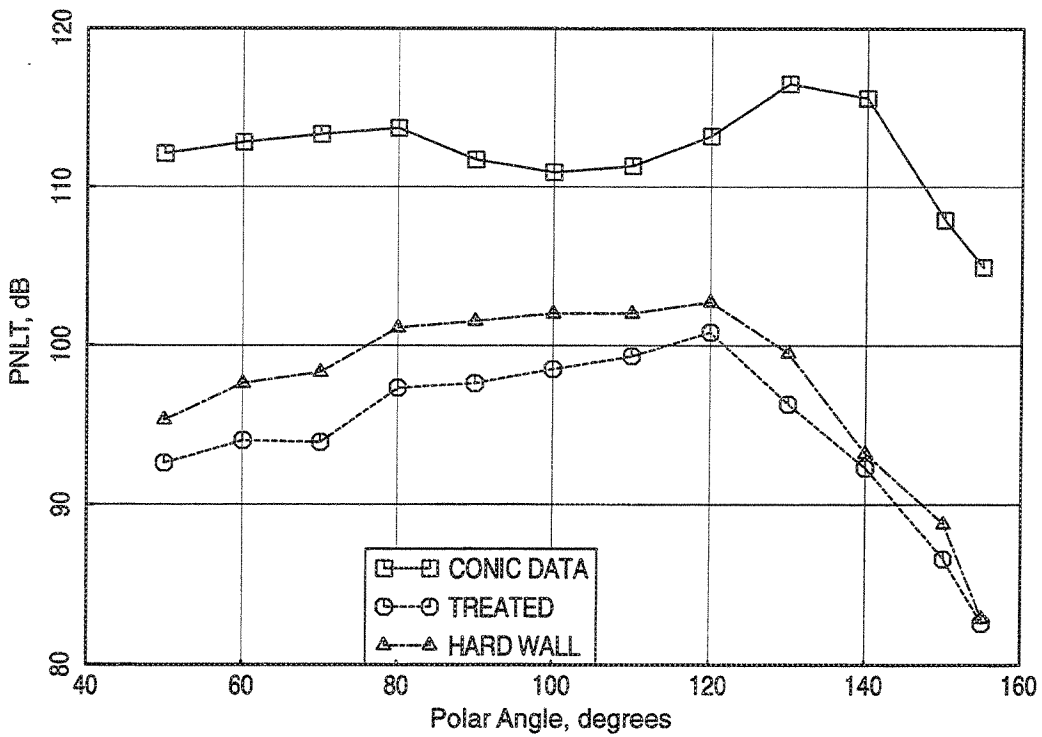


Figure 56. Treatment effect on PNL directivities: 120-in flap, SAR = 3.3, MAR = 0.95,  $M_0 = 0.32$ ,  $V_j = 2384$  ft/s, NPR = 3.4,  $T_g = 1590^\circ\text{R}$ , sideline microphones

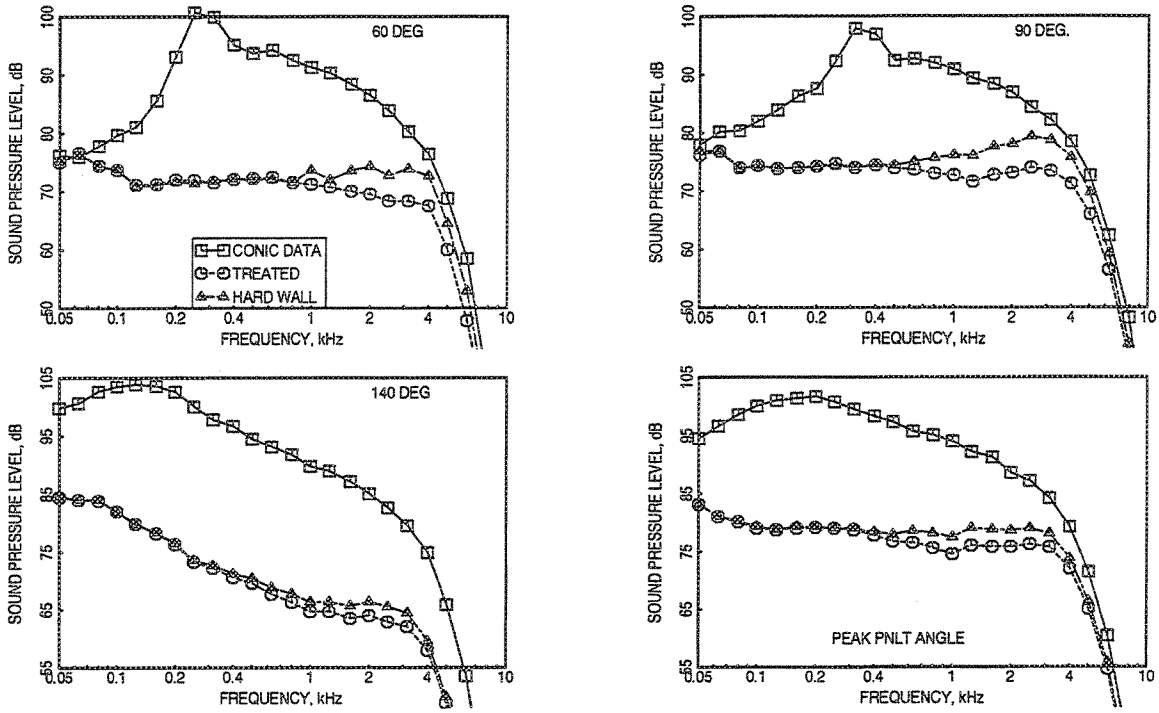


Figure 57. Treatment effect on SPL spectra: 120-in flap, SAR = 3.3, MAR = 0.95,  $M_0 = 0.32$ ,  $V_j = 2384$  ft/s, NPR = 3.4,  $T_8 = 1590^\circ R$ , sideline microphones

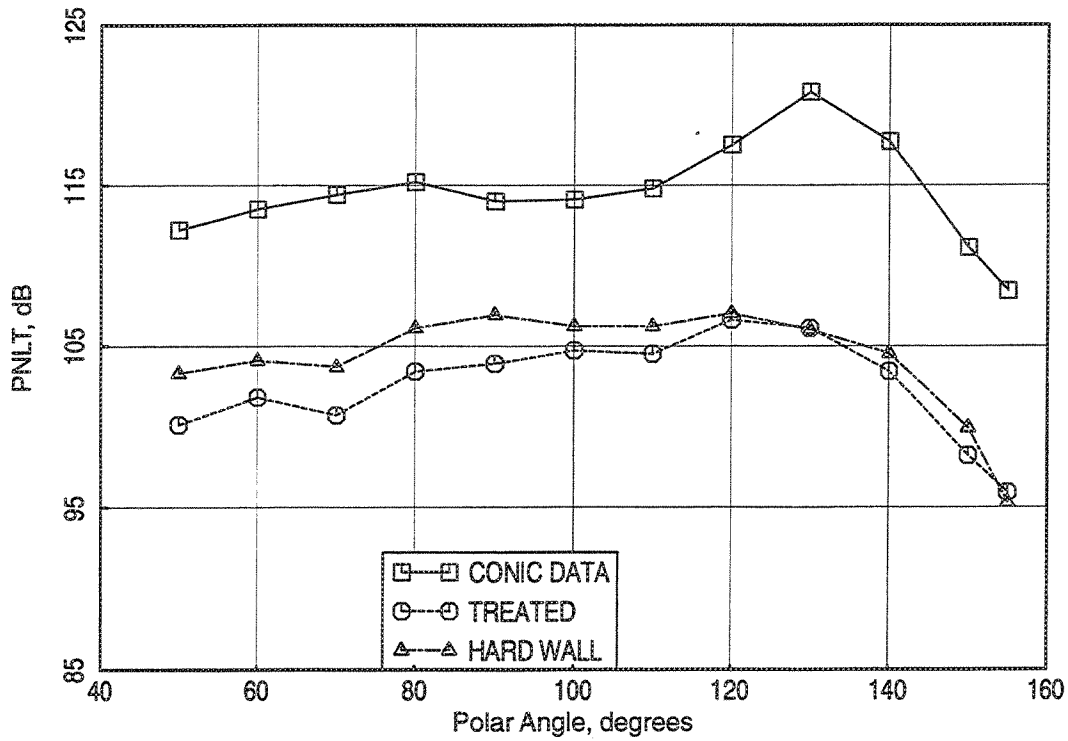


Figure 58. Treatment effect on PNLT directivities: 120-in flap, SAR = 3.3, MAR = 0.95,  $M_0 = 0.32$ ,  $V_j = 2637$  ft/s, NPR = 2.5,  $T_8 = 1325^\circ R$ , sideline microphones

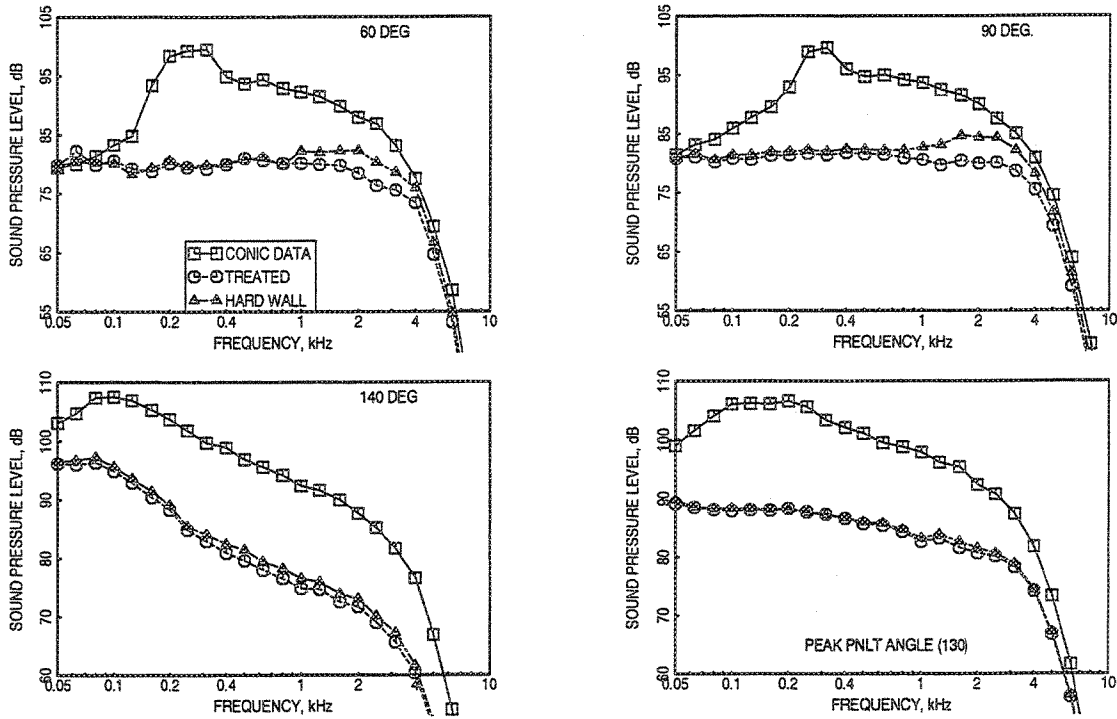


Figure 59. Treatment effect on SPL spectra: 120-in flap, SAR = 3.3, MAR = 0.95,  $M_0 = 0.32$ ,  $V_j = 2637$  ft/s, NPR = 4.5,  $T_8 = 1860^\circ$ R, sideline microphones

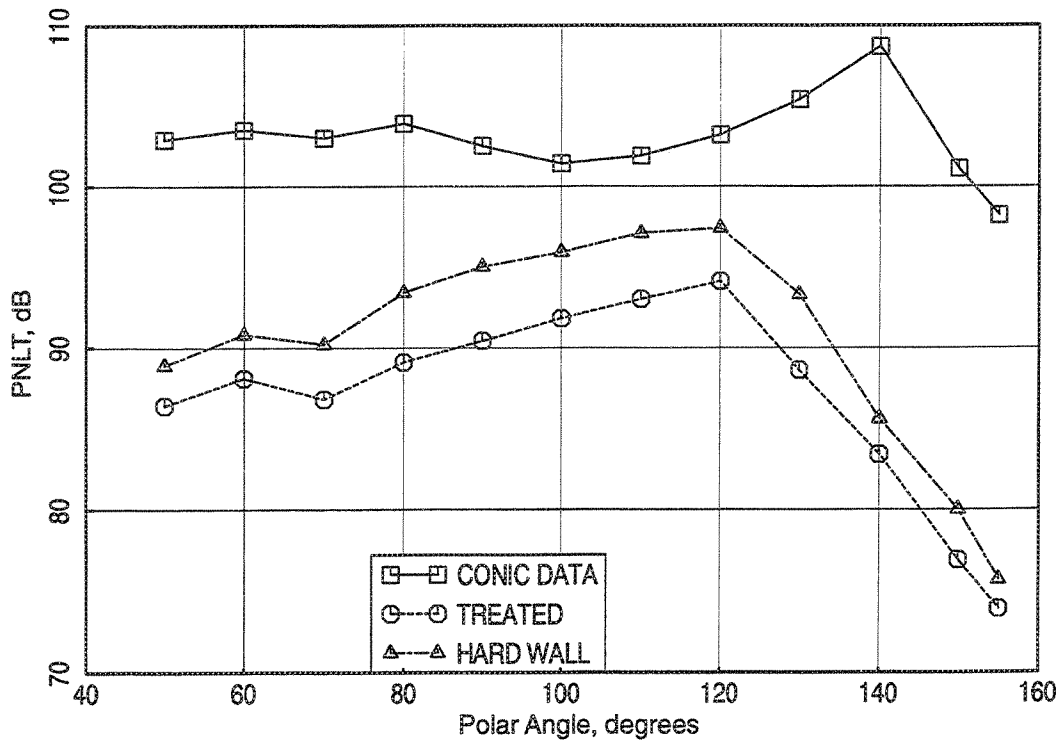


Figure 60. Treatment effect on PNLT directivities: 120-in flap, SAR = 3.3, MAR = 0.95,  $M_0 = 0.32$ ,  $V_j = 1919$  ft/s, NPR = 2.5,  $T_8 = 1325^\circ$ R, sideline microphones

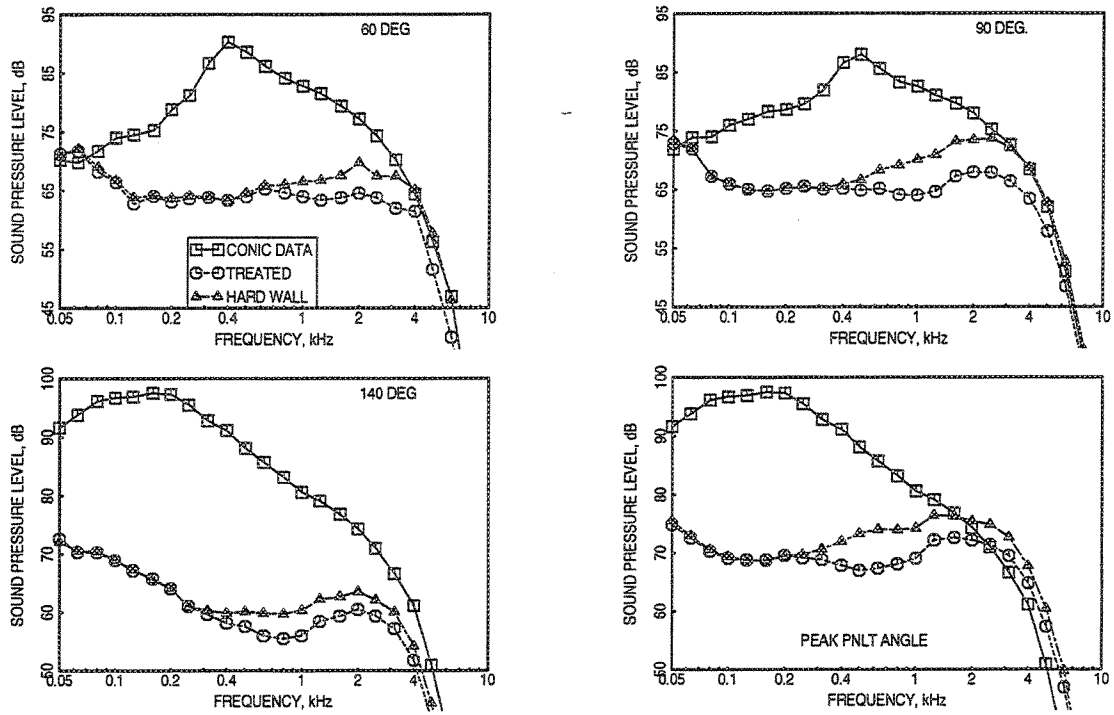


Figure 61. Treatment effect on SPL spectra: 120-in flap, SAR = 3.3, MAR = 0.95,  $M_0 = 0.32$ ,  $V_j = 1919$  ft/s, NPR = 2.5,  $T_g = 1325^\circ$  R, sideline microphones

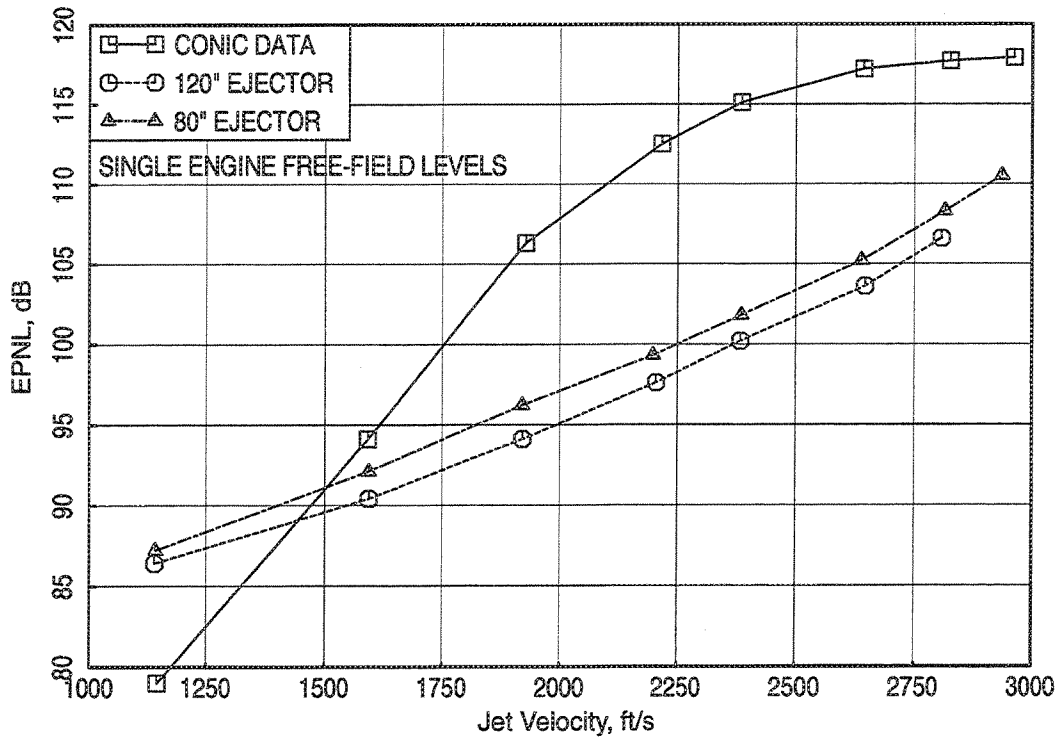


Figure 62. Effect of long- and short-flap, hard-wall configurations on EPNL as a function of  $V_j$ : SAR = 3.3, MAR = 0.95,  $M_0 = 0.32$ , sideline microphones

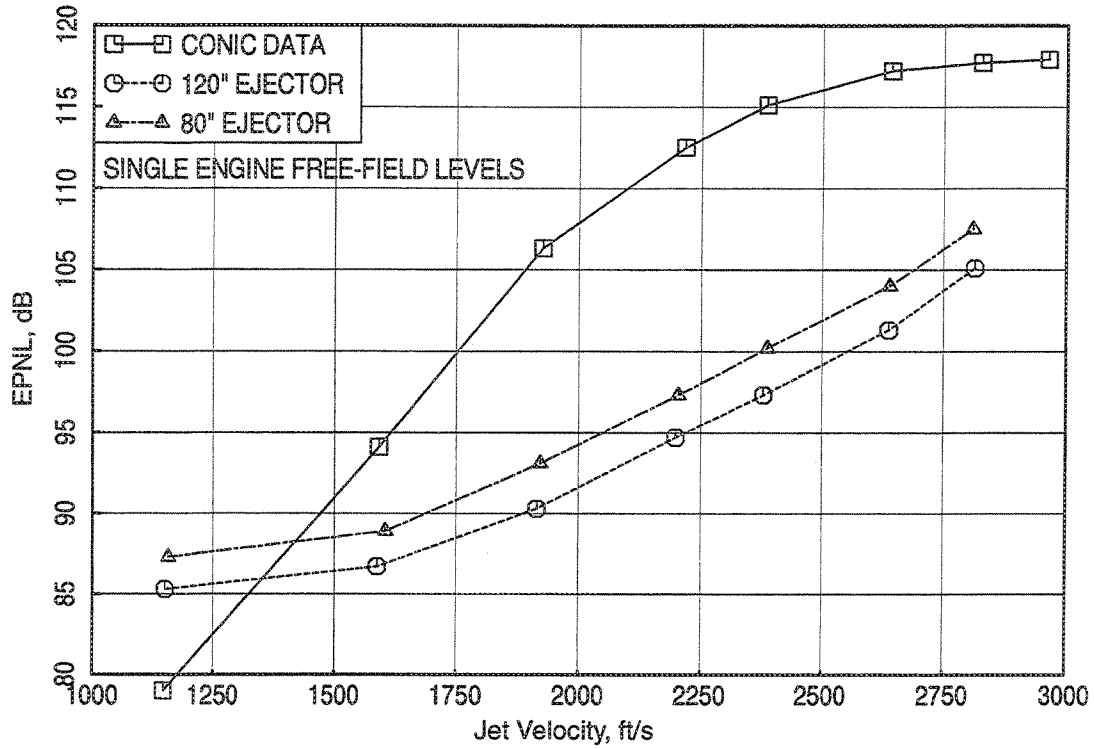


Figure 63. Effect of long- and short-flap, treated-wall configurations on EPNL as a function of  $V_j$ ; SAR = 3.3, MAR = 0.95,  $M_0 = 0.32$ , sideline microphones

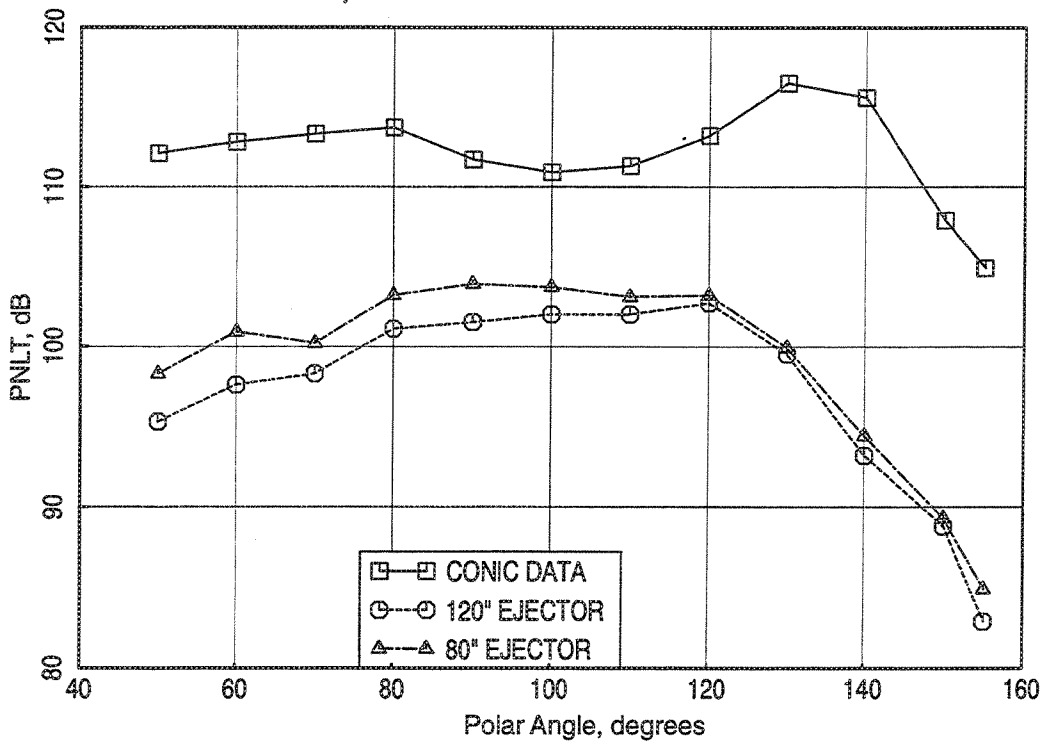


Figure 64. Effect of hard-wall flap length on PNLT directivities: SAR = 3.3, MAR = 0.95, NPR = 3.4,  $V_j = 2384$  ft/s,  $T_8 = 1580$  °R,  $M_0 = 0.32$ , sideline microphones

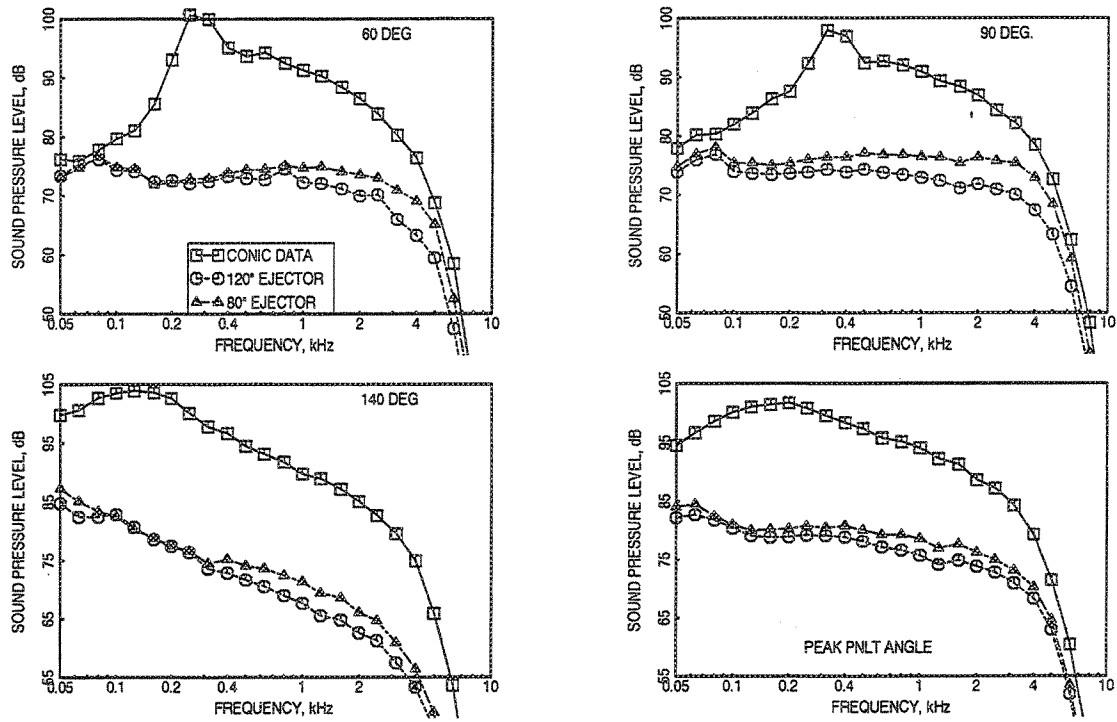


Figure 65. Effect of hard-wall flap length on SPL spectra at selected polar angles ( $\theta$ ):  $V_j = 2384$  ft/s, NPR = 3.4, MAR = 0.95, SAR = 3.3,  $T_g = 1580^\circ R$ ,  $M_0 = 0.32$ , sideline microphones

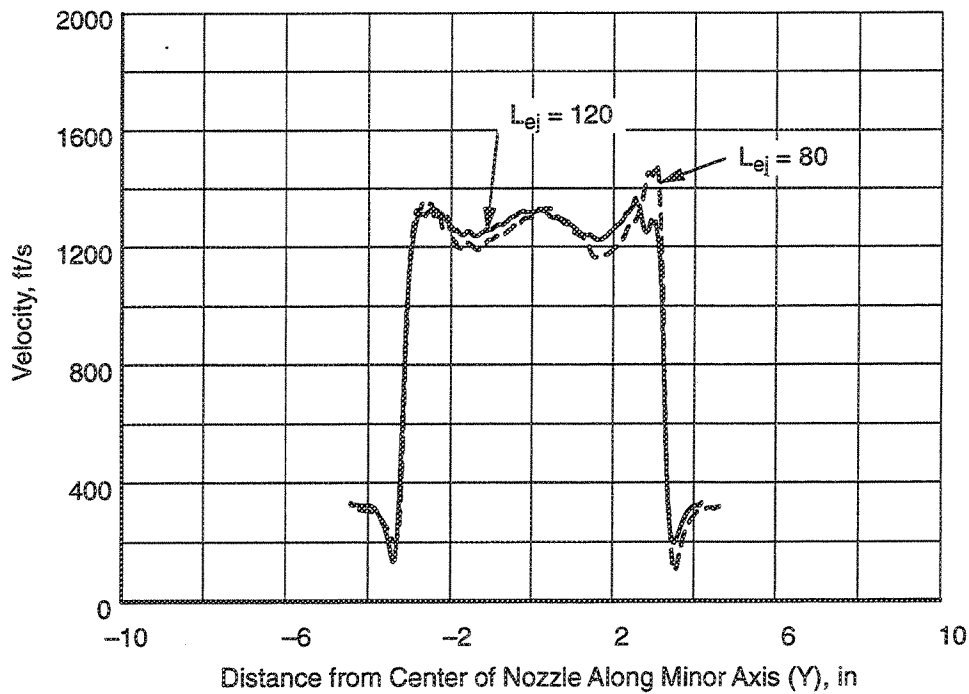


Figure 66. Effect of flap length on axial velocity distribution at nozzle exit along the minor axis:  $V_j = 2384$  ft/s, NPR = 3.4,  $T_g = 1580^\circ R$ ,  $M_0 = 0.32$ , MAR = 0.95, SAR = 3.3

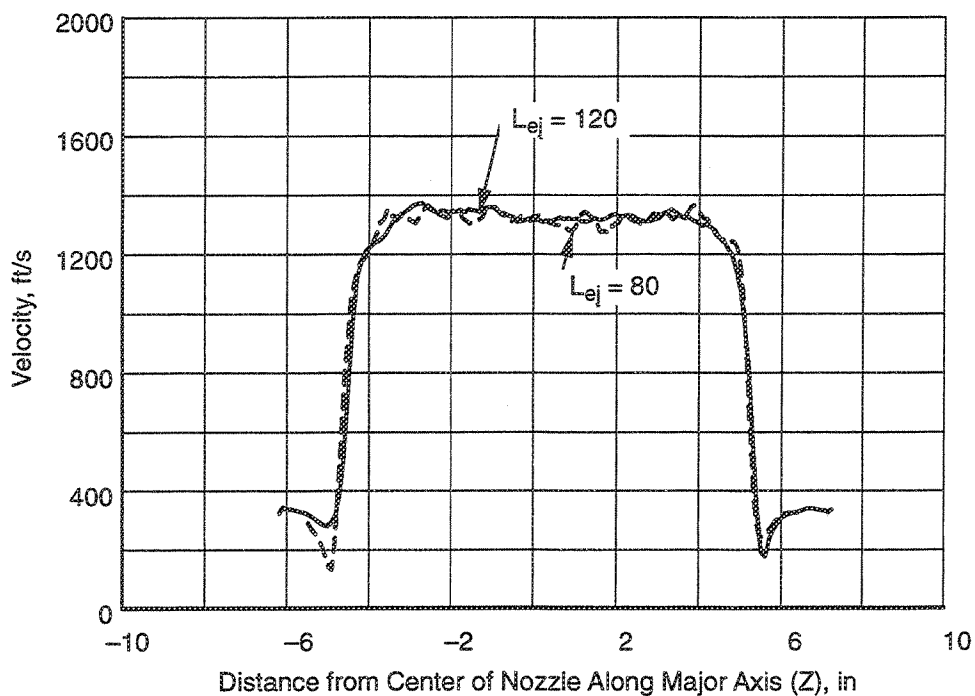


Figure 67. Effect of flap length on axial velocity distribution at nozzle exit along the major axis:  $V_j = 2384$  ft/s,  $NPR = 3.4$ ,  $T_g = 1580^\circ R$ ,  $M_0 = 0.32$ ,  $MAR = 0.95$ ,  $SAR = 3.3$

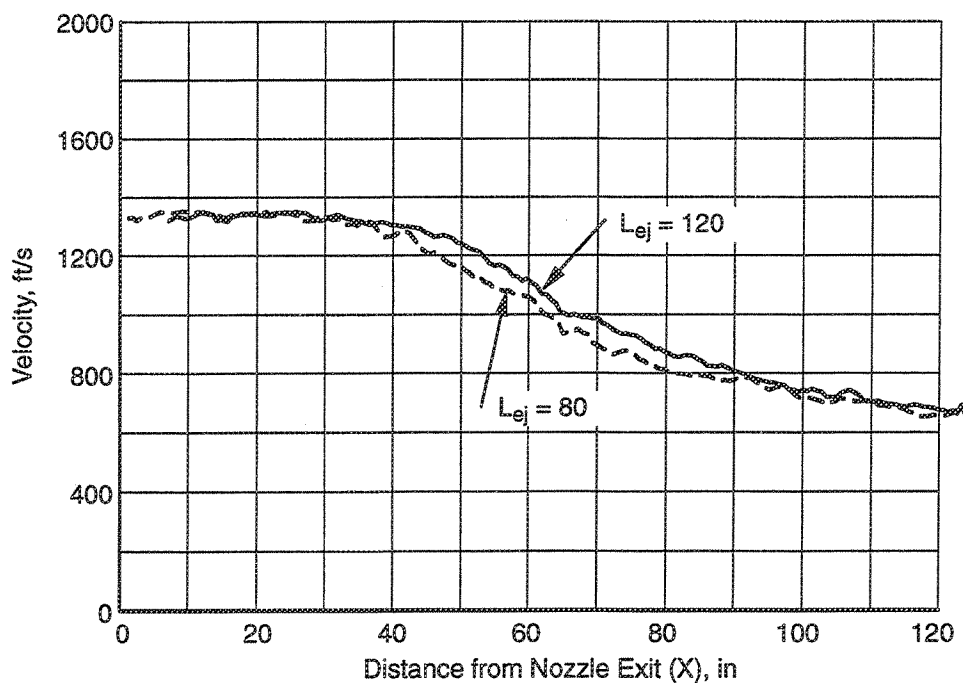


Figure 68. Effect of flap length on plume decay at nozzle exit along the nozzle centerline:  $V_j = 2384$  ft/s,  $NPR = 3.4$ ,  $T_g = 1580^\circ R$ ,  $M_0 = 0.32$ ,  $MAR = 0.95$ ,  $SAR = 3.3$

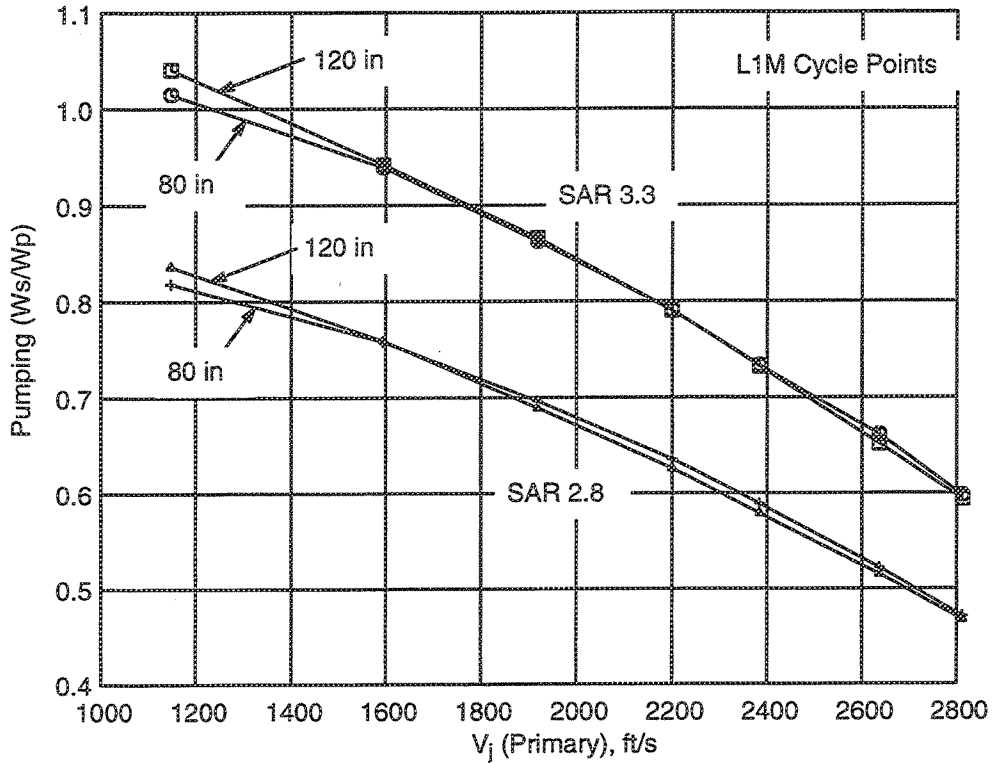


Figure 69. Effect of flap length on pumping characteristics:  $M_0 = 0.32$ ,  $MAR = 0.95$

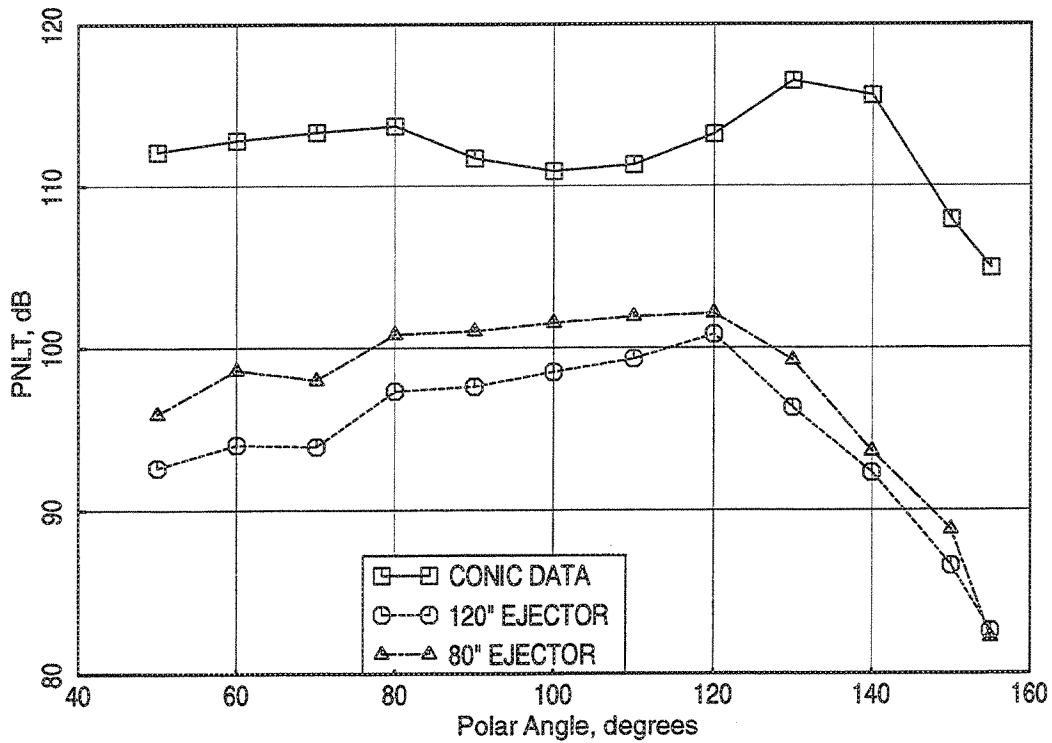


Figure 70. Effect of long- and short-flap treated-wall configurations on PNLT directivities:  $SAR = 3.3$ ,  $MAR = 0.95$ ,  $NPR = 3.4$ ,  $V_j = 2384$ ,  $T_g = 1580^\circ R$ ,  $M_0 = 0.32$ , sideline microphones

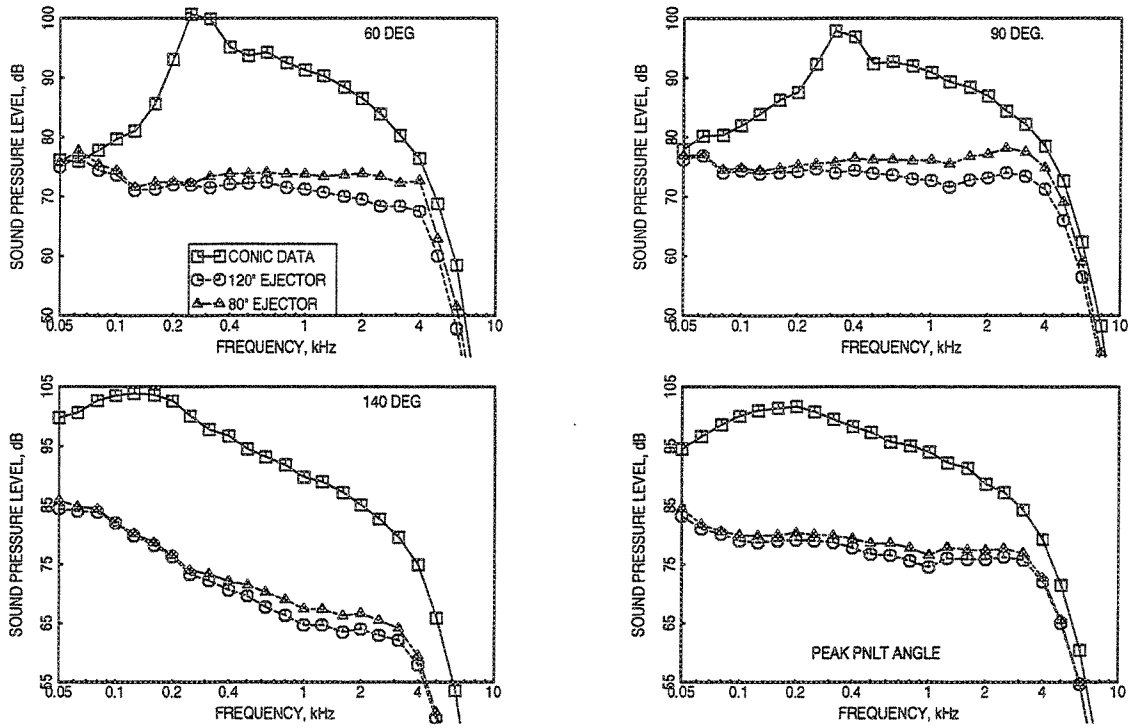


Figure 71. Effect of treated-wall flap length on SPL spectra at selected polar angles ( $\theta$ ):  $V_j = 2384$  ft/s, NPR = 3.4, MAR = 0.95, SAR = 3.3,  $T_8 = 1580^\circ R$ ,  $M_0 = 0.32$ , sideline microphones

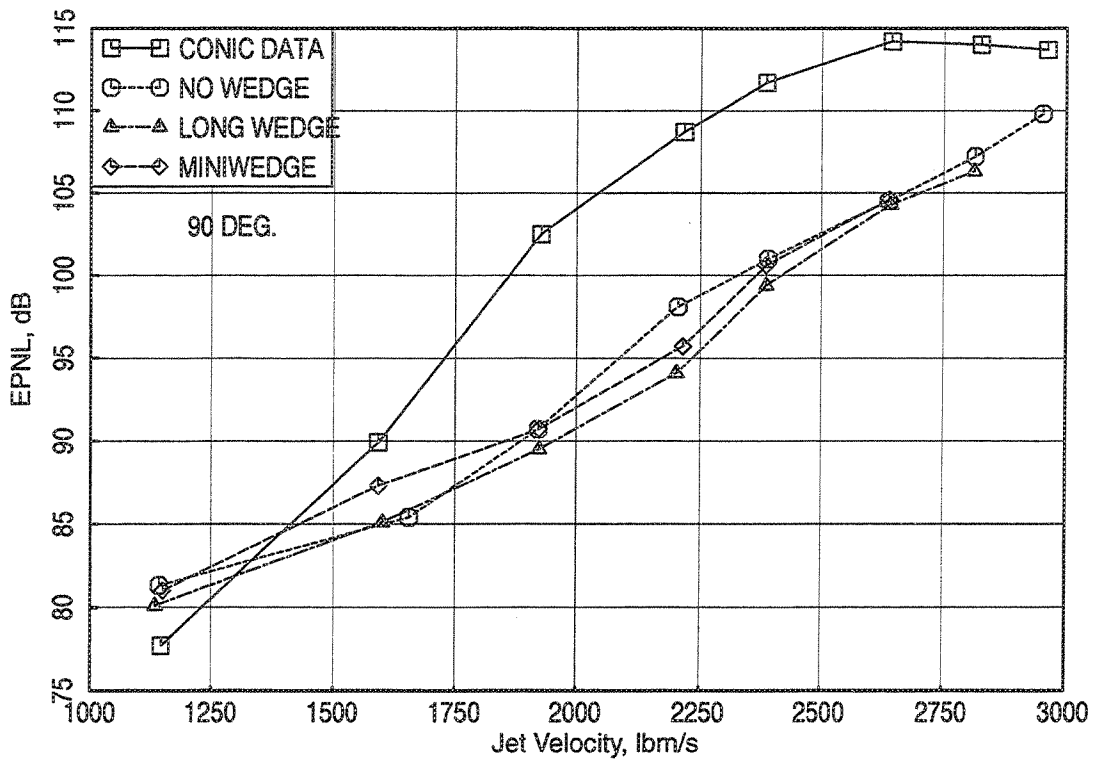


Figure 72. Effect of center wedge on EPNL as a function of  $V_j$ ; SAR = 3.3, MAR = 1.2, long-flap 2DME nozzle,  $M_0 = 0.32$ , sideline microphones

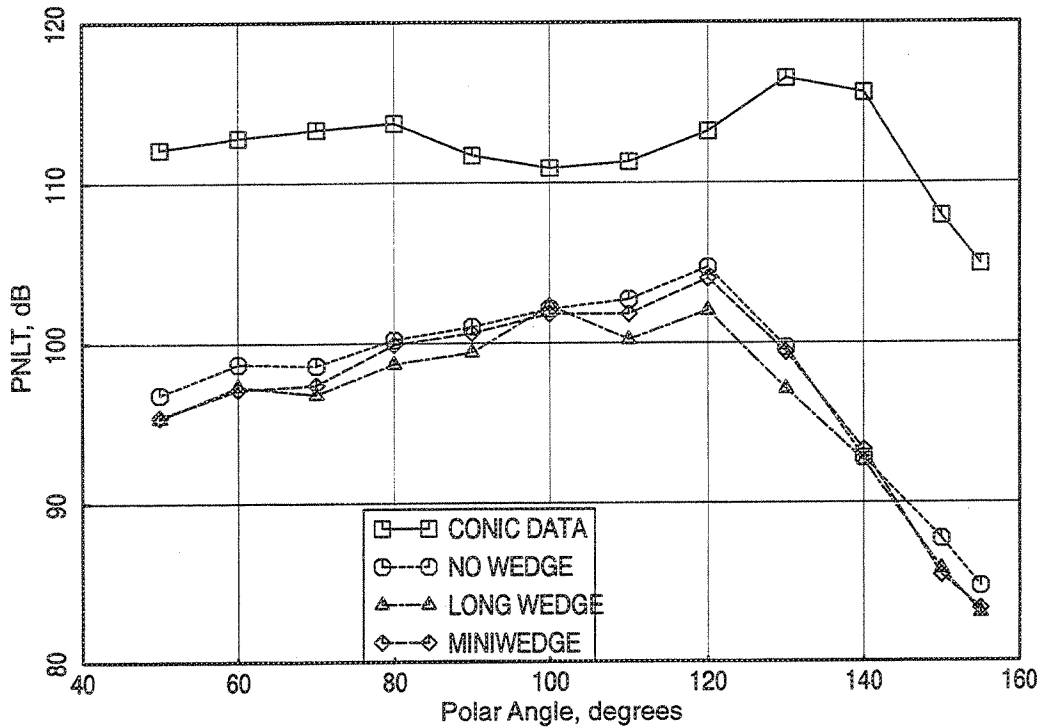


Figure 73. Effect of center wedge on PNLT directivities: SAR = 3.3, MAR = 1.2, long flap, NPR = 3.4,  $V_j = 2384$  ft/s,  $T_8 = 1580^\circ\text{R}$ ,  $M_0 = 0.32$ , sideline microphones

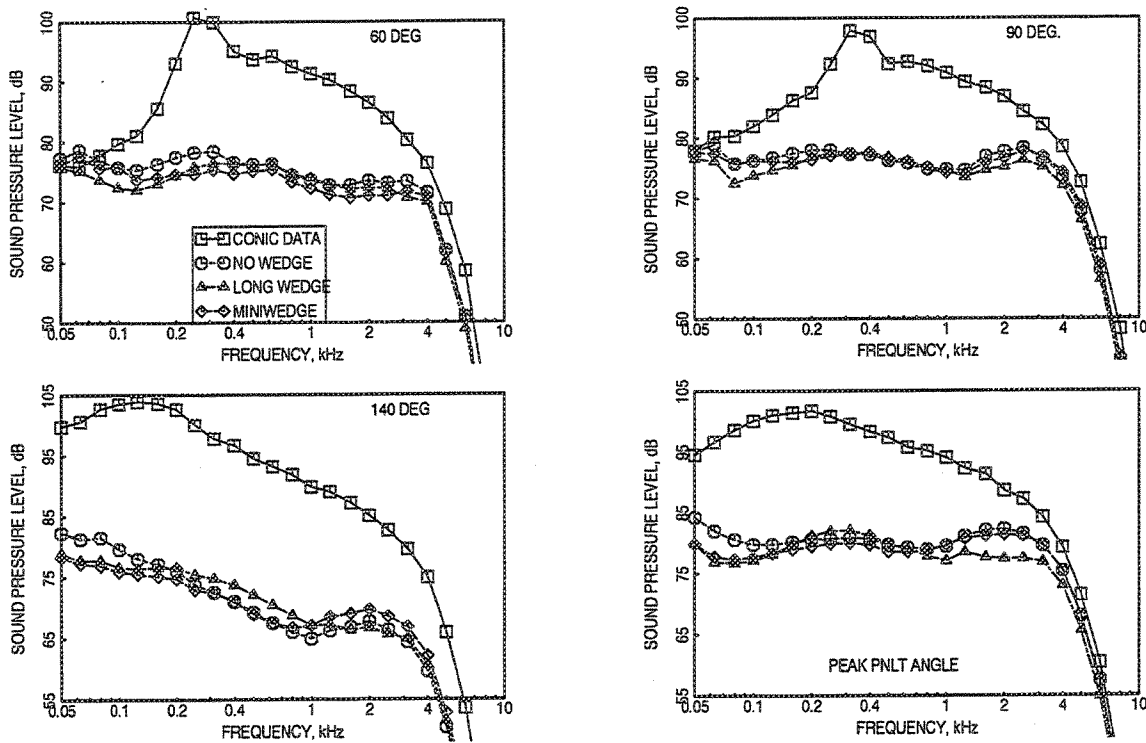


Figure 74. Effect of center wedge on SPL spectra at selected polar angles ( $\theta$ ):  $V_j = 2384$  ft/s, NPR = 3.4, long flap, MAR = 1.2, SAR = 3.3,  $T_8 = 1580^\circ\text{R}$ ,  $M_0 = 0.32$ , sideline microphones

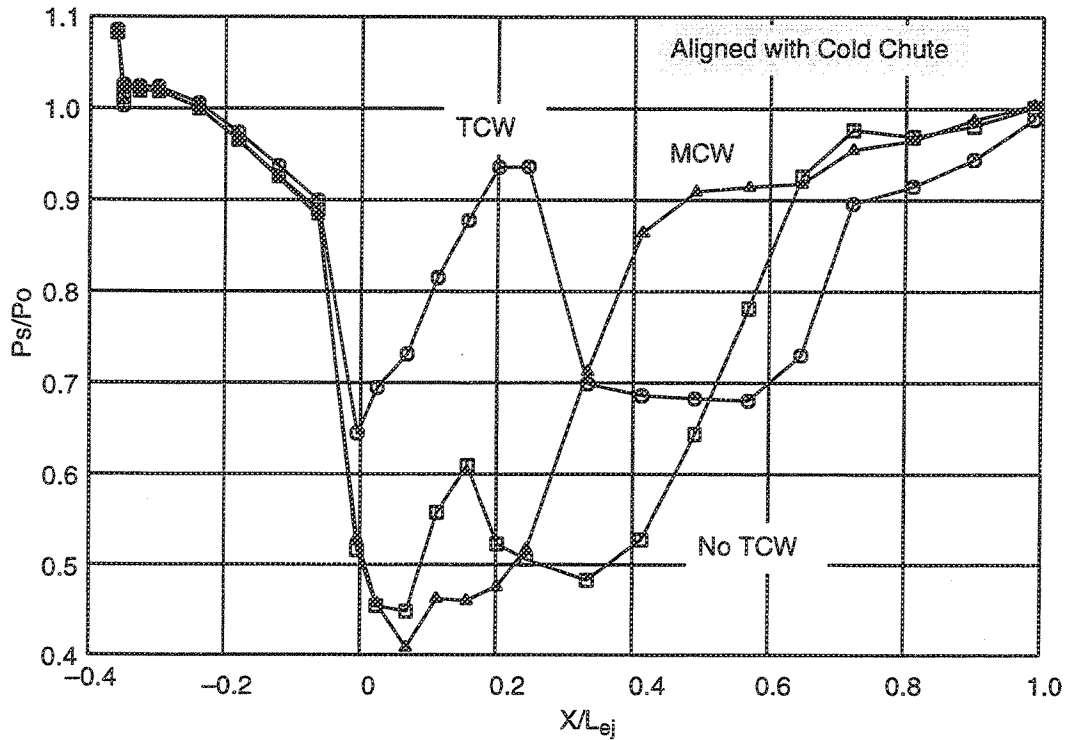


Figure 75. Effect of wedge on flap static pressure distribution:  $V_j = 2400$  ft/s,  $NPR = 3.4$ , long flap,  $MAR = 1.2$ ,  $SAR = 3.3$ ,  $M_0 = 0.32$

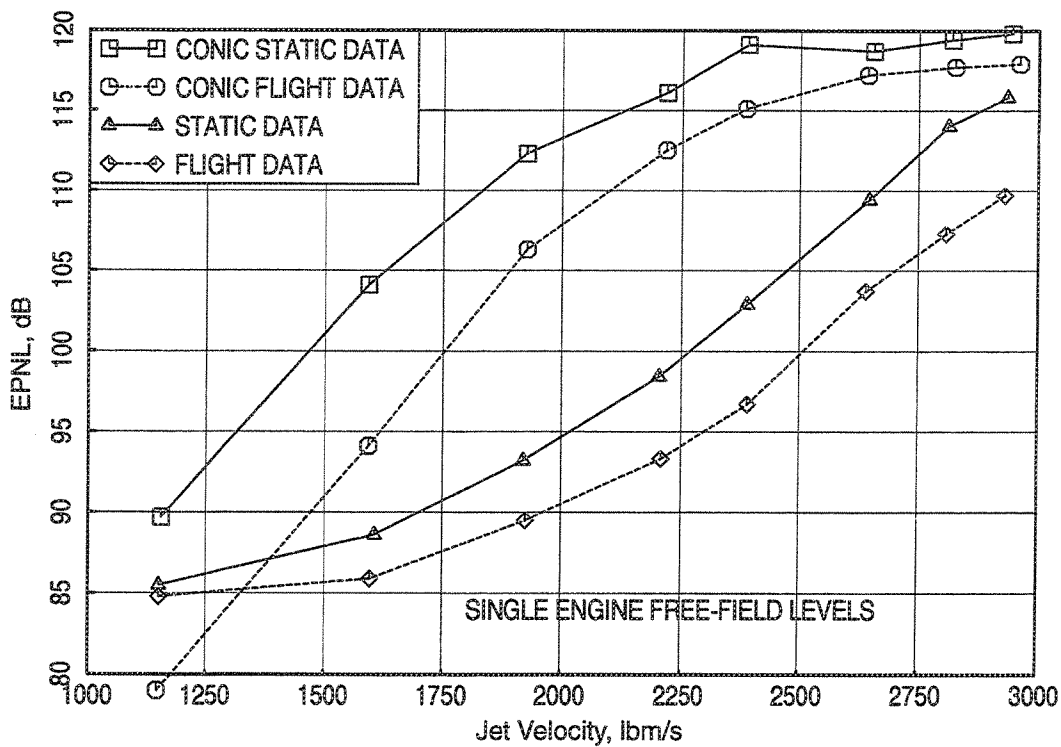


Figure 76. Effect of simulated flight on EPNL:  $SAR = 2.8$ ,  $MAR = 0.95$ , long flap, sideline microphones

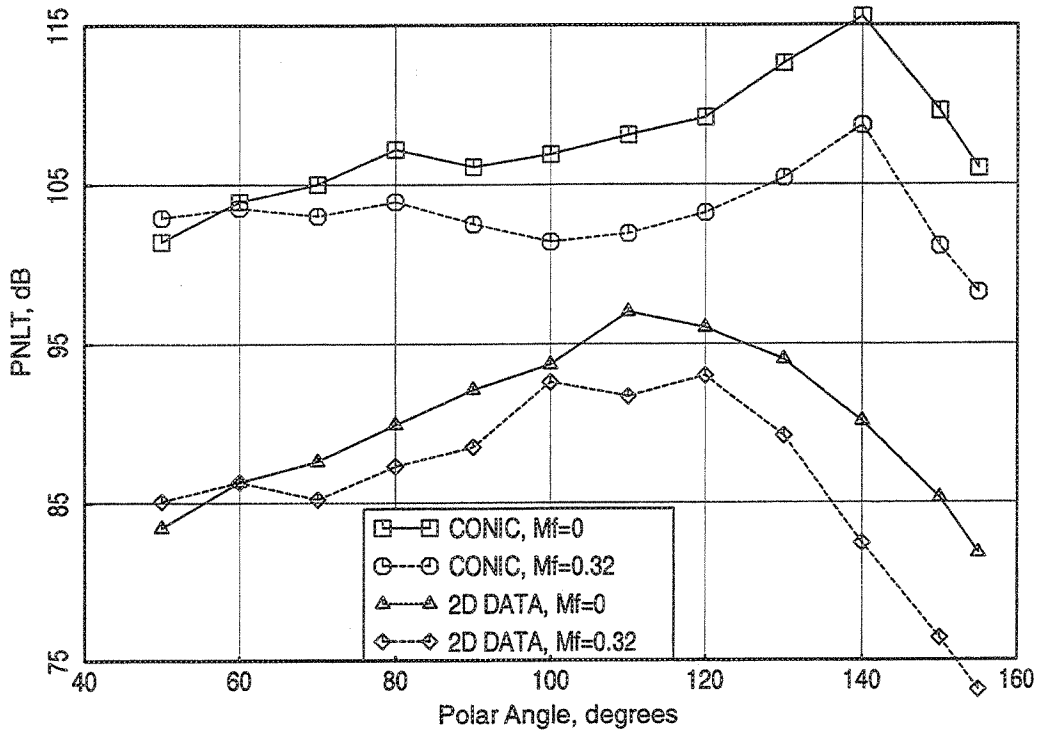


Figure 77. Effect of simulated flight on PNL1 directivities: SAR = 2.8, MAR = 0.95, long flap,  $V_f = 1900$  ft/s, NPR = 2.5,  $T_0 = 1325^\circ R$ , sideline microphones

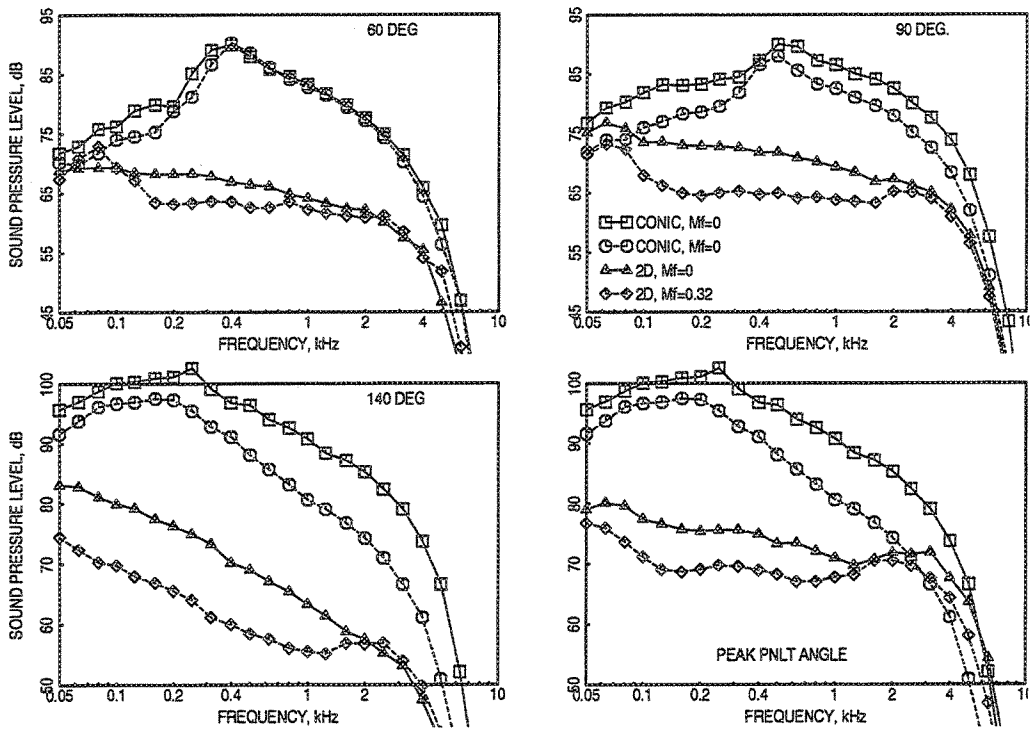


Figure 78. Effect of simulated flight on SPL spectra at selected polar angles ( $\theta$ ): SAR = 2.8, MAR = 0.95, long flap,  $V_f = 1900$  ft/s, NPR = 2.5,  $T_0 = 1325^\circ R$ , sideline microphones

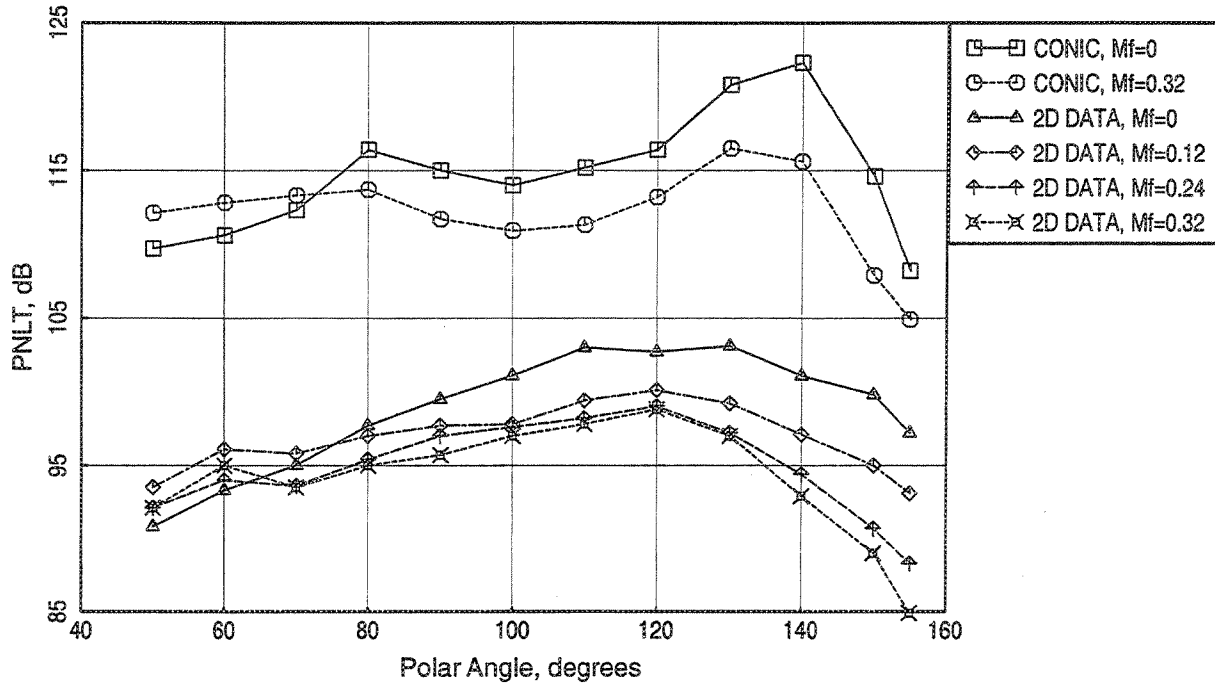


Figure 79. Effect of simulated flight on PNLT directivities: SAR = 2.8, MAR = 0.95, long flap,  $V_j = 2400$  ft/s, NPR = 3.4,  $T_8 = 1580^\circ$ R, sideline microphones

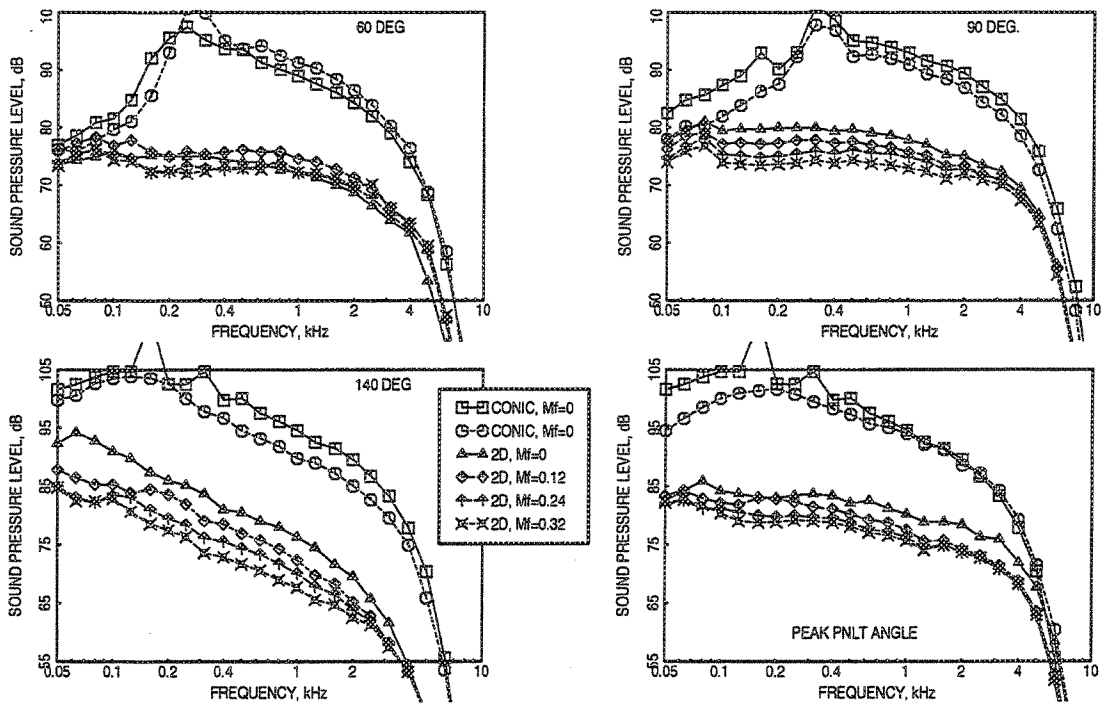


Figure 80. Effect of simulated flight on SPL spectra at selected polar angles ( $\theta$ ): SAR = 2.8, MAR = 0.95, long flap,  $V_j = 2400$  ft/s, NPR = 3.4,  $T_8 = 1580^\circ$ R, sideline microphones

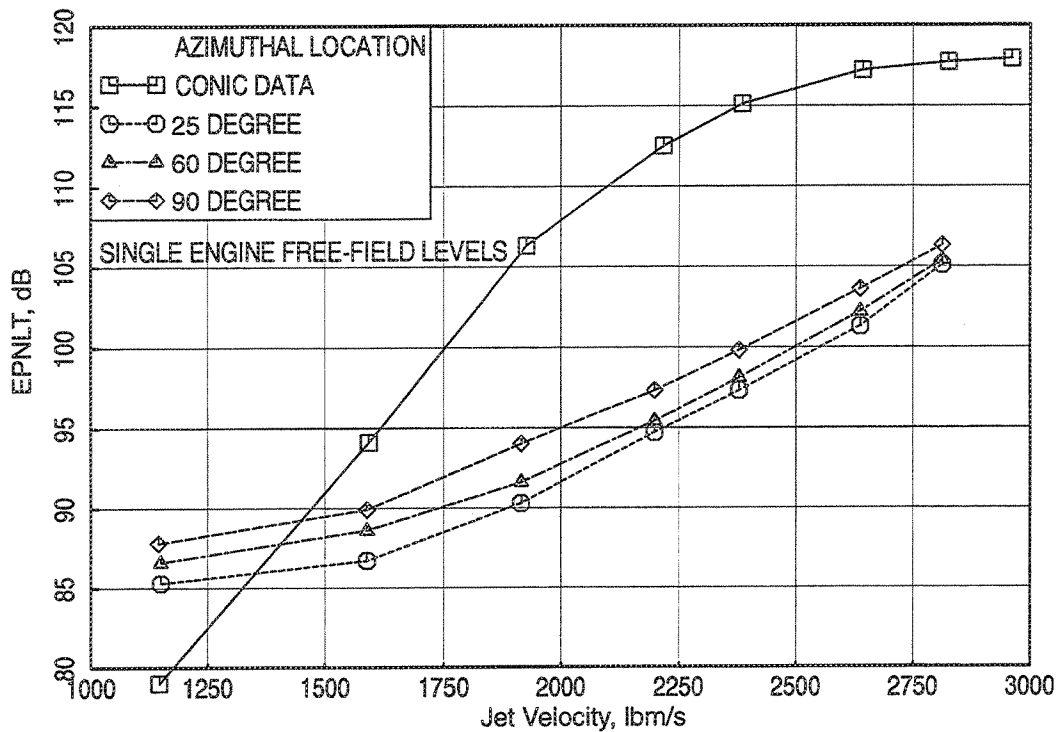


Figure 81. Azimuthal variation of EPNL: SAR = 3.3, MAR = 0.95, long flap,  $V_j = 2400$  ft/s, NPR = 3.4,  $T_8 = 1580^\circ\text{R}$ ,  $M_0 = 0.32$ , sideline microphones

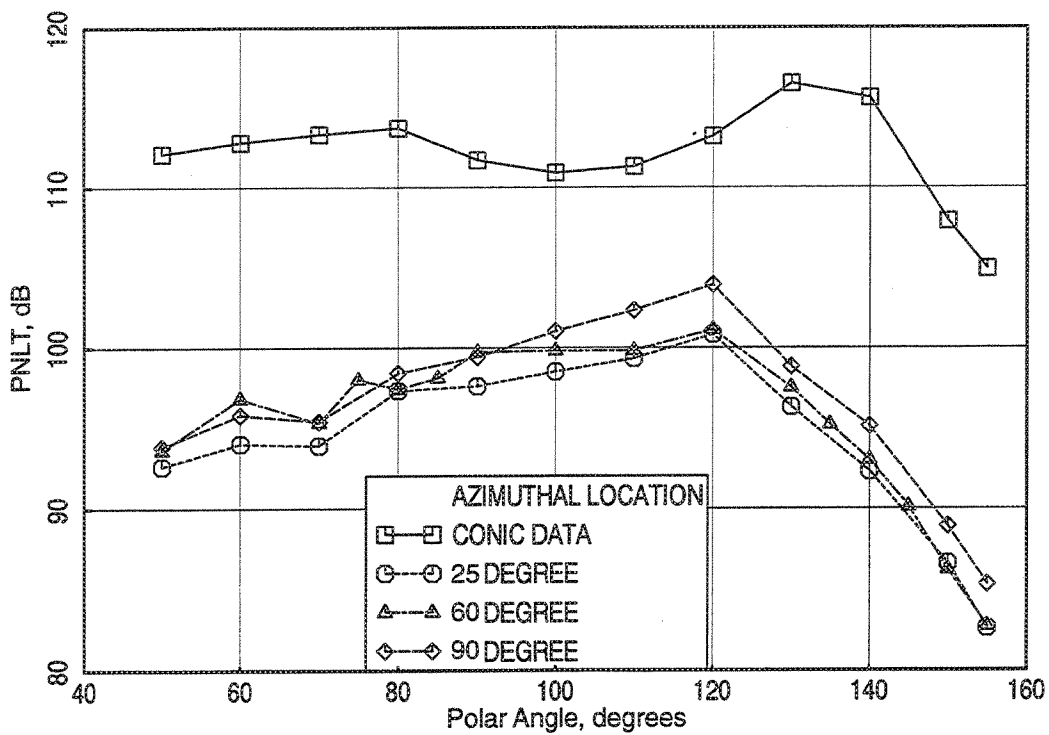


Figure 82. Azimuthal variation of PNLT directivities: SAR = 3.3, MAR = 0.95, long flap,  $V_j = 2400$  ft/s, NPR = 3.4,  $T_8 = 1580^\circ\text{R}$ ,  $M_0 = 0.32$ , sideline microphones

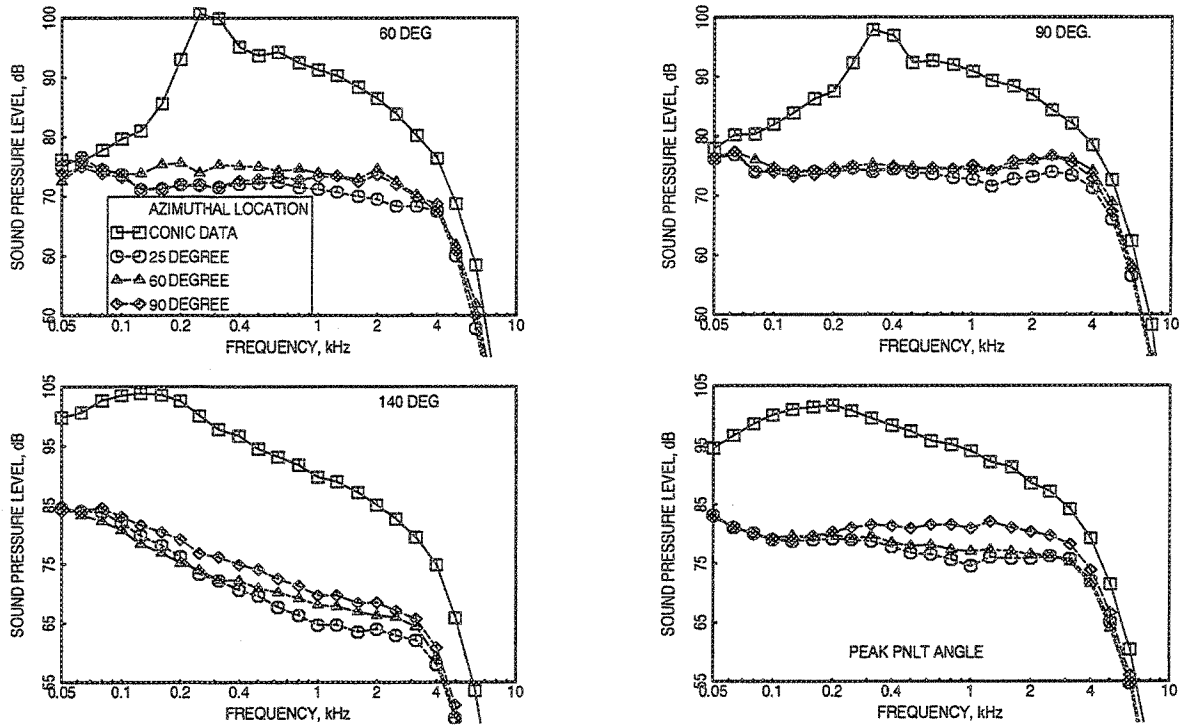


Figure 83. Azimuthal variation of SPL spectra at selected polar angles ( $\theta$ ): SAR = 3.3, MAR = 0.95, long flap,  $V_1 = 2400$  ft/s, NPR = 3.4,  $T_p = 1580^\circ R$ ,  $M_0 = 0.32$ , sideline microphones

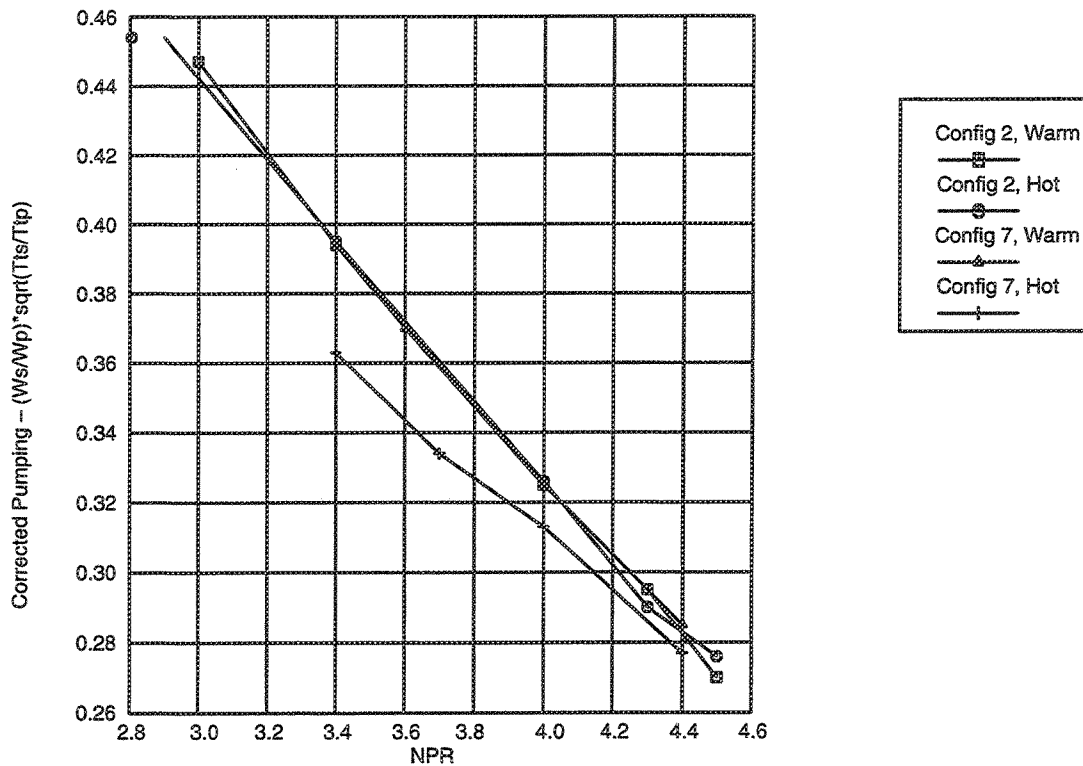


Figure 84. Effect of  $T_{78}$  on pumping characteristics: SAR = 3.3, long flap, static conditions

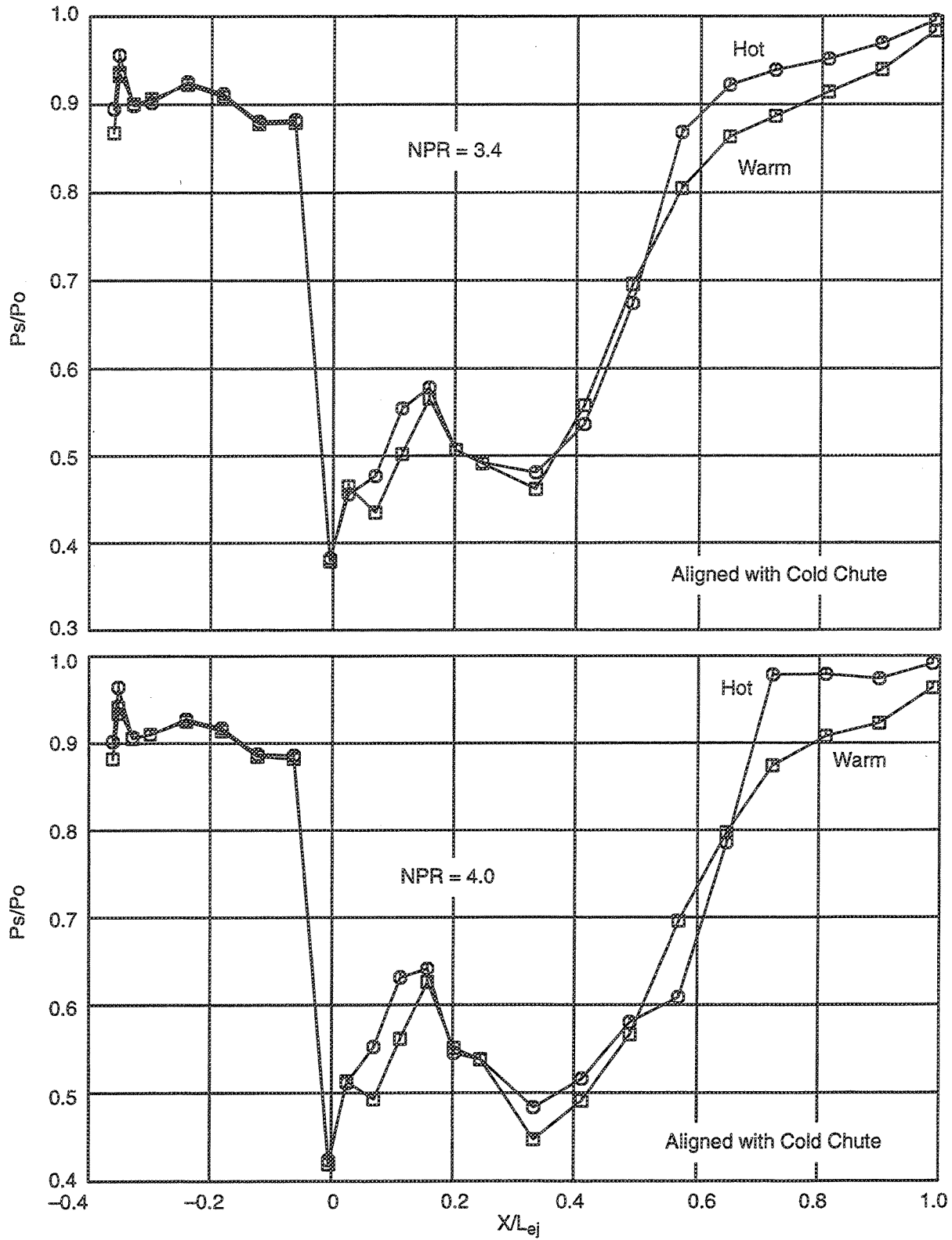


Figure 85. Effect of  $T_{79}$  on flap static pressure distribution: SAR = 3.3, MAR = 1.2, long flap, static conditions

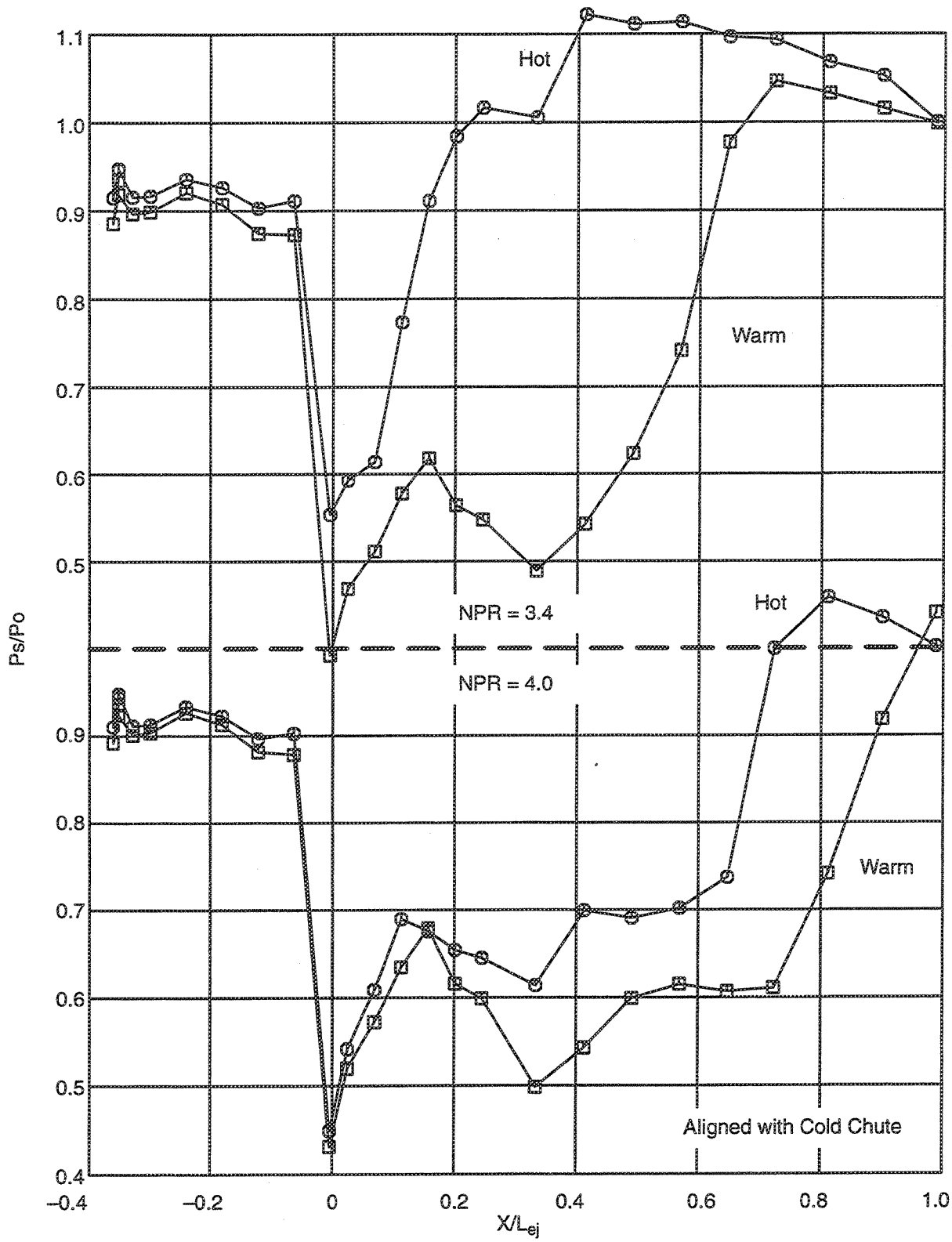


Figure 86. Effect of  $T_{TB}$  on flap static pressure distribution:  
 SAR = 3.3, MAR = 0.95, long flap, static conditions

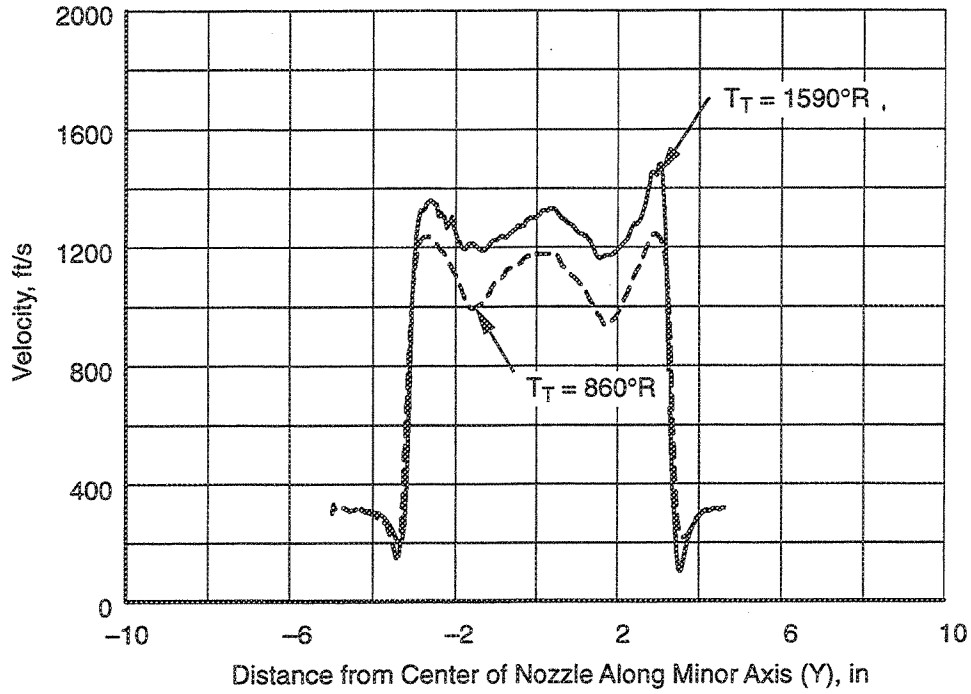


Figure 87. Effect of  $T_{T8}$  on nozzle exit axial velocity distribution along the minor axis: SAR = 3.3, MAR = 0.95, short flap, NPR = 3.4,  $M_0 = 0.32$

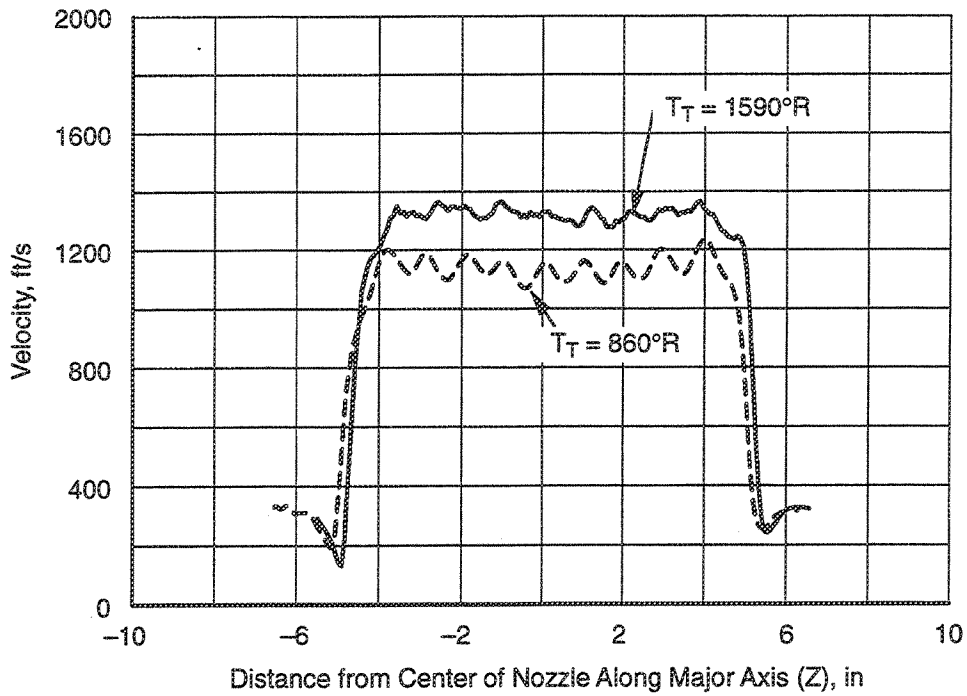


Figure 88. Effect of  $T_{T8}$  on nozzle exit axial velocity distribution along the major axis: SAR = 3.3, MAR = 0.95, short flap, NPR = 3.4,  $M_0 = 0.32$

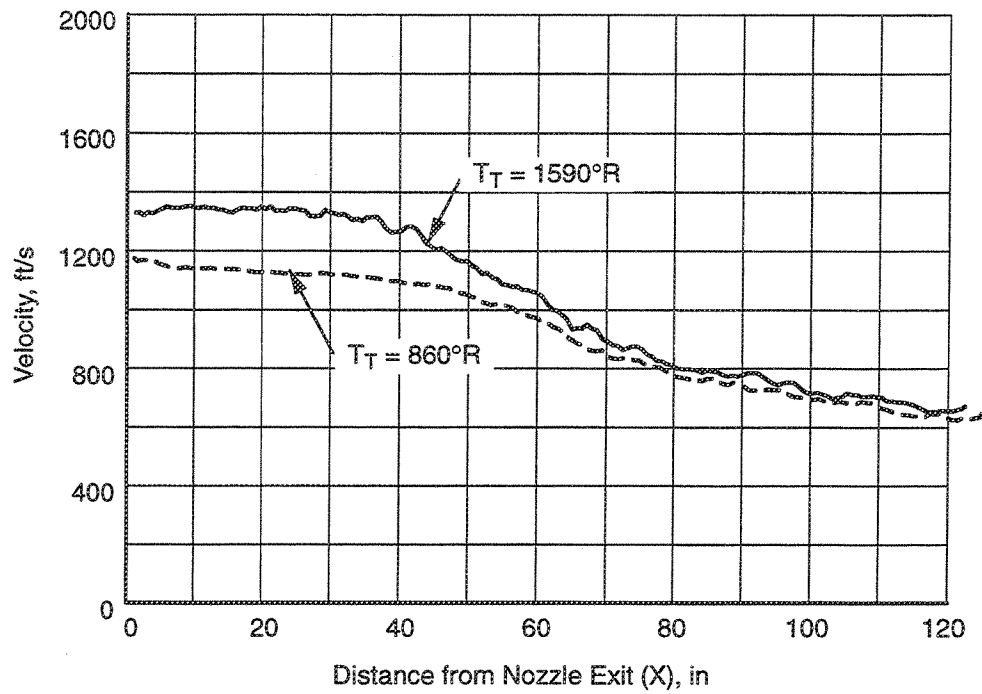


Figure 89. Effect of  $T_{T8}$  on nozzle exit plume decay along the nozzle centerline: SAR = 3.3, MAR = 0.95, short flap, NPR = 3.4,  $M_0 = 0.32$

## 5.0 Aeroperformance Test Program

The aerodynamic performance of the 2D mixer/ejector (2DME) nozzle 1/11th scale-model designs configured to represent the takeoff suppressed mode were evaluated at the NASA Langley 16-ft *Transonic Wind Tunnel* to compliment the acoustic performance evaluation of similar configurations carried out at GEAE's Cell 41 anechoic acoustic-test facility. The details of the acoustic performance evaluation and the results were discussed in Section 4.

The overall objective of the NASA Langley wind tunnel test program was to establish the aerodynamic performance design database needed to develop a 2DME exhaust nozzle. The specific objectives addressed were to assess the aerodynamic performance effects of:

- Primary/core flow expansion ratio (CER)
- Ejector mixing area ratio (MAR)
- Flap length
- Centerbody/wedge

This section summarizes the testing and the findings. Many figures are used to describe the models, tests, and resulting data. To avoid unwieldy separation of the text, the illustrations are presented collectively at the end of the section.

### 5.1 Aeroperformance Model and Test Matrix

#### 5.1.1 Model Description

The model represents a 2DME nozzle on a GEAE variable-cycle, mixed-flow turbofan with the suppressor deployed in takeoff mode; that is, mixer-suppressor chutes are deployed to break up the primary jet with alternating streams of ambient air entrained through the ejector (as illustrated in Figure 1). Figure 90 is a cross section of the scale model. The 2DME exhaust system in the suppressed mode consists of an upstream plenum in the primary flowpath (representing the mixed-flow turbofan exhaust) and suppressor chutes forming the primary flowpath, followed by the mixing chamber formed by the two sidewalls and the upper and lower flaps (where the ambient secondary flow is entrained and mixed with the primary flow). The secondary flow inlets are located on the top and bottom upstream of the flaps. The secondary flow enters the mixing chamber through the passages formed by adjacent suppressor chutes.

The scale model slightly deviates from the full-scale design because the need for variability of basic geometric parameters had to be addressed while maintaining simplicity of construction and test procedures. The scale model employs a fixed-position, flush inlet lip design (as discussed in Section 4) designed to accommodate large variation in secondary mass flow. The ejector inlet lip/flap leading edge was fixed for all configurations tested. The three-piece flap consists of the leading edge, flap-adjusting wedge piece, and the flap (as shown in Figure 90). By installing different wedge pieces between the leading edge and the flap, the flap divergence angle can be changed.

The ejector sidewalls are fixed for a given flap length. The bottom and top suppressor chute racks are single-piece construction and can be changed independently.

The configuration was varied primarily by changing the suppressor chutes or the flap angle. The ejector pumping can be changed significantly by the design of the suppressor chutes, and the flow area available for the secondary flow can be controlled. As the scale-model nozzle width between the sidewalls and the height at the suppressor chute exit was fixed for all configurations, any change in the secondary flow area through the suppressor chutes resulted in a corresponding change in the primary flow area. Consequently, the various designs tested had different primary throat areas, and the scale factor relative to full scale was slightly different for each configuration.

The primary nozzle design pressure ratio is 4.0 at a flight Mach number of 0.32. All of the scale-model aeroperformance testing was carried out using cold (ambient temperature) primary flow. The data need to be corrected for temperature effects when applied to full scale.

### 5.1.2 Model Design Parameters

The baseline aeroperformance model built under contract NAS3-25415 was designed to represent the corresponding acoustic model that was tested in the GEAE's Cell 41 anechoic acoustic test facility. This model was designed to operate along the GE21/F14 study L1M VCE cycle to power a Mach 2.4 HSCT with a range of 5000 nmi and a payload of 51,900 lbm. The baseline full-scale preliminary design had the following attributes:

- C/D aligned chutes (20) with CER of 1.43 and SAR of 2.8
- Ejector flap length: 80 inches full scale
- Center gap from chute bottom to chute bottom: 2.72 inches full scale
- Full-scale primary throat area ( $A_{p8}$ ): of 1086 in<sup>2</sup>

The baseline aeroperformance scale model differed from the above configuration; the testing was conducted using ambient temperature primary flow. The corresponding CER was 1.38 instead of 1.43. Additional variations of some key parameters were included to reduce the overall acoustic risk in meeting the program goals. The variations are as follows:

- Increased SAR: 3.3
- Longer flap: 120 inches full scale to provide more acoustic treatment (revised baseline)
- Center wedges (two lengths) to eliminate the center gap, thereby reducing the high-velocity center streak as well as increasing acoustic treatment area

The aeroperformance scale-model suppressor chutes for both SAR's were designed with an additional CER of 1.22 to provide reasonably matched static pressure at the chute exit over a wider operating range. Flap-adjusting wedges corresponding to four different MAR variations were also designed. A summary of the model design parameters investigated in this test series is given in Table 4. The variations in CER and MAR possible with this scale model hardware were as follows:

- CER – 1.22 and 1.38
- MAR – 1.40, 1.20, 1.00, and 0.80 (with primary focus on MAR 1.4 and 1.2)

**Table 4. GEAE 2DME mixer/ejector nozzle test at NASA Langley: aeroperformance configurations**

Configuration Variables					MAR			
Chute	SAR	CER	Wedge	Flap	0.80	1.00	1.20	1.40
1000	2.80	1.22	No	Short			W	W
			No	Long	W	W	W	W
	3.17		Yes	Long		W	W	W
2000	2.80	1.38	No	Short			W	W
			No	Long			W	W
	3.17		Yes	Long		W	W	W
3000	3.30	1.22	No	Short			W	W
			No	Long			W	W
	3.88		Yes	Long		W	W	W
4000	3.30	1.38	No	Short			W	W
			No	Long			W	W
	3.88		Yes	Long		W	W	W

W: Tested statically and wind-on at 0.32, 0.40, 0.55, and 0.70 Mach numbers.

Wedge: Tested with two different wedges; one long and one short.

### 5.1.3 Test Facility and Test Setup

The performance test was conducted in the NASA Langley 16-ft transonic wind tunnel. This facility is a single-return, continuous-flow-exchange-air-cooled, atmospheric-pressure wind tunnel with an octagonal, slotted throat test section. The wall divergence is adjusted as function of the air stream dew point and Mach number to reduce the impact of any longitudinal static pressure gradient in the test section. Test section Mach number is continuously variable to a maximum of 1.3. The average Reynolds number per foot ranges from about  $1.4 \times 10^6$  at a free-stream Mach number of 0.20 to about  $4.0 \times 10^6$  at a free-stream Mach number of 1.30. Further details on this test facility are available in Reference 7.

The Langley nonaxisymmetric, single-engine propulsion simulator (Reference 7) was used to evaluate the performance of the exhaust system models under investigation. Figure 91 is a detailed sketch of the propulsion simulation system. As illustrated, this simulator/model consists of five major components: a nose/forebody, a low-pressure plenum, an instrumentation section, a transition section, and the test nozzle.

The nose/forebody section is nonmetric, and all sections downstream of the nose/forebody are metric. The five-component force balance was located in the low-pressure plenum section. A low-friction Teflon seal was inserted at the metric break between the nose/forebody and the low-pressure plenum to eliminate crossflow through the nonmetric to metric interface without transmitting axial force across the interface.

The primary flow of the exhaust nozzle was supplied by a high pressure air system external to the simulator. A continuous flow of clean, dry, high-pressure air at a stagnation temperature of 80°F

entered the high-pressure plenum in the nose/forebody through six supply lines in the support strut, as shown in Figure 91. The high-pressure air was discharged radially outward from the high-pressure plenum to the low-pressure plenum through eight equispaced sonic nozzles around the circumference of the high-pressure discharge pipe. This arrangement minimizes the effect of any forces resulting from the transfer of axial momentum as air passes from the nonmetric to the metric part of the simulator. Two flexible metal bellows were used to seal the low-pressure plenum and compensate for any axial forces resulting from pressurization.

The airflow in the low-pressure plenum was diffused over the balance housing and straightened by a 79% open-area baffle plate. The airflow then passed through the instrumentation section, where the stagnation temperature and pressure of the air supply entering the test hardware were measured. The airflow, then passed through the transition section. In the transition section, the internal geometry changed from circular to rectangular, compatible with the 2DME nozzle test hardware. From the transition section, the airflow was exhausted through the test hardware.

The single-engine propulsion simulator with the 2DME exhaust system model was supported in the tunnel by a sting/strut support system as shown in Figure 91. The nose/forebody of the simulator, at 12 o'clock position, was attached to the bottom of the support strut. The centerline of the simulator/model was located along the test section centerline, and the centerline of the sting was located 22.0 inches above the test section centerline. The simulator/model blockage was approximately 0.23% of the test section cross section, and the maximum blockage (including the model support) was approximately 0.31%. Figures 92 through 96 are photographs of the installation and model hardware.

#### 5.1.4 Instrumentation

Basic model instrumentation included the five-component force balance shown in Figure 91. A rake of 12 total-pressure probes in the instrumentation section was used to measure the primary nozzle flow total pressure. An iron-constantan thermocouple in the instrumentation section also provided the total temperature of the primary nozzle flow. In addition, the test facility instrumentation measured parameters to define the test conditions: wind tunnel test section total pressure, total temperature, and Mach number. The primary nozzle mass flow supplied by the test facility was also measured using a *Multiple Critical Venturi* system (Reference 7).

**Ejector Inlet Conditions** – The parameters of interest for the secondary flow are the total pressure, total temperature, and secondary mass flow. The total temperature of the secondary flow was assumed to be that of the tunnel free-stream; no separate measurements were made. The secondary flow total pressure at the ejector inlet was measured using 15 probes. The instrumentation consisted of three rakes with five total-pressure probes each. Two of the rakes were located at the top inlet and the other was located in the lower inlet. The average rake total pressure were used to define the ejector inlet secondary flow total pressure.

A total of six wall static pressure taps, two at each rake location, one on the inlet ramp and the other on the inlet scoop/flap leading edge, were used to define the local static pressure. These wall static pressure taps were located to coincide with the tip of the total-pressure probes as shown in Figure 97. Measurements from the rake total pressure probes and corresponding wall static pressures were used to calculate local Mach numbers and the total secondary mass flow rate.

**Ejector Inlet Wall Static Pressures** – A total of 17 wall static pressure taps were located in the ejector inlet. Of these, six were located at the inlet total pressure rake locations, as mentioned above,

and were used for evaluating the mass flow. The remaining 11 static pressures were located in the inlet ramp and scoop/flap leading edge. These provided additional diagnostic information on the inlet flow quality.

A total of four static pressures were located along the upper surface of the inlet ramp, see Figure 97. The remaining seven static pressures were distributed over the leading edge of the flap/internal surface of the inlet scoop.

**Mixer Chute Static Pressures** – Referring to Figure 98, 21 static pressure taps were distributed over the mixer chutes. Six were located on the primary flow side, and the remaining 15 were located on the secondary flow side of the chutes.

**Flap/Ejector Shroud Static Pressures** – Both the short and the long upper flaps were instrumented with two rows of static pressure taps along the length of the flaps. The long flap had a total of 14 taps, and the short flap had a total of 10. Referring to Figure 99, one row was aligned with the primary flow exiting the suppressor chute, and the other row was aligned with the secondary flow exiting the chute.

### 5.1.5 Test Configurations and Procedure

Table 5 is a summary of configurations tested during this series under contract NAS3–25415. For a given suppressor geometry (SAR and CER), MAR was changed by adjusting the flap angle. Nozzle performance was evaluated as a function of primary nozzle pressure ratio (NPR). The performance data were acquired, at constant wind tunnel Mach numbers (0.0, 0.32, 0.40, 0.55, and 0.70), by changing the primary NPR.

Additional testing was conducted to determine the momentum tares of the high-pressure air on the measured forces. This consisted of jet-off and jet-on loadings of the installed model in the model-preparation area (MPA). The jet-off model calibrations were performed on axial force, normal force, and pitching moment. The jet-on calibrations in the MPA were performed using three calibration nozzles having a range of throat areas of 5.711, 8.501, and 11.352 in<sup>2</sup>. For each throat area, at various levels of normal force and pitching moment, the jet-on calibration was performed up to a NPR of 6.0. The jet-on calibration, using the 8.501 in<sup>2</sup> calibration nozzle, was repeated in the wind tunnel immediately after installation and just prior to removal of the model to ensure that calibrations performed in the MPA were valid and no significant changes occurred during the test.

From the measured quantities various performance parameters were calculated by the facility data-reduction program. Details of the calculations are not addressed in this report. The primary calculations based on measured parameters were:

1. Wind tunnel free-stream conditions – free-stream Mach number ( $M_0$ )
2. Balance forces corrected for balance and metric support tares ( $F-D_{noz}$ )
3. Primary flow based on multiple choked-venturi data ( $W_p$ )
4. Primary ideal flow and jet velocity ( $W_{pi}$ ,  $V_j$ )
5. Secondary flow entrainment through integration of flow properties across the inlet — from measured rake total pressures, wall static pressure, and free-stream total temperature

The last calculation assumes no significant spanwise variation of secondary flow properties. The primary source of error is the lack of instrumentation to account for any spanwise distribution in the

Table 5. Aeroperformance Test Matrix (NAS3-25415)

Configuration Code	SAR	CER	MAR	Flap Length ( $L_{ej}$ ), in	Center Body	$A_B$ , in <sup>2</sup>
1110	2.80	1.22	1.20	7.40	Off	9.31
1210			1.40			
1120			1.20			
1220			1.40			
1320*			1.00			
1420*			0.80			
1121			3.17	1.22		
1221	1.40					
1122	1.00	Long				
1222	1.20					
2110	2.80	1.38	1.20	7.40	Off	9.31
2210			1.40			
2120			1.20	11.10		
2220			1.40			
2121	3.17	1.38	1.20	11.10	Short	7.69
2221			1.40			
2122			1.00		Long	
2222			1.20			
3110	3.30	1.22	1.20	7.40	Off	8.04
3210			1.40			
3120			1.20	11.10		
3220			1.40			
3121	3.88	1.22	1.20	11.10	Short	6.42
3221			1.40			
3122			1.00		Long	
3222			1.20			
4110	3.30	1.38	1.20	7.40	Off	8.04
4210			1.40			
4120			1.20	11.10		
4220			1.40			
4121	3.88	1.38	1.20	11.10	Short	6.42
4221			1.40			
4122			1.00		Long	
4222			1.20			

\* These configurations were tested at static conditions only ( $M_0 = 0.0$ ),

flow properties at the inlet. Referring to Figure 97, the rakes for estimating secondary flow were located reasonably away from the wall; consequently, distortions in the flowfield near the end walls are not captured. Such distortion could be significant under static conditions; the secondary flow is entrained from all directions, and the end walls act like a sharp-edged inlet — resulting in poor flow quality. The estimates of secondary flow are probably higher than the real values. The estimated pumping characteristics should be treated for qualitative evaluation only and not for quantitative analysis.

## 5.2 Aeroperformance Data Analyses

The data acquired in this test series were centered around improving pumping characteristics and performance. The data acquired illustrate the effect of some key design parameters on pumping and nozzle performance. This investigation was comprehensive enough to establish the effects of MAR, SAR, CER, flap length, centerbodies, and free-stream Mach number. In addition, some of the basic phenomena on the two possible modes of operation of the ejector (subsonic and supersonic) were established. All of these aspects of ejector performance and their impact on nozzle performance and pumping are discussed.

### 5.2.1 Basic Ejector Nozzle Characteristics

Typical static performance of the ejector nozzle in terms of the thrust minus drag coefficient is presented in Figure 100 as a function of primary nozzle pressure ratio for SAR = 2.8, MAR = 1.2, and CER = 1.22, with long flap. Similar observations can be made for all configurations with MAR > 1, except for the differences in the performance, which are discussed later. The primary contribution of the aeroperformance testing was identification of the significance of MAR as the primary variable. The aeroperformance test series enabled redirection of the primary focus away from MAR > 1 to MAR < 1, and most of the acoustic testing in Cell 41 was carried out at MAR = 0.95 (as discussed in the previous section).

Referring to Figure 100, there seems to be a minimum between NPR = 2.0 and 2.5. The corresponding corrected pumping ratio and physical estimated secondary mass flow rates are shown as functions of primary nozzle pressure ratio in Figures 101 and 102 respectively. The key observations that can be made from these figures are that pumping ratio decreases with increasing NPR. The primary reason for this behavior being the continuous increase in primary flow with increasing NPR. The physical secondary flow increases steeply as NPR is increased from the lowest value and reaches a maximum between NPR = 2.0 and 2.5. Secondary flow then gradually decreases with increasing NPR. It is important to note that the minimum nozzle performance approximately coincides with the maximum physical flow. This aspect will be explored later. The estimated physical secondary flow entrainment is probably in significant error, especially under static conditions, as explained earlier.

The flap internal pressure distributions for all of the above nozzle pressure ratios are given in Figures 103 and 104. The flap static pressures have been nondimensionalized by the free-stream static pressure  $P_o$ , and the corresponding axial locations measured from the suppressor chute exit have been nondimensionalized by the flap length. The plots indicate a distinct characteristic difference at nozzle pressure ratios lower and higher than the nozzle pressure ratio, at which the minimum performance was observed. In evaluating these static pressures, it must be understood that the total pressures are not constant along the length of the flap, due to the mixing process. However, it may

be safe to assume that the primary and secondary flows are essentially unmixed immediately downstream of the suppressor exit. Due to the complicated flow characteristics and the possibility of significant pressure gradients along the height of the nozzle, data from pressure taps at the chute exit and vicinity must be used cautiously.

Figure 103 shows the flap static pressure distributions of pressure taps aligned with primary flow centerline and secondary flow centerline, for all of the NPR's. Figure 104 compares primary and secondary chute aligned flap static pressures at selected NPR's.

At nozzle pressure ratios of 1.5 and 2.0, the flap static pressures (Figure 103) indicate a gradually diffusing pressure distribution downstream of the mixer exit, beyond the first 30 to 40% of the flap length. Considering that the flaps are diverging as indicated by a MAR of 1.2, the flow should be subsonic in the mixing area and downstream along the length of the flap. At nozzle pressure ratios of 2.5 and greater, beyond 5% of the flap length, there is a continuous decrease in pressure levels, indicative of accelerating flow, followed by a significant rise in flap static pressure and a region of nearly flat pressure distribution. The location of the sudden raise in static pressure moves downstream towards the exit of the nozzle with increasing nozzle pressure ratio, from approximately 40% of the flap length at  $NPR = 2.5$  to 70% of the flap length at  $NPR = 4.0$ . Once again considering the MAR, it can be postulated that the mixed flow is supersonic and the mixing chamber acts as a supersonic nozzle. This is consistent with basic ejector theory (Reference 8), as there are two possible solutions for the mixed flow, one subsonic and other supersonic, based on the mixing chamber geometry and inlet and exit flow conditions. The two operating regions of the ejector are named, respectively: subsonic and supersonic modes. In the supersonic mode of operation for a diverging mixing area ratios (that is,  $MAR > 1.0$ ), the location of the shock is a function of the nozzle exit back pressure. As the primary nozzle pressure ratio is increased, the mixed-flow total pressure also increases, and the shock moves towards the exit of the nozzle. At high enough pressure ratios, the mixer/ejector nozzle exit will be fully supersonic. A significant increase in nozzle performance is observed associated with the supersonic mode. Significant model vibration/instability was also experienced with the transition from subsonic to supersonic mode.

The comparison of the primary and secondary flow chute aligned pressure taps, as shown in Figure 104, indicates that at all NPR's the static pressures at and beyond 20% of the flap length from the suppressor chute exit are nearly identical. The primary-chute-aligned static pressure at  $X = 0$  (at the chute exit) for all nozzle pressure ratios of 2.0 and above yields an expansion ratio (primary total pressure to local static pressure ratio) of about 3.8. This could be due to the actual geometry of the scale model. It is also important to note that at NPR's of 1.5 and 2.0 the primary-chute-aligned pressure taps all indicate diffusing flow characteristics, while the NPR's of 2.5 and 4.0 both indicate rapid acceleration followed by sudden diffusion. The primary reason for the behavior at 2.5 and above could be the shape of the primary chute extensions. The static pressure tap at  $X/L_f = 0.02$  is located on the primary chute extension and the static pressure tap at  $X/L_f = 0.058$  is located downstream of the primary chute extension on the flap. The supersonic flows from the primary chutes are vectored in this region by  $15^\circ$  to the flap and consequently must go through a compression turn. This could be the primary reason for the excessive observed acceleration and deceleration. At pressure ratios of 2.0 and above the secondary-flow-aligned pressure taps at the chute exit indicate possible choking as the local static pressure is equal to or lower than the critical pressure ratio of  $0.528 \times P_0$ . Further analysis is needed to evaluate the behavior of these static pressures at  $NPR = 2.0$ . This static pressure tap is located in the area between the adjacent primary chute extensions; flow

could be locally sonic and may not represent the entire flowfield. This reasoning is substantiated by the fact that at  $X/L_f = 0.058$ , the secondary-flow-aligned static pressure at  $\text{NPR} = 2.0$  is reasonable above critical pressure ratio. However, based on the significantly lower values of secondary flow aligned static pressures for  $\text{NPR} \geq 2.5$  and above over a significant part of the flap length immediately downstream of the suppressor, one can conclude that the secondary flow was sonic at these NPR's.

### 5.2.2 Effect of Free-Stream Mach Number

The effect of free-stream Mach number on the performance is illustrated in Figure 105. The most noteworthy trend is the significant reduction in the thrust minus drag coefficient with external flow of about 5 points at a free-stream Mach of 0.32 at  $\text{NPR} = 4.0$  relative to static conditions. The slope of the thrust minus drag coefficient variation with NPR for wind-on cases is also steeper relative to the static case.

The pumping characteristics shown in Figure 106 indicate there is a slight increase in pumping with free-stream Mach number. This increase in pumping is essentially due to the higher total pressure of secondary flow with free-stream Mach number. For a given NPR and ambient static condition, the primary mass flow is essentially same. The ideal secondary flow total pressure is 7.4, 11.6, 22.8, and 38.7% higher than that of the static condition at free-stream Mach numbers of 0.32, 0.40, 0.55, and 0.70 respectively. Consequently, one can expect a significant increase in pumping with free-stream Mach number. However, the actual increase in pumping is lower than the increase in secondary flow total pressure because inlet recovery is significantly lower with increased free-stream Mach number.

Figure 107 shows the estimated secondary flow corrected for the same free-stream static pressure and secondary flow total temperature. It indicates that, at constant NPR, entrainment increases with increasing Mach number, but Mach 0.32 entrainment is not significantly higher than static, in spite of the significant increase in the secondary flow total pressure (about 7 %) relative to the static condition. Caution must be exercised in interpreting these data; possible significant flow distortion in the spanwise direction, especially under static conditions, was not included in estimating the secondary flow.

Under wind-on conditions, a significant boundary layer develops along the model and is ingested along with the free-stream flow. This is illustrated by the total pressure distribution at the inlet as function of the inlet height, Figure 108. The wall statics at the ramp and scoop side of the inlet are also indicated in this figure. There is a significant reduction in total pressure over most of the inlet away from the ramp side at Mach 0.32, while the total pressure distribution is flat over the entire nozzle at Mach 0.0. It can be seen that at high Mach numbers (0.55 and 0.7) the ramp-side total and static pressures are the same over a good portion of the inlet height, indicating separated flow. The overall increase in entrainment observed is not proportional to the increase in free-stream total pressure due to the inlet total pressure recovery.

The performance of the nozzle likewise is affected by two primary sources of losses associated with external flow. First is the external friction and pressure drag of the entire exhaust system due to external flow; second is the ram drag associated with secondary flow entrainment. The external friction drag is essentially constant for a given free-stream condition, except for minor effects due to pumping. Ram drag is directly proportional to both the secondary flow and the free-stream velocity (Mach number). Secondary flow increases from lowest value to maximum with increasing

NPR. The maximum secondary flow occurs in the nozzle pressure ratio range of 2.0 to 2.5, and the secondary flow remains nearly constant up to a nozzle pressure ratio of about 3. The secondary flow then drops gradually with further increase in NPR, as indicated by Figure 107. This implies that the highest ram drag is experienced between  $\text{NPR} = 2.0$  and 3.0. The same is true for total drag as the nozzle external drag is nearly constant for a given Mach number. Simultaneously, both primary flow and ideal thrust increase significantly with increasing NPR, resulting in a steeper thrust minus drag coefficient variation with NPR at wind-on conditions. Consequently, the significant decrease in performance observed is primarily due to the increased external and ram drag contributions at wind-on conditions, both of which are zero at static conditions.

There was no effort to separate the various drag terms described above. Knowledge of these drag terms will enable evaluation of the gross thrust performance of the nozzle and further understanding of the performance characteristics. The primary reason for not including these drag terms in the analysis was uncertainty in the estimated secondary flow and the lack of good definition of the flap external pressure distribution. The scale-model flap and sidewall also had significantly thick trailing edges, about 0.25 in (model size). There was insufficient instrumentation to estimate the base drag accurately, and the overall uncertainty associated with the total drag is considered to be significant. Similar characteristics were observed at all test configurations, so most of the subsequent discussions are limited to static and Mach 0.32 data, where possible.

### 5.2.3 Effect of Chute Expansion Ratio (CER)

The primary reason for varying CER, as explained earlier, is to match the static pressure at the suppressor exit, which can in turn reduce losses associated with underexpansion of the primary flow as well as the internal shock noise associated with mismatched static pressure at suppressor exit.  $\text{CER} = 1.22$  corresponds to the suppressor exit static pressure of the same magnitude as free-stream static at the design nozzle pressure ratio of 4.  $\text{CER} = 1.38$  corresponds to the suppressor exit static pressure of 11.0 psia based on 1D ejector code evaluation of the ejector pumping characteristics. The difference between the aeroperformance model and the Cell 41 acoustic model is the primary stream temperatures. The aeroperformance model uses primary air at ambient conditions, while the acoustic model uses high-temperature air. The difference in the gas properties resulted in different CER's: 1.38 for the cold model and 1.43 for the hot model.

The effect of CER on thrust minus drag coefficient and pumping for two of the configurations is shown in Figures 109 through 112. A close look at these data (Figures 109 and 111) indicates that:

1. the lower CER generally performed slightly better than the higher CER,
2. the differences between the two are significant in the NPR range of 2 to 3, and
3. performance is nearly identical for  $\text{NPR} > 4$ .

The difference between the two thrust/drag coefficients at static conditions is nearly 4 to 5 points at  $\text{NPR} = 2.0$ , and the difference is about 1 to 2 points at  $\text{NPR} = 3.0$ . There is also a significant difference in pumping, especially at lower pressure ratios as indicated in Figures 110 and 112. The possible reasons for this difference at lower pressure ratios could be due to losses associated with the overexpansion and recompression of the primary flow in the chutes. Similar losses are observed any convergent/divergent nozzle, and the magnitude of losses depends on the area ratio (CER) and the back pressure. The internal nozzle pressure ratio (pressure ratio experienced by the primary flow as given by the primary flow total pressure and the pressure just downstream of the suppressor chute

exit) is a function of NPR and pumping. For about the same pumping, the static pressure just downstream of the primary nozzle exit should be same. This will imply that the primary nozzle internal pressure ratio should be the same. The area ratios of 1.22 and 1.38 correspond to internal nozzle pressure ratios of 4.0 and 5.3 respectively, and there is always some losses associated with overexpansion until the respective internal pressure ratios are reached.

Losses associated with the overexpansion are higher at low NPR as the internal pressure ratio is significantly lower than the design CER. Consequently, at low overall primary nozzle pressure ratios, the higher losses associated with higher CER produce lower performance. This is confirmed by the plot of the static pressure variation with NPR, at the exit of the suppressor chutes along the primary side of the flow, in Figure 113. The static pressure at the exit of the suppressor chute is constant for all NPR's above 2.0, indicating that the flow was fully expanded inside the suppressor chutes. This static pressure tap was located at the exit of the suppressor chute along the finger/extension on the primary side of the flowpath as shown in Figure 98. The data presented in Figure 113 indicate that the actual expansion ratio at CER = 1.22 was about 3.8 instead of 4.0, and at CER = 1.38 it was about 5.55 instead of 5.3. These differences could be due to variations in the geometry along the primary chute extensions where these static pressure taps are located.

Figure 114 is a plot of throat static pressure as function of NPR for one of the four suppressors, SAR 3.3 and CER 1.22, under typical test conditions. This figure indicates that the flow is choked at all pressure ratios including NPR of = 1.5. Consequently, it can be concluded that there is a shock inside the suppressor chute at NPR = 1.5, and the flow is fully expanded at all other NPR's. Depending on the back pressure downstream of the suppressor chute, additional losses due to overexpanded flow must have been incurred at pressure ratios higher than 2 and less than 4, which explains the performance differences with CER at lower than design pressure ratios.

#### 5.2.4 Effect of Mixing Area Ratio (MAR)

Performance at constant SAR, NPR, and CER as a function of MAR is plotted in Figures 115 and 116 at static conditions. The nozzle performance, or thrust minus drag coefficient, essentially shows a peak at  $MAR \leq 1.0$  for all pressure ratios tested. The pumping characteristics also shows a peak at a MAR of 1.0 for pressure ratios of 2.5 and higher.

The flap static pressure distributions for MAR = 1.0 and 0.8 are shown in Figure 117. This figure indicates that at MAR = 0.8 the ejector remained in the subsonic mode at all NPR's. At MAR = 1.0 the transition from subsonic to supersonic mode occurs at NPR = 2.5. Referring to Figure 103, discussed earlier, the transition from subsonic to supersonic mode occurs at NPR = 2.5 for MAR = 1.2 also, and a similar characteristic was observed for MAR = 1.4. In addition, there seems to be a movement of the shock inside the nozzle: from about midflap at NPR = 2.5, to the nozzle exit at NPR = 3.5. This movement is probably due to the MAR being slightly greater than 1; behavior is thus like an overexpanded supersonic nozzle.

Figure 118 illustrates nozzle performance  $C_{f-D_{noz}}$  as a function of nozzle pressure ratio, and Figure 119 is a plot of the estimated secondary flow characteristics as a function of nozzle pressure ratio for the four MAR's tested. Figure 118 indicates that the thrust performance characteristics are distinctly different. For MAR = 0.8, nozzle performance increases significantly by about 5 points, up to a pressure ratio of about 3.0 from a low of 0.845 at a pressure ratio of 1.5. There is only a small decrease in performance as the pressure ratio is further increased to 4.5. Comparing this to Figure 119, the peak secondary flow for MAR = 0.8 occurs at NPR = 3.0, where the thrust performance also

peaks. For  $MAR = 1.0$  there are two distinct trends in thrust performance, separated by the NPR of 2.5, at which the transition from subsonic to supersonic mode occurs. The characteristics over the pressure ratios of 1.5 to 2.5 has a peak performance of 0.88 at  $NPR = 2.0$ . Performance once again increases significantly from a low of 0.86 at  $NPR = 2.5$  to 0.95 at  $NPR = 4.5$ . The physical secondary flow characteristics given in Figure 119 indicate that the secondary flow peaks at the transition NPR of 2.5 for  $MAR = 1.0$ . The  $MAR$ 's of 1.2 and 1.4 essentially show the same two distinct trends in performance associated with subsonic and supersonic modes of operation as  $MAR = 1.0$ . The minimum thrust performance occurs at  $NPR = 2.0$ , and the peak secondary flow occurs at the same NPR (2.0) for both  $MAR$ 's. The observations based on flap static pressures discussed earlier indicated that the transition NPR is between 2.0 and 2.5. It is possible that the mode switch occurs closer to  $NPR = 2.0$  than 2.5 for these two  $MAR$ 's, and the reason for the minimum in performance and the peak in secondary flow are observed near NPR of 2.0 for  $MAR > 1.0$ . In subsection 5.2.1, it was also observed that the secondary flow wall static pressure near the chute exit was about critical at  $NPR = 2.0$  for  $MAR = 1.2$ . This reinforces the hypothesis that the transition occurs closer to NPR of 2.0. The secondary flow variation with NPR for  $MAR > 1.0$ , given in Figure 119, indicates very little change in the secondary flow between NPR range of 2.0 to 3.0. The primary reason could be the three-dimensional nature of the flowfield.

### 5.2.5 Effect of Suppressor Area Ratio (SAR)

Effects of SAR for the two baseline configurations are shown in Figures 120 through 123. For the same primary throat area ( $A_{p8}$ ), the secondary flow area of  $SAR = 3.3$  is higher by 28% relative to  $SAR = 2.8$ . Consequently, one would expect the pumping to be higher by about 28% for  $SAR = 3.3$  relative to  $SAR = 2.8$ . Figures 121 and 123 indicate that this indeed the case, and the SAR of 3.3 pumps approximately 25% more than the SAR of 2.8 at all NPR's, for both CER's. Static thrust correspondingly shows a significant improvement of about 3 to 4 points with increased SAR at the lower NPR, in the subsonic mode, as indicated by Figures 120 and 122. Also note that the NPR at which the subsonic to supersonic transition occurs seems to have increased with the higher SAR. In the supersonic mode, the lower SAR performs better than the higher SAR by about 1 to 2 points. The slight benefit in observed static performance seems to disappear under wind-on conditions. Figures 120 and 122 indicate the performance of SAR 2.8 is nearly equal to SAR 3.3 at low NPR's (subsonic mode) and better by 2 to 3 points at high NPR's (supersonic mode). For the same throat area, SAR 3.3 has larger external dimensions and hence larger surface area and higher external drag. Ram drag also increases proportional to the pumping. Consequently, under wind-on conditions, any improvement in the gross thrust performance due to the higher pumping associated with higher SAR seems to have been more than offset by the increase in drag associated with the higher SAR.

It is important to note that the principal region of interest could be the subsonic mode of operation, from nozzle dynamic stability considerations, and transition from subsonic to supersonic mode is affected by both the temperature of the primary flow and  $MAR$ . At  $MAR = 1.2$ , the transition occurs at lower NPR relative to  $MAR < 1.0$ . The cold primary flow also results in earlier transition than the hot primary flow conditions as observed in the Cell 41 acoustic tests described in Section 4.

The precise impact of SAR on performance cannot be quantified at all  $MAR$ 's with available data.

### 5.2.6 Effect of Ejector Flap Length

The effects of flap length for both SAR's and CER's are shown in Figures 124 through 131. Thrust minus drag does not show any significant difference, at either static or wind-on test conditions, with

changes in ejector flap length. The differences, especially in the low NPR range, are within the scatter of the test data. A closer look indicates small decrease in static performance of about 1% between NPR range of 3.5 to 4.5 for the SAR = 2.8 cases, as shown in Figures 124 and 126. The exhaust system is operating in the supersonic mode at these NPR's, and one would expect a slight increase in internal wall friction drag associated with the longer flap. In the absence of external flow, the only significant change could be the internal friction as significant differences in the pumping are not evident in Figures 125 and 127. Possible external flowfield effects under wind-on conditions are essentially the flap drag. The friction drag on the short flap due to external flow should be lower than the long flap. In addition, the boattail angle of the short flap is higher than the long flap, and there is a possible increase in the pressure drag. However, the differences, if any, were not significant as the long flap had no significant impact on thrust performance relative to the short flap.

### 5.2.7 Effect of Center Wedges

Figures 132 through 139 compare the effect of center wedges on the performance and pumping characteristics of the SAR 2.8 and 3.3, CER 1.22 configuration at static and 0.32 Mach test conditions. Two wedges were tested: one was a mini wedge designed to block the center gap and eliminate the primary hot streak; the other was as long as the flap. The long wedge provided a significant increase in acoustic treatment area, in addition to eliminating the primary flow hot streak in the center. The wedges essentially reduced the primary throat area ( $A_{p8}$ ) and increased the overall SAR from 2.8 to 3.17 and 3.3 to 3.88. In addition to the SAR variation, the long wedge essentially altered the MAR from 1.2 to 1.0.

These figures indicate pumping increased proportional to the SAR increase at all test conditions and configurations. The performance of the short wedge was significantly lower at almost all of the test conditions: 4 to 6 points relative to the no-wedge configurations. This is somewhat similar to the SAR effect on performance discussed in subsection 5.2.5, where the higher SAR had 3 to 4 points better performance in the subsonic mode at low NPR's and 1 to 2 points lower performance in the supersonic mode at high NPR's, under static conditions. Under wind-on conditions, the higher SAR performed nearly the same at low NPR's and better by 2 to 3 points at high NPR's.

The additional losses due to the presence of the short wedge seem to have amplified the differences even further, and one can conclude that these losses are very significant. The long wedge, on the other hand, seems to have overcome added losses due to the wedge as well as losses from the higher drag penalty associated with higher SAR. The long wedge, with associated reduction in MAR, has significantly improved performance at all test conditions relative to the no-wedge configuration. The most significant effect seems to be in the region of transition NPR's; the thrust minus drag coefficient is nearly flat over the NPR range of 1.5 to 3.0 for the MAR of 1.0, while the MAR of 1.2 in the same NPR range has a significant valley. The performance is nearly the same at NPR of 1.5 and 3.0 for both cases, and the difference is nearly 6 to 7 points in favor of the lower MAR associated with the long wedge. This is similar to the MAR effect on performance discussed earlier. However, the effect of reduced MAR by the presence of the long wedge on the performance is not as large as the MAR effect without the wedge indicated in Figures 140 and 141.

As discussed in subsection 4.2.7, higher jet noise reductions were obtained by varying MAR rather than by use of the long treated wedge, which leads to increased weight and complexity.

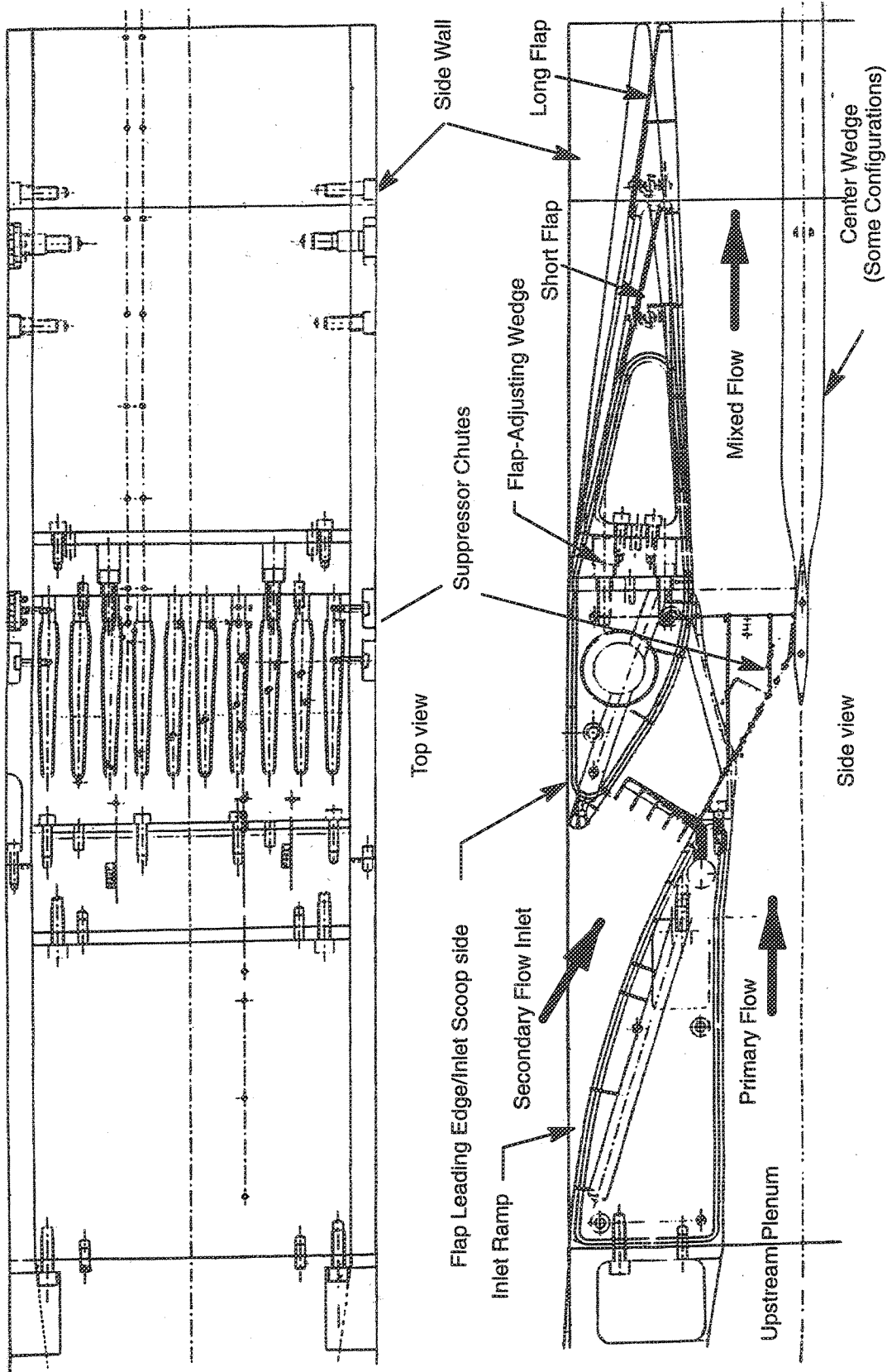
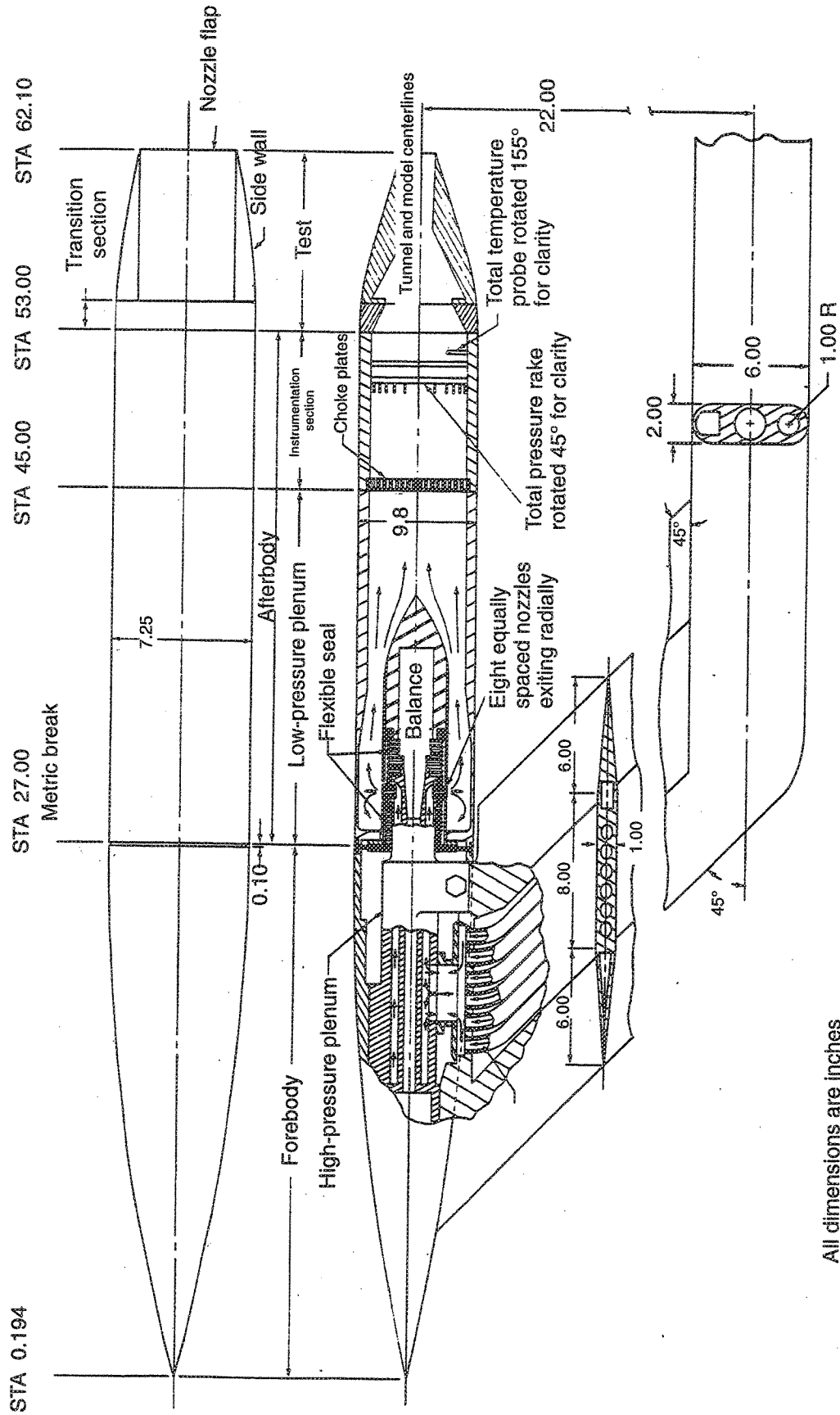


Figure 90. Scale model of 2DME nozzle



All dimensions are inches

Figure 91. Sketch of nonaxisymmetric, single-engine propulsion simulator

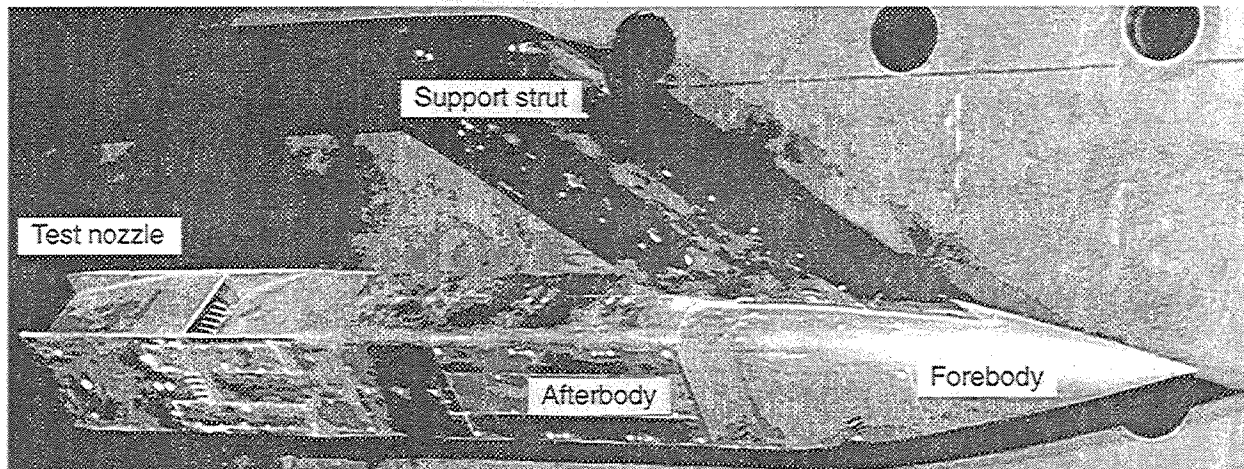


Figure 92. View of the 2DME nozzle scale-model installation

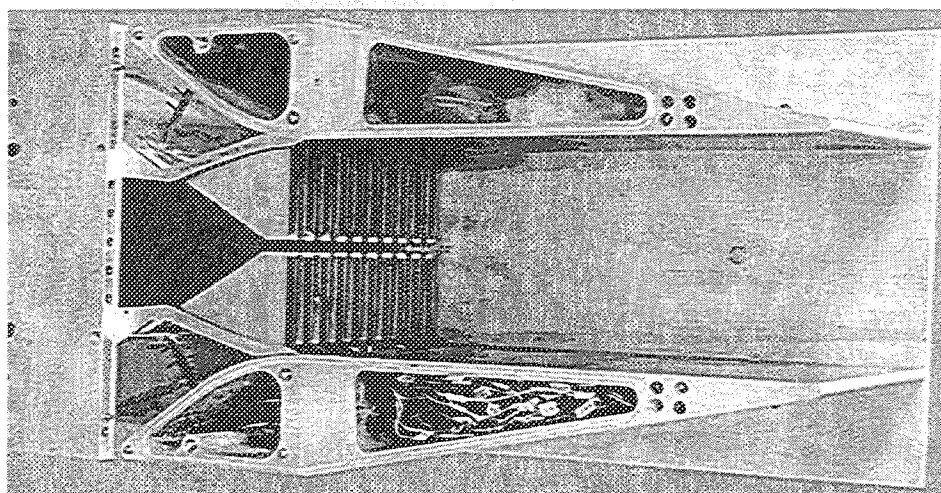


Figure 93. View of 2DME scale-model with long flap, MAR = 1.0 (sidewall removed)

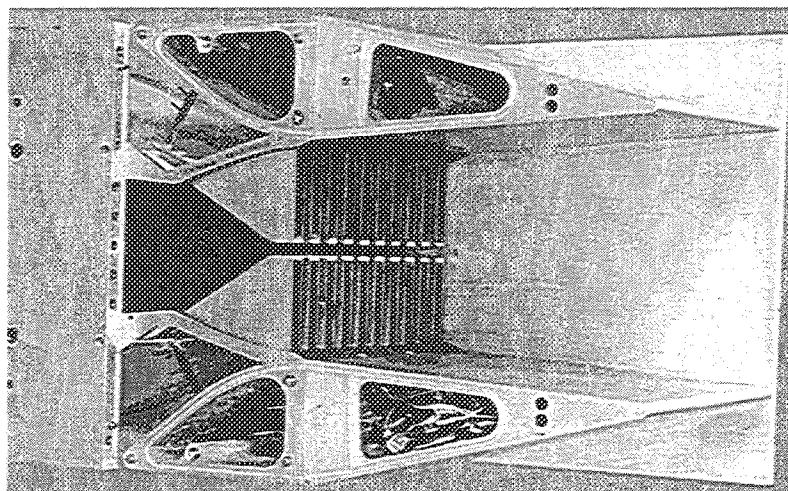


Figure 94. View of 2DME scale-model with short flap, MAR = 1.2 (sidewall removed)

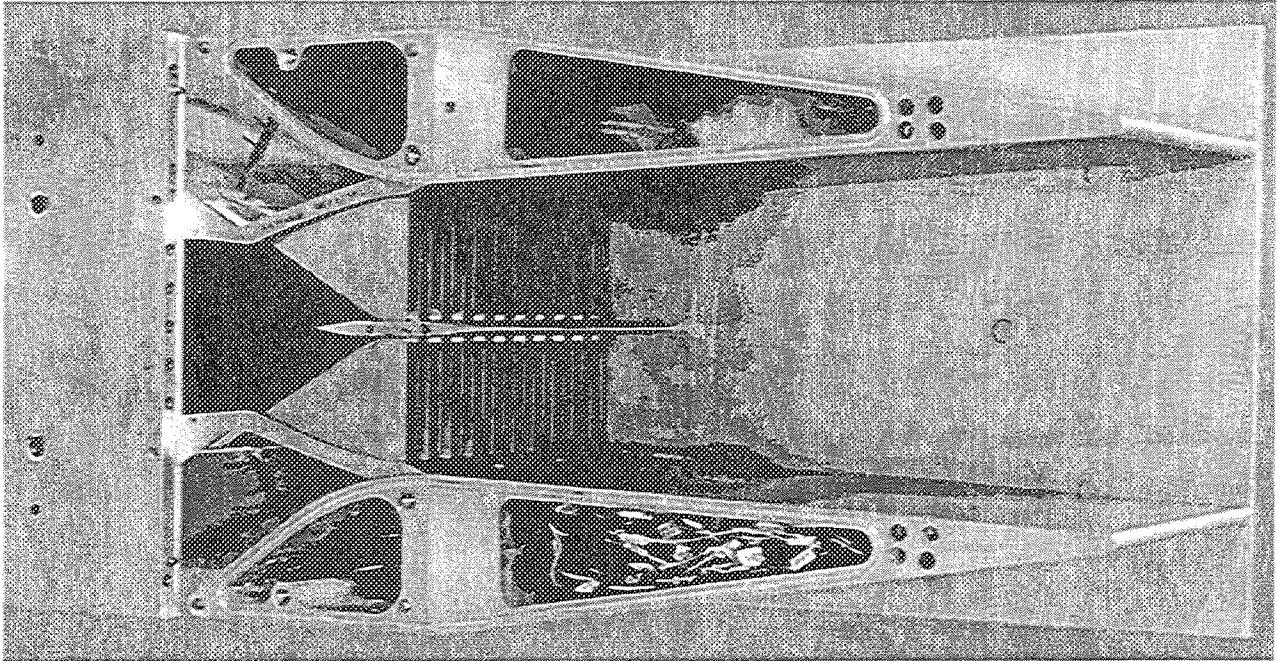


Figure 95. Typical mini center wedge configuration

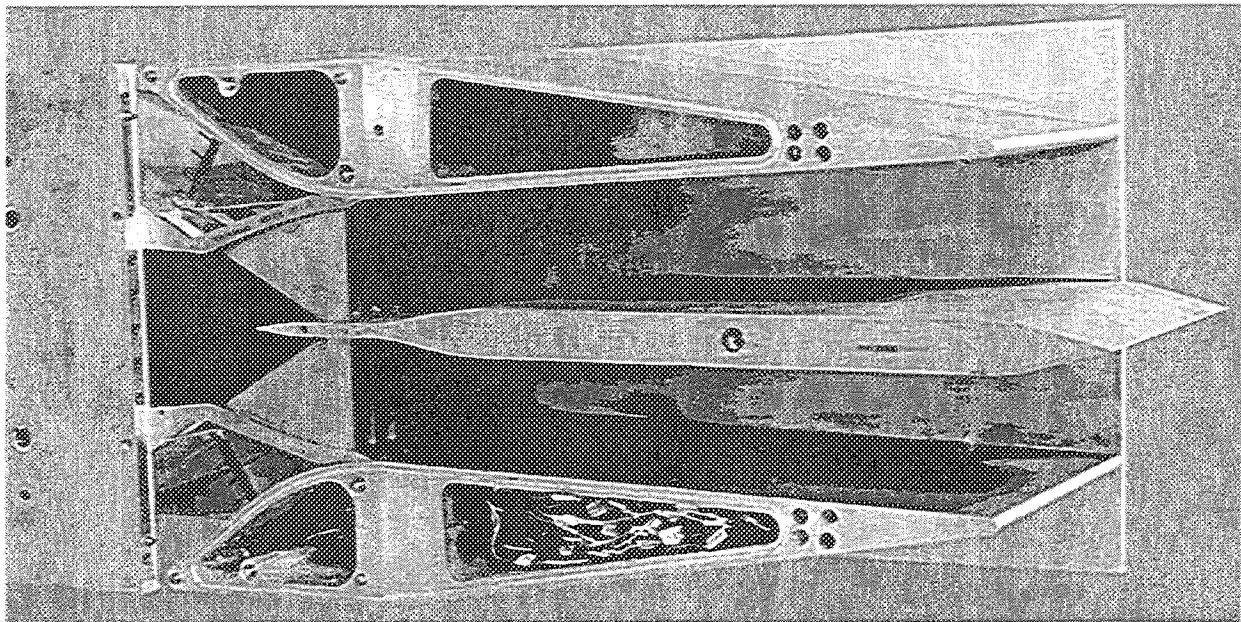


Figure 96. Typical long center wedge configuration

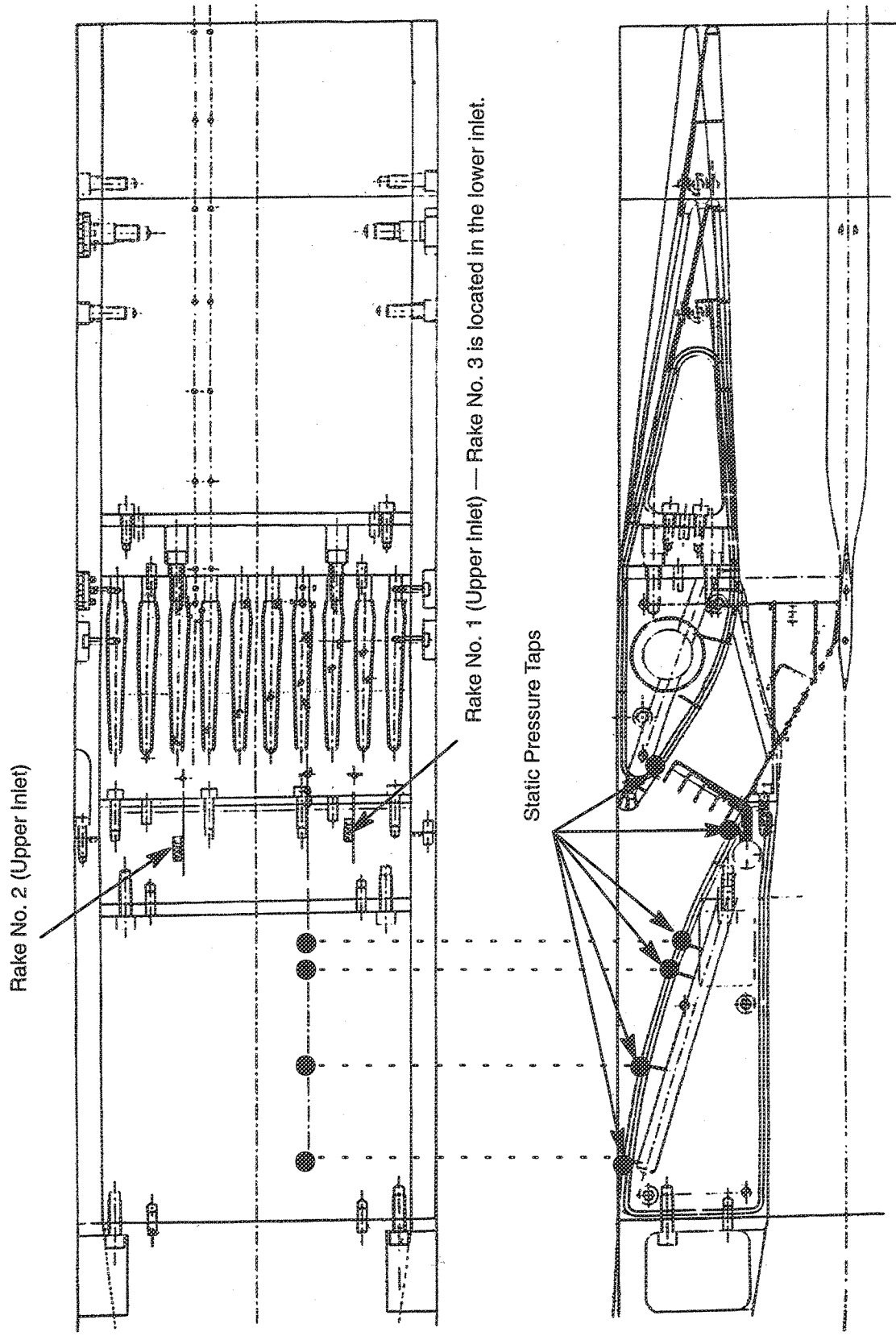
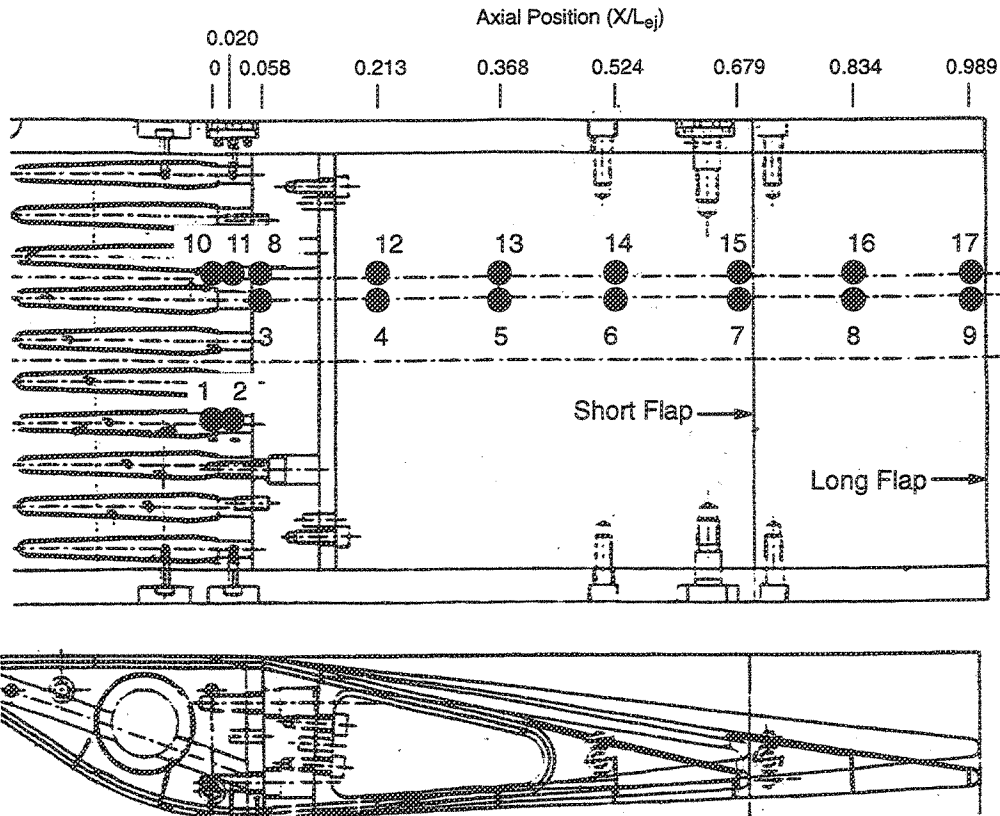
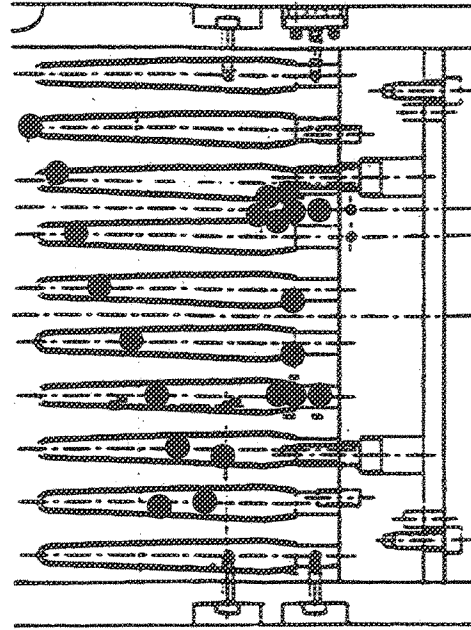


Figure 97. Instrumentation: scale-model 2DME exhaust system secondary flow inlet

Figure 98. Suppressor chute static pressure instrumentation



Static pressure taps arranged in two rows: taps 1–9 aligned with primary chute and 10–17 aligned with secondary. Taps 1 and 2 are located in the mixer; 10 and 11 are located in the adjusting wedge.

Figure 99. Flap static pressure instrumentation

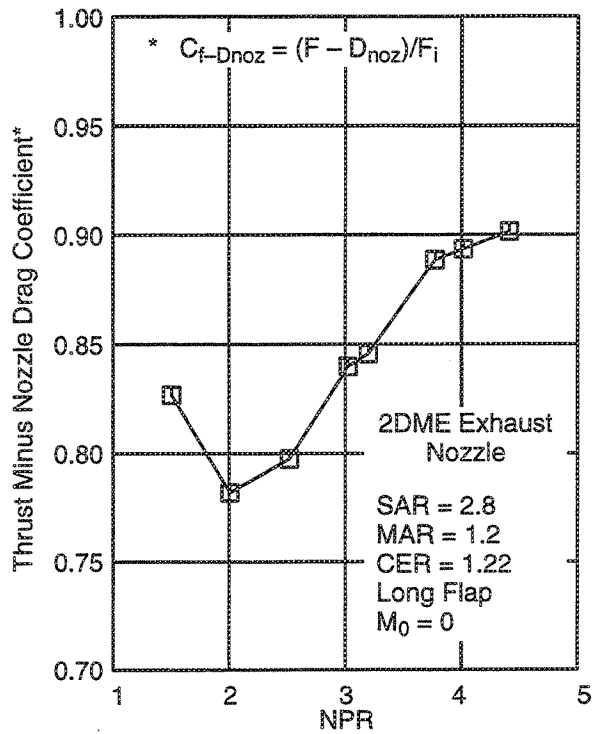


Figure 100. Static thrust performance

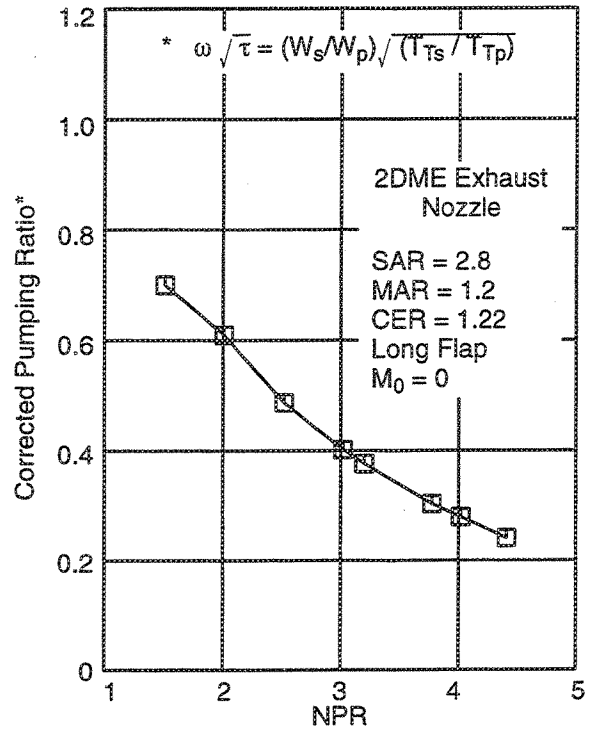


Figure 101. Static pumping characteristics

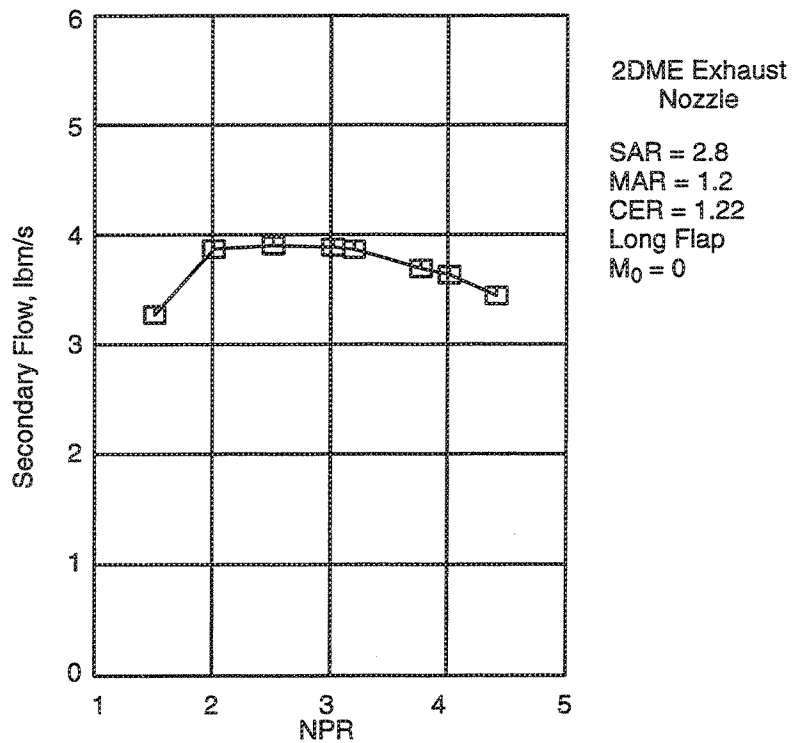


Figure 102. Static secondary flow variation

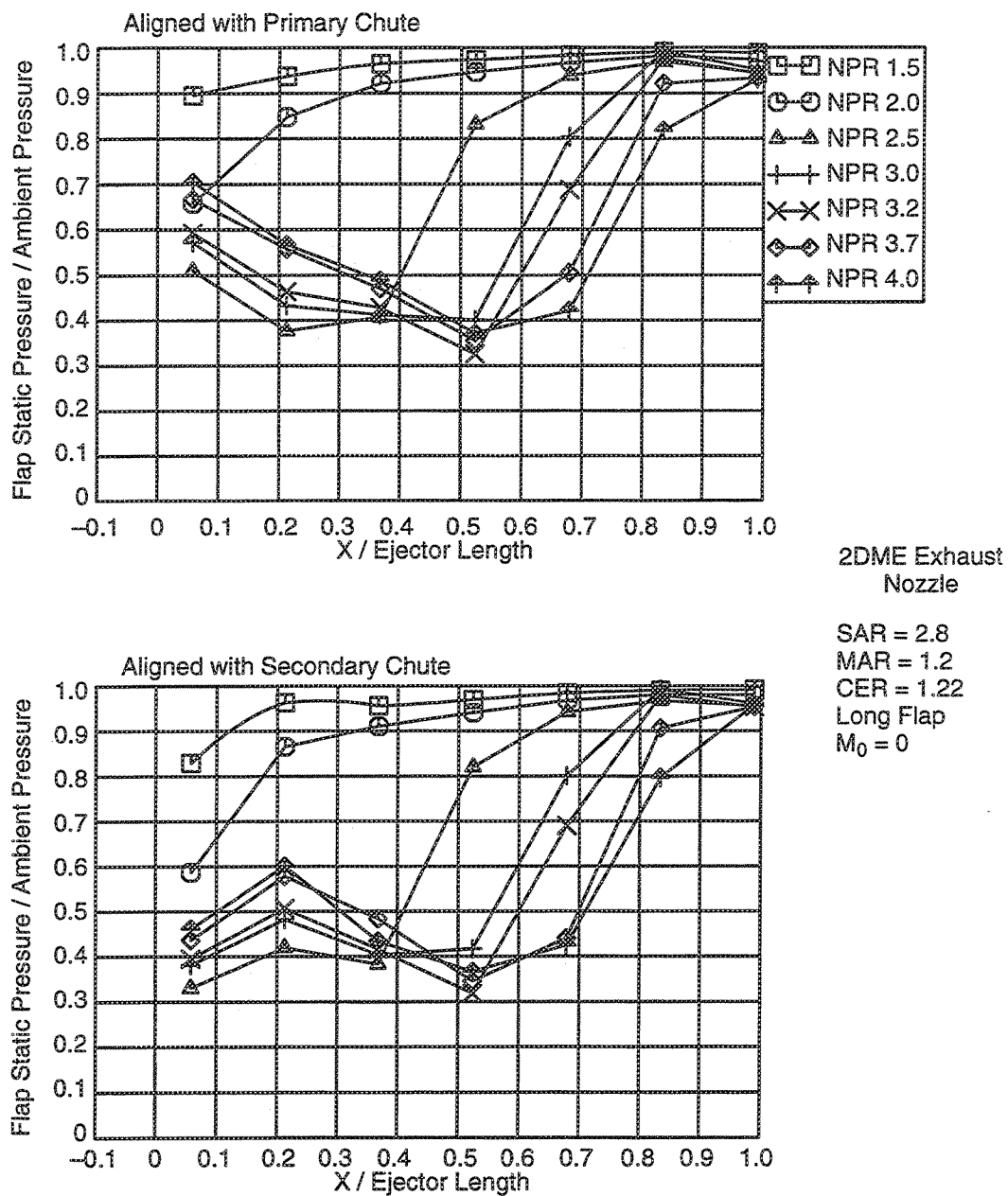


Figure 103. Flap static pressure distribution at various NPR's

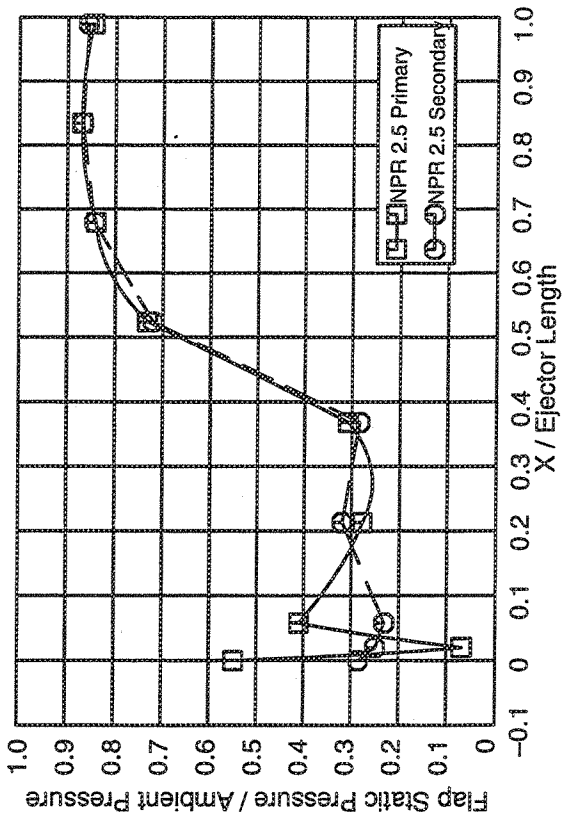
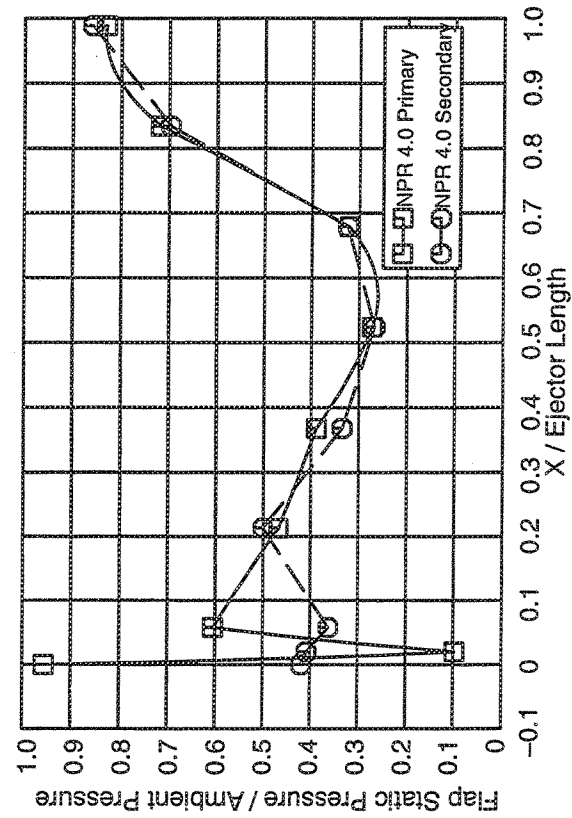
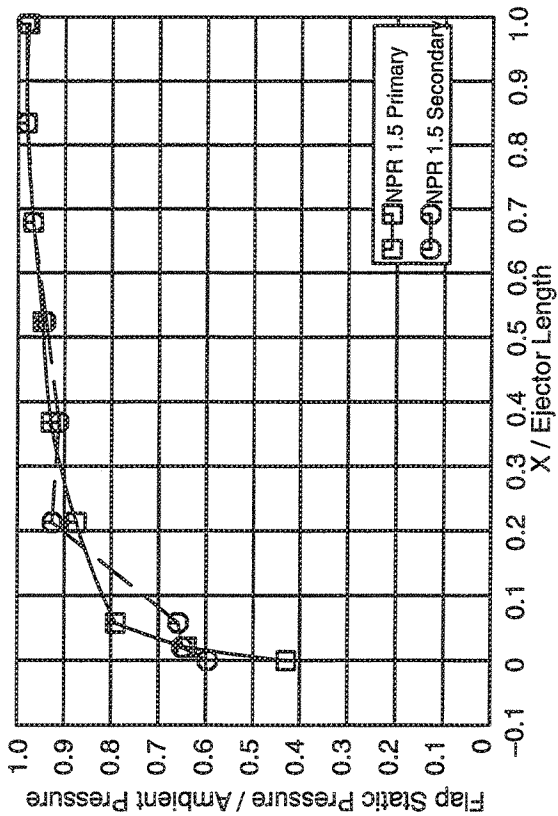
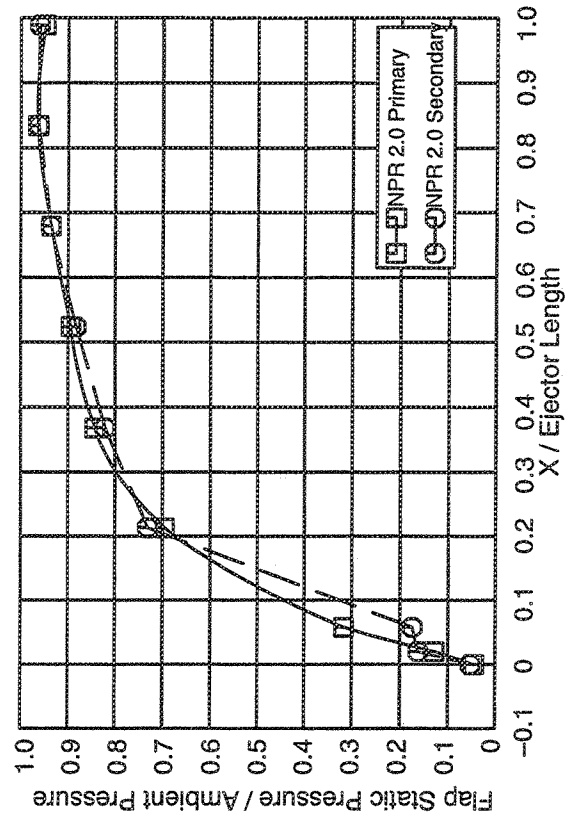


Figure 106. Comparison of primary and secondary aligned flap static pressures at various MPR's

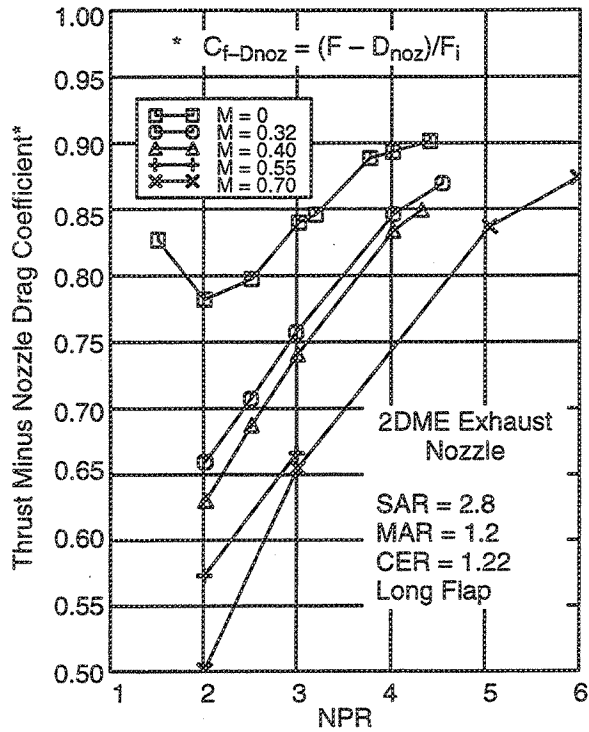


Figure 105. Effect of free stream on thrust performance

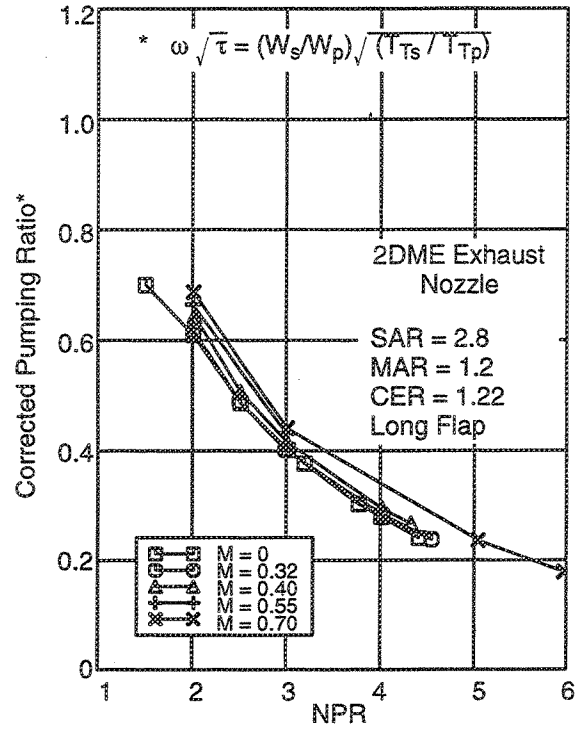


Figure 106. Effect of free stream on pumping characteristics

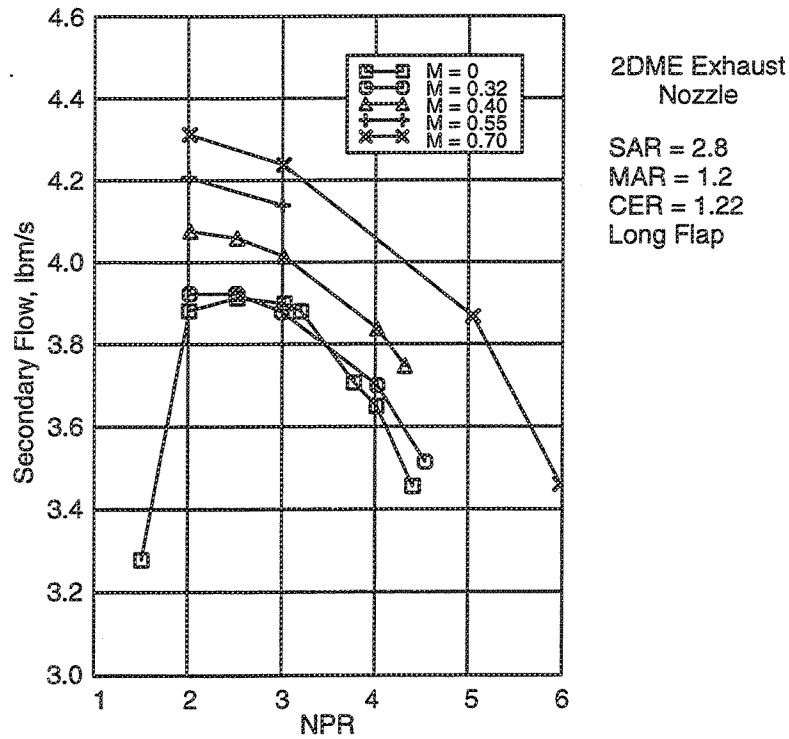


Figure 107. Effect of free stream on physical entrainment

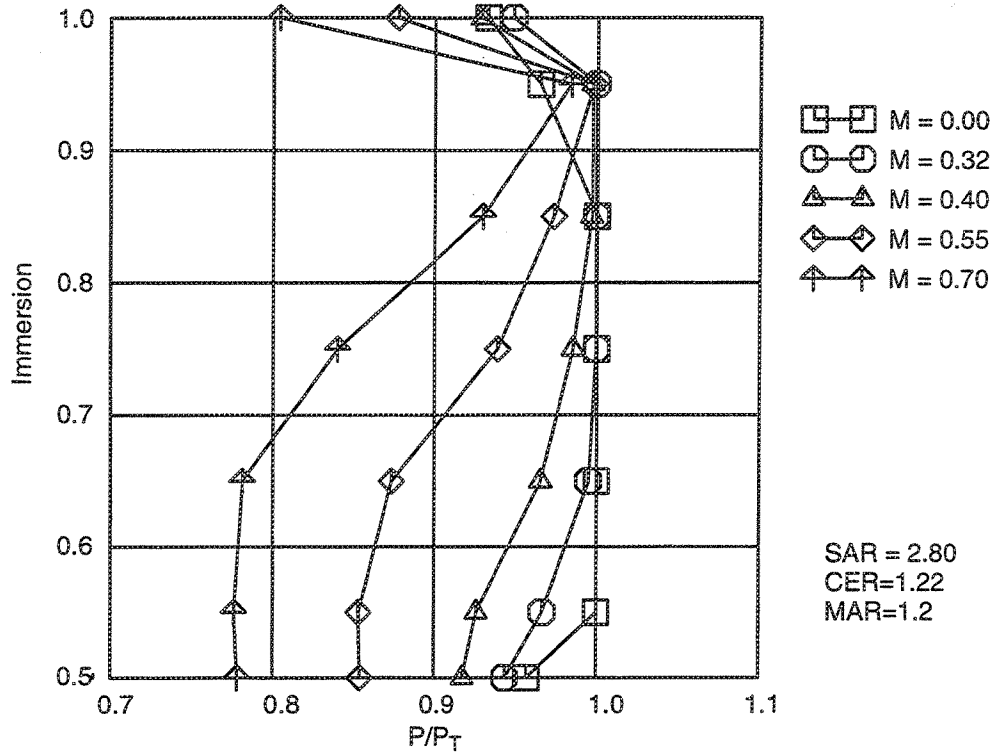


Figure 108. Ejector inlet rake pressure profiles

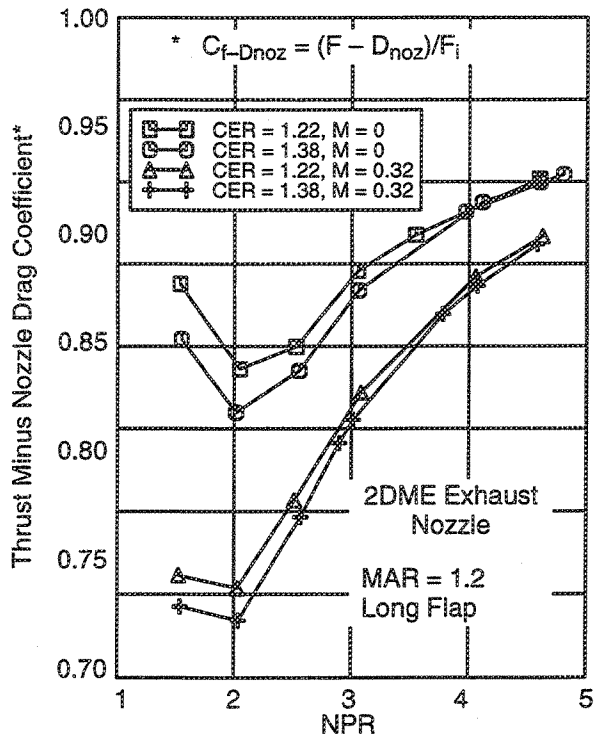


Figure 109. Effect of CER on thrust: SAR = 2.8

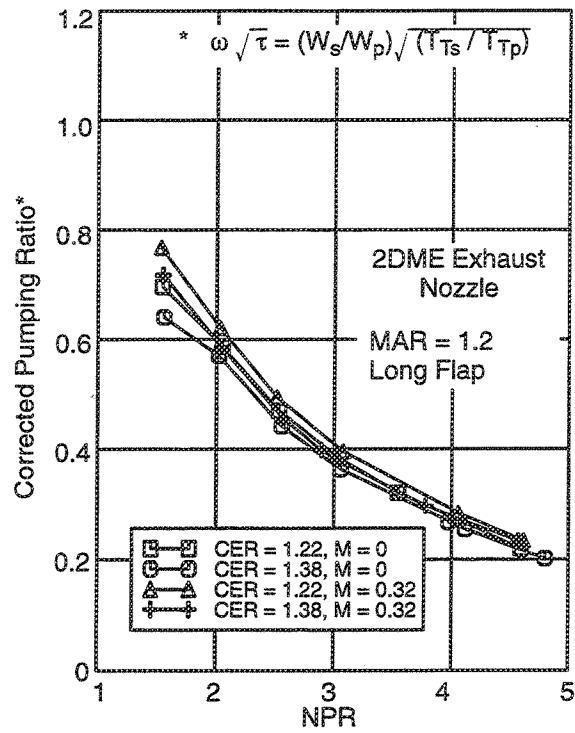


Figure 110. Effect of CER on pumping: SAR = 2.8

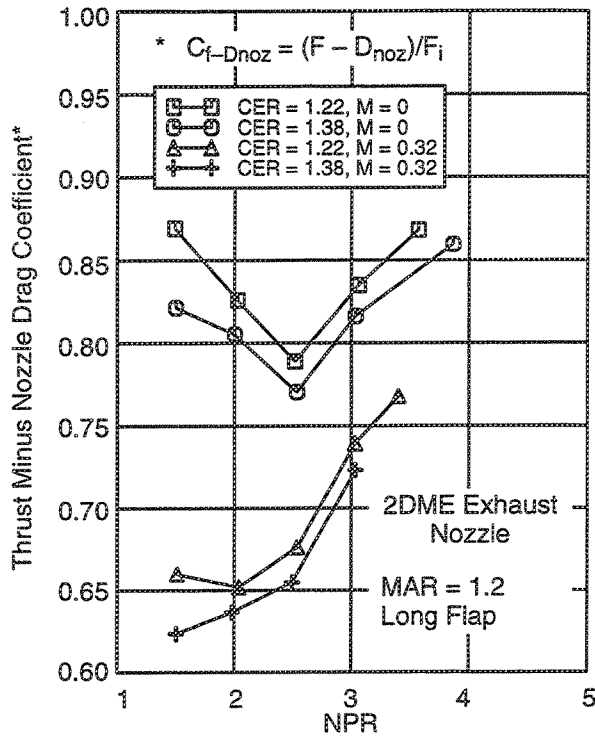


Figure 111. Effect of CER on thrust: SAR = 3.3

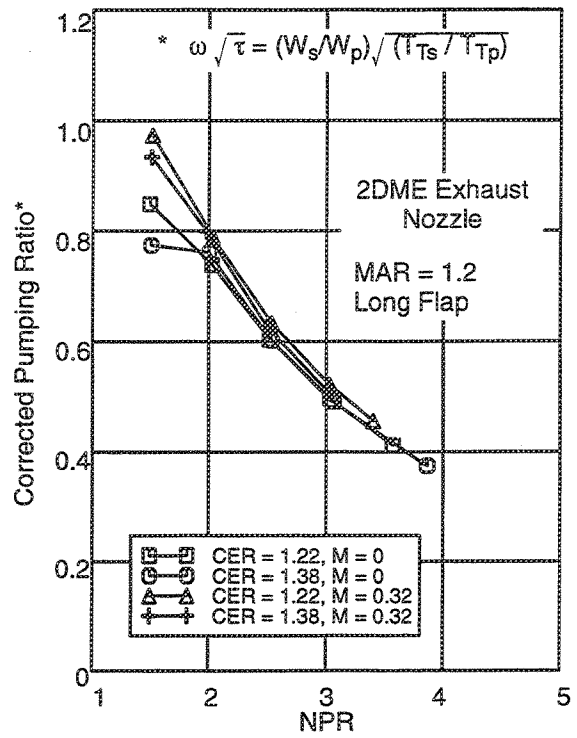


Figure 112. Effect of CER on pumping: SAR = 3.3

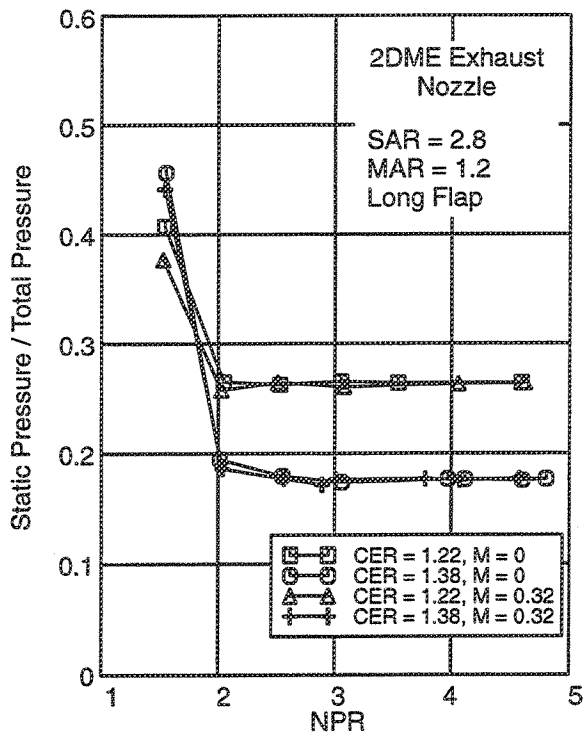


Figure 113. Primary chute trailing-edge static pressure

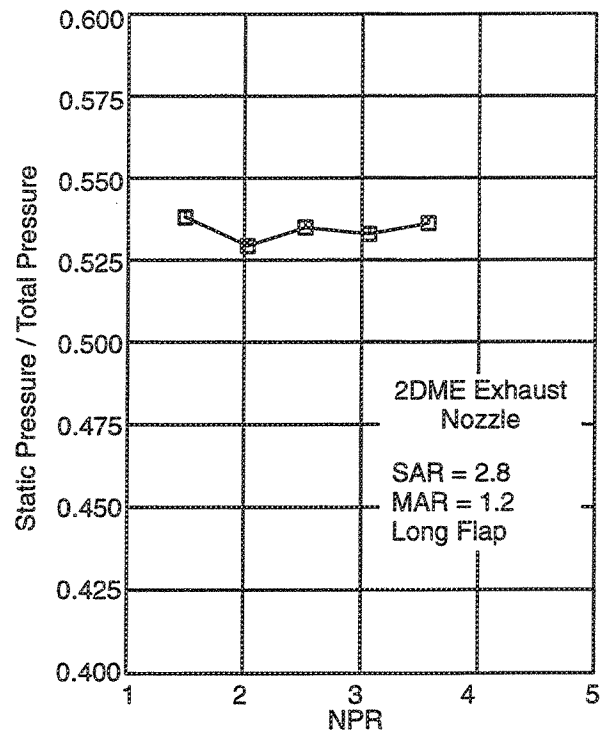
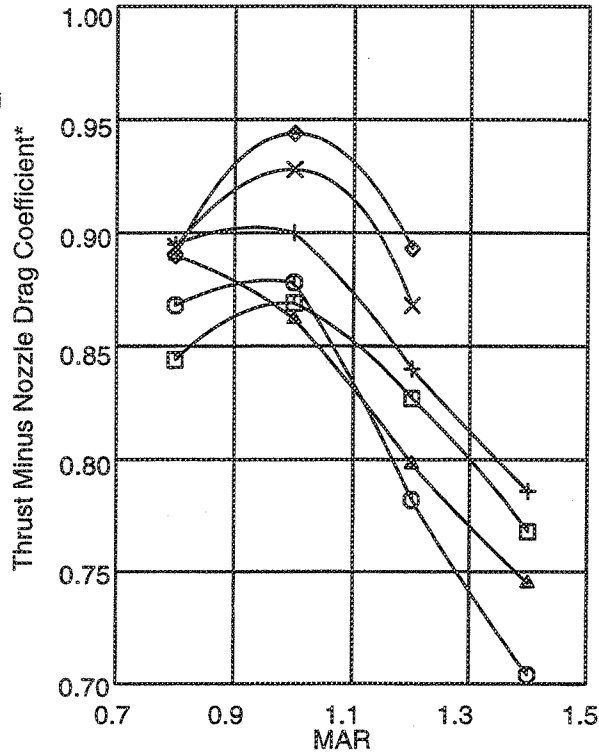


Figure 114. Primary throat static pressure: CER = 1.22

$$* C_{f-Dnoz} = (F - D_{noz})/F_i$$



2DME Exhaust  
Nozzle

CER = 1.22  
SAR = 2.8

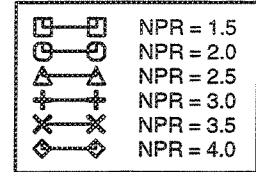
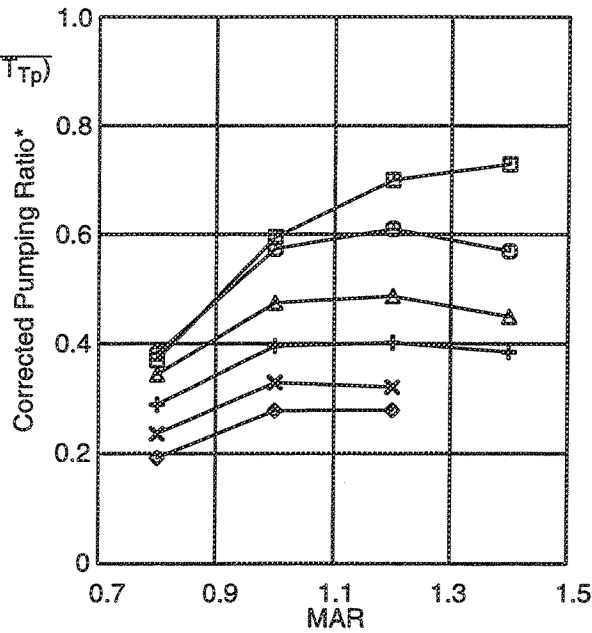


Figure 115. Effect of MAR on static thrust

$$* \omega \sqrt{\tau} = (W_s/W_p) \sqrt{(T_{Ts}/T_{Tp})}$$



2DME Exhaust  
Nozzle

CER = 1.22  
SAR = 2.8

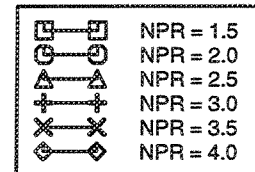


Figure 116. Effect of MAR on static pumping characteristics

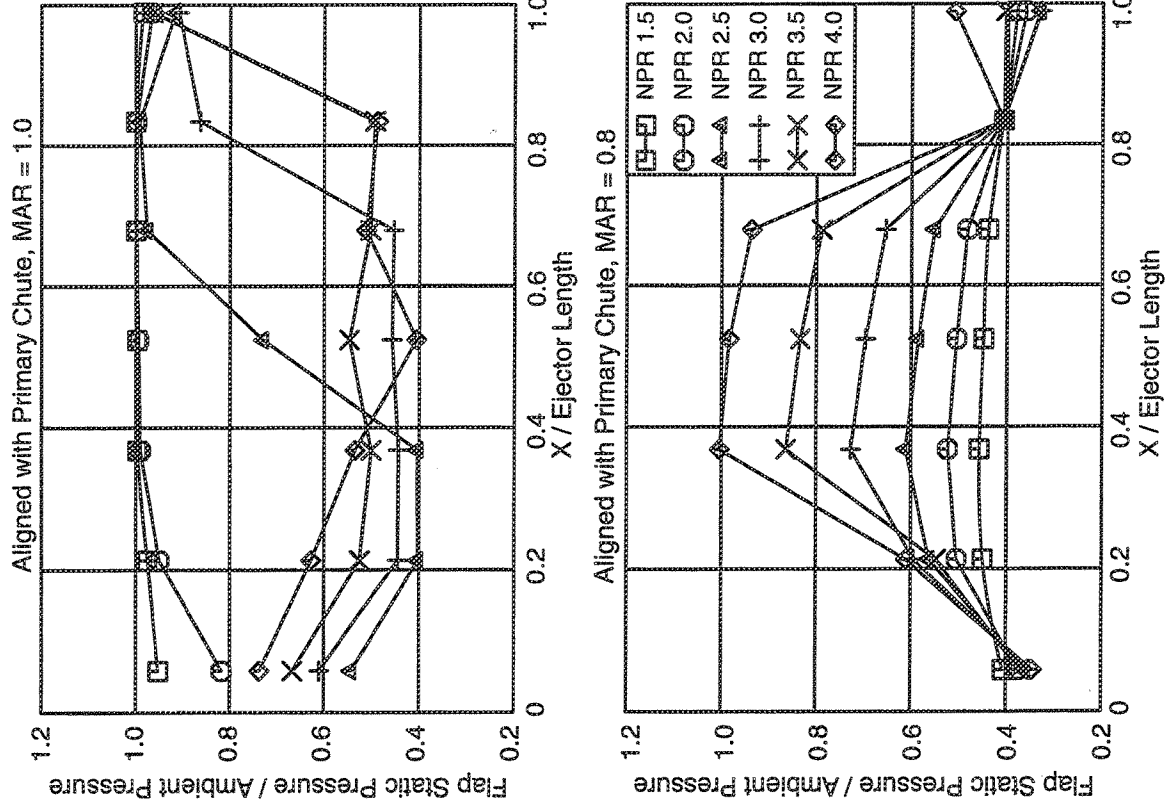
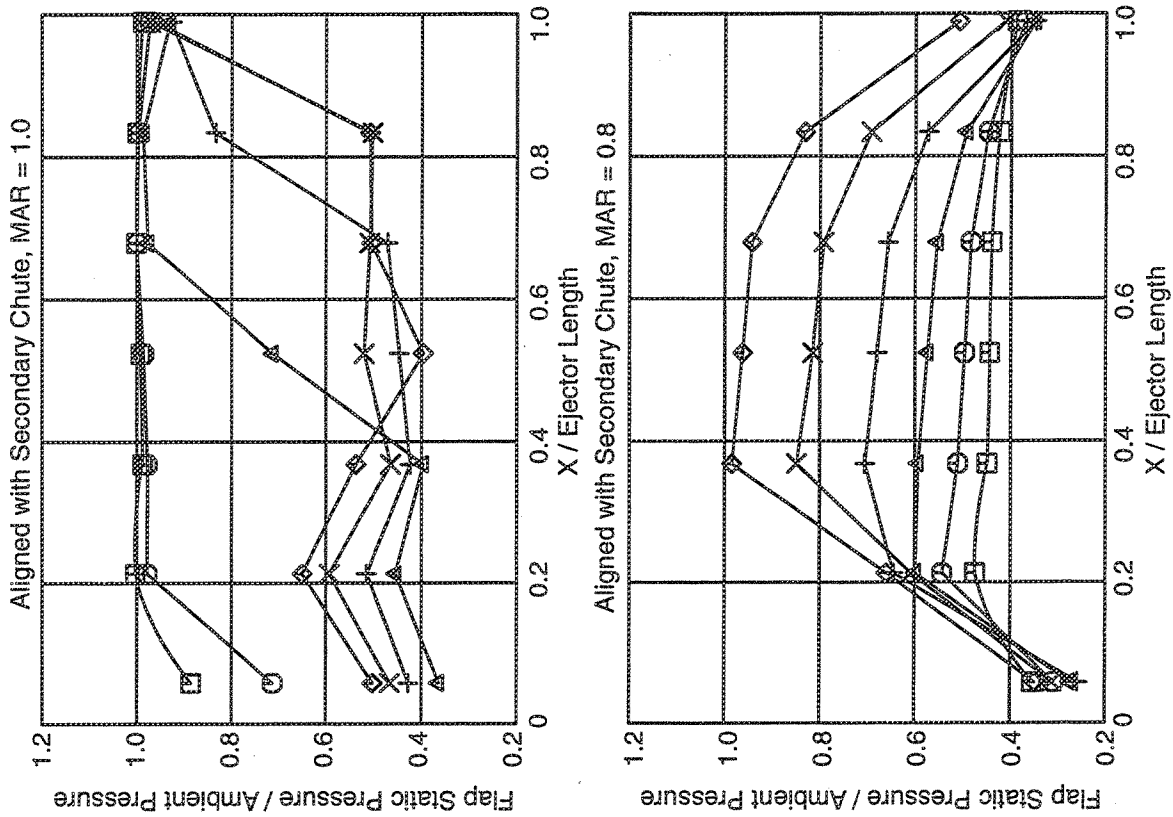


Figure 117. Flap static pressure distributions at MAR 1.0 and 0.8

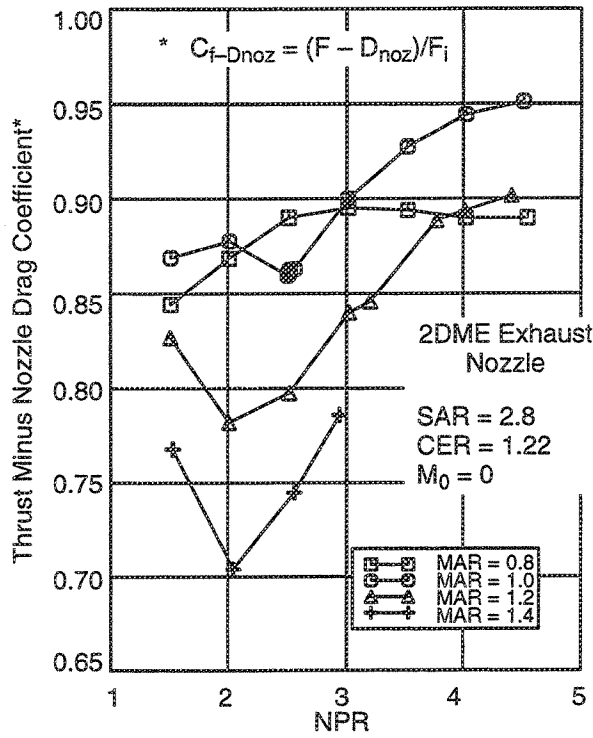


Figure 118. Static thrust performance at various MAR's

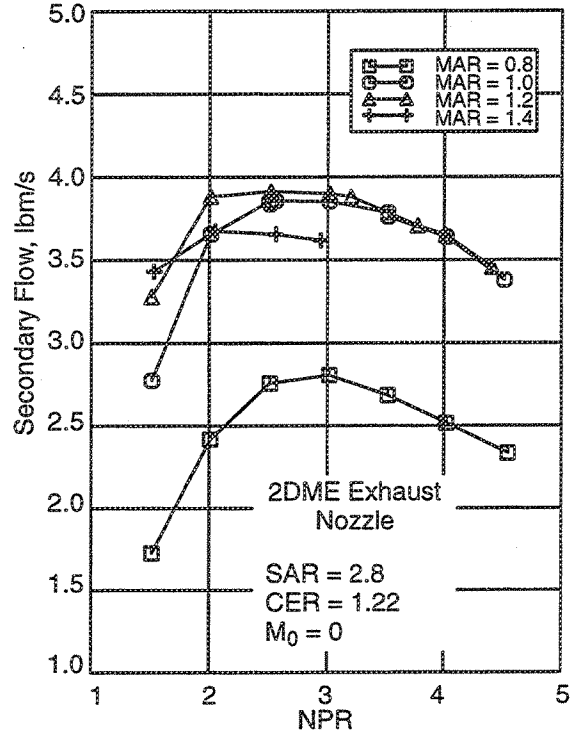


Figure 119. Physical secondary flow at various MAR's

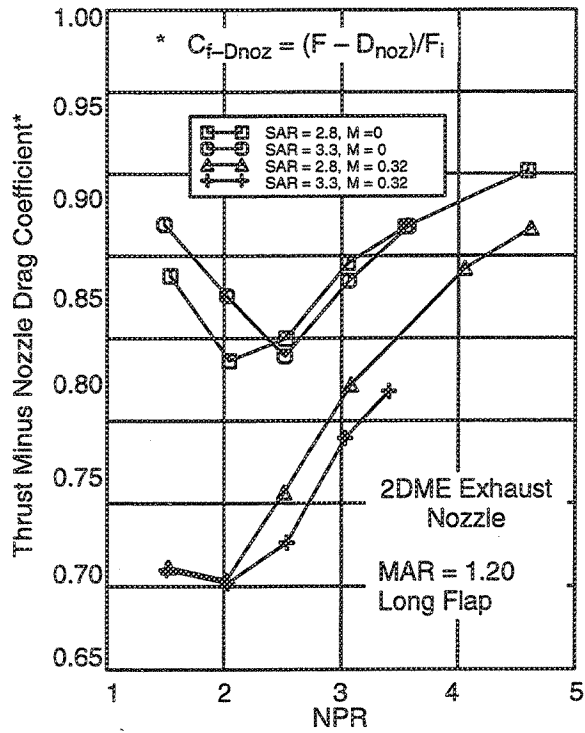


Figure 120. Effect of SAR on thrust: CER = 1.22

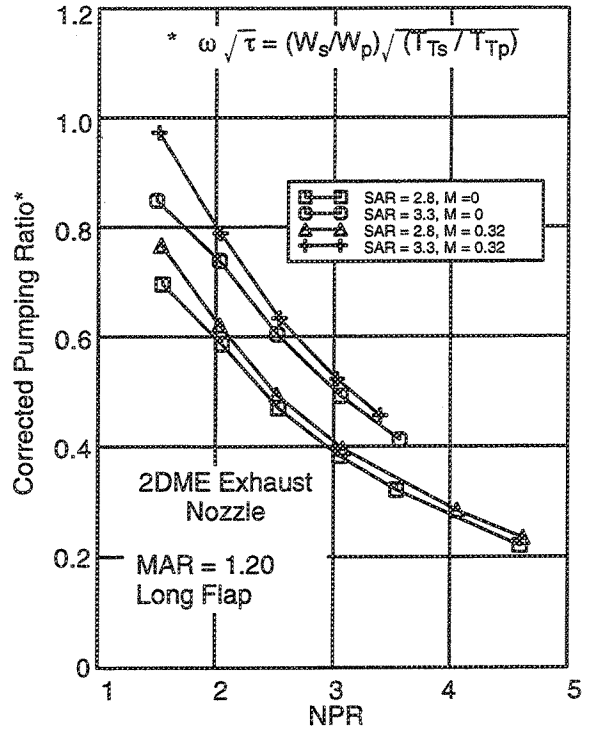


Figure 121. Effect of SAR on pumping: CER = 1.22

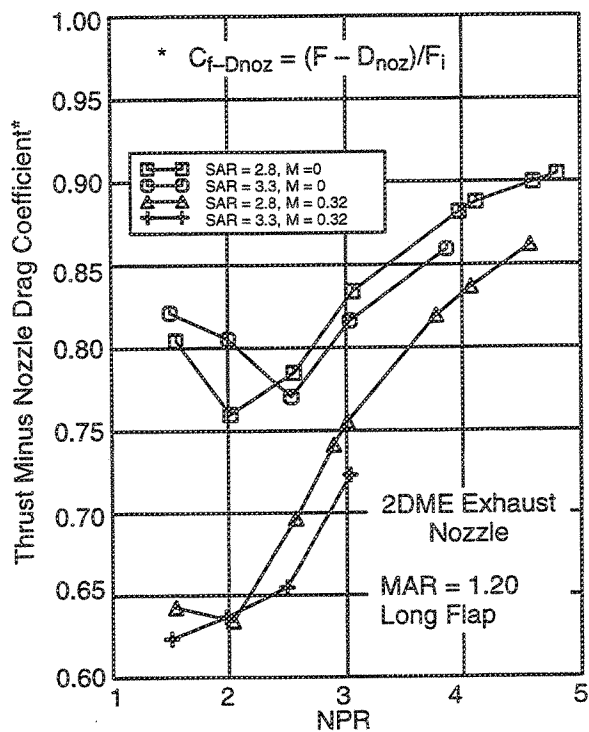


Figure 122. Effect of SAR on thrust:  
CER = 1.38

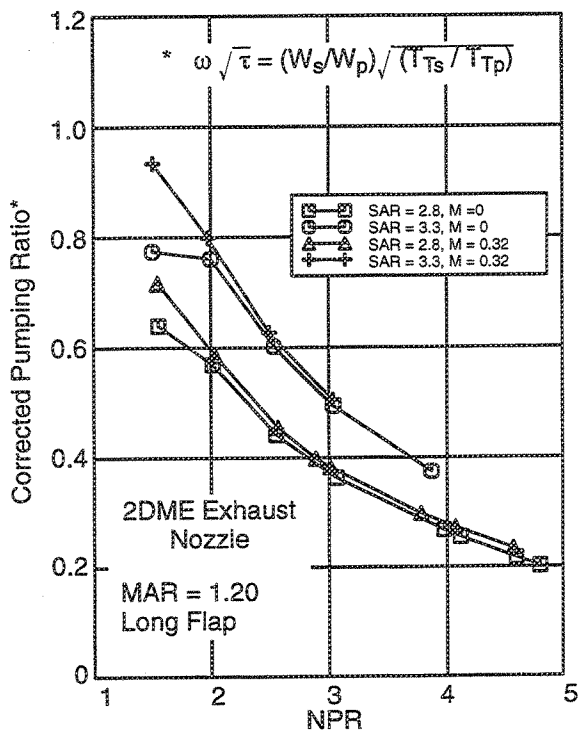


Figure 123. Effect of SAR on pumping:  
CER = 1.38

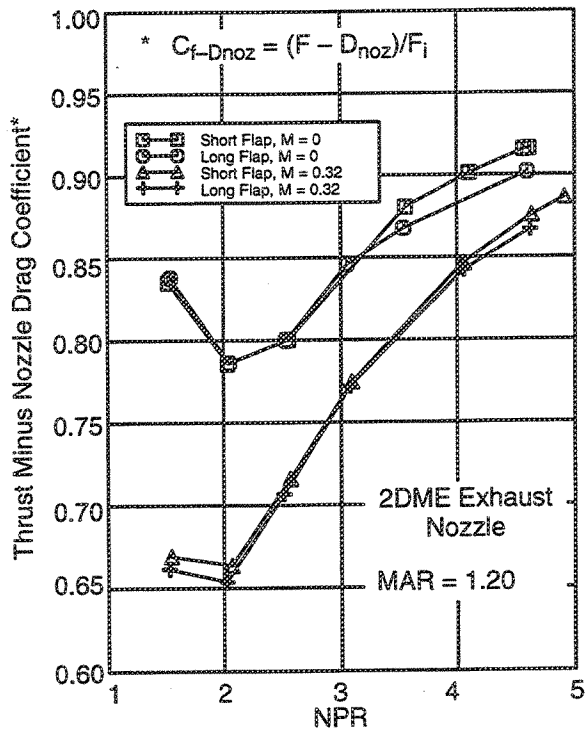


Figure 124. Effect of flap length on thrust:  
SAR = 2.8, CER = 1.22

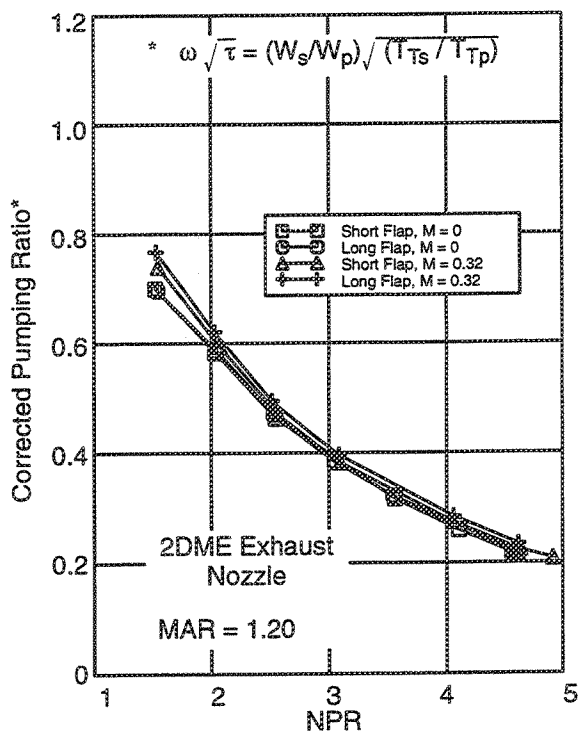


Figure 125. Effect of flap length on pumping:  
SAR = 2.8, CER = 1.22

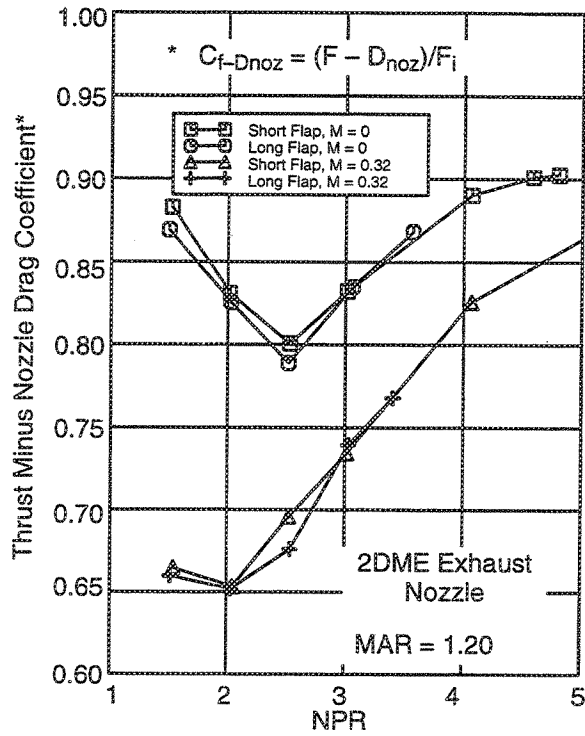


Figure 126. Effect of flap length on thrust:  
SAR = 3.3, CER = 1.22

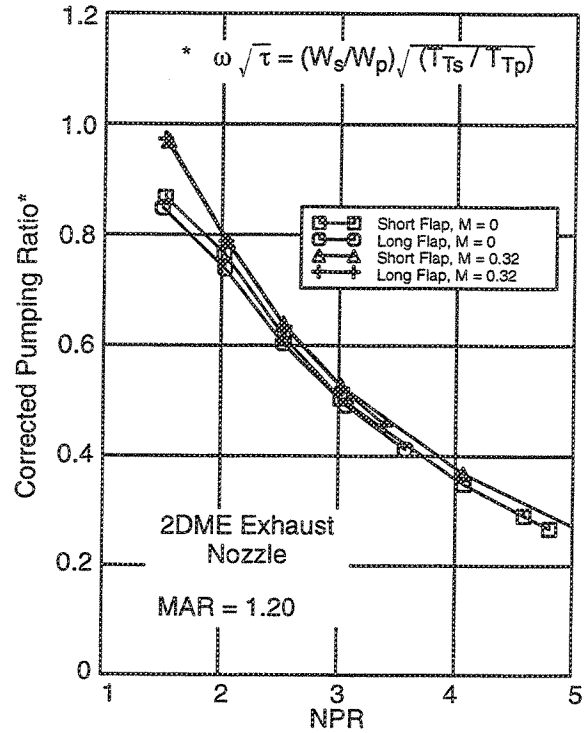


Figure 127. Effect of flap length on pumping:  
SAR = 3.3, CER = 1.22

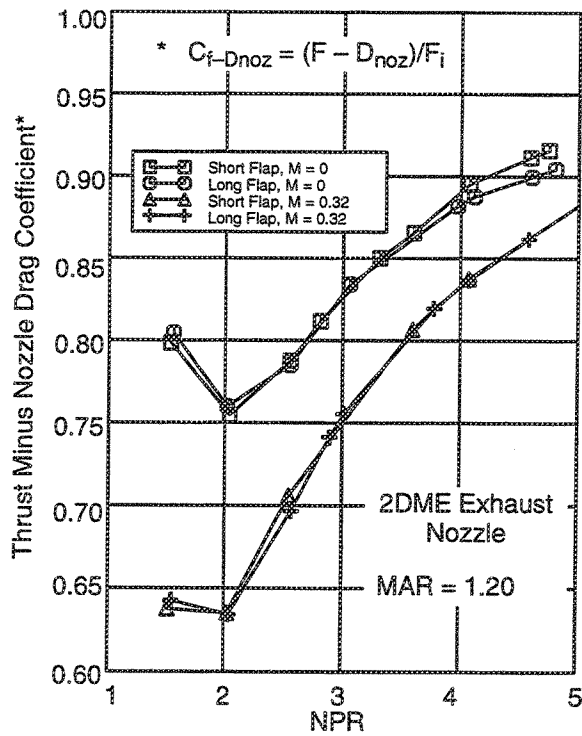


Figure 128. Effect of flap length on thrust:  
SAR = 2.8, CER = 1.38

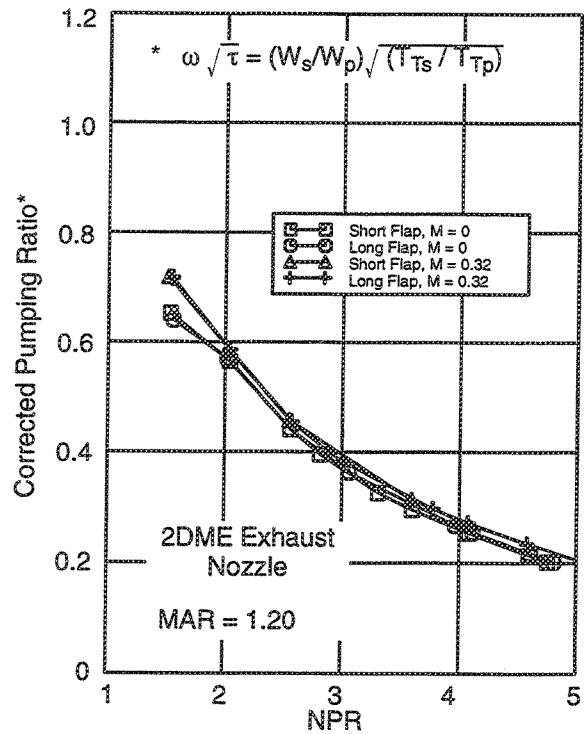


Figure 129. Effect of flap length on pumping:  
SAR = 2.8, CER = 1.38

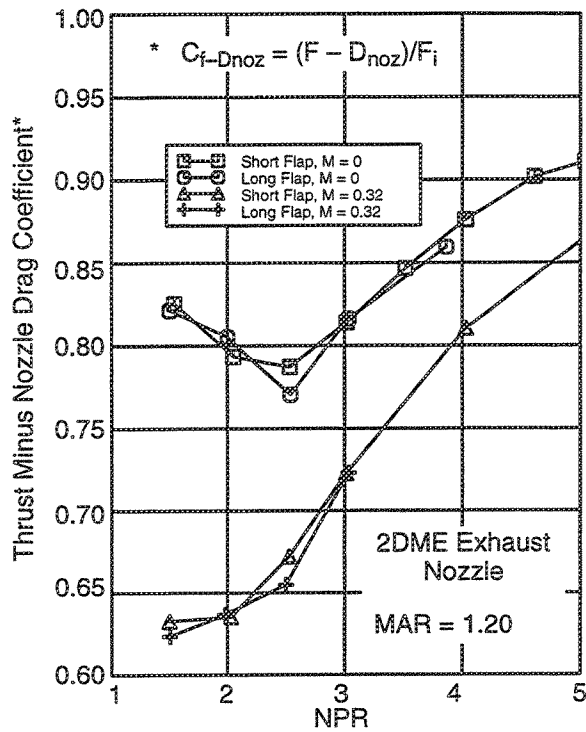


Figure 130. Effect of flap length on thrust: SAR = 3.3, CER = 1.38

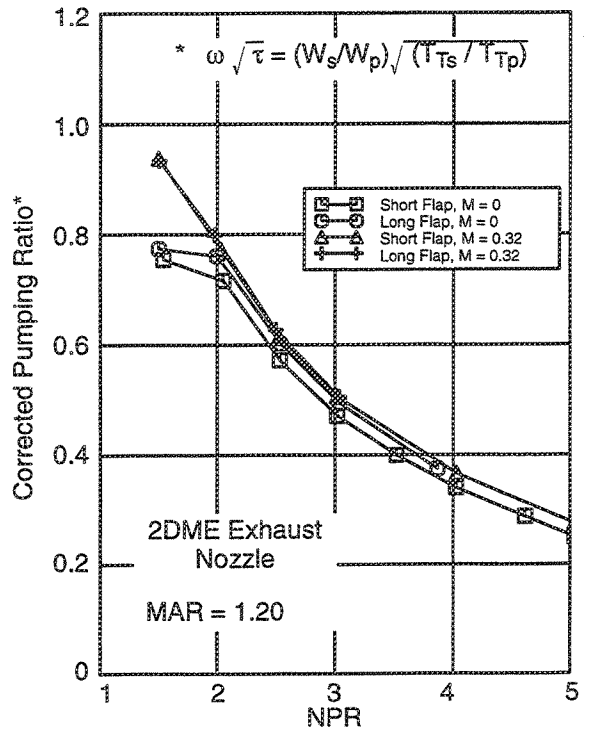


Figure 131. Effect of flap length on pumping: SAR = 3.3, CER = 1.38

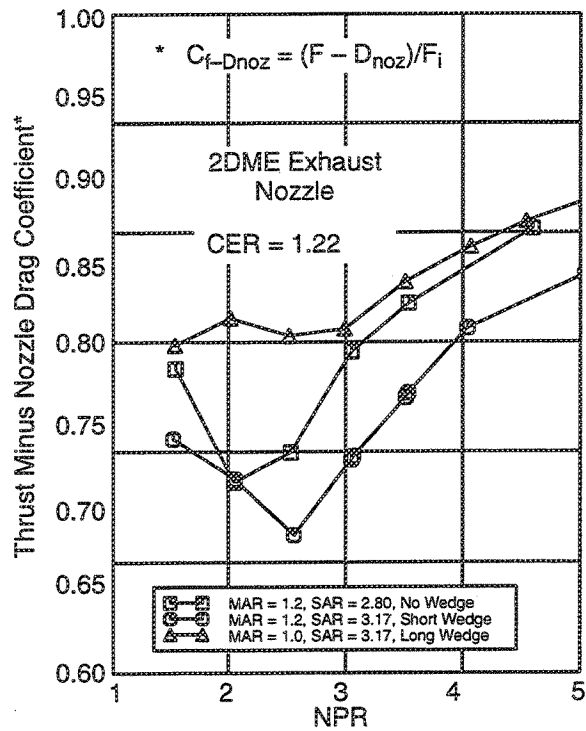


Figure 132. Effect of wedge on thrust: M = 0, SAR = 2.80 and 3.17

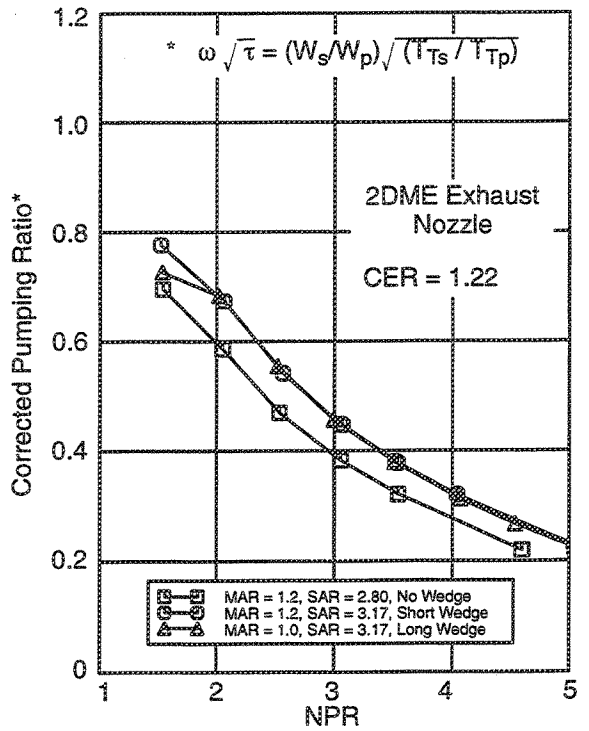


Figure 133. Effect of wedge on pumping: M = 0, SAR = 2.80 and 3.17

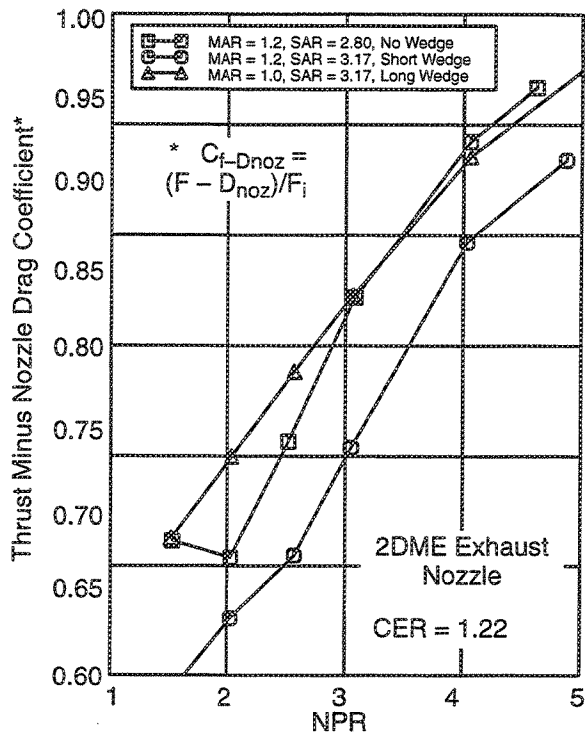


Figure 134. Effect of wedge on thrust:  $M = 0.32$ , SAR = 2.80 and 3.17

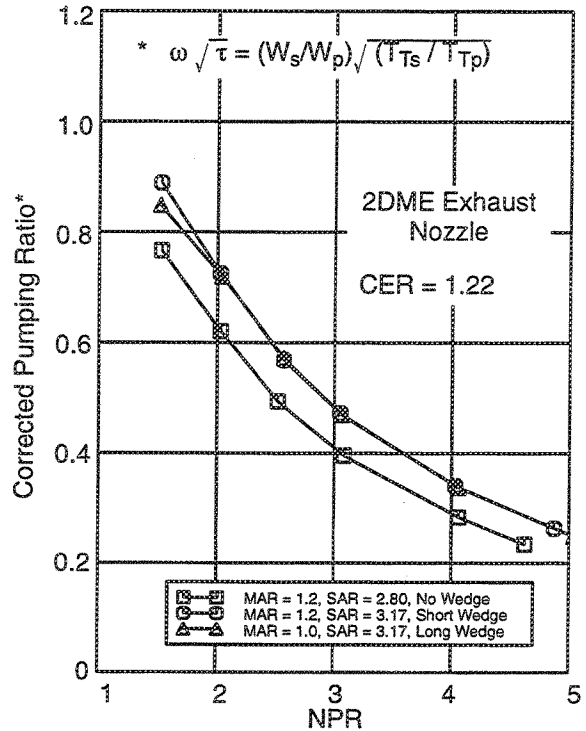


Figure 135. Effect of wedge on pumping:  $M = 0.32$ , SAR = 2.80 and 3.17

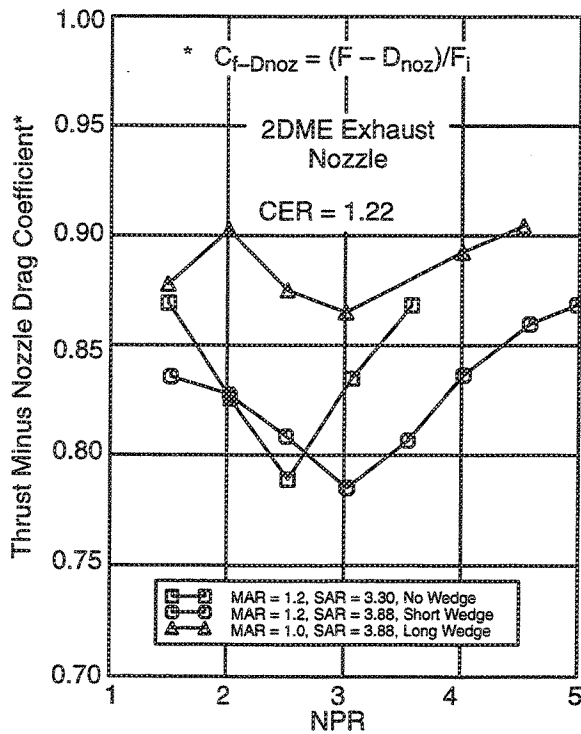


Figure 136. Effect of wedge on thrust:  $M = 0$ , SAR = 3.30 and 3.88

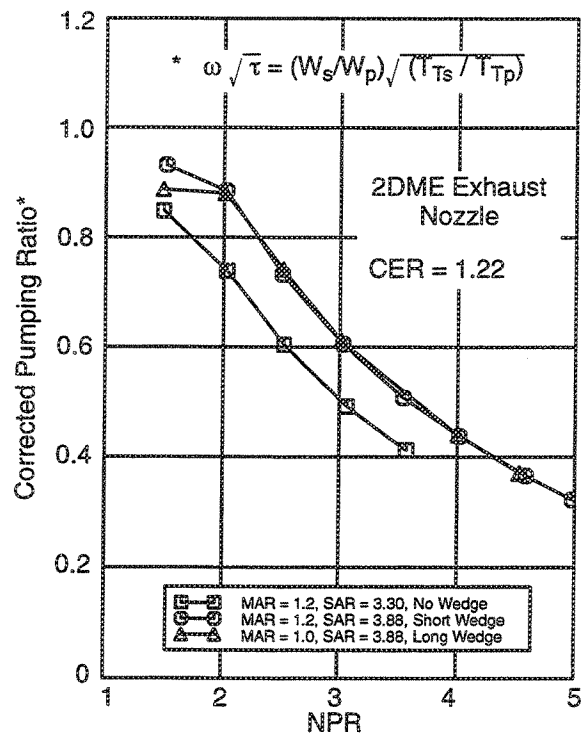


Figure 137. Effect of wedge on pumping:  $M = 0$ , SAR = 3.30 and 3.88

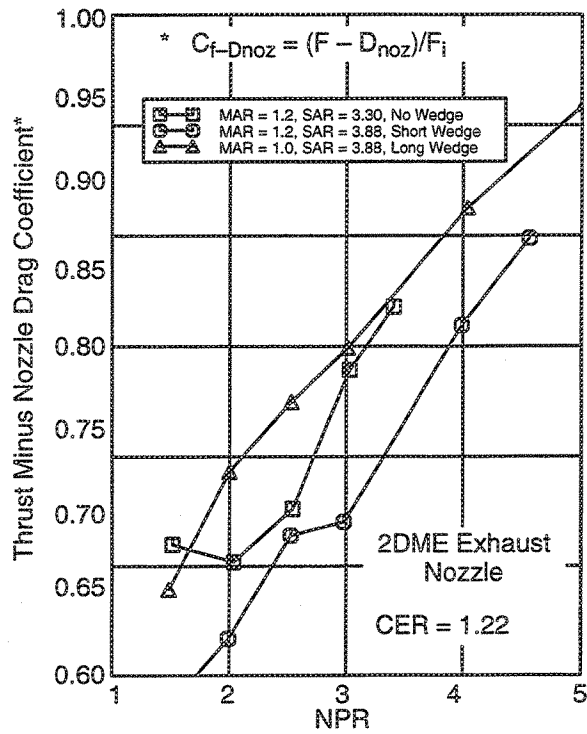


Figure 138. Effect of wedge on thrust:  
M = 0.32, SAR = 3.30 and 3.88

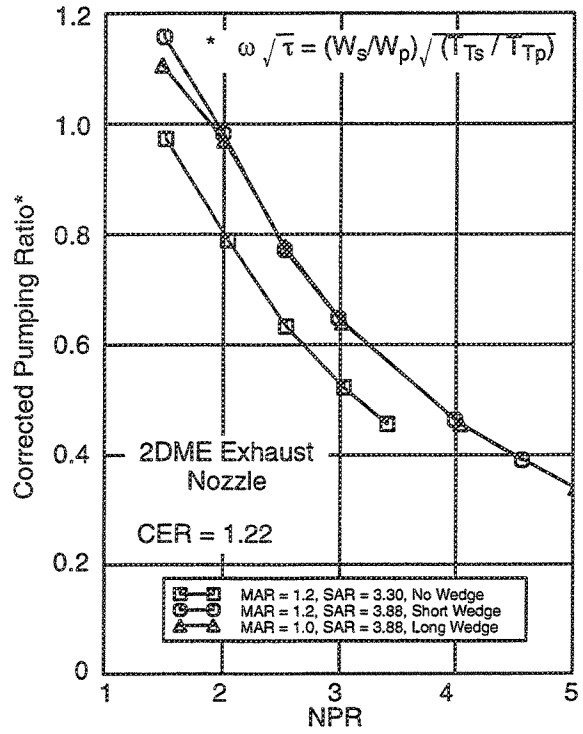


Figure 139. Effect of wedge on pumping:  
M = 0.32, SAR = 3.30 and 3.88

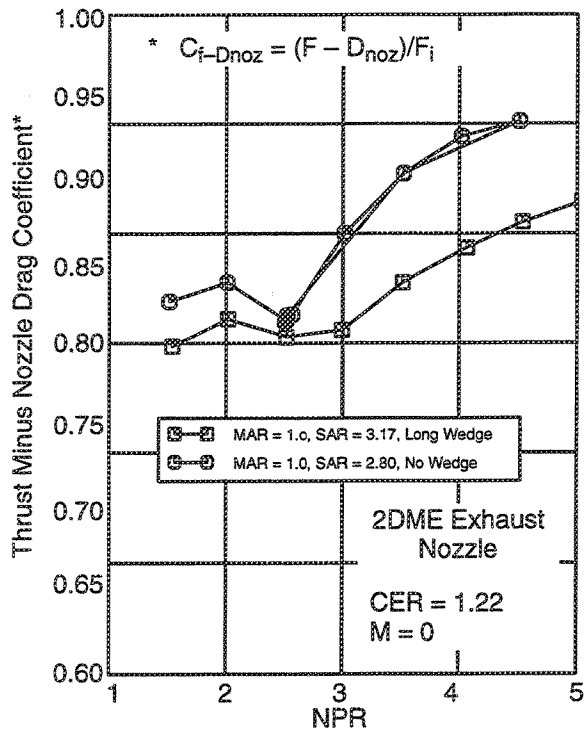


Figure 140. Effect of wedge on thrust:  
MAR = 1.0

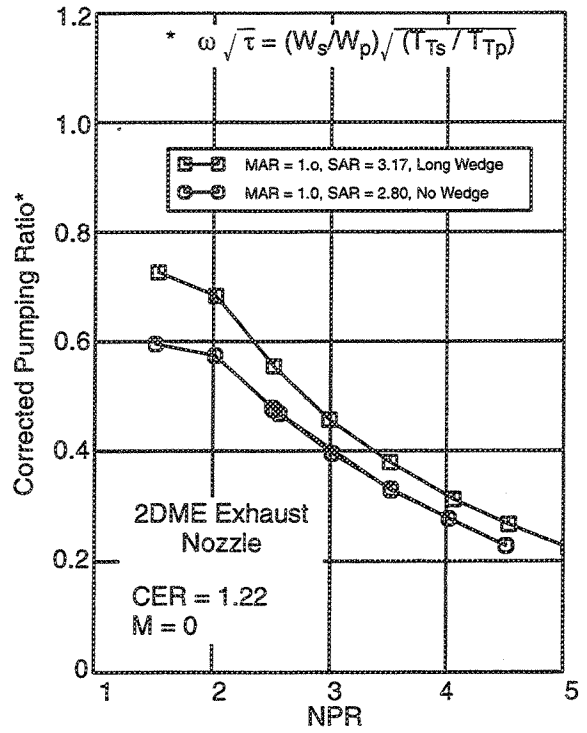


Figure 141. Effect of wedge on pumping:  
MAR = 1.0

## 6.0 Aerodynamic-Mixing Test Program

Fluid dynamic tests were conducted on subscale models of mixer/ejector nozzles in GEAE's *Aerodynamic Research Laboratory* to complement the acoustics and aerodynamic performance tests reported in earlier sections. The major objectives of this test program were to:

1. Obtain better qualitative and quantitative understanding of internal and external flowfields in terms of mixing processes and shock structures.
2. Provide aerodynamic design database.
3. Provide aerodynamic data for code validation, at near-takeoff conditions.

Scaled sector models of the mixer/ejector nozzle were mounted on a sting in ARL's windtunnel. The windtunnel was operated in a free-jet mode to simulate the relative motion of ambient air during takeoff. These tests were conducted to investigate the effects of various geometric parameters and operating conditions on the aerodynamic and mixing, or "aeromixing," characteristics of the nozzle by using internal and external LV measurements in addition to the pressure and temperature measurements. The following subsections describe the ARL windtunnel, the various nozzle models that were built, the aeromixing data obtained, and the conclusions.

### 6.1 Test Facility, Models, and Test Matrix

**Test Facility** – The experimental investigation was conducted in ARL's subsonic wind tunnel. This single-return, continuous-flow-ambient facility was operated as a free jet with a 2 by 2 ft square, open throat capable of providing 300 ft/s (Mach number  $M_0 = 0.25$ ) flow in the test section. The windtunnel flow has controlled temperature and low turbulence.

**Model Support System** – The 2D (rectangular) mixer/ejector nozzle models were supported in the wind tunnel by a sting/strut support system (see Figure 142). The centerlines of the sting and the model were aligned with the test section centerline. The 7.0-in diameter cross section sting is 108.5 in long. The sting has two-flow capability, 5.5 lbm/s each, and either flow passage can be operated with air from ambient temperature to 860°R. For this test program, the inner flow passage was closed off; the models were powered only with the outer (annular) flow. Downstream of the close-off plug for the inner flow, a settling chamber with flow-straightening screens was used to provide uniform flow to the models. The strut supporting the sting is airfoil shaped (NACA 0012) with approximately 42.0 inch chord in the streamwise direction. The maximum sting/model blockage is 6.7% of the cross-sectional area of the test section, and this reduces the maximum wind tunnel speed to about 225 ft/s or a Mach number of approximately 0.2.

The nozzle jet (core or primary) flow was simulated in the model by airflow from a high-pressure supply external to the model support system. In the single-flow mode, a continuous flow of clean, dry, high-pressure air at a stagnation temperature of about 860°R enters the outer annular flow passage of the sting through a supply line in the strut. From the annular flow passage, the pressurized airflow is discharged in a settling chamber where it is straightened by a series of four 65% open-area screens. It then enters the transition section of the model where the internal cross section is changed from circular to rectangular to provide compatible internal geometry at the 2D (rectangular) interface with the nozzle model. After the transition section is the instrumentation section where the total pressure and temperature are measured. The airflow is then exhausted through the 2DME nozzle model.

**Model** – The nozzle designs are based on 2DME considerations described in the earlier section on the acoustic test program. The subscale models used in ARL tests, however, have only 5 secondary chutes at the top and 5 secondary chutes at the bottom, instead of 10 chutes in each row as used in the acoustic and aeroperformance tests. The main reason for using fewer chutes is to reduce the primary throat area in consideration of the facility air supply and test section size and still maintain large individual primary- and secondary-chute flow widths and heights. Figure 143 shows a typical ARL model configuration with key axial stations and transverse dimensions.

The baseline ARL model configuration has the following overall geometric parameters:

1. Suppressor area ratio = 3.3
2. Convergent/divergent (CD) core nozzles with chute expansion ratio = 1.23
3. Aligned-top-and-bottom chute rows (mirror symmetric about the middle plane) without any central gap
4. Secondary chute inlet angle = 27.5°
5. Primary flow exit angle at top of chute = 15.3°
6. Flush inlet lip with 30° ramp angle
7. Nominal flap length = 9.706 in
8. Ejector nozzle internal width,  $w_9 = 5$  in and  $h_9 = 1.36$  in
9. Mixing area ratio = 1.2

Additional hardware was fabricated; however, due to available test time and budget limitations, only selected configurations were tested.

1. Five sets of chute racks (see Table 6)
2. One set of ejector flaps with  $L_{ej} = 6.706$  in
3. Wedge pieces to achieve MAR = 1.0 and 1.4
4. One set of glass sidewalls for internal LV measurements

**Table 6. Chute configuration summary**

Chute	Primary Throat Area ( $A_{p8}$ ), in <sup>2</sup>	SAR	CER	Chute Alignment	Center Gap ( $h_{gap}$ ), in
Baseline	4.10	3.32	1.23	Aligned	0
2	5.11	2.66	1.23	Aligned	0
3	5.11	2.66	1.23	Staggered	0
4	4.65	2.80	1.38	Aligned	Cell 41 Simulative

Basic model instrumentation is similar to that used for aero and acoustic scale models.

**Test Matrix** – Seven mixer/ejector model configurations were tested in this program for operating conditions, defined by NPR and  $M_0$ . These comprised 17 test points, summarized in Table 7.

**Table 7. Test matrix**

Note: Ejector exit total pressure and temperature Kiel probe Survey at all test conditions.

Configuration Variables							Test Conditions	
Config.	SAR	CER	$L_{ej}$ , in	Gap	Aligned	MAR	$M_0$	NPR
1	3.32	1.23	6.7	No	Yes	1.2	0.0	2
								4
							0.2	2
								4
2	3.32	1.23	9.7	No	Yes	1.2	0.0	2
								4
							0.2	1.5
								2
4								
3	2.66	1.23	9.7	No	Yes	1.0	0.2	4
4	2.66	1.23	9.7	No	No	1.0	0.2	4
5	2.66	1.23	9.7	No	No	1.2	0.2	4
6	2.80	1.38	9.7	Yes	Yes	1.0	0.2	4
7	2.80	1.38	9.7	Yes	Yes	1.2	0.0	2
								4
							0.2	2
								4

For all of these test points, the pressure and temperature data from the model instrumentation was first obtained. Further, in order to gain more insight into the fluid-dynamic processes both internal and external to the ejector, two types of surveys were also made for certain configurations:

1. Total pressure and total temperature surveys at the ejector exit plane with a Kiel probe.
2. Internal and external velocity surveys using a laser two-focus (L2F) system.

The L2F velocimeter measures the velocity of gas nonintrusively by detecting the light scattered by small particles in the flow as they pass through the focal volumes formed by two highly focused laser beams. Velocity is derived from the time of flight of particles moving from one beam to another with known beam separation — a technique known as laser transit anemometry or laser transit velocimetry. This system essentially gives the two components of the mean velocity vector projected on the vertical plane orthogonal to the laser beams (that is, the axial and the transverse vertical components). It can also give a measure of the turbulent intensity at that point.

Typically, internal LV surveys were performed selectively: (1) at the centerlines of the primary flow or the secondary chutes; (2) transverse planes near the chute exit (plane A) at the middle of the ejector (plane B); (3) at different distances from the nozzle major axis. The external plume LV surveys were performed selectively (1) at the transverse plane at the ejector exit (plane C), (2) along the centerline of the nozzle, (3) along the major and minor axes of the nozzle at various downstream stations from the ejector exit plane (4, 8, 16, and 24 inches).

## 6.2 Experimental Results and Analysis

The results for the baseline model (SAR = 3.3, CER = 1.23, aligned chutes with no central gap) are presented and the effects of different operating conditions analyzed. Next, the results for the model that is similar to the acoustic model (SAR = 2.8, CER = 1.38, aligned chutes with central gap) are discussed. Lastly, the effects of selected geometric parameters are presented.

### 6.2.1 Baseline Model

Consider the baseline model at NPR = 4.00 and  $M_0 = 0.2$  ( $V_0 = 225$  ft/s), the intended design condition. Figure 144 shows contour plots of the magnitude of the mean velocity vector (resultant of  $V_x$  and  $V_y$  axial and vertical components) in transverse (Y-Z) planes at three axial stations *inside* the ejector: (A) chute-exit plane, (B) middle plane, and (C) ejector-exit plane. Figure 145 shows the vertical components of velocity vectors and should be considered in conjunction with Figure 144. The following observations are made from Figures 144 and 145.

**Chute Exit, Plane A** – The maximum measured primary jet velocity is 2056 ft/s ( $M_p \approx 1.87$ ) and the nominal secondary air velocity is 473 ft/s ( $M_s = 0.42$ ). The difference in the axial velocity components creates *transverse* vorticity around the chute trailing edge (vorticity component in the plane *transverse* to the main axial flow direction) and is seen to be approximately constant along the chute heights. The flow is similar from chute to chute, at least in the middle portion, but is slightly distorted near the sidewalls.

Based on the vertical component and mean velocity, the primary jet flow diverges from the central axis (from  $0^\circ$  at the central portion to about  $12^\circ$  or  $13^\circ$  at the chute height); whereas, the secondary flow converges towards the central axis (from  $0^\circ$  at bottom to  $30^\circ$  at top of chutes). This is consistent with the flowpaths for the two flows governed by the corresponding wall angles and implies *axial* vorticity distribution at this plane due to nonequal vertical components of the two flows. Differences in spanwise velocity components ( $V_z$ ) can also contribute to axial vorticity, but at the chute trailing edges, which are vertical, they cannot contribute to axial vorticity as applied to these mixer configurations. The maximum axial vorticity is at the top of the chutes (near the flaps); whereas, the minimum axial vorticity is near the bottom of the chutes. This is consistent with the mirror symmetry about the central major axis in this aligned-chute configuration.

**Middle of the Ejector, Plane B** – Minimum and maximum values are considerably different than at the chute exit plane. Minimum speed of secondary flow near the central region is now 1158 ft/s, a large increase from the chute exit value, and primary flow is accelerated to 2254 ft/s. In addition:

- There is horizontal spreading of the high-velocity region in the top and bottom portions near the flaps.
- High-velocity “tongues” protrude in the vertical center planes of secondary chutes from top and bottom and moving towards the major axis of the ejector.
- High-velocity primary flow is migrating from the central portion to the top and bottom; hence, there is consequent “pinching” in the middle.
- There is loss of spanwise periodicity (but the two central jets appear similar).
- Flows between the top and bottom portions are roughly symmetric.
- Flow angularity is decreasing (the flow is becoming axial).

The spreading of the supersonic primary jets does not appear to be significant. However, the vortex sheets from adjacent chute sidewalls appear to curl on the top and bottom. These features are present due to horizontal spreading of the high-velocity primary jet impinging on the top and bottom flaps. Further, the axial vorticity component distorts and stretches the vortex sheets due to self-induction. The original contact surface area between the two flows thus increases significantly and enhances the mixing process.

**Ejector Exit, Plane C** – The flow is still highly nonuniform in the vertical direction with high speeds (1629 ft/s) at the top and bottom and low speeds (517 ft/s) in the central region. These are so-called “inverted” velocity profiles. In the spanwise direction, there appears to be fairly good mixing.

The average exit speed is much slower than that at the chute exit plane, and the flow direction is fairly horizontal. The three-dimensional velocity profile shows several minima and maxima; also, there are several saddle points, between the minima, that can assist in more rapid mixing downstream of the exit plane.

There appears to be low-speed regions on the sides that are related to the growth of the internal sidewall boundary layers.

**Effect of wind tunnel Mach Number on Mixing** – Similar features were observed when the wind tunnel free stream was off ( $M_0 = 0$ ). Figures 146 and 147 show, respectively, the mean velocity magnitude and vertical component of velocity at the same axial locations A, B, and C for the wind-off case. Comparison of these figures with Figures 144 and 145 for the wind-on case shows very similar flow evolution for the static case as well.

**Proposed Mixing Mechanism** – Such internal LV plots allow proposal of a model of the dominant internal mixing mechanism for such mixer/ejector nozzles, using vortex dynamics as depicted in Figure 148. It is seen that vortex sheets are shed from the chute sidewalls. These have two vorticity components: transverse (largely due to the difference in the axial velocity components of the two streams) and axial (largely due to the difference in the vertical velocity components). The transverse vorticity will lead to the usual Kelvin–Helmholtz instability; however, because the initial axial convective Mach number (near the chute exit plane) is estimated to be in the high subsonic range ( $M_c \approx 0.67$ , Figure 144) the compressibility effect on the spreading rate of this shear layer will be large, and spread rate will be relatively much smaller than in the incompressible case ( $M_c \ll 1$ ). Thus mixing due to this mechanism is not expected to be dominant, at least in the upstream regions closer to the chute exit plane.

The strong axial vorticity in the upstream regions can significantly stretch the vortex sheet through self-induction. Stretching of the shear or material interface between the two fluids increases the rate of mixing (per unit axial distance) between the two fluids. How this stretching progresses depends very much on the vertical distribution of axial vorticity at the chute trailing edge and also the proximity of the flap to the chute top.

As shown in the top part of Figure 148, the ejector flap can be replaced by an image vortex system for examining the flow in the transverse plane, where the transverse velocity components have very low subsonic Mach numbers. Self-induction pulls the vortex sheets from each chute together at the top and pushes them outwards in the middle. The neighboring primary jets, which impact the flaps, spread horizontally to meet each other at the center of secondary chutes and proceed towards the nozzle major axis as “tongues.”

This leads to double vortex layers in the middle vertical planes of secondary chutes with opposite vorticity on their two surfaces, as shown in the middle schematic of Figure 148. The axial vorticity, already maximum at the top of the chutes, convects upward due to the higher vertical velocity component of the primary flow and gets concentrated at the tip of this double vortex sheet. The tip will thus start curling in two opposite directions, due to self-induction, as shown in the bottom of Figure 148, and will form “mushroom type” vortices in the middle of the secondary chutes.

The curling and stretching of the vortex sheet increase the effective shear or material interface area and increase the rate of mixing. The two concentrated vortices in the “mushroom” then travel, as a vortex pair, away from the flaps towards the nozzle major axis. At the same time, viscous and thermal diffusion through this shear layer are also progressing, and the mixing rate will decrease once the axial and transverse vorticity has decayed to some critically small value and the material surface is diffused and not well defined.

Such vortex dynamics can also be inferred from computational fluid dynamics (CFD) simulations done by deBonis (Reference 9). The migrations of the primary and the secondary flows as described here also explain why the vertically stratified flow at the chute exit plane eventually becomes almost horizontally stratified at the ejector exit plane in many cases. The vertical tongues of primary flow at the secondary chute centerlines at the ejector exit plane still evident imply that the ejector length was insufficient to achieve full mixing and viscous diffusion has not progressed enough to result in horizontal stratification.

Similar mixing mechanism has been proposed by Qiu (Reference 10), but certain subtle differences exist in the vortex dynamics. The median of the axial vorticity in Qiu’s case is concentrated at the midheight of the chutes, rather than on the chute tops as in the case described herein, and leads to formation of the vortex cores at midchute height. Further interaction progresses from this point onwards as the vortex sheets from the chute sidewalls deform to form vortex cores at midchute heights and start migrating as a vortex pair not towards the flaps but towards each other and the middle horizontal plane.

To complete the flow description at the ejector exit plane, total temperature and total pressure contours are shown in Figures 149 and 150 for the wind-on and static cases at NPR = 4. The general topological features are similar to the corresponding exit velocity profiles in the bottom plots of Figures 144 and 146; both exhibit the “inverted” profile and relative uniformity in the spanwise direction. These effects are quantified by the use of a term called “mixing effectiveness” ( $M_T$ ) at the ejector exit plane based on total temperature,  $T_T$ , as given in Roshko (Reference 11):

$$M_T = 1 - \int |T_T^* - T_{Tav}| dA / [(1 - T_{Tav}) A_1 + T_{Tav} A_2]$$

where  $T_T^* = [T - T_{Ts}] / [T_{Tp} - T_{Ts}]$

and  $T_{Tav} = (1/A) \int T_T^* dA$

$A_1$  is the area for which  $T_T^* > T_{Tav}$ ,  $A_2$  is the area for which  $T_T^* < T_{Tav}$ ,  $A = A_1 + A_2$  is the area over which the integration is carried out, and  $T_{Tp}$  and  $T_{Ts}$  are total temperatures of the primary and secondary flows taken at the chute exit plane. This gives  $M_T = 1$  for the fully mixed condition and  $M_T = 0$  at the chute exit plane.

Table 8 summarizes the mixing effectiveness for these two test points as well as some other test points that will be discussed later. The table also lists corrected pumping ratio ( $\omega \sqrt{\tau}$ ).

**Table 8. Mixing effectiveness and pumping**

Configuration Variables				Test Conditions		$M_T$	$\omega \sqrt{\tau}$
Config.	SAR	CER	MAR	$M_0$	NPR		
1	3.32	1.23	1.2	0.0	2		
					4	0.702	
				0.2	2		
					4		
2	3.32	1.23	1.2	0.0	2	0.873	
					4	0.709	0.512
				0.2	1.5		
					2	0.889	0.804
					4	0.731	0.508
3	2.66	1.23	1.0	0.2	4	0.775	0.338
4	2.66	1.23	1.0	0.2	4	0.754	0.352
5	2.66	1.23	1.2	0.2	4	0.694	
6	2.80	1.38	1.0	0.2	4	0.801	0.389
7	2.80	1.38	1.2	0.0	2	0.857	
					4	0.732	
				0.2	2	0.885	
					4	0.731	0.426

Note: Configuration 1 is short flap  
 Configurations 4 and 5 are staggered chutes  
 Configurations 6 and 7 are with center gap

From the wind-on and wind-off readings, we conclude that wind tunnel Mach number or takeoff speed only slightly improves mixedness at the exit plane (0.731 versus 0.709) and the pumping ratio does not change very much (0.508 versus 0.512). Note that at higher wind tunnel speeds the convective Mach number at the chute exit plane (which is proportional to the difference between the speed of the primary and the secondary flow) will go down; this will slightly increase the spreading rate of the shear layer (Reference 12) and give better mixing.

**Effect of NPR on Mixing** – Consider the effect of lowering NPR to 2 from the previous value of 4 with the wind tunnel off. Figure 151 shows the velocity contour plots at the chute-exit plane, middle of the ejector and the exit plane and should be compared to Figure 146 (NPR = 4,  $M_0 = 0$ ). The speeds are obviously much lower at this smaller NPR value. The velocity profile at the ejector plane appears slightly more uniform than when NPR = 4, as are the total temperature contour plots at the exit plane (Figure 152). It is better quantified in Table 8 by mixedness parameter  $M_T$  of 0.873 versus 0.709 for NPR = 4. Halving the NPR, with the same chute exit supersonic primary Mach number (which depends only on the core expansion ratio), essentially halves the density ratio between the primary and the secondary flow with not much change in the convective Mach number. Reduction in density ratio is known to increase the shear-layer growth rate (Reference 13) and may be partially responsible for the increased mixing. Note that the estimated corrected pumping ratio

is also much higher at the lower NPR (0.804 versus 0.512) as expected. With the wind tunnel on at NPR = 2, the mixing improves only a little (0.889 versus 0.873).

### 6.2.2 Model with Central Primary Gap

The geometry of this configuration is described in Table 7. Note that not only is the SAR different than the baseline model but the CER is also different. Hence, one-to-one comparison between these two models cannot be made, and the focus here will be to examine the effect of the central gap which is a common feature of all the acoustic and performance models discussed in Sections 4 and 5, respectively.

For NPR = 4,  $M_0 = 0.2$  (Configuration 7, MAR = 1.2 with long flap), Figure 153 shows vertical distribution of the velocity vector plots at the chute exit plane. Besides the *convergent* secondary flow and the *divergent* primary flow features as in the baseline case, the central gap between the secondary chutes now has high-velocity, hot, primary flow. It is interesting to see if this central gap helps in filling up the void in the no-gap case created by the slower secondary fluid accumulating in the central portion.

Figure 154 shows mean velocity, total temperature, and total pressure contour plots at the ejector exit plane. The hills, valleys, saddle regions, and the “inverted” profiles still appear at the exit plane for this configuration and are better characterized by the mixing effectiveness,  $M_T$  (see Table 8) value of 0.731 and is similar to the baseline case. At this low primary temperature (860°R), the central gap does not seem to have helped much so far as mixing at the exit plane is concerned. The central hot streak has also migrated towards the flaps. (Note that, in contrast, the corresponding acoustic model at higher temperatures has shown a considerably flatter velocity profile in the minor-axis direction at the ejector exit plane and, hence, better mixing — see subsection 4.2.8.)

The effect of  $M_0$  on mixing appears to be negligible again (compare 0.731 vs 0.732) and lowering NPR to 2 again improves mixing ( $M_T = 0.885$ ) as in the baseline case. Hence, the trends of the operating conditions on the mixing behavior do not seem to have changed.

Various internal axial LV surveys were also done at different heights to capture this shock-cell structure, and Figure 155 shows a typical sample at 74% mixing height. As many as six to seven shock cells can be discerned in the traverse along the primary-chute centerline with the characteristic progressively decreasing shock strengths and shock-cell lengths.

### 6.2.3 Effect of Geometric Parameters

The effect of flap length, MAR and stagger are discussed from the perspective of mixing effectiveness at the exit plane,  $M_T$ , and internal shock structures.

#### 6.2.3.1 Flap Length

There were nominally two flap lengths: 6.7 in (short) and 9.7 in (long) for the baseline mixer (configurations 1 and 2, respectively). At NPR = 4 and static conditions ( $M_0 = 0$ ), the shorter flap showed considerably more nonuniformity in the exit total temperature (Figure 156), but this is not reflected as much in the exit “mixedness” — 0.702 versus 0.709; the corrected pumping level is higher for the longer flap: 0.512 versus 0.367.

#### 6.2.3.2 Chute Stagger

The effect of chute stagger is evaluated for configurations 3 and 4. These have 9.7-in flaps at MAR = 1, with the same SAR, CER, and no central gap. Figures 157 and 158, respectively, show velocity

and total temperature contour plot comparisons at the ejector exit plane for the aligned chutes and the fully staggered chutes at  $NPR = 4$  and  $M_0 = 0.2$ . The velocity and temperature profiles near the flaps for the staggered case are essentially shifted by a half-chute period according to the chute placement; however, the strong valley in the middle still remained with similar spanwise distribution on top and bottom. Mixedness at the exit plane is slightly better for the aligned case, 0.775 versus 0.754, and the pumping is slightly better for the staggered case: 0.352 versus 0.338.

In this particular staggered configuration, the primary and secondary flow directions at the bottom of the chute were kept axial or horizontal; hence, the asymmetry provided by the staggered placement was not used to provide more axial vorticity at the chute bottoms.

In another computational study at GEAE (Reference 14), it has been shown that the initial rate of mixing per unit axial distance in the staggered case can be higher than the aligned case. However, in the staggered case, before the flow reaches the ejector exit plane the inefficient viscous diffusion starts dominating much earlier, compensates for the earlier increased mixing efficiency, and makes it comparable with the mixedness of the aligned case at the exit plane. Obviously, more work is needed for understanding the effect of stagger.

### **6.2.3.3 Mixing Area Ratio**

The effect of MAR can be evaluated by comparing configurations 4 and 5, as well as 6 and 7, at an  $NPR = 4$  and  $M_0 = 0.2$ . Considering configurations 4 and 5 ( $SAR = 2.66$ ), mixing improved with the lower MAR (0.754 versus 0.694) while pumping decreased slightly (0.352 versus 0.385).

The same conclusions appear to hold for the configuration with central gap (configuration 6). When  $MAR = 1$ , mixing effectiveness is slightly better than at  $MAR = 1.2$  (0.801 versus 0.731) and pumping is slightly higher (0.389 versus 0.426).

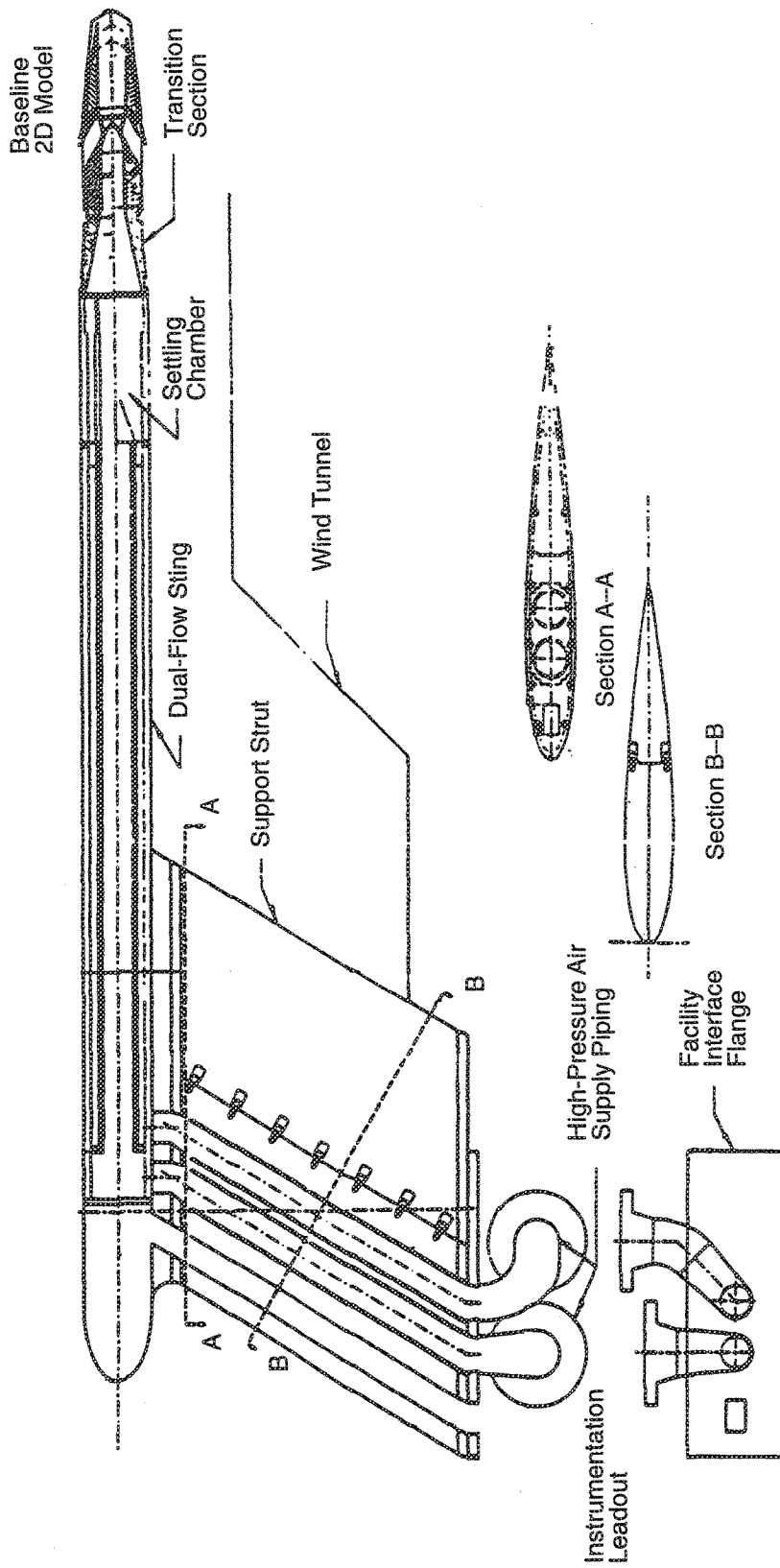


Figure 142. Model support system and model installation

All dimensions are inches.

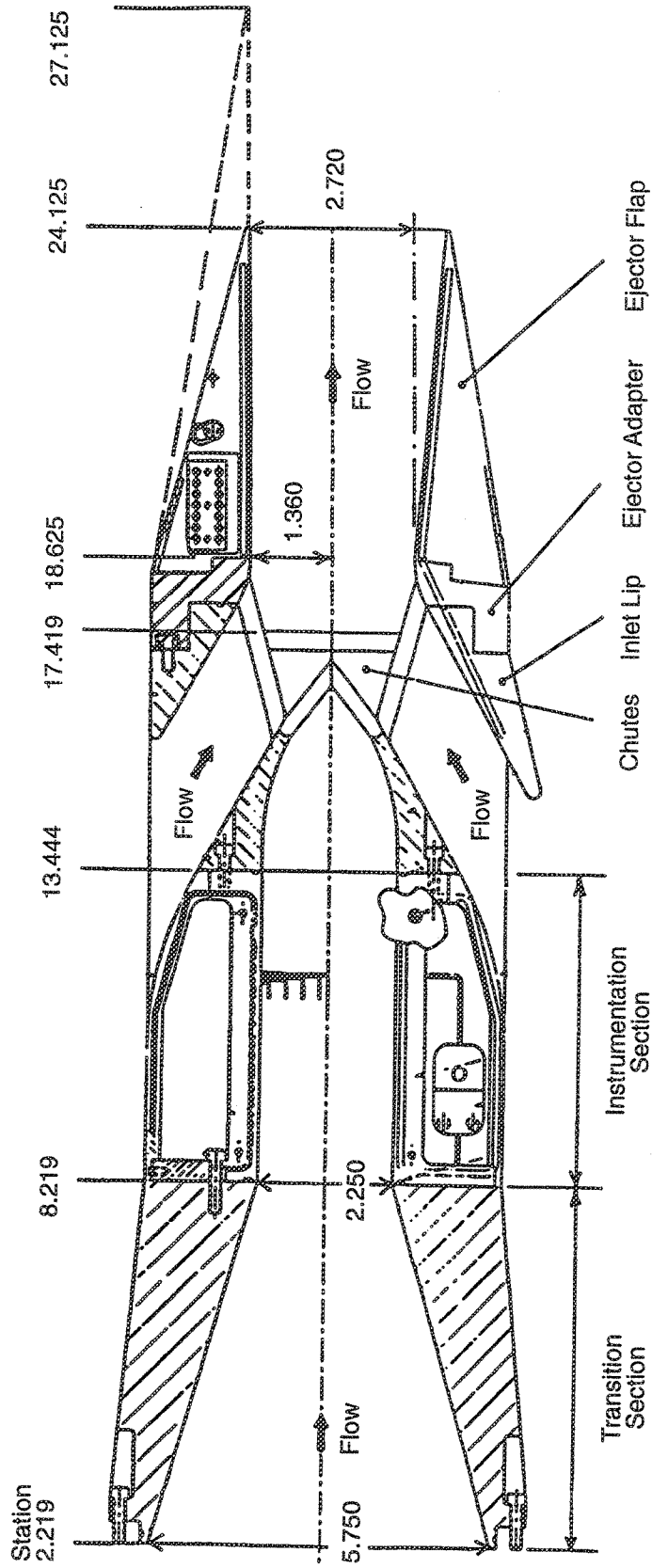
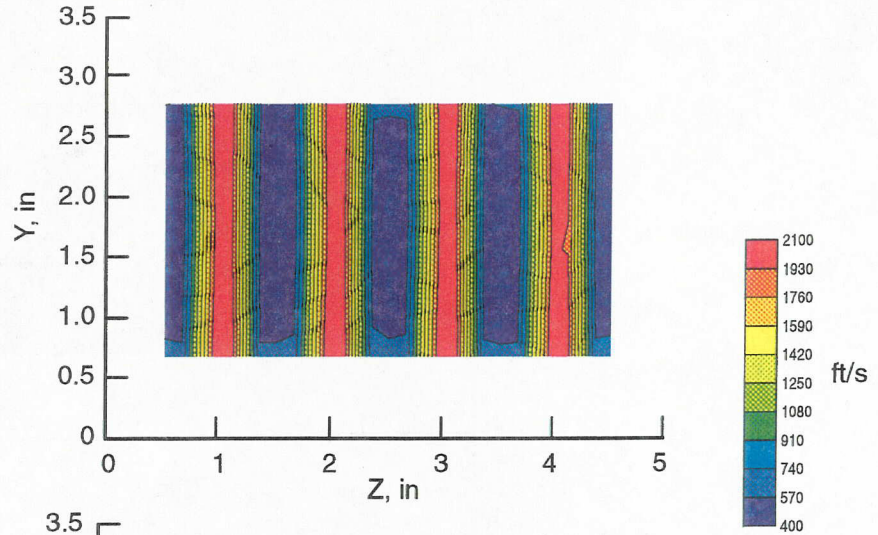
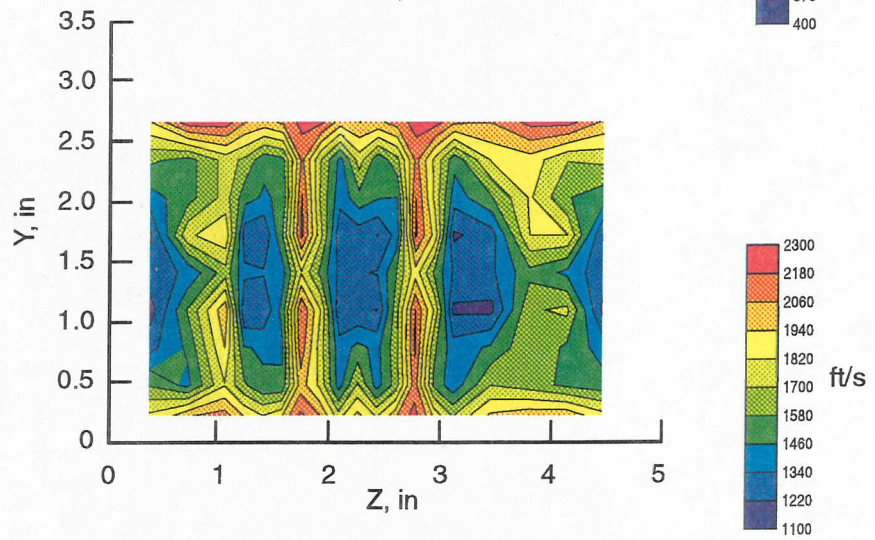


Figure 143. Typical ARL mixer/ejector model configuration

A. Chute Exit



B. Middle Plane



C. Nozzle Exit

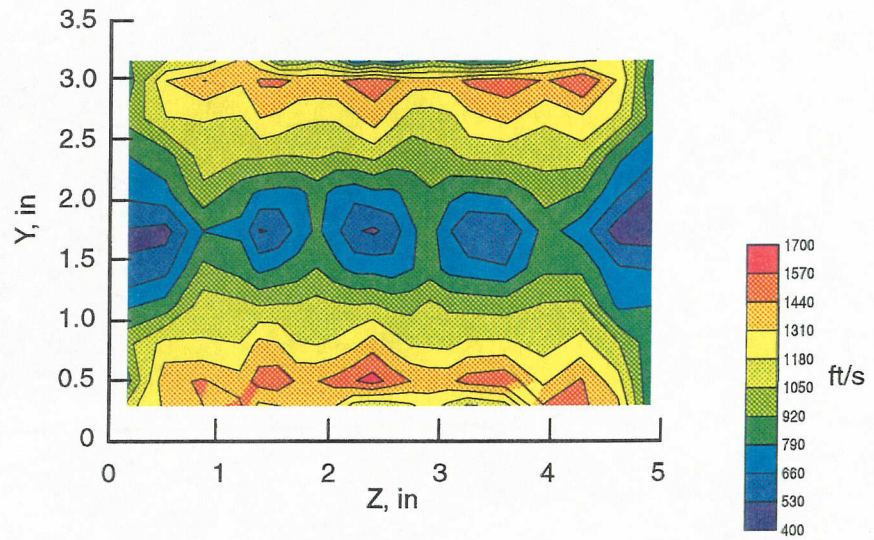
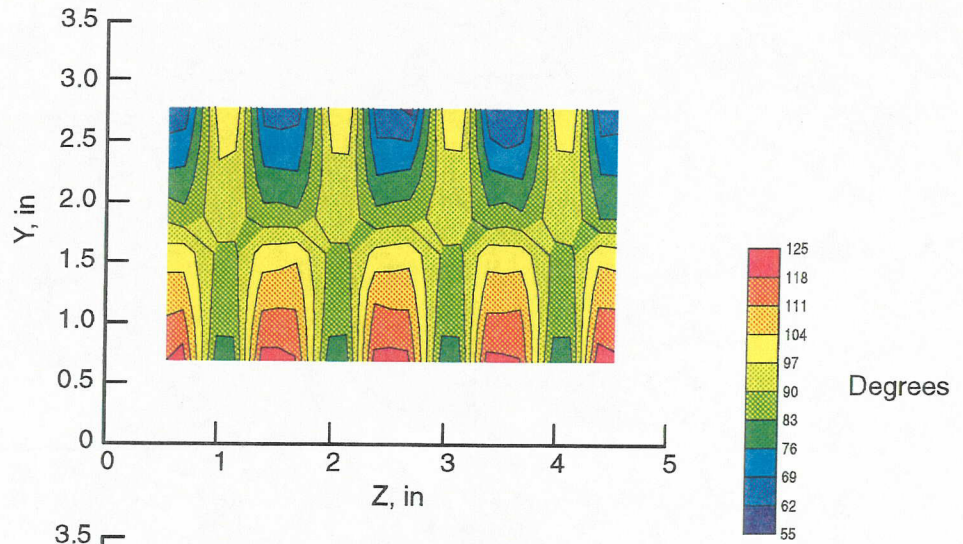
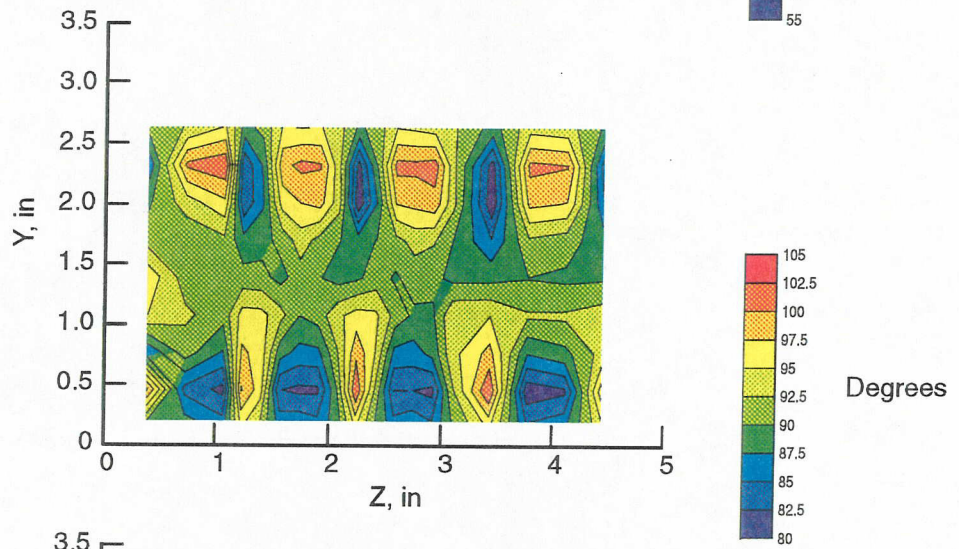


Figure 144. Internal axial evolution of mean velocity distribution for baseline case with  $\text{NPR} = 4$ ,  $M_0 = 0.2$

A. Chute Exit



B. Middle Plane



C. Nozzle Exit

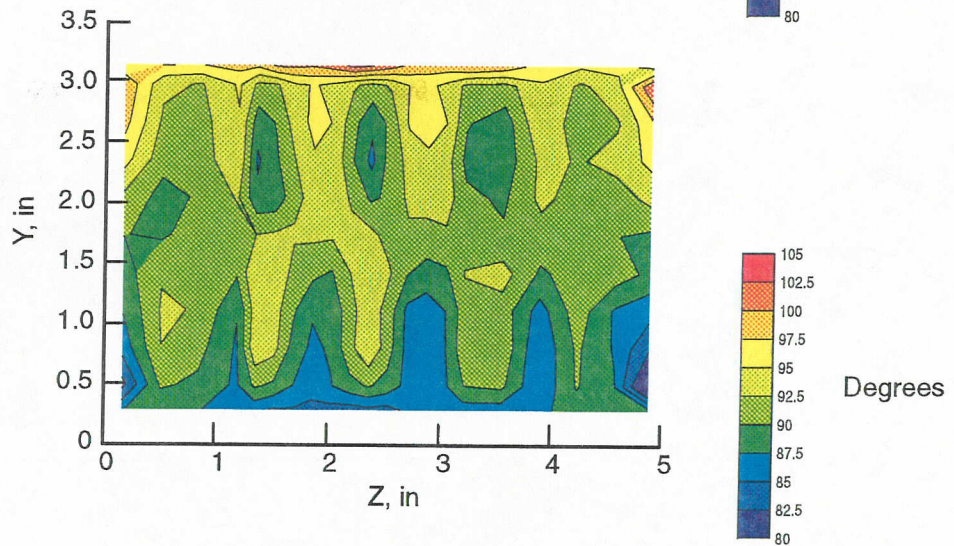
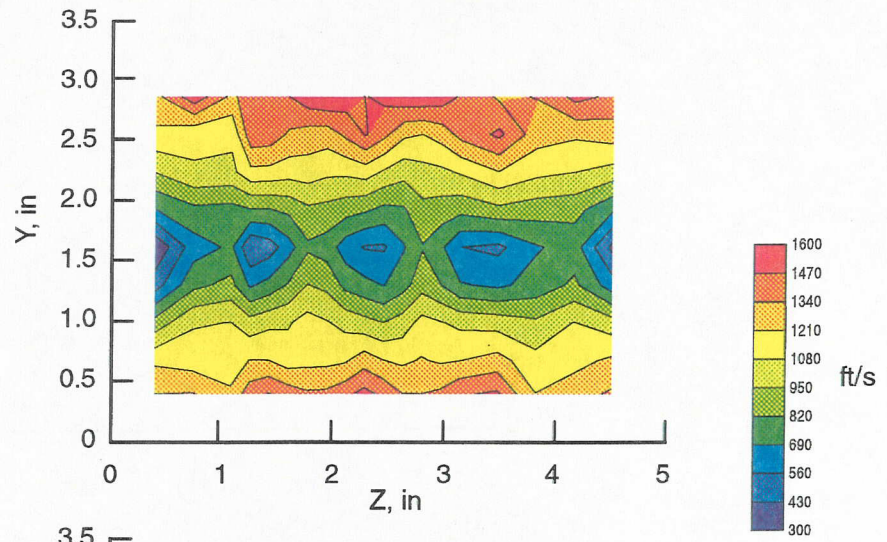
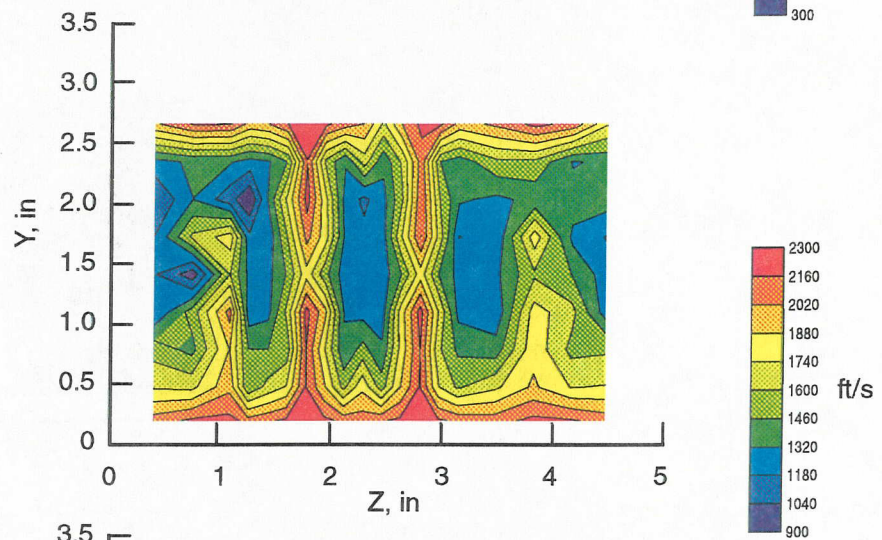


Figure 145. Internal axial evolution of mean velocity angular distribution for baseline case with  $\text{NPR} = 4$ ,  $M_0 = 0.2$

A. Chute Exit



B. Middle Plane



C. Nozzle Exit

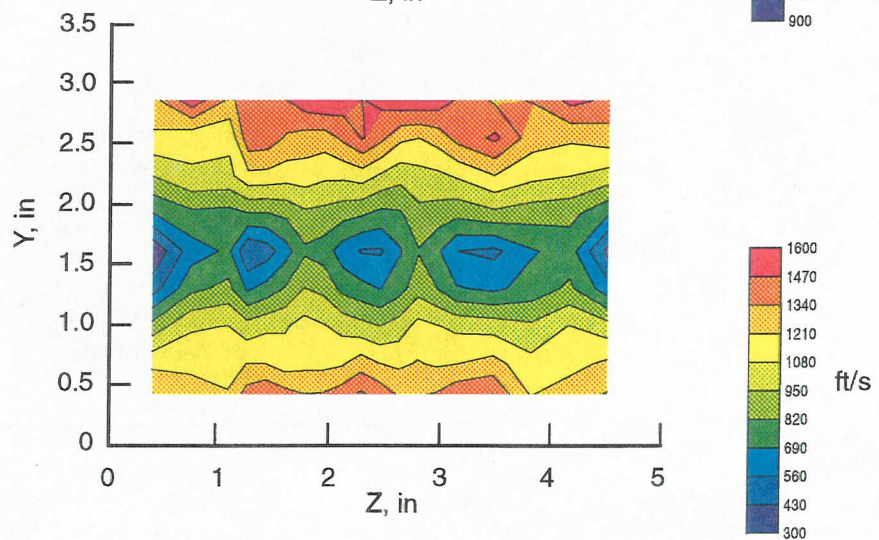
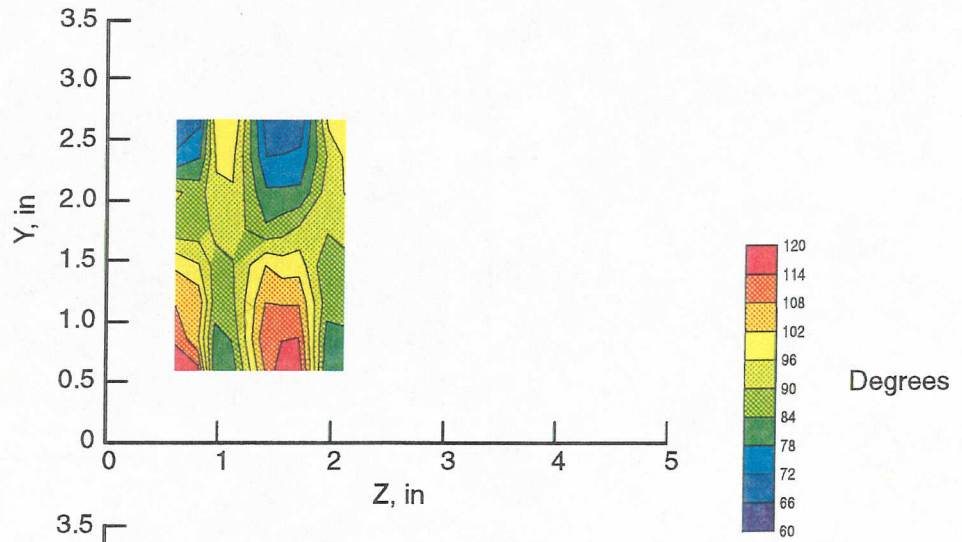
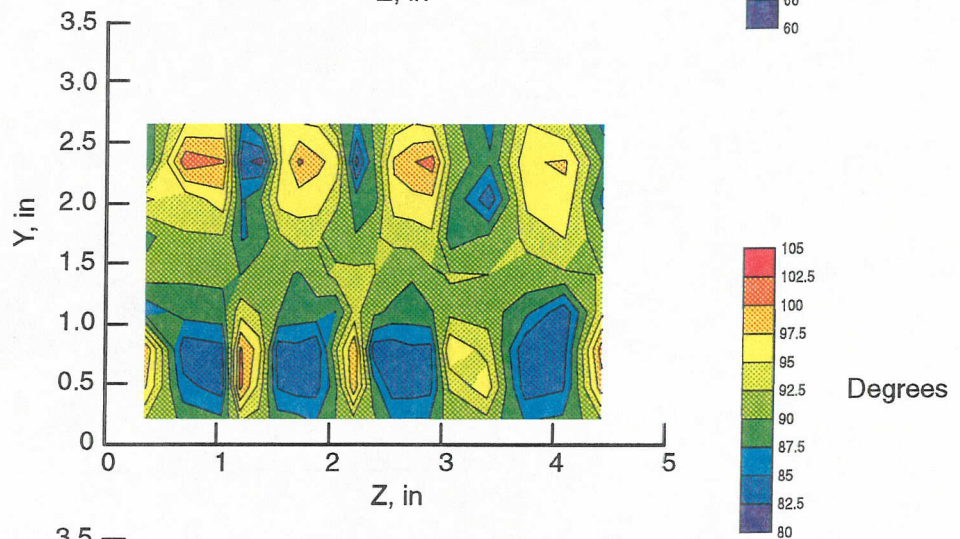


Figure 146. Internal axial evolution of mean velocity distribution for baseline case with  $NPR = 4$ ,  $M_0 = 0$

A. Chute Exit



B. Middle Plane



C. Nozzle Exit

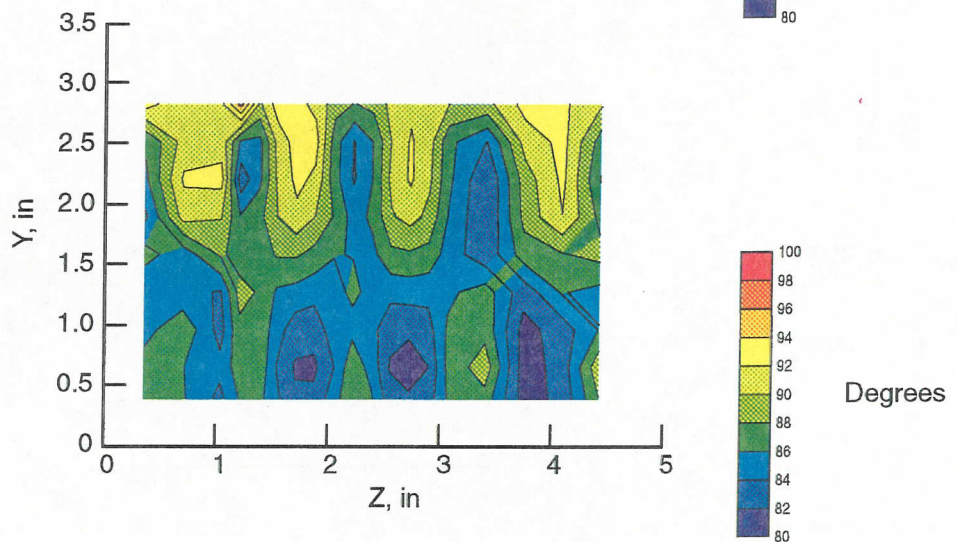


Figure 147. Internal axial evolution of mean velocity angular distribution for baseline case with NPR = 4,  $M_0 = 0$

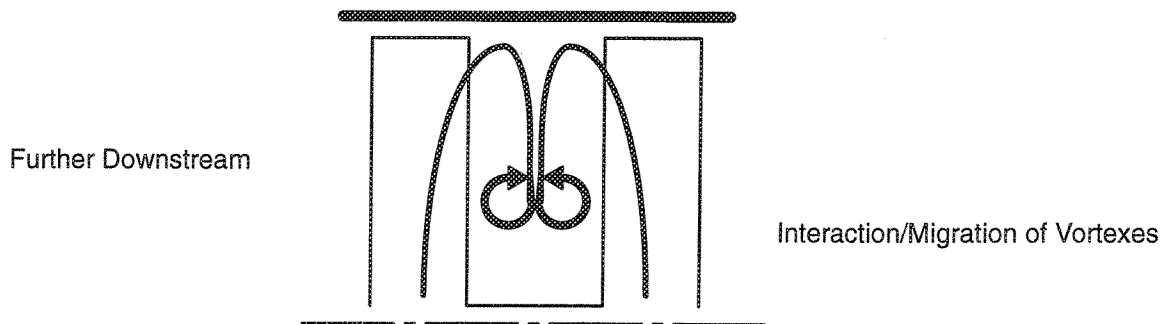
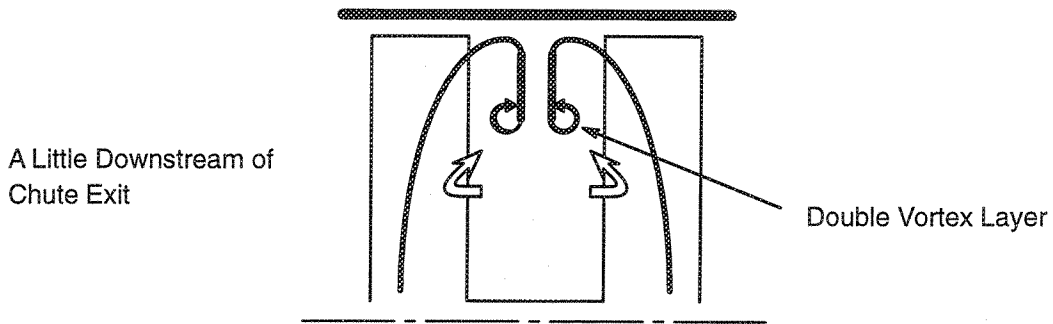
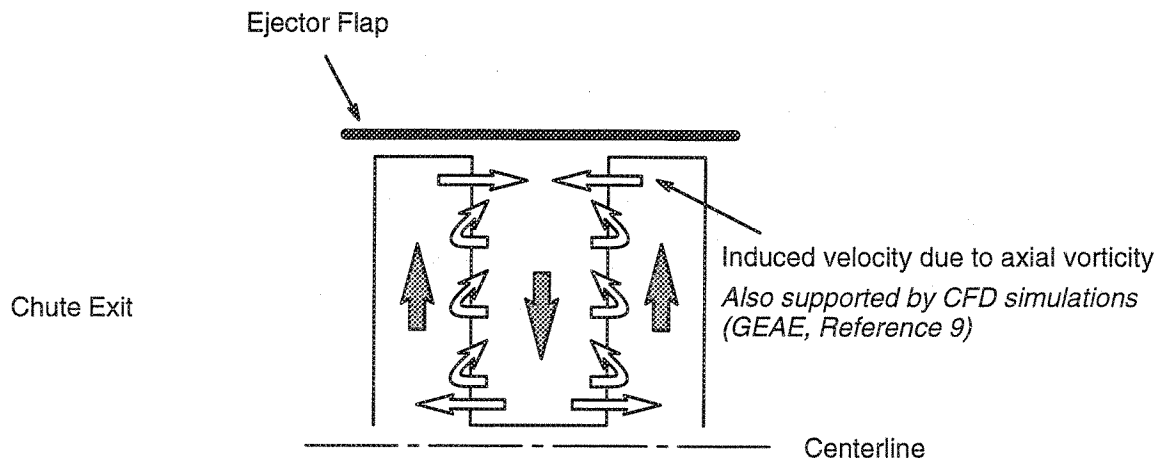


Figure 148. Proposed mixing mechanism

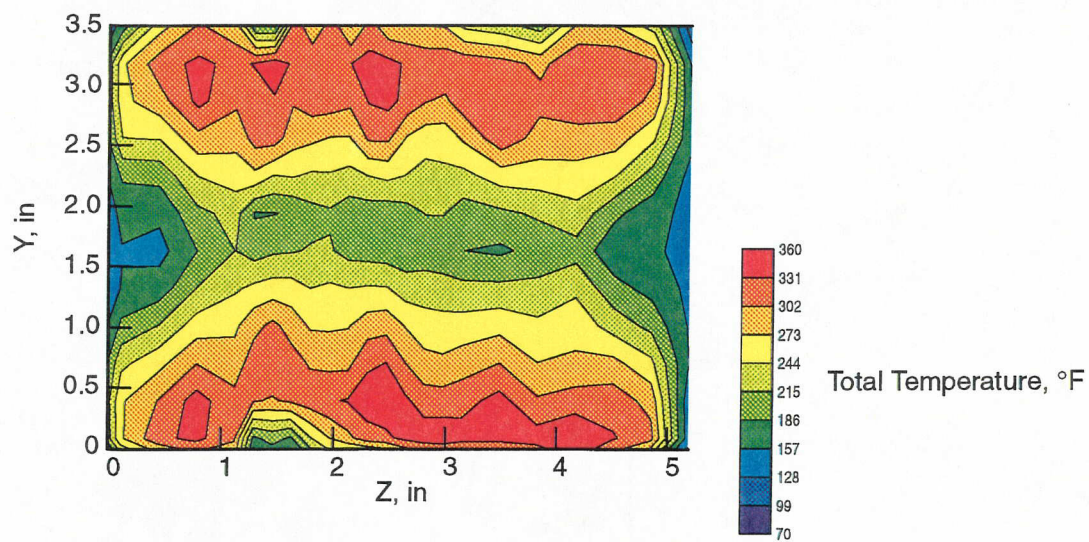
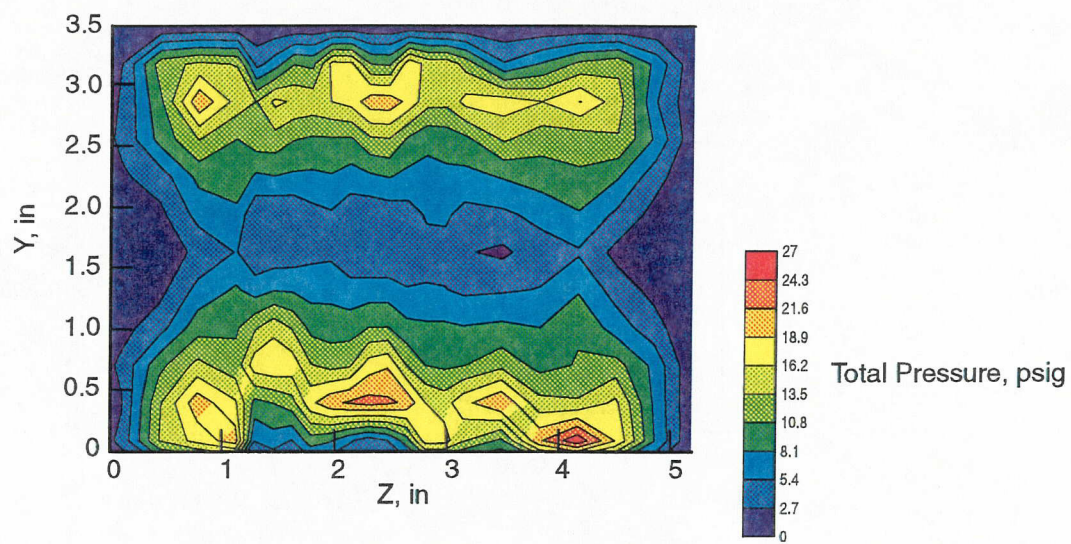


Figure 149. Total temperature and total pressure contour plots at ejector exit for baseline case

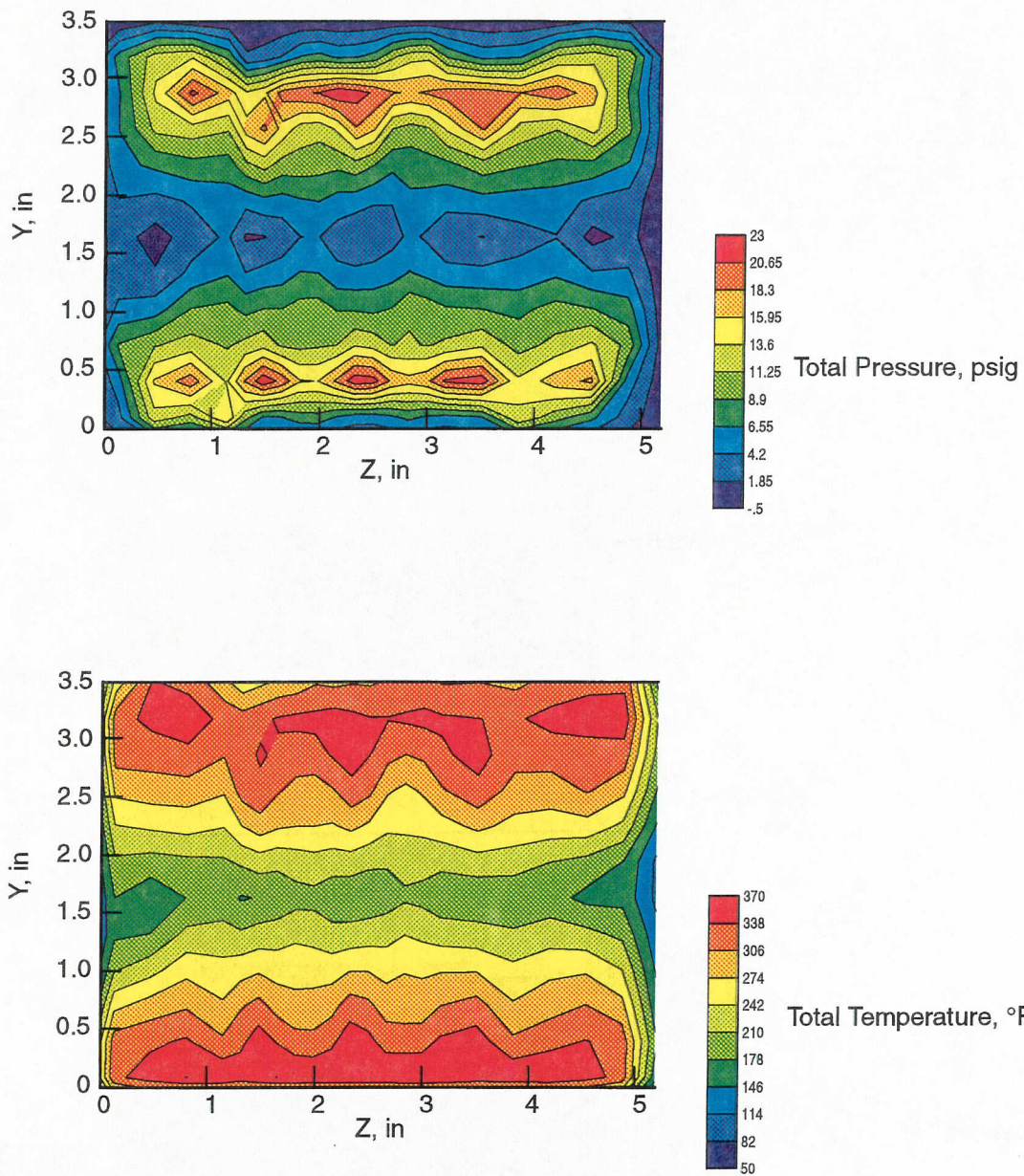
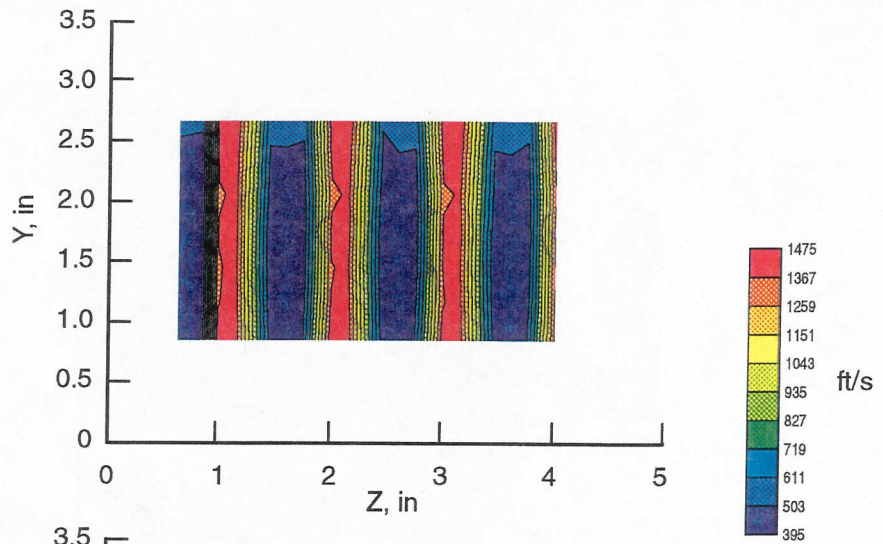
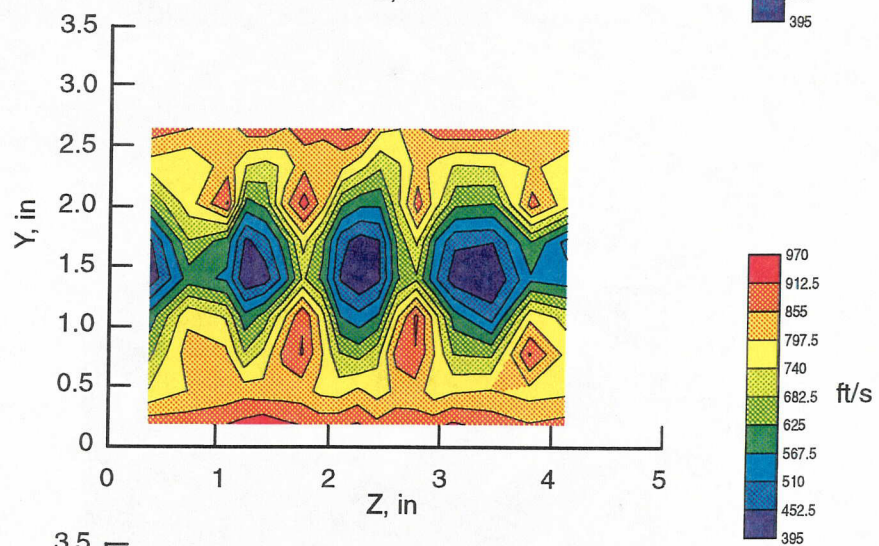


Figure 150. Total temperature and total pressure contour plots at ejector exit for baseline case under static conditions

A. Chute Exit



B. Middle Plane



C. Nozzle Exit

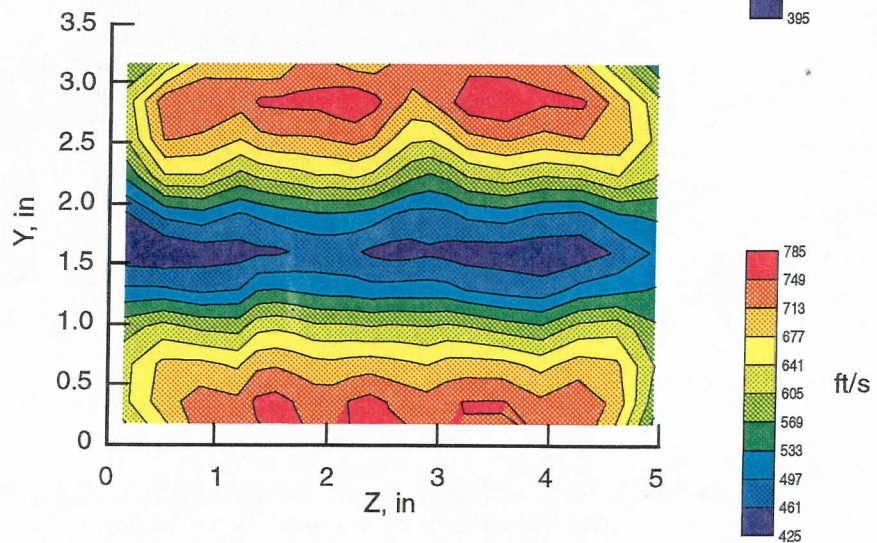


Figure 151. Internal axial evolution of mean velocity distribution for baseline case with  $NPR = 2$ ,  $M_0 = 0$

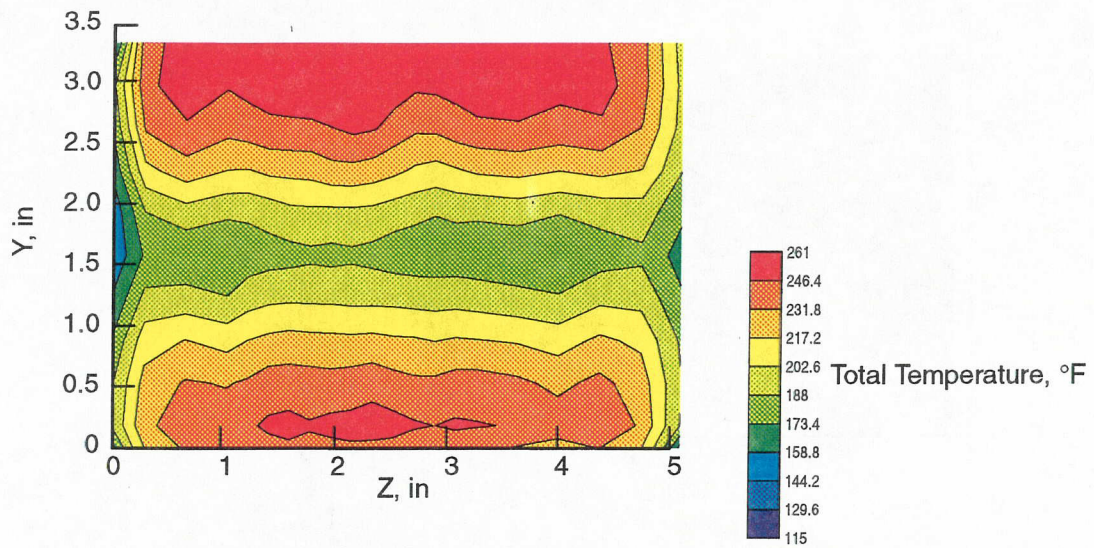


Figure 152. Total temperature contour plot at exit for baseline case with NPR = 2 under static conditions

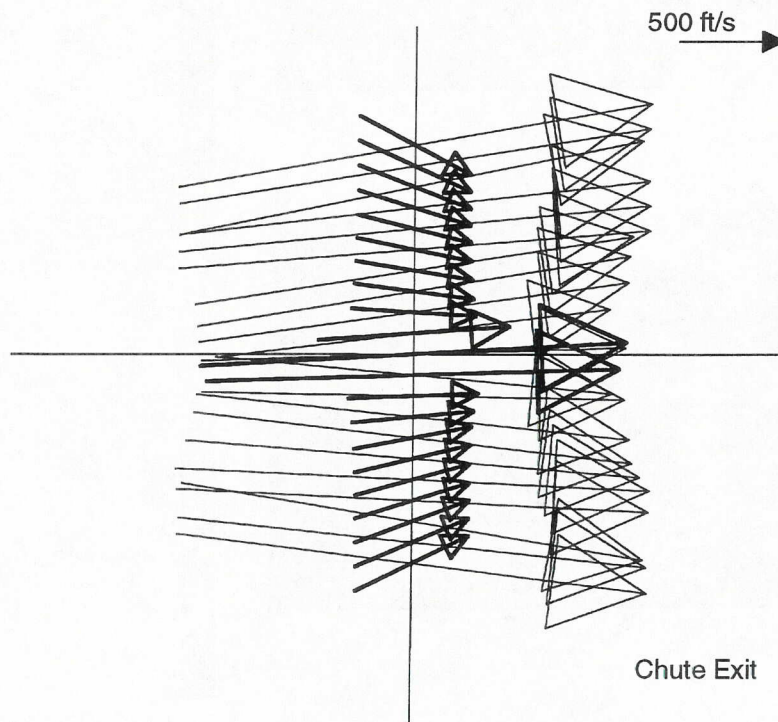


Figure 153. Velocity vector plots at chute exit for configuration with central gap

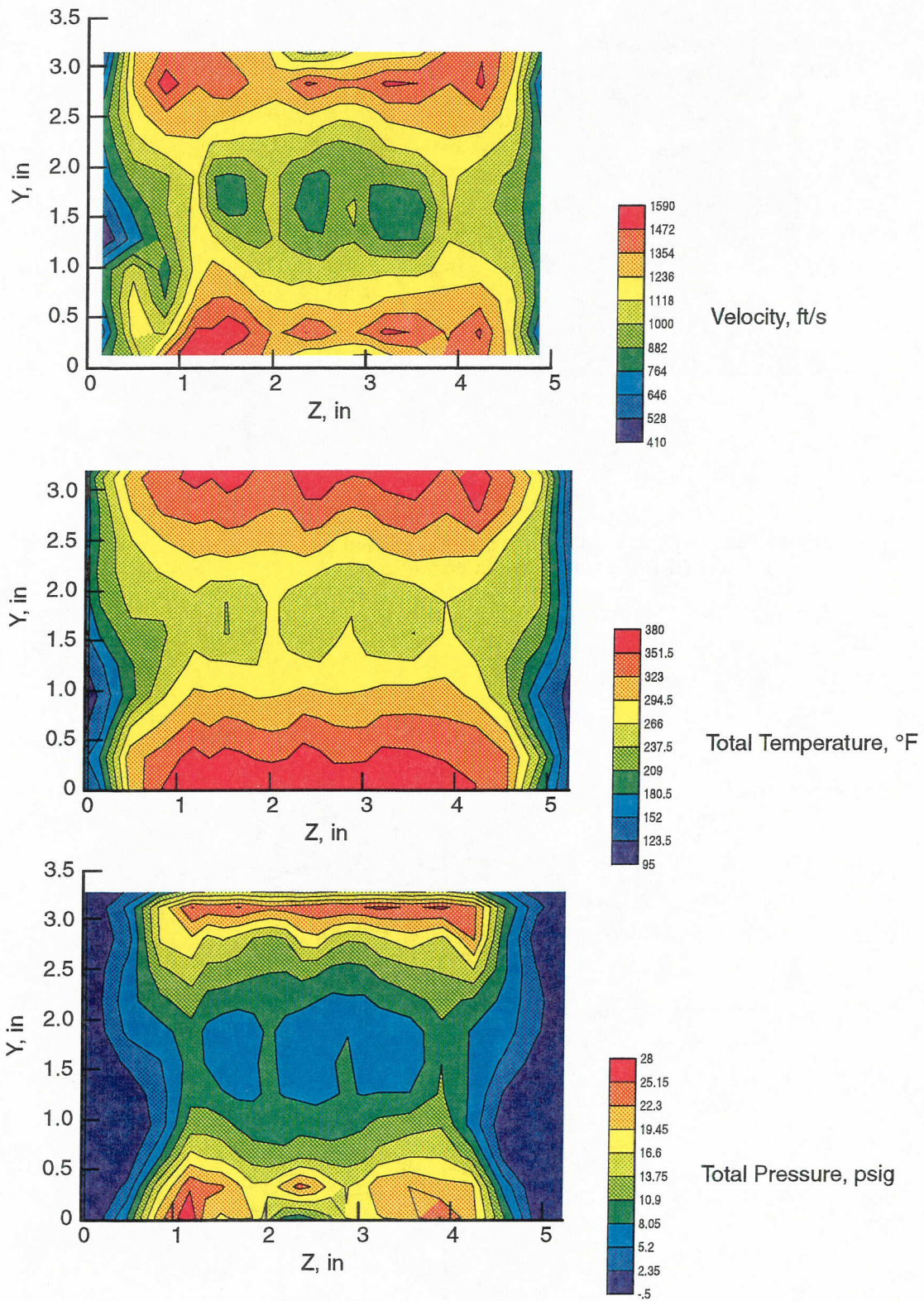
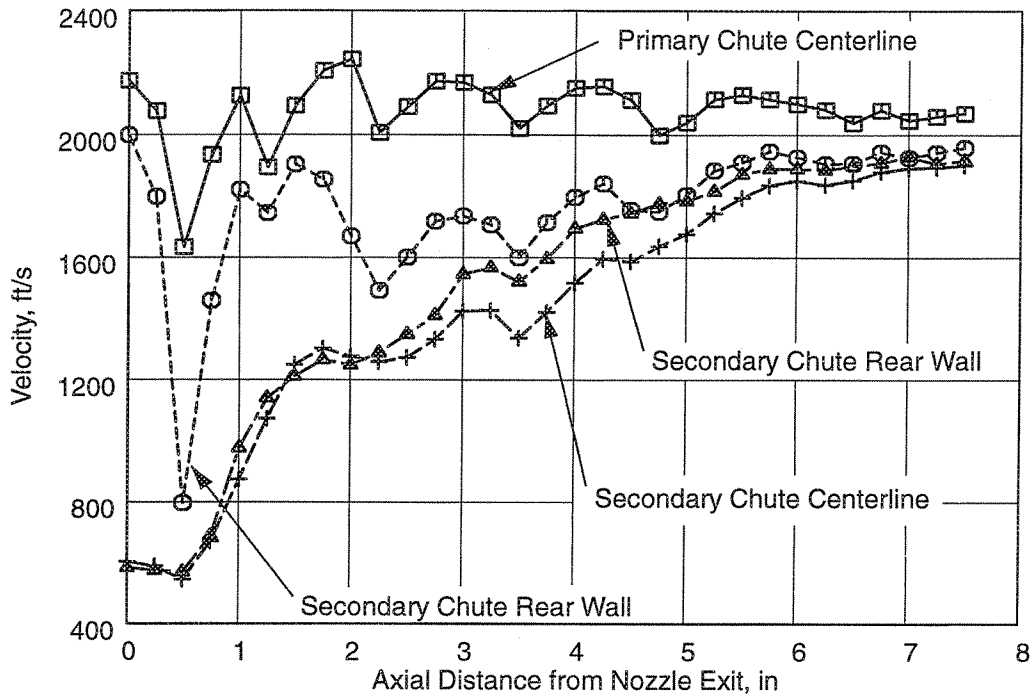
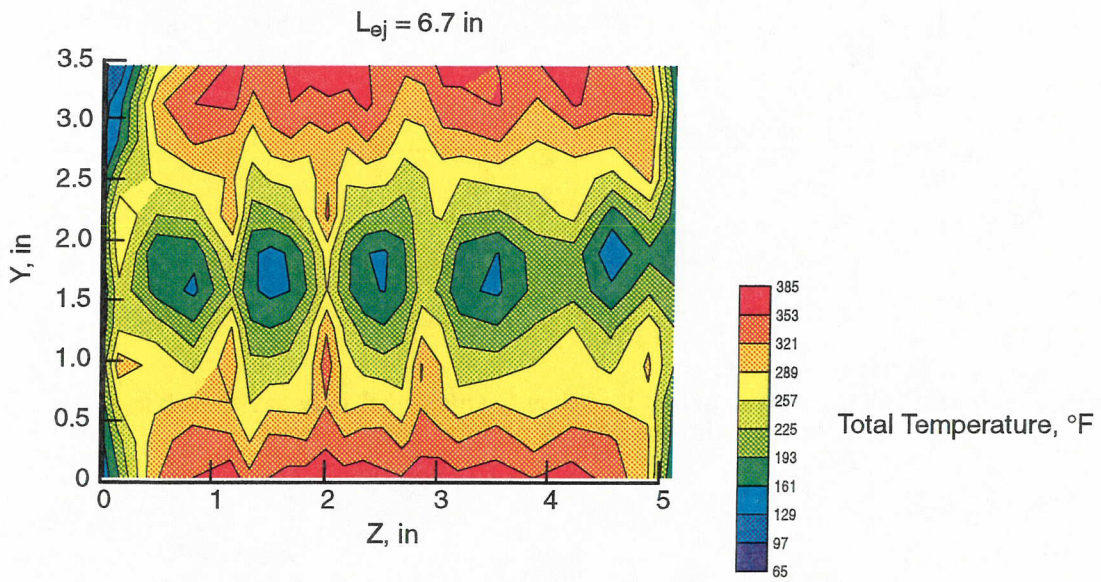
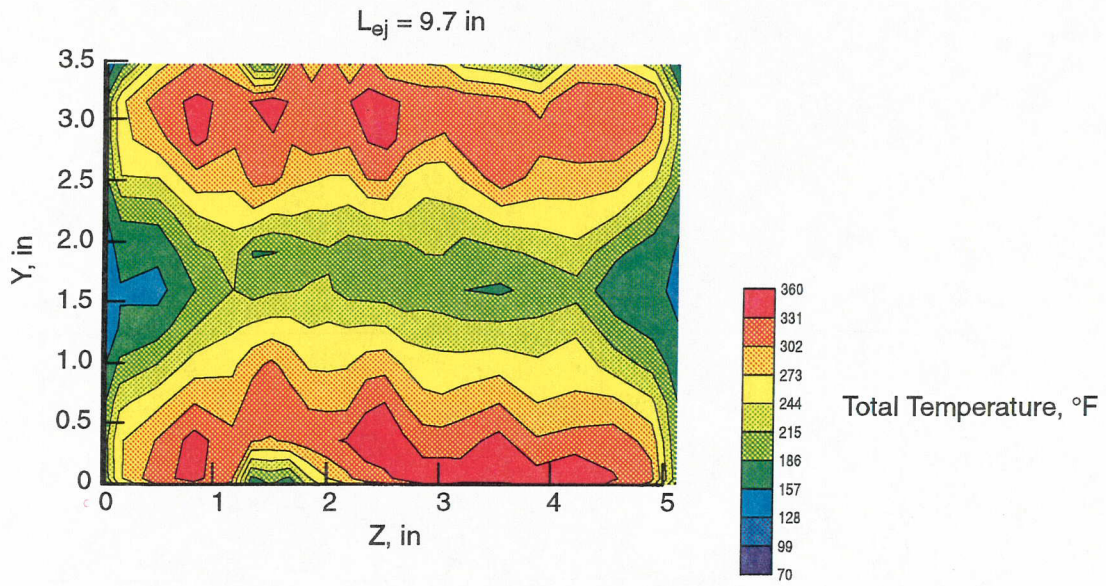


Figure 154. Contours of mean velocity, total temperature, and total pressure at ejector exit plane; NPR = 4,  $M_0 = 0.2$



**Figure 155. Internal axial LV survey for mean velocity at 74% mixing height with the central primary gap**



**Figure 156. Ejector exit total temperature contour plot comparisons for the effect of flap length**

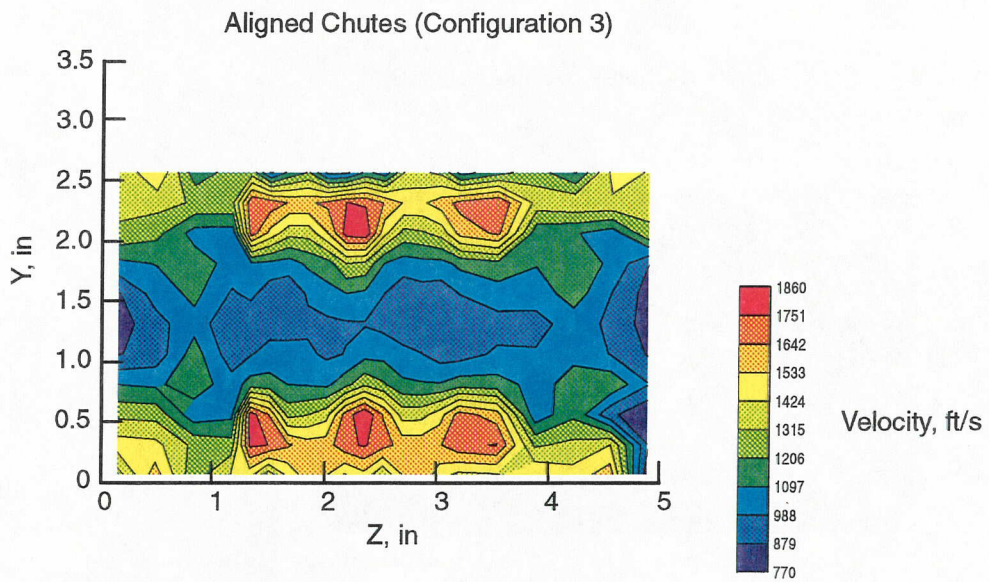
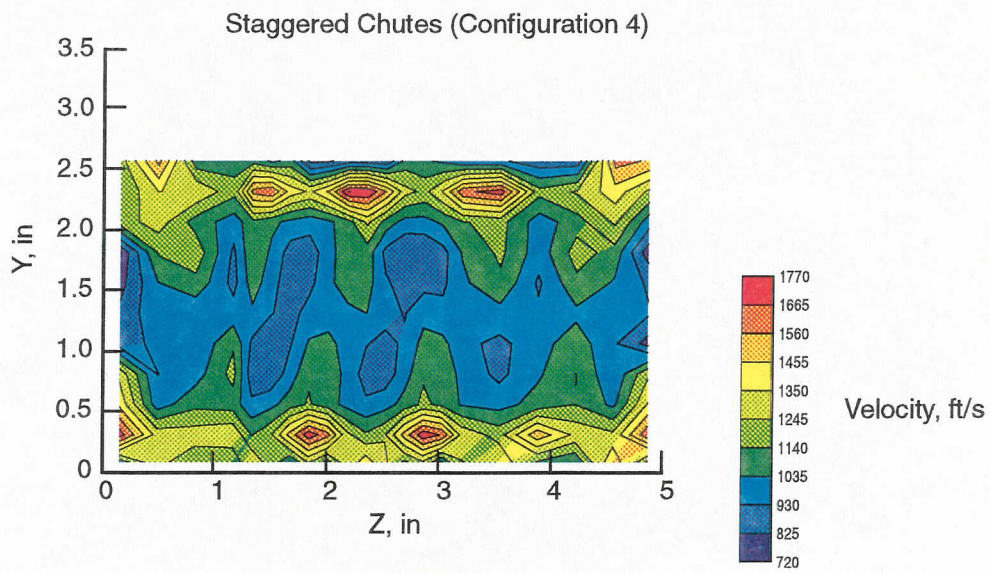


**Figure 157. Ejector exit mean velocity contour plot comparisons for staggered and aligned case**

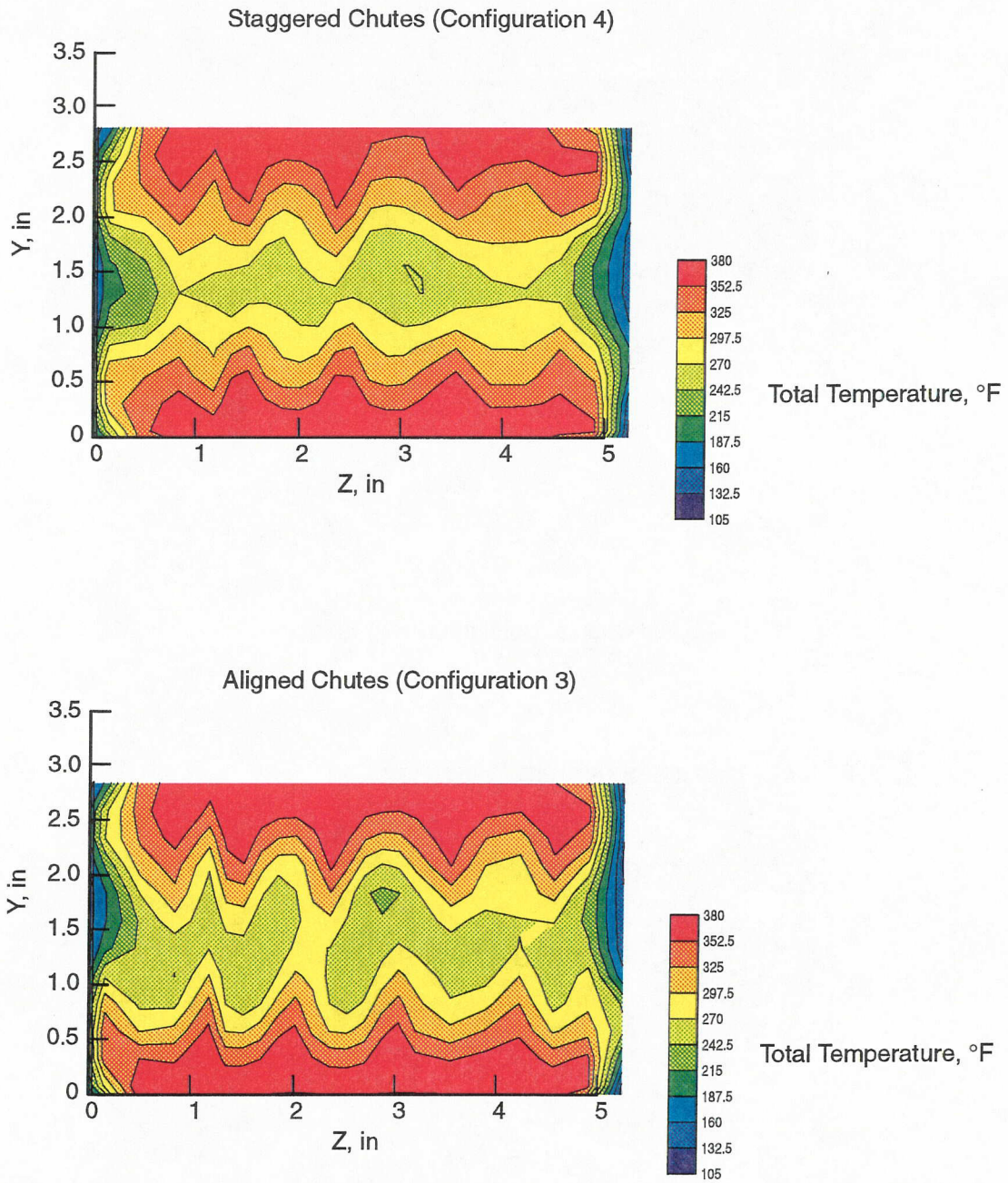


**Figure 158. Ejector exit total temperature contour plot comparisons for staggered and aligned case**

## 7.0 Conclusions and Recommendations

Some of the key objectives and results were described in the technical highlights of the overall program in the Introduction – Section 2. Here, more details are presented along with recommendations for further enhancement of the knowledge base of 2DME exhaust nozzles to enable HSCT to achieve environmental acceptability and economic viability.

### 7.1 Conclusions

#### 7.1.1 Acoustic Performance

Both SAR 2.8 and SAR 3.3, treated-wall, long-flap (120-in full scale) configurations meet FAR36 Stage 3 sideline noise level limits for ideal primary jet velocities  $V_j \leq 2400$  ft/s.

For jet velocities below 2450 ft/s, the SAR = 2.8 nozzle is slightly quieter than the SAR = 3.3 nozzle, but the trend reverses for jet velocities higher than 2500 ft/s. The noise-generation mechanisms of the mixer/ejector nozzles are complex, covering a wide range of turbulence length scales and frequencies, and the dominance of these different mechanisms are dependent on SAR and jet velocity. Broad generalizations that larger SAR will yield lower jet noise levels are not necessarily true.

For  $V_j > 2200$  ft/s, the MAR 0.95 nozzle is approximately 3 EPNdB quieter than the MAR 1.2 nozzle. Although MAR 1.2 entrains more secondary flow than MAR 0.95, noise levels for MAR 0.95 are significantly lower compared to MAR 1.2, due to various flowfield differences. Hence, it should be kept in mind that noise characteristics of the mixer/ejector nozzles are not at all single-valued functions of entrainment ratio; many factors impact measured noise characteristics.

Acoustic treatment yields approximately 3-EPNdB noise suppression at a nominal  $V_j \approx 2400$  ft/s, and the noise suppression due to treatment increases to approximately 4 EPNdB for velocities  $< 2000$  ft/s. However, as  $V_j$  increases to approximately 2600 ft/s, noise suppression by the acoustic treatment reduces to approximately 2.5 EPNdB. Increase in jet velocity beyond 2600 ft/s results in less noise suppression by the acoustic treatment.

Increasing the flap length from 80 to 120 inches in full scale for treated configuration results in an average noise reduction of 2.6 EPNdB in the  $V_j$  range of 1600 to 2800 ft/s; the effect for hard-walled configurations is 1.7 EPNdB reduction in the same  $V_j$  range. This implies that the 0.9 EPNdB reduction is provided by the acoustic treatment in the additional 40-in length of the flap. Also, the EPNL reduction due to treatment is fairly uniform over most of the  $V_j$  range. The LV data also indicate more uniformly mixed exit velocity profile for the 120-in flap compared to the 80-in flap.

The treated center wedge yielded approximately 1.7 to 4 EPNdB suppression relative to no-center-wedge configuration at a MAR of 1.2. However, the MAR 0.95 configuration without any center wedge yielded approximately 3-EPNdB noise reduction, compared to MAR 1.2 configuration without a center wedge, for  $V_j = 2200$  ft/s. The added weight, complexity, and performance loss associated with a long, treated, center wedge — in relation to the noise suppression provided — is deemed an unfavorable design trade to be pursued. MAR seems to be a more effective controlling parameter to simultaneously achieve noise suppression and improve takeoff  $C_{f_g}$ .

At all jet velocities, the EPNL's at sideline azimuthal location of  $25^\circ$  are the lowest, and as the azimuthal angle increases the EPNL values increase. At  $V_j \approx 2400$  ft/s, EPNL at the sideline

azimuthal location is approximately 2.5 EPNdB lower compared to at cutback azimuthal location of 90°. This EPNL difference increases to a maximum of approximately 4 EPNdB at  $V_j \approx 1900$  ft/s and reduces at  $V_j$  below 1900 ft/s. As  $V_j$  increases beyond 2400 ft/s, the azimuthal variation in EPNL reduces.

### 7.1.2 Aeroperformance

Two operating modes of the ejector — subsonic and supersonic — were identified. A significant increase in nozzle performance is observed associated with the supersonic mode. Peak static  $C_{f_g}$  of 0.95 was obtained at NPR of 4.0, for the SAR = 2.8, CER = 1.22, MAR 1.0 configuration, in the supersonic mode of ejector operation. Model vibration/instability was also experienced with the transition from subsonic to supersonic mode. The primary stream total temperature had a significant effect on transition from subsonic to supersonic mode. The NPR at which the transition to supersonic mode occurs increased with increasing primary total temperature.

Significant reduction is observed in the thrust minus drag coefficient with external flow: about 5 points at a free-stream Mach number of 0.32 at NPR = 4.0, relative to static conditions. The slope of the thrust minus drag coefficient with NPR for wind-on case is also steeper, relative to the static case. Pumping increased with increasing free-stream Mach Number. The actual increase in pumping with increased free-stream Mach number is lower than the corresponding increase in secondary flow total pressure due to the inlet recovery.

In general, the lower CER of 1.22 performed slightly better than the higher CER of 1.38, the differences between the two are significant in the NPR range of 2 to 3, and performance is nearly identical for NPR > 4. The difference between the two thrust/drag coefficients at static conditions is nearly 4 to 5 points at NPR of 2.0 and the difference is about 1 to 2 point at NPR = 3.0. There is also a significant difference in pumping, especially at lower pressure ratios. The possible reasons for this difference at lower pressure ratios could be losses associated with overexpansion and recompression of the primary flow in the chutes.

The mixing area ratio had significant effect on performance. The nozzle static performance, or the thrust coefficient  $C_{f_g}$ , essentially shows a peak at MAR  $\leq 1.0$  for all pressure ratios tested. The pumping characteristics also show a peak at a MAR of 1.0 for all pressure ratios  $\geq 2.5$ . At MAR of 0.80, the ejector operated in the subsonic mode at all NPR's tested.

The SAR of 3.3, with 28% higher secondary flow area than SAR of 2.8, pumps approximately 25% more at all NPR's, for both CER's. The static thrust performance correspondingly shows a significant improvement, about 3 to 4 points, with increased SAR at the lower NPR, in the subsonic mode. Also, the NPR at which the subsonic to supersonic transition occurs increased slightly with the higher SAR. In the supersonic mode, the lower SAR performs better than the higher SAR, by about 1 to 2 points. The slight benefit in the observed static performance disappeared under wind-on conditions, due to inlet ram drag and external form and friction drag.

The thrust minus drag performance does not show any significant difference, at static or wind-on test conditions, with changes in ejector flap length. The differences, especially in the low NPR range, are within the scatter of the test data.

The performance of the short wedge was significantly lower at almost all of the test conditions, 4 to 6 points relative to the no-wedge configurations. The long wedge, with associated reduction in MAR, has significantly improved performance at all test conditions relative to the no-wedge

configuration. However, the effect of reduced MAR by the presence of the long wedge on the performance is not as large as the MAR effect without the wedge.

### 7.1.3 Aeromixing

The LV data on nozzle exit velocity profiles at the same NPR indicates peak-to-valley variation for 860°R primary total temperature to be higher than that of 1590°R primary total temperature in the top-to-bottom (row-to-row or flap-to-flap) direction. In the spanwise (chute-to-chute or sidewall-to-sidewall) direction, the peaks and valleys corresponding to the primary and secondary chutes are clearly visible at lower temperature. However, at higher temperature, there are no discernable peaks and valleys, indicating better mixing in the spanwise direction with increased primary total temperature. The jet plume also decays faster downstream of the nozzle with increased primary total temperature.

Lower primary total temperature, 860°R tests also show good spanwise mixing. However, top-to-bottom mixing appears poor with lower velocity (as manifested by lower total temperature and pressure flow) in the middle (near the forward/aft centerline) and higher velocity (higher total temperature and pressure flow) near the two flaps.

At NPR = 4, divergent flaps (MAR = 1.2) showed strong rear shock with possible boundary layer separation, but parallel flaps (MAR = 1) pushed the rear shock outside the ejector in the plume. Detailed internal shock cells from overexpanded CD chutes inside the nozzle at suppressor exit were also observed.

## 7.2 Recommendations

- Evaluate the effect of MAR on aeroperformance further to establish optimum pumping and performance characteristics.
- Evaluate the effect of CER, especially convergent chutes (CER = 1.0) on both aerodynamic and acoustic performance.
- Evaluate the effect of lower SAR to establish optimum aerodynamic and acoustic performance, especially under wind-on conditions.
- Evaluate effect of chute alignment on aerodynamic and acoustic performance.

## 8.0 Symbols and Nomenclature

1D	One dimensional
2D	Two dimensional
2DCD	Two dimensional, convergent/divergent (exhaust nozzle configuration)
2DME	Two dimensional, mixer/ejector (exhaust nozzle configuration)
3D	Three dimensional
A	Cross-sectional area, in <sup>2</sup>
A <sub>8</sub>	Exhaust nozzle primary flow throat area
A <sub>9</sub>	Exhaust nozzle exit area, $2 \times h_9 \times w_9$
A <sub>E</sub>	Aerodynamic effective area
A <sub>m</sub> or A <sub>mix</sub>	Total mixed-flow area, $A_{p8} + A_{s8} = 2 \times h_{mix} \times w_9 - 2n \times (h_{mix} - h_8) \times w_{p8}$
A <sub>p8</sub>	Primary nozzle throat area, $(h_8 - h_{gap}) \times w_{p8} \times 2n + 2 \times h_{gap} \times w_9$
A <sub>p89</sub>	Suppressor exit plane area, $(h_{mix} - h_{gap}) \times w_{s8} \times 2n$
A <sub>s8</sub>	Secondary flow area at throat plane, $(h_{mix} - h_{gap}) \times w_{s8} \times 2n$
ARL	Aerodynamic Research Laboratory (GEAE facility)
CD	Convergent/divergent
C <sub>D8</sub>	Primary nozzle flow coefficient: ratio of actual mass flow to the ideal mass flow
CER	Chute expansion ratio: ratio of the primary flow area at the suppressor exit to the primary throat area, $A_{p89} / A_{p8}$
CFD	Computational fluid dynamics
C <sub>f-Dnoz</sub>	Thrust minus nozzle drag coefficient: ratio of measured nozzle thrust minus drag to the primary nozzle ideal thrust, $(F - D_{noz}) / F_i$
C <sub>f<sub>g</sub></sub>	Nozzle thrust coefficient or coefficient of gross thrust: ratio of measured exit gross thrust to ideal gross thrust
CTC	Climb to cruise
D	Total drag, lbf
d	Characteristic length scale, such as jet diameter
D <sub>noz</sub>	Nozzle drag
EGA	Extra ground attenuation
EPNdB	Effective perceived noise decibel
EPNL	Effective perceived noise level based on PNLT, dB
F	Thrust, lbf
f	Frequency, Hz

F-D	Measured thrust minus drag corrected for balance tare
F-D <sub>noz</sub>	Measured thrust minus nozzle drag
F <sub>i</sub>	Primary nozzle ideal thrust based on measured weight flow rate, $W_p \times V_j$
F <sub>N</sub>	Net thrust, $F - D$
GEAE	GE Aircraft Engines
h	Height (usually half height), inches
h <sub>8</sub>	Chute height from centerline at throat plane
h <sub>9</sub>	Half height of nozzle from centerline to flap trailing edge (exit)
h <sub>ex</sub>	Half height at ejector exit
h <sub>gap</sub>	Half height from nozzle centerline to suppressor chute foot
h <sub>m</sub> or h <sub>mix</sub>	Chute height from nozzle centerline at mixing plane
HSCT	High Speed Civil Transport
L	Length, in
LDV	Laser doppler velocimeter (or velocimetry)
L <sub>ej</sub>	Ejector length (divergent flap)
L2F	Laser two-focus (velocimeter system)
LV	Laser velocimeter
M	Mach number (free-stream unless otherwise designated)
M <sub>0</sub>	Free-stream Mach number, calculated
MAR	Mixing area ratio: ratio of mixer exit to inlet area, $A_9 / A_{mix}$
M <sub>c</sub>	Eddy convection Mach number
MCW	Mini center wedge; a short wedge that blocks off the hot central streak of the nozzle
MFTF	Mixed-flow turbofan
M <sub>p</sub>	Primary chute Mach number
MPA	Model preparation area
M <sub>s</sub>	Secondary chute Mach number
M <sub>T</sub>	Mixing effectiveness
n	Number of chutes in each half of suppressor
NPR	Primary nozzle pressure ratio: calculated as $P_{tp} / P_0$
NPR <sub>C</sub>	Critical primary nozzle pressure ratio
P	Static pressure, psia
PLR	Program lapse rate

PNdB	Perceived noise decibel
PNL	Perceived noise level, dB
PNLT	Tone-corrected perceived noise level, dB
$P_T$	Total pressure, psia
$P_{T0}$	Free-stream total pressure, measured
$P_{Tp}$	Primary nozzle inlet total pressure, measured
$P_{Ts}$	Secondary inlet total pressure, measured
SAR	Suppressor area ratio: ratio of mixed-flow area to primary nozzle throat, $A_{mix} / A_{p8}$
SPL	Sound Pressure Level, dB
RC	Reference conic (exhaust nozzle)
T	Static temperature, °R
$T_0$	Free-stream static temperature, calculated
$T_8$	Nozzle throat static temperature
TCW	Treated center wedge; a long wedge that blocks the hot central streak, extends the full length of the nozzle flap (120 inches in full scale), and has acoustic treatment on the top and bottom sides of the wedge
TOGW	Takeoff gross weight, lbm
$T_T$	Total temperature, °R
$T_{T0}$	Free-stream total temperature, measured
$T_{T8}$	Total temperature at nozzle throat (primary jet)
$T_{Tp}$	Primary nozzle inlet total temperature, measured
$T_{Ts}$	Secondary nozzle inlet total temperature
V	Flow velocity, ft/s
$V_0$	Free-stream velocity (simulated flight speed)
VCE	Variable-cycle engine
$V_j$	Primary nozzle ideal jet velocity, ft/s, calculated based on $NPR$ and $T_{T8}$
W	Fluid flow, lbm/s
w	Width, in
$w_9$	Exhaust system width from sidewall to sidewall
$W_s$	Secondary inlet flow, calculated
$W_T$	Total nozzle flow rate: $W_p + W_s$
$W_p$	Primary nozzle flow
$W_{pi}$	Primary nozzle ideal flow, calculated

X	Major axis of model and measurement array; forward/aft direction
Y	Vertical axis of model and measurement array; top/bottom, row-to-row, or flap-to-flap direction
Z	Horizontal axis of model and measurement array; spanwise, chute-to-chute, or sidewall-to-sidewall direction
$\gamma$	Ratio of specific heat at constant pressure to specific heat at constant volume
$\omega$	Pumping ratio: ratio of secondary to primary flow rates, $W_s / W_p$
$\omega \sqrt{\tau}$	Corrected pumping ratio, $(W_s / W_p) \sqrt{(T_{Ts} / T_{Tp})}$
$\theta$	Polar directivity angle measured from the inlet axis, degrees
$\phi$	Azimuthal angle measured from the nozzle major axis, degrees

#### Plane (Engine Station) Designations and Other Subscripts

0	Free stream
2	Fan inlet
7	Exhaust nozzle inlet
8	Nozzle throat
9	Nozzle exit
89	Suppressor exit
$\infty$	Ambient: static air conditions outside the engine
ej	Ejector
f	Flap
noz	Nozzle
mix, m	Mixing plane
p	Primary chute
S	Static
s	Secondary chute
T	Total
x	Forward/aft direction (X axis)
y	Vertical direction (Y axis)
z	Horizontal (chute-to-chute) direction (Z axis)

## 9.0 References

1. Majjigi, R.K. et al., "Low Noise Exhaust Nozzle Technology Development – Preliminary Design Report and Test Plan Review," Contract Report Prepared by GEAE for Contract NAS3-25415, January 1993.
2. Brausch, J.F. et al., "Simulated Flight Acoustic Investigation of Treated Ejector Effectiveness on Advanced Mechanical Suppressors for High Velocity Jet Noise Reduction," NASA CR-4019, November 1986.
3. Elliott, J.K., Manning, T.A., Qiu, Y.J., Greitzer, E.M., Tan, C.S., and Tillman, T.G., "Computational and Experimental Studies of Flow in Multi-Lobed Forced Mixers," AIAA Paper 92-3568.
4. Hubbard, H., Ed., "Aeroacoustics of Flight Vehicles: Theory and Practice, Chapter 15 – Jet Noise Suppression," NASA Reference Publication 1258, Vol. 2, August 1991.
5. Mani, R., Clapper, W.S., et al., "High Velocity Jet Noise Source Location and Reduction, Task 4 – Development/Evaluation of Techniques for Inflight Investigation," FAA-RD-76-79, IV, February 1977.
6. Der, J. Jr., "Improved Methods of Characterizing Ejector Pumping Performance," AIAA Paper 89-0008, 1989.
7. Staff of the Propulsion Aerodynamic Branch, "A User's Guide to the Langley 16-Foot Transonic Wind Tunnel Complex," NASA TM102750, September 1990.
8. Braden, R.P., Nagaraja, K.S., and Von Ohain, H.J.P., "Proceedings: Ejector Workshop for Aerospace Applications," AFWL-TR-82-3059, Wright-Patterson Air Force Base, June 1982.
9. DeBonis, J.R., "Full Navier-Stokes Analysis of a Two-Dimensional Mixer/Ejector Nozzle for Noise Suppression," AIAA-92-3570, 1992.
10. Qiu, Y.J., *A Study of Streamwise Vortex Enhanced Mixing in Lobed Mixer Devices*. PhD Thesis (MIT), 1992, p 208.
11. Roshko, A., "Structure of Turbulent Shear Flows: A New Look," AIAA J., vol. 14.10, 1976, pp 1349-1357.
12. Papamoschuo, D. and Roshko, A., "The Compressible Turbulent Shear Layer: An Experimental Study," *J. Fluid Mech.*, Vol. 197, 1988, pp 453-477.
13. Brown and Roshko, "On Density Effects and Large Structure in Turbulent Mixing Layers," *J. Fluid Mech.*, vol. 64 pt.4, pp 775-816, 1974.
14. Mengle, V.G., Uenishi, K., and Majjigi, R.K., "Generation 1.5 HSCT Nozzle Model Test Program – Model Concept Definition & Planning Study," NASA Contract NAS3-26617, Task Order 18, Monthly Report No. 5, 1993.

# REPORT DOCUMENTATION PAGE

*Form Approved*  
*OMB No. 0704-0188*

Public reporting burden for this collection of information is estimated to average 1 hour per response, including the time for reviewing instructions, searching existing data sources, gathering and maintaining the data needed, and completing and reviewing the collection of information. Send comments regarding this burden estimate or any other aspect of this collection of information, including suggestions for reducing this burden, to Washington Headquarters Services, Directorate for Information Operations and Reports, 1215 Jefferson Davis Highway, Suite 1204, Arlington, VA 22202-4302, and to the Office of Management and Budget, Paperwork Reduction Project (0704-0188), Washington, DC 20503.

<b>1. AGENCY USE ONLY</b> <i>(Leave blank)</i>	<b>2. REPORT DATE</b> February 2005	<b>3. REPORT TYPE AND DATES COVERED</b> Final Contractor Report	
<b>4. TITLE AND SUBTITLE</b>  Low Noise Exhaust Nozzle Technology Development		<b>5. FUNDING NUMBERS</b>  WBS-22-714-09-46 NAS3-25415	
<b>6. AUTHOR(S)</b>  R.K. Majjigi, C. Balan, V. Mengle, J.F. Brausch, H. Shin, and J.K. Askew			
<b>7. PERFORMING ORGANIZATION NAME(S) AND ADDRESS(ES)</b>  General Electric Aircraft Engines One Neumann Way Cincinnati, Ohio 45125-1988		<b>8. PERFORMING ORGANIZATION REPORT NUMBER</b>  E-14785	
<b>9. SPONSORING/MONITORING AGENCY NAME(S) AND ADDRESS(ES)</b>  National Aeronautics and Space Administration Washington, DC 20546-0001		<b>10. SPONSORING/MONITORING AGENCY REPORT NUMBER</b>  NASA CR-2005-213325	
<b>11. SUPPLEMENTARY NOTES</b>  This research was originally published internally as HSR044 in November 1996. Responsible person, Diane Chapman, Ultra-Efficient Engine Technology Program Office, NASA Glenn Research Center, organization code PA, 216-433-2309.			
<b>12a. DISTRIBUTION/AVAILABILITY STATEMENT</b>  Unclassified - Unlimited Subject Categories: 01, 05, and 07 Available electronically at <a href="http://gltrs.grc.nasa.gov">http://gltrs.grc.nasa.gov</a> This publication is available from the NASA Center for AeroSpace Information, 301-621-0390.		<b>12b. DISTRIBUTION CODE</b>	
<b>13. ABSTRACT</b> <i>(Maximum 200 words)</i>  NASA and the U.S. aerospace industry have been assessing the economic viability and environmental acceptability of a second-generation supersonic civil transport, or High Speed Civil Transport (HSCT). Development of a propulsion system that satisfies strict airport noise regulations and provides high levels of cruise and transonic performance with adequate takeoff performance, at an acceptable weight, is critical to the success of any HSCT program. The principal objectives were to: 1. Develop a preliminary design of an innovative 2-D exhaust nozzle with the goal of meeting FAR36 Stage III noise levels and providing high levels of cruise performance with a high specific thrust for Mach 2.4 HSCT with a range of 5000 nmi and a payload of 51,900 lbm, 2. Employ advanced acoustic and aerodynamic codes during preliminary design, 3. Develop a comprehensive acoustic and aerodynamic database through scale-model testing of low-noise, high-performance, 2-D nozzle configurations, based on the preliminary design, and 4. Verify acoustic and aerodynamic predictions by means of scale-model testing. The results were: 1. The preliminary design of a 2-D, convergent/divergent suppressor ejector nozzle for a variable-cycle engine powered, Mach 2.4 HSCT was evolved, 2. Noise goals were predicted to be achievable for three takeoff scenarios, and 3. Impact of noise suppression, nozzle aerodynamic performance, and nozzle weight on HSCT takeoff gross weight were assessed.			
<b>14. SUBJECT TERMS</b> High speed civil transport; Exhaust nozzles; Suppressor ejector nozzles; Convergent/divergent chutes; Ejector/chute inlets		<b>15. NUMBER OF PAGES</b> 166	
		<b>16. PRICE CODE</b>	
<b>17. SECURITY CLASSIFICATION OF REPORT</b> Unclassified	<b>18. SECURITY CLASSIFICATION OF THIS PAGE</b> Unclassified	<b>19. SECURITY CLASSIFICATION OF ABSTRACT</b> Unclassified	<b>20. LIMITATION OF ABSTRACT</b>



